# Spectroscopie $\gamma$ du noyau exotique 79Cu

Massyl Kaci

## To cite this version:

Massyl Kaci. Spectroscopie $\gamma$ du noyau exotique 79Cu. Nuclear Experiment [nucl-ex]. Université Paris-Saclay, 2024. English. NNT : 2024UPASP071 . tel-04845596

**HAL Id: tel-04845596**
**https://theses.hal.science/tel-04845596v1**

Submitted on 18 Dec 2024

THÈSE DE DOCTORAT

NNT: 2024UPASP071

# $\gamma$ spectroscopy of the exotic $^{79}$Cu nucleus

*Spectroscopie $\gamma$ du noyau exotique $^{79}$Cu*

**Thèse de doctorat de l'université Paris-Saclay**

École doctorale n°576, Particules, hadrons, énergie et noyaux :
instrumentation, image, cosmos et simulation (Pheniics)
Spécialité de doctorat : Physique Nucléaire
Graduate School : Physique, Référent : Faculté des sciences d'Orsay

Thèse préparée dans l'unité de recherche **IJCLab** (Université Paris-Saclay, CNRS),
sous la direction de **Serge FRANCHOO**, Directeur de recherche

**Thèse soutenue à Paris-Saclay, le 26 Septembre 2024, par**

## Massyl KACI

### Composition du Jury

Membres du jury avec voix délibérative

| | |
|---|---|
| **Araceli LOPEZ MARTENS**<br>Directrice de recherche, IJCLab, Orsay | Présidente |
| **Emmanuel CLÉMENT**<br>Directeur de recherche , CNRS, GANIL, Caen | Rapporteur & Examinateur |
| **Caterina MICHELAGNOLI**<br>Directrice de recherche, Institut Laue Langevin, Grenoble | Rapporteuse & Examinatrice |
| **Joa Ljungvall**<br>Directeur de recherche, IPHC, Strasbourg | Examinateur |
| **Korten WOLFRAM**<br>Directeur de recherche, CEA/IRFU, Saclay | Examinateur |

université
PARIS-SACLAY

**ÉCOLE DOCTORALE**
Particules, hadrons, énergie et noyau :
instrumentation, imagerie, cosmos
et simulation (PHENIICS)

**Titre :** Spectroscopie gamma du noyau exotique $^{79}$Cu

**Mots clés :** Gamma, spectroscopie, cuivre, période radioactive, noyaux exotiques, structure nucléaire

**Résumé :** Le $^{78}$Ni est un noyau emblématique pour les études de structure nucléaire loin de la ligne de stabilité, au centre de nombreuses expériences récentes auprès des accélérateurs autour du monde. Bien qu'un caractère magique soit attendu pour les couches de protons (Z = 28) et de neutrons (N = 50), des travaux théoriques et expérimentaux suggèrent un affaiblissement important. Cela donne lieu à des déformations qui pourront exister dans le noyau à des énergies qui sont proches, un phénomène connu comme la coexistence de formes et aujourd'hui un sujet de recherche très actif. L'expérience vise à exploiter l'opportunité unique de combiner la spectroscopie gamma de haute résolution avec les faisceaux de grande intensité qui sont actuellement disponibles à RIBF au Japon, afin d'étudier les noyaux au voisinage du $^{78}$Ni. La thèse se focalisera sur le noyau exotique $^{79}$Cu, noyau contenant un proton autour d'un coeur de $^{78}$Ni dont on pourra suivre le comportement détaillé, poursuivant ainsi les travaux initiés par notre équipe.

**Title :** Gamma spectroscopy of the exotic $^{79}$Cu nucleus

**Keywords :** Gamma, spectroscopy, copper, lifetime, exotic nuclei, nuclear structure

**Abstract :** $^{78}$Ni is an iconic neutron-rich nucleus for structure studies located far from the line of stability and the primary focus of many recent experimental investigations. Though a closed magic character for both the proton (Z=28) and neutron (N=50) shells is expected, theoretical and experimental work has suggested that either shell gap may be weakened. This may give rise to deformed shapes that exist in the nucleus at nearby energies, a phenomenon known as shape coexistence and an active topic of research these days. The experiment aims to profit from the unique opportunity of gamma-ray spectroscopy with a high-resolution detector array, combined with the high-intensity beam provided by the RIBF facility in Japan to investigate the nuclei around $^{78}$Ni. In particular the thesis will focus on the exotic nucleus $^{79}$Cu, which contains one proton orbiting around an inner core of $^{78}$Ni, continuing the previous work that was initiated by our group.

# Remerciements

La thèse est une expérience à la fois longue et courte. La mienne ayant eu lieu au sein de l'équipe SDF du pôle de physique nucléaire à IJCLab, chaque personne a joué un rôle plus ou moins important pour le bon déroulement de cette expérience. Je tiens donc à exprimer ma profonde gratitude à toutes les personnes qui ont contribué à l'élaboration de cette thèse et m'ont soutenu durant cette période exigeante.

Je souhaite d'abord remercier les membres de mon Jury d'avoir pris le temps de lire attentivement mon manuscrit et pour leurs commentaires et suggestions d'amélioration de ce dernier.

Ensuite, je tiens à remercier Laure-Amélie, qui m'a toujours assisté lors de mes problèmes sur le serveur du laboratoire, notamment ceux liés à l'espace disque, sans que je n'aie à passer par le système de tickets, car je me rendais directement à son bureau. Son aide a été indispensable pour me permettre de travailler sereinement sur mes données.

Je suis reconnaissant envers tous les membres de la collaboration HiCARI pour les échanges enrichissants, en particulier Kathrin pour les codes qu'elle a fournis facilitant l'utilisation d'Anaroot, ainsi que Ryo, Freddy et Léo. Les discussions informelles que nous avions régulièrement m'ont aidé à bien mieux gérer les subtilités de l'analyse des données.

Je remercie également mes frères et sœurs, ainsi que mes parents, pour leur soutien permanent, eux qui ne connaissent pas grand chose à mon sujet de recherche.

Un grand merci à mes amis jammeurs, François, Jihane, Jimmy et Malia, avec qui on jouait de temps en temps pour se changer les idées.

Je tiens à exprimer ma gratitude à Jean-Yves et Marine pour leur bienveillance et leur aide précieuse dans la préparation des parties administratives liées aux missions de travail.

Je suis également reconnaissant envers tous les membres du pôle nucléaire, avec qui j'ai partagé repas et moments de pause, qu'ils soient permanents ou étudiants. Pour les permanents, je pense particulièrement à Iolanda, la première personne que j'ai connue au laboratoire et qui m'a encadrée lors de mon stage de M1. C'est en quelque sorte grâce à elle que j'ai pu débuter cette aventure en revenant pour mon stage de M2. Je remercie également David, qui a joué un rôle crucial pour moi. En tant que professeur de physique nucléaire en M2 et référent à l'école doctorale, ses conseils et son expertise m'ont grandement aidé. C'était aussi avec un grand plaisir que nous organisions ensemble les sessions mensuelles de CAPHYNes.

Aux étudiants, je suis reconnaissant pour tous les moments de convivialité et festivités partagées, au laboratoire ou ailleurs. Je pense en particulier aux doctorants avec qui j'ai partagé le bureau : Sarah, qui m'a beaucoup aidé avec son expérience et sa connaissance du laboratoire, surtout au début, et Alessandro, avec qui nous parlions souvent de football. Je souhaite bonne chance aux doctorants qui vont bientôt soutenir après moi : Corentin (qui est SDF comme moi), Praveen et Wenling. Ensuite, ce sera le tour d'Émile, Hugo, Omar, Sarah, Brigitte, Maroua, Malia, Tania et Elia.

Je remercie les responsables des unités d'enseignement que j'ai assurées à la faculté des sciences d'Orsay : Jacques, Kévin et Claire, ainsi que mes collègues moniteurs et monitrices, avec qui nous échangions souvent nos séances pour nous permettre par exemple d'aller à des conférences ou à des expériences.

Enfin, le meilleur pour la fin, je souhaite exprimer ma plus profonde gratitude à mon directeur de thèse, Serge, avec qui j'ai travaillé depuis le début de mon stage de M2 jusqu'à la fin de ma thèse, pour la confiance qu'il m'a accordée. Son expertise et son dévouement ont été essentiels au bon déroulement de mes travaux. Je le remercie également pour ses encouragements à participer à des expériences et des conférences en dehors du laboratoire, pour découvrir des installations et une physique différente de celle de mon sujet de recherche. Au-delà du costume de physicien, les autres discussions que nous avions de temps à autres sur des sujets divers comme la politique internationale, ont été particulièrement enrichissantes.

Massyl

# Contents

> *"It is obvious that the difficulties which we have to surmount in order to make any progress in understanding the fundamental interrelations of the nucleons are quite formidable and have, in fact, grown little less over the past decades despite the efforts of many people.".*
>
> Richard Feynman

Nuclear physics occupies a unique and pivotal position within the realm of physical sciences, existing at an intermediary scale between atomic physics and high energy physics. This field of science deals with the atomic nucleus which is a complex and intriguing system that exhibits a diverse range of behaviors, including deformation, collective excitation, radioactive decay and particle emission. Since its discovery by E. Rutherford [1] and his students Geiger and Marsden, with the famous gold-foil experiment, several models were developed to understand its numerous properties. However, despite more than a century of experimental and theoretical studies, a unified theory that explains all nuclear phenomena has yet to be established.

Early research proposed that the nucleus possessed a shell structure akin to that of electrons in an atom. This was motivated by the observation of an enhanced stability for nuclei having some special numbers of protons and/or neutrons (2, 8, 20, 28, 50, 82 and 126), known as magic numbers. These numbers, highlighted in figure 1 on the nuclear chart, were evidenced from several observations such as the extra-binding energy or the higher relative abundances of their corresponding isotopes and isotones as compared to their neighbors. In order to reproduce these numbers, several nuclear potentials were used in the Hamiltonian describing the nucleus. In these models, an independent-particle picture was assumed, where each nucleon independently moves in an average potential generated by the other nucleons. Many potentials such as the infinite square-well, the harmonic oscillator or the more realistic Woods-Saxon potential were tested. Nevertheless, all the latter could only establish the three first magic numbers (2, 8 and 20) and failed for the remaining ones.

The solution to this issue was found in 1949 by Goeppert Mayer [2] and Haxel, Jensen and Suess [3], who introduced a spin-orbit term, again by analogy with atomic physics. The addition of this interaction led to the mentioned numbers. However, the latter are only valid close to the valley of stability, and are not universal throughout the nuclear chart, and understanding the evolution of shell structure for extreme neutron over proton $N/Z$ ratios remains one of the greatest challenges in nuclear structure research. The development of radioactive-ion beam facilities worldwide over the past decades has enabled researchers to explore increasingly exotic regions of the nuclear chart. A variety of experimental methods, such as laser spectroscopy, mass measurement, $\beta$-decay studies, Coulomb excitation and nuclear reactions involving a wide range of energies, have been developed to access multiple facets of the nucleus. These techniques are complementary, and their combined use offers a promising avenue for advancing the understanding of nuclear structure.

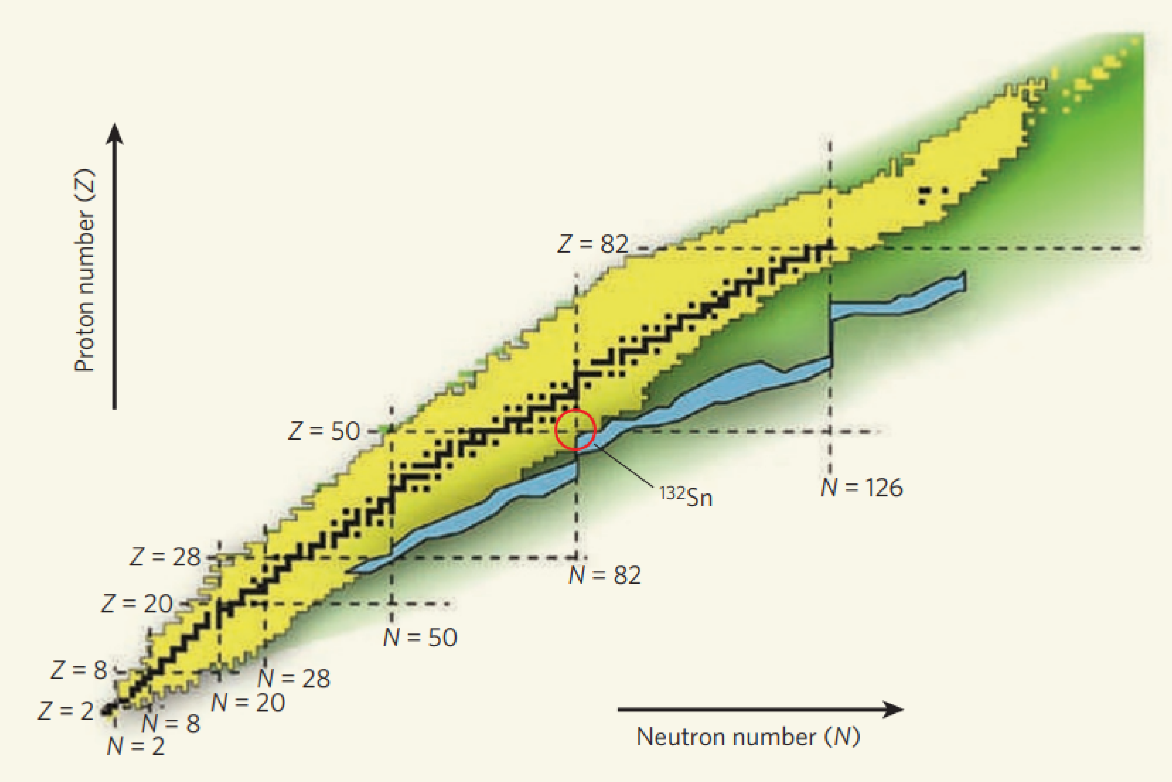

Figure 1: The chart of nuclides, the conventional magic numbers are indicated and the stable nuclei are illustrated in black color. The $^{132}$Sn isotope is highlighted as an example of a nucleus with a magic number for both protons ($Z = 50$) and neutrons ($N = 82$). Image taken from [4].

This thesis focuses on the evolution of the proton shell towards the $^{78}$Ni nucleus ($Z = 28$, $N = 50$), which is believed to be a doubly-magic nucleus. We investigate the evolution of the $Z = 28$ gap towards $N = 50$ by examining the single-particle character of states in the copper isotopic chain, which has one additional proton compared to nickel. Specifically, we study the $^{79}$Cu isotope at $N = 50$, which is produced through proton-knockout reactions and analyzed using in-beam $\gamma$-ray spectroscopy.

Chapter 1 describes the physics motivations behind this study, while chapters 2 and 3 detail the experimental setup and the data analysis steps, respectively. In chapter 4, the procedure for lifetime extraction is described and tested on a known case for the validation of the methodology. This procedure is then applied on the $^{79}$Cu case of interest in chapter 5. Finally, the results are interpreted and compared with theoretical calculations in chapter 6.

# 1

# Physics motivation

## Contents

## 1.1 Nuclear shell model

In dealing with the many-body problem of atomic nuclei, the nuclear shell model has established itself as an efficient technique. Its reliability for nuclei of the valley of stability and its vicinity is well-established, and in this work, the fundamental aspects of this model are outlined, as well as the processes intervening in exotic nuclei.

### 1.1.1 Independent particle model

.

To describe the properties of a nucleus ${}^{A}_{Z}\mathrm{X}$, with the Hamiltonian $\hat{H}$ and the $A$-body wave function $\psi_A$, the solution to the Schrödinger equation is required:

$$\hat{H}\ \psi_A = \left[\sum_{i=1}^{A}\left(-\frac{\hbar^2}{2m}\Delta_i\right) + \sum_{i<j} W(i,j)\right]\psi_A = E\ \psi_A \tag{1.1}$$

where the first term of the Hamiltonian represents the sum of the kinetic energies of the individual nucleons and the second term is the many-body interaction. Here, for simplicity, only the two-body interaction is shown, but the same reasoning applies to terms involving more bodies.

The nuclear shell model's fundamental hypothesis posits that each nucleon moves independently within a mean field that represents the average interaction with other nucleons, denoted by a one-body potential $U(i)$. The Hamiltonian is then expressed as:

$$\hat{H} = \left[\sum_{i=1}^{A}\left(-\frac{\hbar^2}{2m}\Delta_i + U(i)\right)\right] + \left[\sum_{i<j} W(i,j) - \sum_{i=1}^{A} U(i)\right] = \hat{H}^{(0)} + \hat{V} \tag{1.2}$$

where $\hat{H}^{(0)}$ is the sum of the single-particle Hamiltonians and $\hat{V}$ is the residual interaction that can be minimized and neglected in the independent-particle model with an appropriate choice of $U$. The nearly constant nucleon density in stable nuclei and the short-range nature of nuclear forces[1] justify using a Woods-Saxon potential for $U$, or approximating it with a harmonic oscillator potential. The nucleon orbitals derived from such potentials are depicted in figure 1.1, showing large gaps between shells corresponding to the harmonic oscillator magic numbers: 2, 8, 20, 40, and 70. The Woods-Saxon potential is more realistic than the harmonic oscillator one since the latter is infinite[2]. Its use lowers the overall energies and partially lifts the energy

---

[1] The range of the nuclear force is of the order of 1 fm = $10^{-15}$ m, and all the known nuclei have a radius of 1 to 8 fm.

[2] With an infinite potential, the nucleons would be trapped in the well, and their separation from the nuclei would not be possible.

degeneracy by separating the states with different orbital angular momentum quantum number $l$ into different sub-shells. However, the resulting energy gaps still do not allow to establish all the conventional magic numbers.

To solve this issue, Goeppert Mayer [2], along with Haxel, Jensen, and Suess [3], independently suggested adding a spin-orbit term to the potential, similar to the interaction in atoms. In this fashion, good quantum numbers for the eigenstates are the orbital quantum number $l$ and the total angular momentum[3] $j$. Then, the spin-orbit partners are affected in an opposite manner such that the upper $j$ state $(l + 1/2)$ is lowered in energy while the lower $j$ state $(l - 1/2)$ is raised in energy with a splitting that is roughly proportional[4] to $l$, each $j$ state having a degeneracy of $2j + 1$. The resulting energy gaps finally lead to successfully reproduce the full list of the observed magic numbers, as illustrated on the right side of figure 1.1.

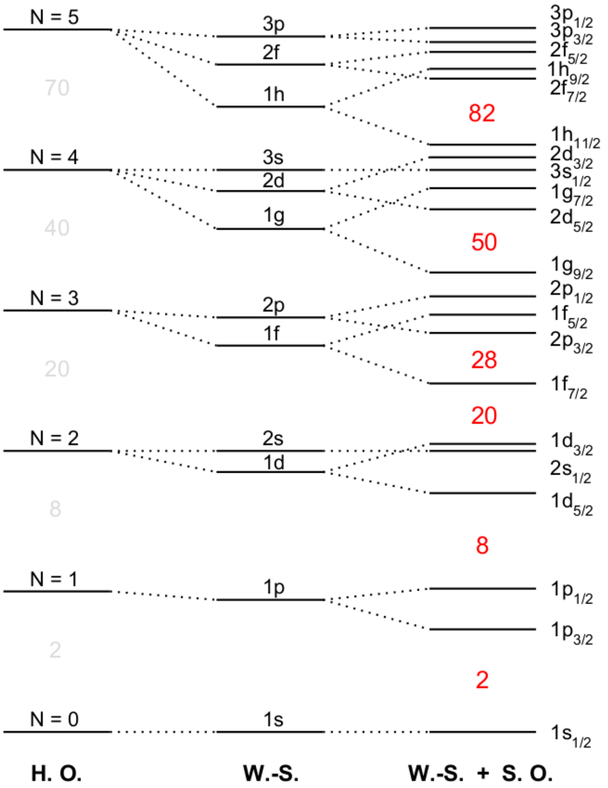

Figure 1.1: Energy of single-particle orbitals as predicted by the shell model using (left) a harmonic oscillator potential, (middle) a Woods-Saxon potential, and (right) a Woods-Saxon potential with a spin-orbit coupling. Image taken from [5].

The independent-particle model is essentially valid for closed-shell nuclei with one

---

[3] $\vec{J} = \vec{L} + \vec{S}$ is the total angular momentum, and $j$ is the corresponding quantum number, such that $\vec{J}^2 = j(j+1)\hbar^2$ where $\hbar$ is the reduced Planck constant.

[4] With the exception for the "$s$" states ($L = 0$) which are not affected by the spin-orbit splitting.

additional particle or hole. However, as the number of protons or neutrons deviates from the magic numbers, the residual interaction becomes significant. Furthermore, these magic numbers are not universal across the nuclear chart. Nuclear forces far from stability can lead to displacements of the energy levels and structural rearrangements, causing some magic numbers to disappear, while new magic numbers can emerge [6]. The first hints to these phenomena came through experimental evidences, such as atomic mass [7], nuclear radii and $2_1^+$ excitation energies trends [8–11].

An example of structural evolution away from stability is depicted in figure 1.2, which shows the disruption of the $N = 28$ shell closure. The energy of the first excited $2_1^+$ state is plotted against the neutron number $N$. For calcium isotopes ($Z = 20$), there is a significant rise in energy at $N = 28$ and $N = 20$, indicating that these isotopes are doubly magic. However, for argon ($Z = 18$) and sulfur ($Z = 16$) isotopes, the increase in $E(2_1^+)$ at $N = 28$ is much smaller, suggesting a gradual disappearance of this shell closure as one moves below calcium and reaches a larger $N/Z$ ratio. This is confirmed by the $2_1^+$ energies of silicon isotopes, which show no increase at $N = 28$.

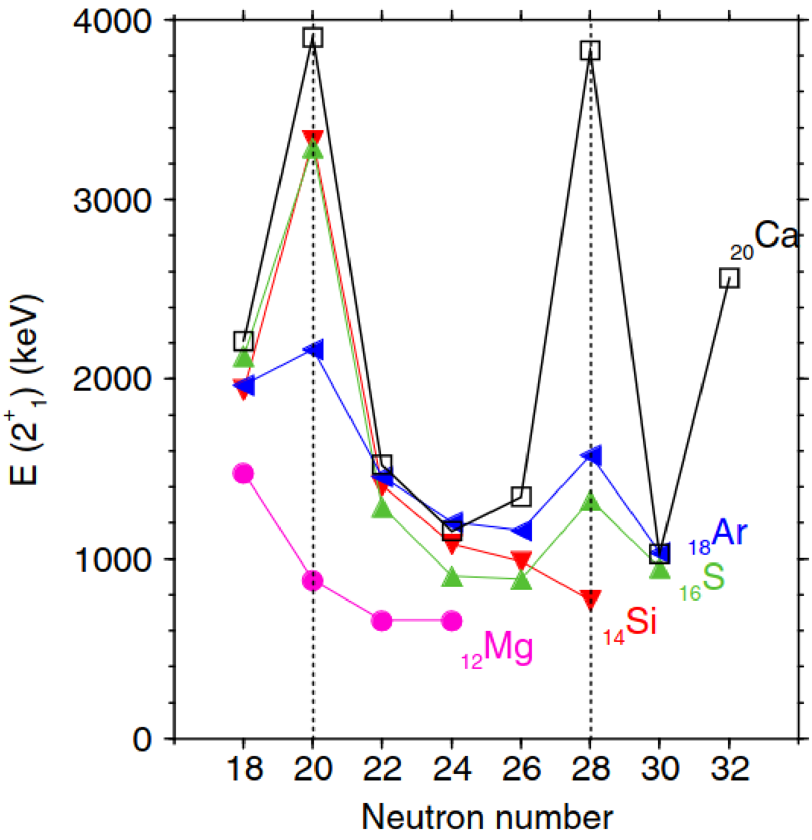

Figure 1.2: Experimental values of the energy of the $2_1^+$ state for the isotopic chains from Mg to Ca. Image taken from [12].

This raises questions about the persistence of the $Z = 28$ gap in exotic regions of the nuclear chart, and leads us to the study of the proton shell gap in the neutron-rich copper isotopes, and particularly the $^{79}$Cu, with one proton above the core of the supposedly doubly magic $^{78}$Ni.

### 1.1.2 The nature of nuclear force

The nuclear force is the result of one of the 4 fundamental interactions in the standard model of particle physics. It originates from the interaction of color-charged particles, the quarks and gluons. The nucleus components, the protons and neutrons are each made of 3 valence quarks and the study of their internal structure is the field of Quantum Chromo-Dynamics. This theory accurately reproduces the properties of the nucleons, but for a system with an increasing number of nucleons, the computational cost of the calculations grows exponentially, and such a treatment quickly becomes undoable. Instead, one takes the degrees of freedom as the individual nucleons and studies the nature of the interaction between these composite particles. The characteristics of the force between two nucleons are derived in first place from nucleon-nucleon scattering experiments and the study of the deuteron, the simplest and only bound two-nucleon system. From these observations, several general properties of the nucleon-nucleon ($NN$) interaction can be identified:

- It has a short range of the order of 1 fm. At these distances the force is attractive and leads to the binding of nucleons within a nucleus.

- At much shorter distances, the potential is repulsive. This prevents the collapse of nuclear matter when the distance between the two nucleons tends to zero and ensures the validity of the Pauli exclusion principle. For instance, for two nucleons with coupled spin $S = 0$ (spin-singlet), relative orbital angular momentum $L = 0$, and isospin[5] $T = 1$, the potential exhibits these characteristics, as illustrated in figure 1.3.

- It has a spin dependence, evidenced by the fact that no nucleon pair with $S = 0$ is bound, unlike the $S = 1$ ground state of the deuteron[6].

---

[5] The isospin $T$ is a quantum number used to describe the symmetry between protons and neutrons (or up and down quarks). In particle physics, the convention assigns isospin $T_3 = +1/2$ to up quarks and $T_3 = -1/2$ to down quarks, where $T_3$ is the isospin projection on a chosen axis. In nuclear physics, the opposite convention is used, with protons having $T_3 = -1/2$ and neutrons $T_3 = +1/2$.

[6] The ground state of the deuteron has a total angular momentum of unity and a positive parity $J^{\pi}{=}1^{+}$.

- It includes a non-central component[7], lacking spherical symmetry, which consists of the spin-orbit term $\vec{L} \cdot \vec{S}$ and the tensor term $S_{12}$ given by:

  $$S_{12} = \frac{3(\vec{\sigma}_1 \cdot \vec{r})(\vec{\sigma}_2 \cdot \vec{r})}{r^2} - \vec{\sigma}_1 \cdot \vec{\sigma}_2$$

  where $r = |\vec{r}_1 - \vec{r}_2|$ is the distance between the two nucleons and $\vec{\sigma}_i$ are their three-dimensional spin vectors.

- The interaction is charge-independent.

These main features result in the saturation of nucleon density and a typical distance between nucleons. Various potentials can be constructed by combining spin ($\vec{\sigma}_1 \cdot \vec{\sigma}_2$), isospin ($\vec{\tau}_1 \cdot \vec{\tau}_2$), spin-orbit ($\vec{L} \cdot \vec{S}$), and tensor ($S_{12}$) terms to match experimental data.

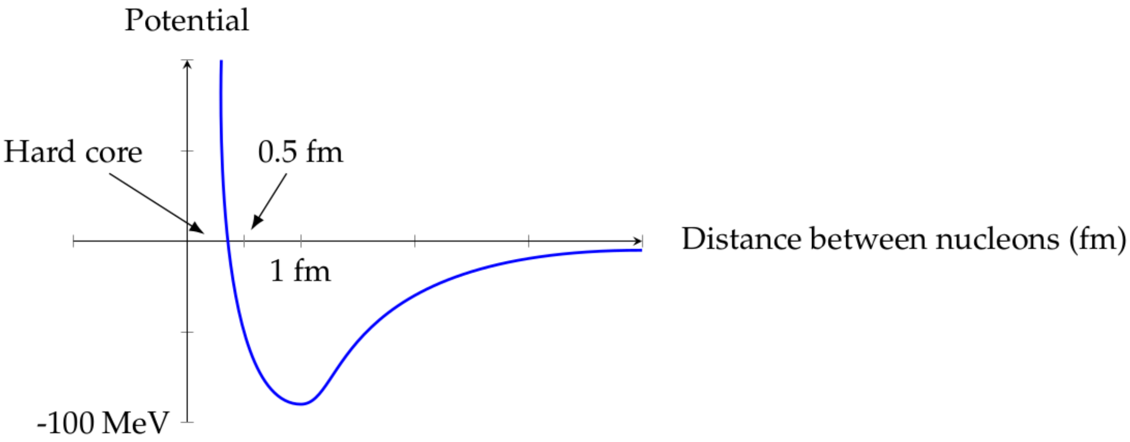

Figure 1.3: Representation of the nucleon-nucleon potential for a spin-singlet state as a function of the distance between the two nucleons. Image taken from [13].

In practice, to simplify the many-body problem, shell-model calculations use an effective $NN$ interaction within a valence space involving only a few orbitals above an inert core. This effective interaction is typically derived from the free $NN$ interaction as a starting point. The Pauli principle is then incorporated with the strong repulsive component in the $NN$ interaction at very short distances, and in-medium effects are handled using perturbation theory.

However, an effective interaction based solely on the bare $NN$ potential does not accurately reproduce nuclear saturation properties or spin-orbit magic numbers. This limitation is likely due to the exclusion of three-body forces [14], which, when included, have shown better agreement with experimental data [15,16]. For example, an effective interaction with a three-body term in the oxygen isotope region correctly predicts the

---

[7] The wavefunction describing the ground state of the deuteron is a mixture of $L = 0$ and $L = 2$.

neutron drip-line at $^{24}$O [17,18], whereas a two-body interaction misplaces it at $^{28}$O. In valence spaces without available effective three-body interactions, a solution is found through the multipole decomposition of the Hamiltonian.

### 1.1.3 Multipole decomposition of the Hamiltonian

The Hamiltonian can be divided into a monopole component, which governs the spherical mean field and defines shell gaps, and higher multipole components, which contain particle-particle correlations that lead to collectivity and deformation. The creation or disappearance of magic numbers arises from a delicate interplay between these two components and their underlying elements, such as central, spin-orbit, and tensor forces.

#### a/ The monopole interaction

The monopole part of the Hamiltonian is regarded as the average interaction over all directions between two nucleons. It describes a spherical mean field and it is responsible for global saturation properties and single-particle behavior. Considering a two-body interaction $V$, the monopole part of the Hamiltonian can be expressed as follows [19]:

$$\hat{H}_m = \sum_j \epsilon_j^\pi \hat{n}_j^\pi + \sum_j \epsilon_j^\nu \hat{n}_j^\nu + \sum_{j,j'} V_{jj'}^{\pi\nu} \hat{n}_j^\pi \hat{n}_{j'}^\nu + \sum_{j\leq j'} \frac{V_{jj'}^{\nu\nu} \hat{n}_j^\nu (\hat{n}_{j'}^\nu - \delta_{jj'})}{1+\delta_{jj'}} + \sum_{j\leq j'} \frac{V_{jj'}^{\pi\pi} \hat{n}_j^\pi (\hat{n}_{j'}^\pi - \delta_{jj'})}{1+\delta_{jj'}} \tag{1.3}$$

where $\epsilon_{\pi,\nu}$ are the proton and neutron single-particle energies (SPE), $\hat{n}_{\pi,\nu}$ are the proton and neutron number operators, $j$ represents the set of quantum numbers of a given orbital, and $V_{jj'}^{\tau\tau'}$ is the monopole component of $V$ which can be expressed as:

$$V_{jj'}^{\tau\tau'} = \frac{\sum_J (2J+1) \langle jj' | V | jj' \rangle_J}{\sum_J (2J+1)} \tag{1.4}$$

where $J$ is the total angular momentum of a two-body state, and $\tau$ represents the type of nucleon[8]. This monopole term contributes to the spacing of the effective single particle energies (ESPE) [20,21], which can be understood as the opposite of the nucleon separation energy for occupied orbits and as the opposite of the binding energy gain for unoccupied orbits. These ESPE are linear functions of the occupation numbers $\langle \hat{n}_{j'}^{\tau'} \rangle$ of orbitals $j'$ above a core $A_0$:

$$\tilde{\epsilon}_j^\tau(A) = \epsilon_j^\tau(A_0) + \sum_{j',\tau'} V_{jj'}^{\tau\tau'} \langle \hat{n}_{j'}^{\tau'} \rangle \tag{1.5}$$

---

[8] $\pi$ for protons and $\nu$ for neutrons.

where the sum runs over all valence orbitals, and

$$\Delta\epsilon_j = \tilde{\epsilon}_j^{\tau}(A) - \epsilon_j^{\tau}(A_0) = \sum_{j',\tau'} V_{jj'}^{\tau\tau'} \langle \hat{n}_{j'}^{\tau'} \rangle \tag{1.6}$$

This term, called the monopole drift, can be large enough to cause the disappearance of some magic numbers and the emergence of new ones, such as $N = 16$ in $^{24}$O [22,23].

The contribution to shell evolution from different components of the monopole part of the nucleon-nucleon ($NN$) interaction has been widely discussed. The central part of the $NN$ interaction primarily drives the global trend of the ESPE, while the tensor part can significantly modify the ESPE splitting between spin-orbit partners. The tensor force, when filling a neutron (proton) orbital $j' = l' \pm 1/2$, impacts proton (neutron) spin-orbit partners $j_> = l + 1/2$ and $j_< = l - 1/2$:

$$(2j_> + 1)V_{j_>j'}^{\pi\nu} + (2j_< + 1)V_{j_<j'}^{\pi\nu} = 0 \tag{1.7}$$

indicating that the monopole part of the tensor force acts oppositely on spin-orbit partners and vanishes when both $j_>$ and $j_<$ orbitals are full, thus acting only on valence orbitals. Furthermore, $j'_< - j_>$ and $j'_> - j_<$ interactions are attractive while $j'_> - j_>$ and $j'_< - j_<$ interactions are repulsive. This effect is schematically illustrated in figure 1.4. This can impact the shell gaps that are delimited by spin-orbit partners, like in the case of the $Z = 28$ gap in $^{78}$Ni.

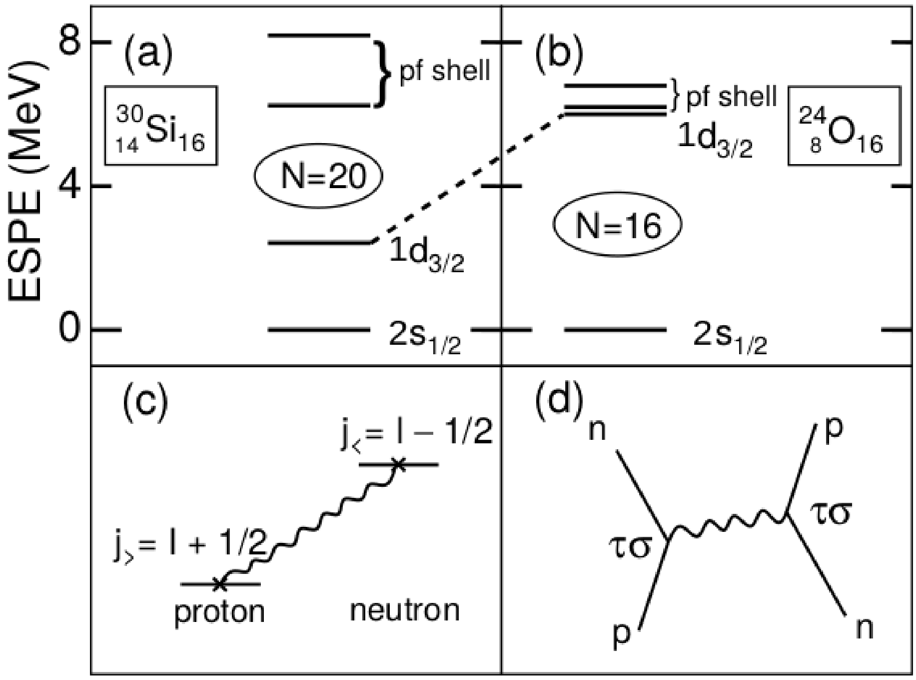

Figure 1.4: Neutron ESPE's for (a) $^{30}$Si and (b) $^{24}$O, relative to $2s_{1/2}$. The dotted line connecting (a) and (b) is drawn to indicate the change of the $1d_{3/2}$ level. Such a change is due to the interaction between the upper $j$ proton $1d_{5/2}$ orbit and the lower $j$ neutron $1d_{3/2}$ orbit, as schematically illustrated in (c). The Feynmann diagram of the interaction process with the meson exchange is represented in (d). Image adapted from [23].

### b/ The multipole part

The higher-order multipole terms of the nucleon-nucleon interaction of the Hamiltonian can describe correlations between valence nucleons, such as pairing and quadrupole interactions, resulting in particle-hole excitations across shell gaps. These terms also contribute to deformation and influencing nuclear observables across the nuclear landscape. The decrease of a shell gap, due to a monopole drift that brings closer the two orbitals defining the gap, can lead to intruder deformed configurations at low energy if the correlation energy of such configurations is larger than the energy required to create them. When this correlation is greater than the creation energy, these intruder states can dominate the ground state configuration.

## 1.2 Collective behaviors

The shell model, despite its simplicity, successfully explains the spins and parities of nearly all odd-A ground states and provides a reasonably good, though slightly less precise, description of magnetic dipole and electric quadrupole moments (defined in section 1.3 ) [24]. In the extreme independent particle model, one assumes that all nucleons except one are paired, with the nuclear properties determined by the motion of the unpaired nucleon. While this is an evident simplification, a more advanced approximation would account for the contributions of all particles in the partially filled subshell. This is still, however insufficient to explain some nuclear properties like in even-even nuclei. While the model correctly predicts the $0^+$ spin-parity of the ground state in these isotopes, it is not able to reproduce some other properties such as the energies of the first $2^+$ excited states (the experimentally measured values are lower than those that would be obtained by displacements of nucleons between the shell-model states). The configurations leading to these $2^+$ states turned out to be the result of the collective properties of the nucleus. Their origin lies in the nuclear collective motion, in which several nucleons contribute cooperatively to the nuclear excitation. In fact, there are two main types of collective structures, which are vibrations and rotations.

### 1.2.1 Nuclear vibrations

In the atomic nuclei where nuclear vibrations occur, a convenient way to represent their shapes is to use the instantaneous coordinate $R(t)$ of a point on the nuclear surface at a given angle $(\theta, \phi)$, in terms of the spherical harmonics $Y_{\lambda\mu}$ with some time-dependent weights $\alpha_{\lambda\mu}(t)$:

$$R(t) = R_{\text{av}} + \sum_{\lambda \geq 1} \sum_{\mu=-\lambda}^{+\lambda} \alpha_{\lambda\mu}(t) Y_{\lambda\mu}(\theta, \phi), \tag{1.8}$$

with an average radius $R_{av}$ [9]. For $\lambda = 0$, the $Y_{00}$ term is a constant that is included in $R_{av}$. The fist time-dependent term arises with $\lambda = 1$, which corresponds to a dipole vibration (one phonon). The second term is obtained for $\lambda = 2$ and represents the quadrupole vibration (2 phonons), and so on. For the latter case, the addition of this $Y_{2\mu}$ component to the $0^+$ wavefunction of the ground state in even-even nuclei results in a $2^+$ state for the first excited level, which could not be explained by the simple single-particle states of the shell model. More generally, the addition of other phonons successfully explains the states in vibrational bands of these nuclei.

---

[9] $R_{av} = R_0 A^{1/3}$, with $R_0$= 1.2 fm and $A$ is the mass number.

In practice, the vibrational model makes possible some predictions that can experimentally be checked. For instance, if the equilibrium shape is spherical, the quadrupole moments of the first $2^+$ state should be zero, as it was indeed measured in the region $A< 150$. Therefore, the reduced transition $B(E2)$ probabilities (defined in section 1.3.3 ) which are linked with these quadrupole moments may shed light on the collective behaviors in the studied nuclei.

### 1.2.2 Nuclear rotations

Rotational motion can be observed in nuclei with nonspherical equilibrium shapes. These nuclei can have substantial distortions from spherical shape and are often called deformed nuclei. They were initially found in the mass ranges $150<A<190$ and $A > 220$ (rare earths and actinides). It is customary to represent their shape with an ellipsoid of revolution, of which the outer surface is described by:

$$R(\theta, \phi) = R_{\text{av}} \left[1 + \beta Y_{20}(\theta, \phi)\right], \tag{1.9}$$

where $\beta$ is the deformation parameter (defined in section 1.3.1.b). An indicator of a permanent deformation in a nucleus is a large electric quadrupole moment, as it will be explained in section 1.3.1.b.

## 1.3 Nuclear moments and transition rates

The atomic nucleus exhibits a complex duality in its behavior: it can both display single-particle and collective properties. While the nuclear shell model effectively describes the independent motion of nucleons in an average potential, many nuclei, especially those away from closed shells can manifest collective behaviors. This collective motion involves correlated nucleonic interactions and leads to phenomena such as nuclear deformation, rotational bands, and enhanced electromagnetic transition probabilities. Understanding nuclear collectivity requires a detailed examination of multipole moments, their corresponding operators, and the interplay between single-particle and collective degrees of freedom. This section explores the roles of electric and magnetic multipole moments, their corresponding operators as well as their connection with deformation and electromagnetic transition strengths.

### 1.3.1 Nuclear moments

Any system where there is a distribution of electric charges and currents produces electric and magnetic fields that vary with distance in a characteristic fashion. In the atomic nucleus, the nucleons are responsible for the creation of the latter fields and it is possible to assign electromagnetic multipole moments to the resulting charge and current distributions. Here, we shall pay attention to magnetic dipole and electric quadrupole moments, since these are the ones that are well measured in several mass regions including the neighborhood of $^{78}$Ni which we are interested in.

### a/ Magnetic dipole moment

To a charged particle that is moving, a current $i$ can be associated together with its corresponding magnetic dipole moment. In the simple case of a circular trajectory, the orbital angular momentum $\vec{l} = \vec{r} \times \vec{p}$ , has a magnitude $|\vec{l}| = mvr$ and the magnetic dipole moment is obtained as:

$$\vec{\mu} = \pi r^2 i \vec{u} \tag{1.10}$$

where $\vec{p}$ is the linear momentum of the moving particle, $\vec{r}$ is its position vector and $\vec{u}$ is a unit vector that is perpendicular to the plane of the circular motion. For a proton, the magnetic dipole moment equals:

$$\vec{\mu} = \pi r^2 \frac{ev}{2\pi r}\vec{u} = \frac{e}{2m_p}\vec{l} \tag{1.11}$$

where $v$ is the velocity of the proton, $m_p$ is its mass and $e$ its charge. In order to go from this classical picture to the quantum formalism, one has to replace the orbital angular momentum and the magnetic dipole moment vectors by their corresponding operators. In this fashion, the following formulae are used[10]:

$$\hat{\mu}_l = \frac{e}{2m_p}\hat{l}, \tag{1.12}$$

$$\hat{\mu}_{l,z} = \frac{e}{2m_p}\hat{l}_z. \tag{1.13}$$

With this definition, the "$l$" subscript is added to precise that this magnetic moment is associated to the orbital motion since there exists also a magnetic moment $\hat{\mu}_s$ corresponding to the intrinsic spin of the particles. Therefore, the total magnetic moment of the nucleon is a sum of both the orbital and intrinsic spin contributions with some multiplying constants. This can be done for each individual nucleon and without going into the details of the mathematical derivation, the following result is obtained:

---

[10] When projecting on a chosen z-axis, the eigenvalues of the magnetic operator are proportional to those of the $\hat{l}_z$ operator, with a proportionality constant $\mu_N = e\hbar/2m_p c$ , which is called the nuclear magneton.

$$\hat{\mu}_{j,z} = g_j \mu_N \hat{\mu}_z. \tag{1.14}$$

where $\hat{\mu}_{j,z}$ is the projection of the total magnetic dipole moment of a nuclear state with a total angular momentum $\vec{j}$, and $g_j$ is the gyromagnetic factor of the state. From an experimental point of view, the measurement of the magnetic dipole moment corresponds to the expectation value of the operator in equation 1.14.

In the cases of vibrational and rotational collective motions, a magnetic moment is generated for the nucleus. The motion of protons can be considered equivalent to an electric current, and a single proton with angular momentum quantum number $l$ would produce a magnetic moment of $\mu = l\mu_N$. However, the total angular momentum of a nuclear state is not solely due to the protons; neutrons also play a role. Assuming that protons and neutrons exhibit identical collective motion (a reasonable, though slightly imprecise assumption), the contribution of protons to the total nuclear angular momentum is approximately $Z/A$, where $Z$ represents the number of protons and $A$ the total number of nucleons. This assumes that neutron motion does not contribute to the magnetic moment and that all protons and neutrons are pairwise coupled, canceling out their spin magnetic moments. Under this framework, the collective model predicts the magnetic moment of a vibrational or rotational nuclear state with angular momentum $J$:

$$\mu(J) = \frac{Z}{A} J \mu_N \tag{5.20}$$

For light nuclei, the ratio $Z/A$ is approximately 0.5, leading to a magnetic moment of $\mu(2) \simeq +1\mu_N$ for the $2^+$ state. In contrast, for heavier nuclei, $Z/A \simeq 0.4$, resulting in $\mu(2) \simeq +0.8\mu_N$. These predictions were indeed experimentally verified [24].

In this work, there will be no measurement of the magnetic moment. Instead, the action of the latter operator on the nuclear states is required for the calculation of the decay rates through the so-called $M1$ transition operator. When it is applied to a shell-model state that is characterized by the quantum numbers $n$, $l$ and $j$, a spin-flip is induced and the orbital angular momentum remains unchanged after the $\gamma$ decay. This means that only transitions between spin-orbit partners with the same "$l$" orbital angular momentum are permitted, and all other kinds of deexcitation are said to be l-forbidden. This picture will be used in the final chapter to get an insight on the content of the wavefunctions of the states we observe in $^{79}$Cu.

### b/ Electric quadrupole moment

The electric multipole moments $Q_\lambda$ quantify the charge distribution's departure from spherical symmetry. Here, we study the quadrupole ($\lambda = 2$) moment, given by:

$$Q = \int \rho(r)\,(3z^2 - r^2)\,d^3r, \tag{1.15}$$

where $\rho(r)$ is the nuclear charge density, $r$ is the radial distance from the nucleus's center, and $z$ is the axis of quantization. A nonzero quadrupole moment reflects nuclear deformation:

- Prolate deformation (cigar-shaped nucleus) occurs for $Q > 0$.
- Oblate deformation (pancake-shaped nucleus) occurs for $Q < 0$.

In spherical nuclei, $Q$ vanishes due to symmetry. It is customary to describe such departures from sphericity using the $\beta$ deformation parameter which is related to the intrinsic quadrupole moment of the nucleus with the following equation at first order:

$$Q_0 = \frac{3}{\sqrt{5\pi}} Z R^2 \beta, \tag{1.16}$$

where $Z$ is the proton number, $R$ is the nuclear radius. Nuclei with significant deformation can exhibit rotational bands, where states are connected by $E2$ transitions with enhanced reduced transition probabilities $B(E2)$ (defined more in detail in section 1.3.3). This $B(E2)$ rates are proportional to the square of the electric quadrupole moment and the deformation parameter, linking observed transition rates to the intrinsic shape of the nucleus [25]. Similarly, the moment of inertia of a rotational band depends on the quadrupole moment, giving a connection between deformation, collectivity and transition rates.

This relationship will be discussed in the final chapter for the states in $^{79}$Cu using the associated electric quadrupole transition operator.

Following a knockout reaction, like in the $^{80}$Zn→$^{79}$Cu case of our study, the reaction residue can be produced in an excited state and then decays via $\gamma$ emission to a lower energy level. The time difference between the production of the residue at some excited state and its $\gamma$ deexcitation (its lifetime) can span different orders of magnitudes, going from very long radioactive periods (isomeric states) to very short values (femtoseconds or less). For a given energy level, the lifetime depends on several factors, including the number of allowed decay branches, its spin and parity, and the spin and parity of the levels to which it decays. In general, there is also a link between the single-particle character of a state and its half-life. The stronger this character, the longer its half-life. Therefore, a measurement of the lifetime gives hints about the collectivity and single-particle behaviors, through the reduced transition probabilities defined in section 1.3.3. The study of these decay rates provides a good test of the nuclear wavefunctions which are the solutions of the Schrödinger equation in the shell-model framework, and an indicator of the spin and parity properties of the states involved in the deexcitation. Before going through the explanation of these transition rates, we recall some of the useful properties of $\gamma$ rays.

### 1.3.2 Angular momentum and parity

Let us consider a nucleus in an initial excited state with an energy $E_i$ and a $J_i^{\pi_i}$ spin-parity. When it deexcites to a final state $J_f^{\pi_f}$ having a lower energy $E_f$, a $\gamma$ photon is emitted with an energy[11] $E_\gamma = E_i$ - $E_f$
In this process, the angular momentum must be conserved. As a consequence, the multipolarity $L$ of the transition, defined as the angular momentum carried by the generated photon satisfies the following inequality:

$$|J_i - J_f| \leq L \leq J_i + J_f \quad (L \neq 0) \tag{1.17}$$

Transitions can be categorized into two types: electric (E) and magnetic (M). For electric transitions, the parity between the initial and final states changes by $(-1)^L$. For magnetic transitions, the associated parity is $(-1)^{L+1}$. Therefore, based on the parity of the initial ($\pi_i$) and final ($\pi_f$) states, we can have the following transitions:

- If $\pi_i = \pi_f$:
    - · Even $L$: electric (E)
    - · Odd $L$: magnetic (M)
    - · Examples: $M1, E2, M3, E4, \ldots$
- If $\pi_i = -\pi_f$:
    - · Odd $L$: electric (E)
    - · Even $L$: magnetic (M)
    - · Examples: $E1, M2, E3, M4, \ldots$

In general, the type of transition with the lower $L$ is dominant[12], and for a fixed $L$, the electric transitions are favored with respect to the magnetic ones[13]. In practice, we will be interested in electric quadrupole $E2$ and magnetic dipole $M1$ types of transitions, since these are the ones that are experimentally observed (the higher $L$ electric decay can compete with the lower $L$ magnetic decay). Often, we encounter

---

[11] The recoil of the nucleus is neglected.

[12] The probability of a decay of $\sigma L$ type is about 5 orders of magnitude higher than for $\sigma(L+1)$.

[13] A transition of type $EL$ is about 100 times more probable than a transition of type $ML$.

cases where both multipolarities are observed. The competition between the latter is evaluated through the multipolarity mixing ratio $\delta$ defined as:

$$\delta^2(E2/M1) = \frac{\lambda_{E2}}{\lambda_{M1}} \tag{1.18}$$

where $\lambda_{E2}$ and $\lambda_{M1}$, defined in the next section, are the decay rates of electric quadrupole and magnetic dipole transitions, respectively.

### 1.3.3 Lifetimes, transition probabilities and collectivity

The probability per time unit of a transition of type $\sigma = E$ or $M$ with a multipolarity $L$ between an initial state described by the wavefunction $\Psi_i$ and a final state $\Psi_f$, which carries the nuclear structure information, can be calculated with the following formula:

$$\lambda(\sigma L) = \frac{8\pi}{\hbar} \frac{L+1}{L[(2L+1)!!]^2} k^{2L+1} B(\sigma L) \tag{1.19}$$

with $k = \frac{E_\gamma}{\hbar c}$, $E_\gamma$ the energy of the emitted photon, and $B(\sigma L)$ the reduced transition probability which depends on the nature of the initial and final states. In the simple case where only one final state is allowed[14], this quantity is theoretically evaluated as the expectation value of the multipole transition operator $\hat{O}$ between the two states:

$$B(\sigma L) = \frac{1}{2J_i+1} |\langle \Psi_f | \hat{O} | \Psi_i \rangle|^2 \tag{1.20}$$

For electric transitions, this operator includes a term of the form $r^L Y_L^M(\theta, \phi)$, where $r$, $\theta$ and $\phi$ are the usual spherical coordinates and $Y_L^M$ are the spherical harmonics [26]. For magnetic transitions, the operator includes a term that is proportional to $\nabla[r^L Y_L^M(\theta, \phi)]$.

In the case of a single-particle transition, only one nucleon is involved, reducing the number of accessible decay branches. On the other hand, collective states involve more nucleons, and thus more possibilities for the decay. This increases the transition probability. Therefore, the degree of collectivity or single-particle character of the states in a given transition can be evaluated by comparing the experimental transition probability to the single-particle transition probability which is given by the Weisskopf estimates:

$$B(EL) = \frac{1}{4\pi} \left( \frac{3}{L+3} \right)^2 \left(1.2A^{1/3}\right)^{2L} \; e^2 fm^{2L} \tag{1.21}$$

---

[14] If there are $N$ possible final states $\Psi_f^k$, with reduced transition probabilities $B_k$ to each final state, with $1 \leq k \leq N$, then the individual reduced transition probabilities need to be multiplied by the transition energy dependent factor in equation 1.19, and summed to obtain the total decay rate.

$$B(ML) = \frac{10}{\pi}\left(\frac{3}{L+3}\right)^2 \left(1.2A^{1/3}\right)^{2L-2} \left(\frac{e\hbar}{2m_pc}\right)^2 fm^{2L-2} \tag{1.22}$$

with $m_p$ the proton mass, $c$ the speed of light in vacuum and $e$ is the elementary charge. The units for $B(EL)$ and $B(ML)$ depend on the multipolarity, and they are equal to $\mathrm{e}^2\mathrm{fm}^4$ for $E2$ transitions and $\mu_N^2$ for $M1$ transitions[15]. These two expressions in equations 1.21 and 1.22 are derived assuming a transition of a single nucleon from an initial state $J_i = L_i + S_i = L + 1/2$ to a final state $J_f = L_f + S_f = 1/2$, meaning that $\Delta J = 2$ for an electric quadrupole radiation and $\Delta J = 1$ for a magnetic dipole one. These formulae are nevertheless used regardless of the difference in angular momenta between the initial and final states, as they are not meant to be true theoretical calculations to be compared with measured transition rates. These estimates still allow for reasonable relative comparisons of transition rates. For instance, if the observed decay rate of a specific $\gamma$ transition is significantly lower than the Weisskopf estimate, it may indicate that a poor overlap between the initial and final wavefunctions is impeding the transition. Conversely, if the transition rate is much higher than the Weisskopf estimate, it could suggest that multiple nucleons are contributing to the transition. For such comparisons, the decay probability in Weisskopf units (W.u.) is often used. This is the ratio between the experimental value and the Weisskopf estimate. Therefore, if this ratio is much larger than unity, this hints to an underestimated collective character of the transition.

The half-life[16] $T_{1/2}$ of an excited state is defined as the time after which the number of nuclei remaining in this state is equal to the initial number divided by 2. For the simple case where only[17] one decay branch is allowed, this half-life is related to the transition probability $\lambda$ with the following formula:

$$\lambda = \frac{\ln 2}{T_{1/2}} \tag{1.23}$$

Therefore, a measurement of the lifetime can be used to deduce the transition probability and subsequently quantify the single-particle character of a given state through the Weisskopf estimates. In this thesis, this relation will be used for the states in the $^{79}$Cu nucleus.

---

[15] We remind that $\mu_N = e\hbar/2m_pc$ is the nuclear magneton.

[16] The half-life $T_{1/2}$ and the lifetime $\tau$ are linked with the relation : $T_{1/2} = \tau \ln 2$

[17] If there are several possible final states, the total transition probability $\lambda_{tot}$ is the sum of the individual transition probabilities $\lambda_i$ to each final state.

### 1.3.4 Internal conversion

Occasionally, the excitation energy of the nucleus can be absorbed by an electron[18] of the atomic cloud. This electron is subsequently ejected from the atom with an energy that equals the difference between the absorbed one and its binding energy. Consequently, the total transition rate for the deexcitation of a given nuclear level is the sum of the transition rate through $\gamma$ emission $\lambda_\gamma$ and the rate of internal conversion $\lambda_{ic}$:

$$\lambda = \lambda_\gamma + \lambda_{ic} = \lambda_\gamma(1+\alpha) \tag{1.24}$$

where $\alpha = \lambda_{ic}/\lambda_\gamma$ is the internal conversion coefficient that describes the competition between the two processes, and can be estimated using the following expressions [24]:

$$\alpha(EL) \approx \frac{Z^3}{n^3}\left(\frac{L}{L+1}\right)\left(\frac{e^2}{4\pi\epsilon_0\hbar c}\right)^4\left(\frac{2m_ec^2}{E_\gamma}\right)^{L+5/2} \tag{1.25}$$

$$\alpha(ML) \approx \frac{Z^3}{n^3}\left(\frac{e^2}{4\pi\epsilon_0\hbar c}\right)^4\left(\frac{2m_ec^2}{E_\gamma}\right)^{L+3/2} \tag{1.26}$$

where $Z$ is the atomic number, $m_e$ is the electron mass, $n$ is the principal quantum number of the bound electron wavefunction, and $E_\gamma$ is the energy of the nuclear transition. These relations show that these corrections are more important for heavy nuclei and very low energy $\gamma$ rays (in practice, below 100 keV).

The BrIcc internal conversion coefficient database has been developed [27] and in all our discussions in section 1.4.2 and chapter 6, we used this database[19] to calculate these coefficients whenever the relation between the transition probabilities and lifetimes was considered.

## 1.4 Magicity in the $^{78}$Ni region

$^{78}$Ni is an iconic neutron-rich nucleus for structure studies, located far from the line of stability and the focus of many recent experimental investigations. Though a closed magic character for both the proton ($Z = 28$) and neutron ($N = 50$) shells is expected, theoretical [28] and experimental [29] works suggested a possible weakening of these

---

[18] The electrons of the K-shell are the most likely to absorb this energy since their wavefunction is non-zero at the center of the nucleus.

[19] In this database, the electron-positron pair conversion coefficients (IPC) were also taken into account. These parameters describe the phenomenon where the nucleus converts the energy difference between two states into an electron-positron pair. Of course, this process concerns only high energy $\gamma$ rays, the threshold being at 1.022 MeV, which is twice the electron mass.

shell gaps. This weakening may give rise to deformed shapes at nearby energies, a phenomenon known as shape coexistence. The mechanisms at work far from stability previously described, particularly through monopole drifts of single-particle energies, may influence these gaps. We present here the current state of experimental knowledge regarding the magicity near this key nucleus.

### 1.4.1 $\beta$-decay lifetimes

One of the observables that can help to shed light on the double-magicity of $^{78}$Ni is the $\beta$-decay lifetime. The shorter its value, the larger the $Q_\beta$ of the disintegration, which increases if the neutron that is converted into a proton originates from a high energy level or if the generated proton fills a shell with low energy. Therefore, if this neutron in the parent nucleus is located above a shell gap, the $Q_\beta$ that is released is sharply increased, and the lifetime is sharply decreased. Similarly, if the new proton in the daughter nucleus is below a shell gap, the lifetime is decreased. The systematics of the $\beta$-decay half-lives for the nuclei in the neighborhood of $^{78}$Ni is illustrated in figure 1.5, where two main observations can be made on the $Z = 28$ and $N = 50$ gaps:

- For cobalt ($Z = 27$), the lifetimes are much smaller than for the nuclei with $Z > 27$. This can be understood with the following reasoning:
  + When Co goes to Ni, the resulting proton can occupy the last available state before closing the $Z = 28$ gap. In this case, this proton goes to a low energy orbital, which increases the $Q_\beta$ value and decreases the half-life.
  + On the other hand, for $Z > 27$, this new proton must occupy a state that is located above the $Z = 28$ gap, and thus drastically decreasing the $Q_\beta$ and increasing the lifetime if the gap is large. Consequently, this shows that the proton shell gap remains large, which provides an indirect evidence of the robust $Z = 28$ magic number.

- For the nickel isotopes, the lifetime suddenly decreases for $N > 50$. Indeed, the decaying neutron originates from a high energy level (above the shell gap), leading to a high $Q_\beta$ and a short lifetime, contrary to the other nickel isotopes ($N \leq 50$) where the neutron originates from a low energy state in the $\nu g_{9/2}$ orbital. Therefore, this sharp decrease of the lifetime is a signature of a large $N = 50$ shell gap and provides an indirect evidence of the persistence of the this shell closure.

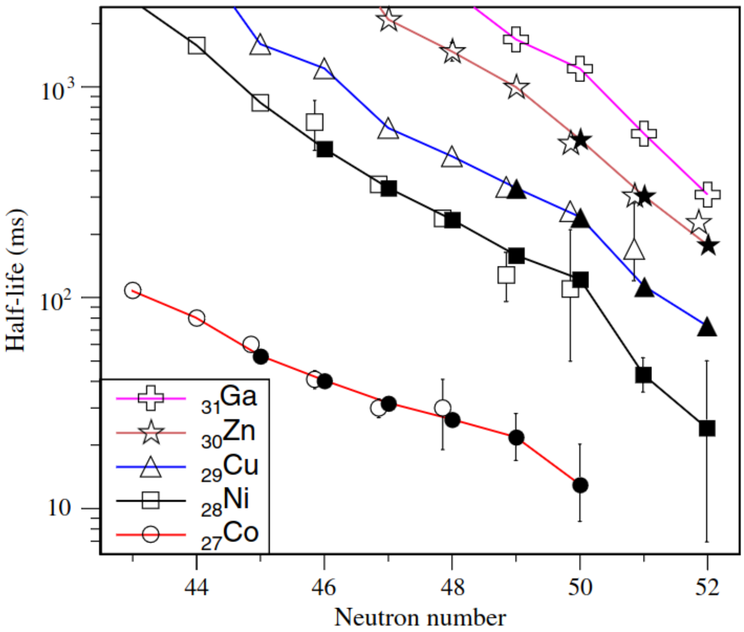

Figure 1.5: Experimental $\beta$-decay half-lives of the $Z = 27$ to 31 isotopic chains. The solid symbols represent the half-lives determined in [30], while the open symbols are the half-lives taken from Refs [31–34]. Image taken from [30].

### 1.4.2 Systematics of B(E2) in even-A nickel isotopes

The magicity in the neutron-rich nickel isotopes can be evaluated through the reduced transition probability rates $B(E2)$, defined in section 1.3.3. For $^{68}$Ni with $N = 40$, a semi-magic character is expected since it defines a sub-shell closure, with a low $B(E2; 0^+ \rightarrow 2^+)$, as compared to its neighbors. In an experiment at GANIL[20], the interaction of a 65.9 AMeV $^{70}$Zn beam with a $^{58}$Ni target allowed to produce $^{66}$Ni and $^{68}$Ni isotopes [35]. Their reduced transition probabilities have been measured at 600(100) e$^2$fm$^4$ and 255(60) e$^2$fm$^4$, respectively. Later on, another Coulomb excitation experiment took place at the same facility, where $^{70}$Ni nuclei were produced [36]. The result of the measurement was a sharp rise of the $B(E2; 0^+ \rightarrow 2^+)$ value to 860(140) e$^2$fm$^4$. Such a fast increase was an indication that the additional neutrons in the $1g_{9/2}$ orbital strongly polarize the $Z = 28$ proton core and of a reduction of the corresponding shell gap. Above $N = 42$, the behavior of $^{74}$Ni was first analyzed in an experiment [37] at NSCL [21]. This nucleus was studied with inverse-kinematics inelastic proton scattering on a liquid hydrogen target. Its deformation length $\delta$, defined as the product between

---

[20] Grand Accélérateur National d'Ions Lourds in Caen (France).

[21] National Superconducting Cyclotron Laboratory at Michigan State University (USA).

the quadrupole deformation parameter[22] $\beta$ and the nuclear radius $R = 1.2\ A^{1/3}$ fm ($A$ being the mass number), was measured. A value of 1230(380) e$^2$fm$^4$ was deduced for $B(E2; 0^+ \to 2^+)$ using the following formula:

$$\delta = \frac{4\pi}{3ZeR}\sqrt{B(E2, 0^+ \to 2^+)} \tag{1.27}$$

where $Z$ is the atomic number and $e$ is the elementary charge. This measurement suggested an even higher increase of the collectivity compared to $^{70}$Ni with the filling of the $\nu g_{9/2}$ level. After that, a Coulomb excitation experiment [38] was carried out at the same facility, and a reduced transition probability of 640(230) e$^2$fm$^4$ was obtained for $^{74}$Ni, thus exhibiting a collectivity that is less[23] than what was suggested by the result derived from the deformation length's measurement and the authors concluded that the quenching of the $Z = 28$ gap does not occur. This same conclusion was made on $^{72}$Ni, in which a reduced transition probability of 370(50) e$^2$fm$^4$ was obtained, still at NSCL [39]. This was deduced from a lifetime measurement of the $2^+$ state using the DSAM[24]. Furthermore, a recent Coulomb excitation experiment at RIKEN [40] allowed to measure a $B(E2; 0^+ \to 2^+)$ of 428(210) e$^2$fm$^4$ in $^{70}$Ni, twice lower than the previous measurement of 860(140) e$^2$fm$^4$. This new result is closer to theoretical predictions. The total systematics of the reduced transition probability along the even nickel isotopes is shown in figure 1.6. So far, there is no available information on $B(E2)$ beyond $N = 46$, for $^{76}$Ni and $^{78}$Ni, to shed light on the collectivity in the latter. Therefore, the $^{77}$Cu and $^{79}$Cu isotopes shall be used as tools for an indirect investigation of the eventual weakening of the $Z = 28$ gap.

---

[22] As already mentioned in section 1.3.1.b, the dimensionless deformation parameter $\beta$ is directly proportional to the the intrinsic quadrupole moment $Q$ which is itself proportional to the square root of $B(E2)$. It characterizes the shape of the nucleus, and its value is negative for oblate nuclei, positive for prolate and zero for spherical shapes.

[23] This small value was attributed to the fact that in Coulomb excitation, only protons are involved, while in the deformation length's measurement, the collectivity contributions of both protons and neutrons are taken into account.

[24] Doppler Shift Attenuation Method.

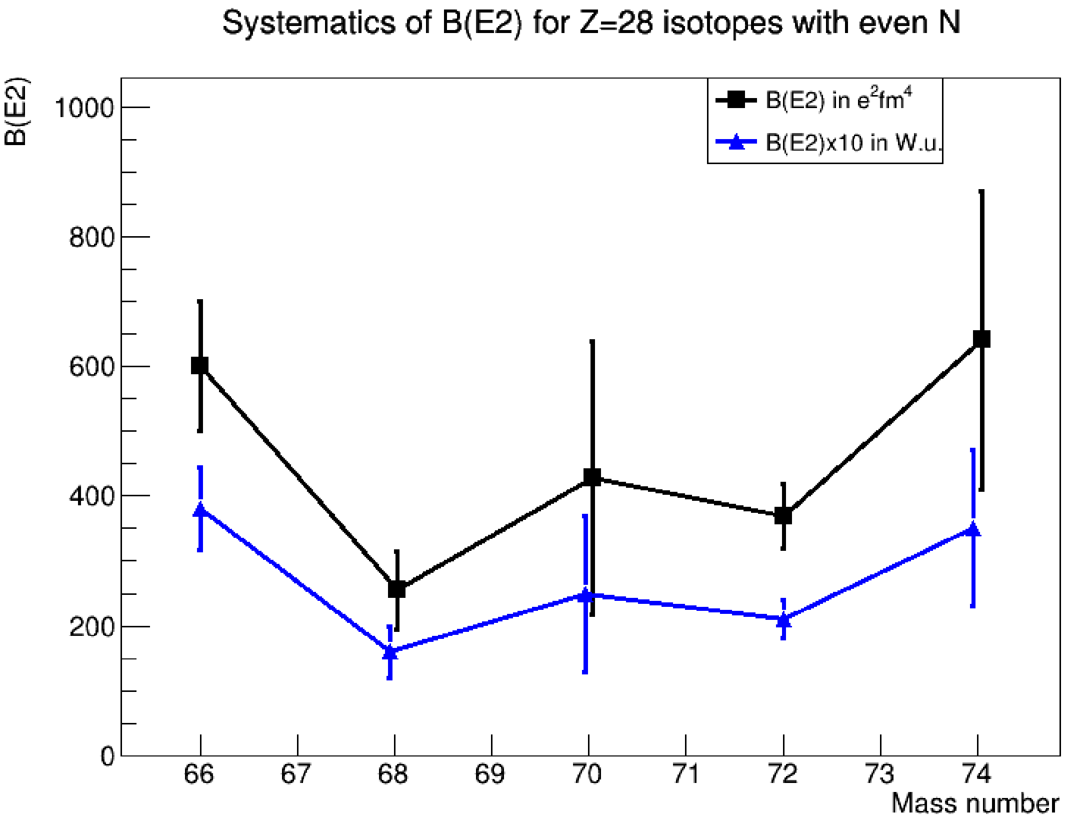

Figure 1.6: Systematics of $B(E2; 0^+ \rightarrow 2^+)$ in nickel neutron-rich isotopes, as obtained from Coulomb excitation or lifetime measurement (only for $^{72}$Ni) experiments.

### 1.4.3 First spectroscopy of $^{78}$Ni

So far, the only spectroscopic study of $^{78}$Ni was carried out at the radioactive beam facility of RIKEN during the SEASTAR[25] campaign (2014), an experimental program aiming at the spectroscopy of neutron-rich nuclei [41]. The $^{78}$Ni isotopes were produced through nucleon knock-out reactions that took place in the MINOS[26] secondary target, and their emitted $\gamma$ rays were detected by the DALI2[27] scintillator array. In that experiment, two different reaction channels with sufficient statistics allowed to reconstruct two different level schemes:

- From the events of the $^{79}$Cu(p,2p)$^{78}$Ni reaction, which was the one proton knock-

---

[25] Shell Evolution And Search for Two-plus energies At the RIBF.

[26] MagIc Numbers Off Stability is a device that is composed of a thick liquid-hydrogen target coupled to a compact time projection chamber (TPC) serving as a vertex tracker. The achieved resolution on the position of the reaction during the SEASTAR experiment was about 5 mm (FWHM) [5].

[27] Detector Array for Low Intensity radiation 2 [42].

out from $^{79}$Cu, the most intense observed $\gamma$ ray was at 2.6 MeV and was tentatively assigned to the deexcitation from the first excited state $2_1^+$ to the ground state $0_{gs}^+$. Such a high energy for the first excited state is a signature of large gaps above the $Z = 28$ and $N = 50$ shells and provides a direct evidence of the maintaining of the shell closure and a robust magicity. The systematics of the $2_1^+$ state for even-even nickel isotopes and a comparison with the predictions of theoretical models are illustrated in figure 1.7. Here, a sharp rise for this energy is noticed at $N = 50$, with a value that is comparable with the well-known 2.7 MeV excitation energy of the doubly magic $^{56}$Ni.

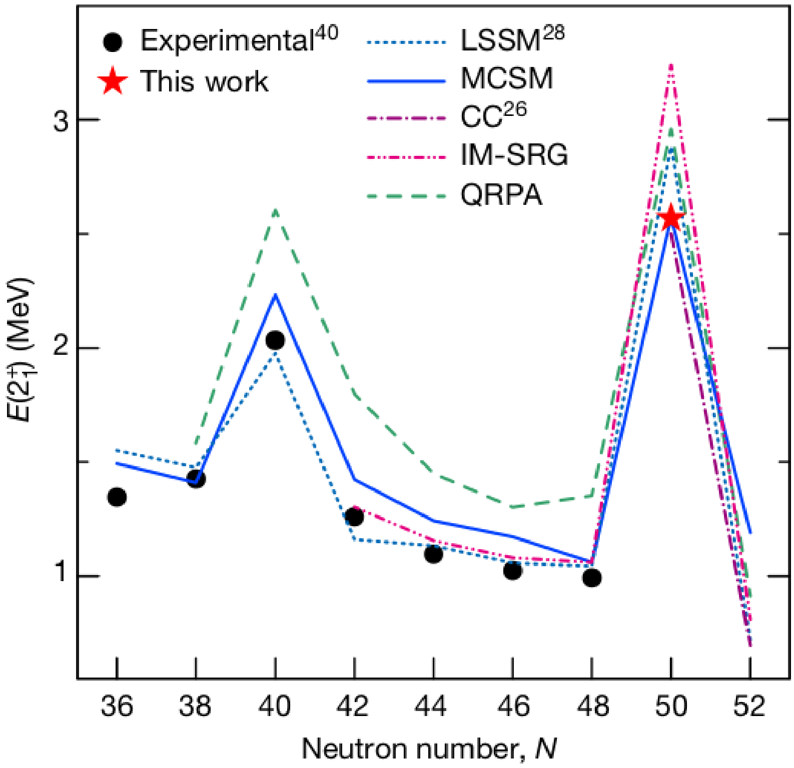

Figure 1.7: Experimental E($2_1^+$) values for even–even nickel isotopes and their comparison with calculations using phenomenological shell-model interactions (LSSM and MCSM), the beyond-mean-field approach (QRPA), the ab-initio approach (IM-SRG and CC), as a function of neutron number $N$. The result for $^{78}$Ni is indicated by the red star. Image taken from [41].

Furthermore, $\gamma\gamma$ coincidences were applied with a gate on the 2.6 MeV transition, and the resulting proposed level scheme is shown at the very left of figure 1.8. In the latter, the 583 keV $\gamma$ ray was tentatively assigned to the $4_1^+ \rightarrow 2_1^+$ transition. This leads to a ratio of $R_{4/2} = 1.22(2)$ between E($2_1^+$) and E($4_1^+$) , which is comparable to those of the well known doubly magic nuclei such as $^{40}$Ca (1.35), or $^{48}$Ca (1.18), suggesting the preservation of the magicity for $^{78}$Ni.

- From the events of the $^{80}$Zn(p,3p)$^{78}$Ni reaction, which was the two-proton knockout from $^{80}$Zn, a transition was observed at 2.9 MeV. The corresponding decaying state was either weakly or not populated in the (p,2p) channel. This was interpreted as the deexcitation of a second $2_1^+$ state, which is deformed, to the ground state $0_{gs}^+$, as illustrated in figure 1.8.

The conclusions from this work have provided the first direct experimental evidence for the preservation of the $Z = 28$ and $N = 50$ shell closures in $^{78}$Ni. A low-lying second $2^+$ state indicates the competition between spherical and deformed configurations. Additionally, a breakdown of the proton $Z = 28$ shell closure that favours prolate deformed ground states for heavier nickel isotopes is predicted, which sets $^{78}$Ni as a doubly magic stronghold before deformation in more neutron-rich nuclei.

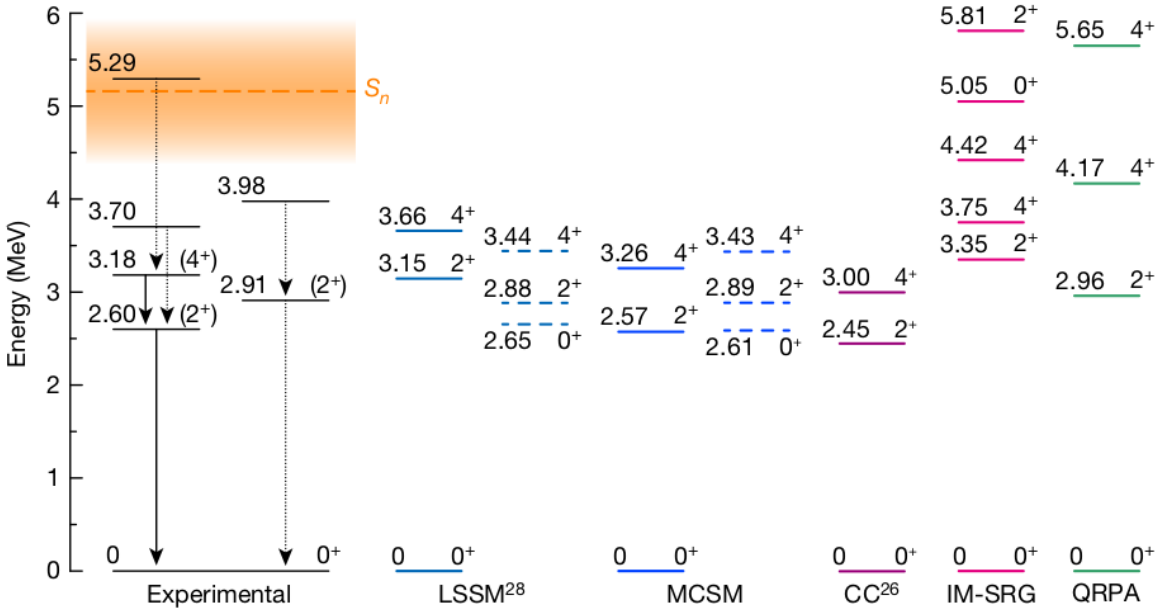

Figure 1.8: Experimental level schemes of $^{78}$Ni built from the (p,2p) and (p,3p) reaction channels (left), compared with theoretical calculations (right). Image taken from [41].

## 1.5 Neutron-rich odd-A copper isotopes

Copper isotopes contain one more proton than nickel isotopes, and thus offer a valuable means to investigate the nuclear structure near $^{78}$Ni, especially to characterize its proton single-particle nature. We present here the latest experimental findings on this isotopic chain, with particular highlights on $^{79}$Cu, seen as one proton above a core of $^{78}$Ni. As regards the valence space for protons, the orbitals of interest are $1f_{7/2}$, which is assumed to be full, and $2p_{3/2}$, $1f_{5/2}$, and $2p_{1/2}$. For neutrons, the focus is on the $1g_{9/2}$ orbital, which is empty at $N = 40$ and fully occupied at $N = 50$.

### 1.5.1 Inversion of the ground state

As illustrated in figure 1.1, in the shell model as it was initially formulated, the proton $\pi f_{7/2}$ orbital separates from the $3\hbar\omega$ harmonic oscillator shell due the spin-orbit splitting and forms the $Z = 28$ gap. Therefore, this suggests that for copper isotopes, the 29th proton belongs to the $\pi p_{3/2}$ shell, leading to a $3/2^-$ ground state, and a $5/2^-$ first excited state once this odd proton is promoted to $\pi f_{5/2}$ orbit, in the case of an even number of neutrons. This picture is valid and was experimentally confirmed for the lightest copper species, as it is the case for $^{69}$Cu, $^{71}$Cu and $^{73}$Cu, as established from $\beta$ decay of nickel isotopic chain, where a single-particle character was assumed for the states [43,44]. However, as the isospin increases, when filling the neutron $1g_{9/2}$ orbital, above the $N = 40$ subshell, the energy of the excited $5/2^-$ state decreases relative to the energy of the $3/2^-$ ground state. Such a displacement of the energy levels is caused by the monopole migration phenomenon previously explained in section 1.1.3.a, as the neutron occupation increases in the $1g_{9/2}$ orbital. This effect subsequently leads to the inversion of the two states in $^{75}$Cu [45,46], where two nearly degenerate states were observed at 61.7(4) keV and 66.2(4) keV[28]. When reaching $N = 48$, the relative displacement of the two states keeps its trend leading to an excitation energy of 293 keV for the $3/2^-$ state. The spin assignment was found using laser spectroscopy at ISOLDE-CERN[29], based on the measurement of magnetic dipole moments, confirming also the ground state spin of $^{75}$Cu [47]. A confirmation of the spin of the first excited state in $^{77}$Cu was obtained from the $\beta$ decay of $^{77}$Ni at RIKEN [48]. The authors suggested a single-particle nature for both the $5/2^-$ and the $3/2^-$ states in $^{77}$Cu. Finally, very recently, the first study of the level scheme of $^{79}$Cu (that is discussed in more detail in section 1.5.2) was performed at RIKEN using in-beam $\gamma$-ray spectroscopy [49]. The most intense transition was found at 656(5) keV, which is higher than the energy of the first excited state in $^{77}$Cu, suggesting that the monopole drift keeps increasing the gap between the $\pi p_{3/2}$ and $\pi f_{5/2}$ shells. Consequently, from the systematics of the first $5/2^-$ and $3/2^-$ states in the copper isotopic chain, the tentative spin assignment for the states in $^{79}$Cu were similar to those in $^{77}$Cu and $^{75}$Cu for the ground state and the

---

[28] Based on $B(E2)$ and $B(M1)$ transition rates, the authors concluded that one of these two states is a $3/2^-$.

[29] The Isotope mass Separator On-Line facility.

first excited state. Such a systematics is shown in figure 1.9.

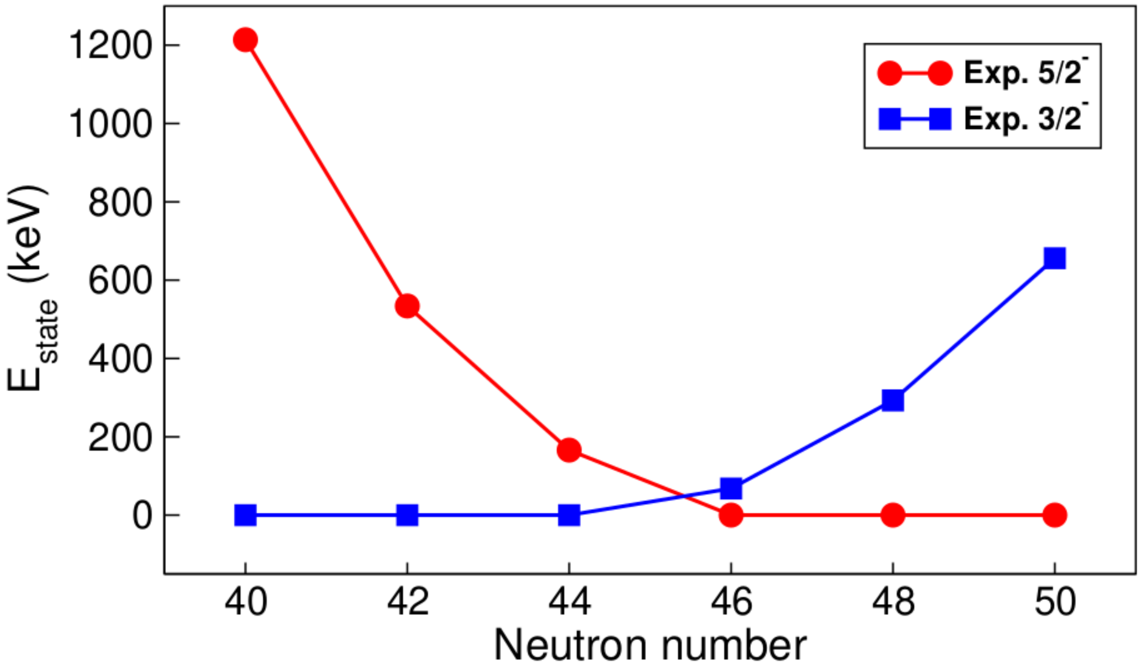

Figure 1.9: Systematics of the first $3/2^-$ and $5/2^-$ states in neutron-rich copper isotopes. The ground-state spin changes for $^{75}$Cu at $N = 46$. Data taken from references [43, 45–51].

### 1.5.2 First spectroscopy of $^{79}$Cu

So far, the only spectroscopic study of $^{79}$Cu was also performed at the radioactive beam facility of RIKEN during the SEASTAR campaign, using in-beam $\gamma$-ray spectroscopy [5, 49]. The $^{79}$Cu isotopes were produced through nucleon knock-out reactions. The main reaction for the production of these isotopes was the $^{80}$Zn(p,2p)$^{79}$Cu, corresponding to the one-proton removal from $^{80}$Zn. The $\gamma$ rays coming from the de-excitation of copper nuclei were detected by the DALI2 scintillator array. Two main transitions with high statistics were identified at 656(5) keV and 855(6) keV, the former being about 3 times more intense than the latter. Gates were set around the energies of these transitions for the application of $\gamma\gamma$ coincidences with background subtraction. This allowed to propose a level scheme for the first time, as shown in figure 1.10. Similarly to $^{77}$Cu and $^{75}$Cu, the ground state and the first excited state at 656 keV had tentative spin assignments of $(5/2^-)$ and $(3/2^-)$, respectively, while the second excited state at 1511 keV had a spin assignment of $(1/2^-)$.

The 2260 keV and 2730 keV levels are shown as dashed lines because the authors could not exclude the coincidence of the 750 keV and 1220 keV transitions with other transitions due to the low statistics and energy resolution.

The experimental results were compared with MCSM calculations. These calculations showed the restoration of the single-particle nature of the low-lying states. There was no significant knockout feeding to the excited states below 2.2 MeV, which hints that the $Z = 28$ gap remains large. Furthermore, the multiplet of states between 2.3 MeV and 3.3 MeV was interpreted as a coupling between a proton in the $\pi p_{3/2}$ or $\pi f_{5/2}$ and the first excited $2^+$ state in $^{78}$Ni, in agreement with the MCSM calculations. These core-coupling states allowed to estimate the energy of the $2_1^+$ in $^{78}$Ni to be at about 3 MeV. Finally, from the cross-section measurements, a lower limit at 2.2 MeV was established for the centroid of the $\pi f_{7/2}^{-1}$ strength, indicating that the $Z = 28$ gap remains large at $N = 50$. The ability to describe the $^{79}$Cu nucleus as a valence proton above a $^{78}$Ni core presented an indirect evidence of the magic character of the latter, as confirmed by its first spectroscopy which provided a direct evidence of its double magicity [41].

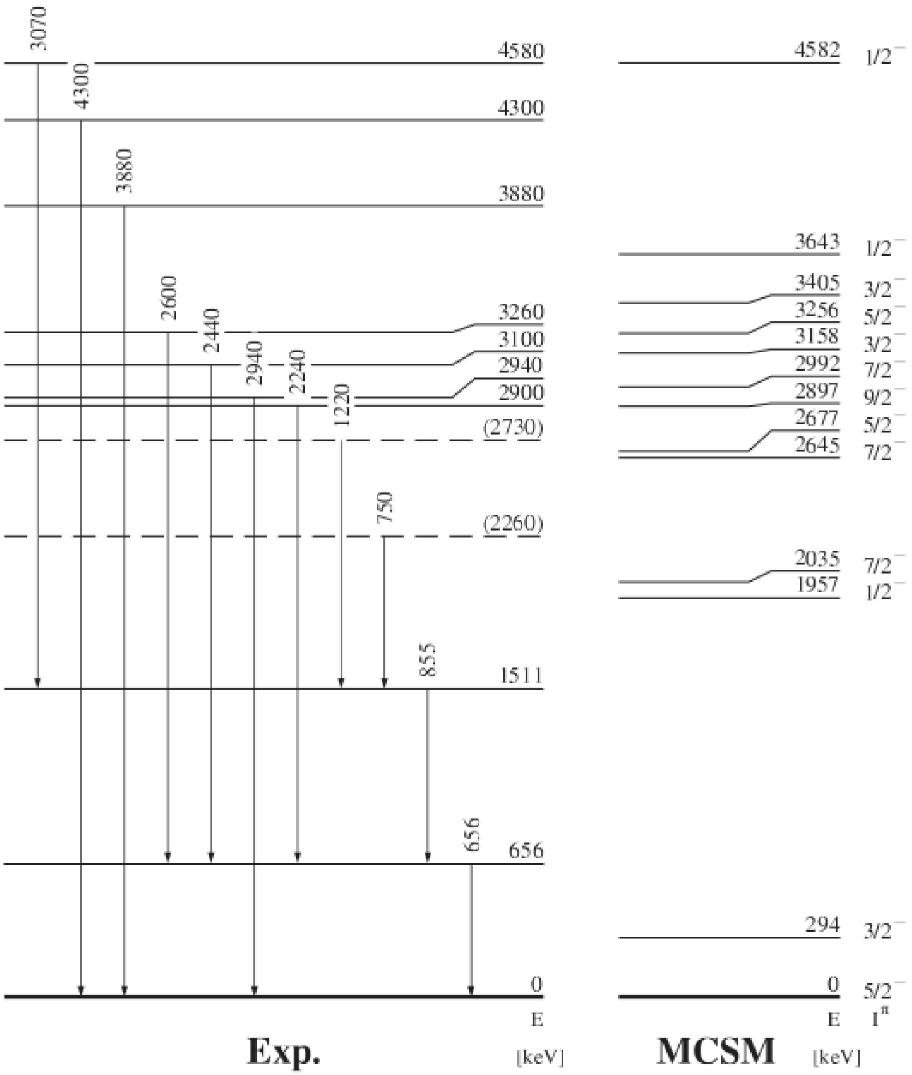

Figure 1.10: Proposed level scheme for $^{79}$Cu. The experimental results (on the left) are compared with the theoretical predictions of MCSM (on the right). Image taken from [49].

Using the data from this experiment, an attempt was initiated to estimate the lifetimes of the deexciting states in $^{79}$Cu. This observable is important since it sheds light on the single-particle character of the involved states. The methodology for the determination of these lifetimes is explained in more detail in the next chapters. Here, we only highlight the main principles. With the in-beam $\gamma$-ray spectroscopy, where the beam nuclei have relativistic velocities, the energy of the emitted $\gamma$ ray as detected in the laboratory frame is shifted with respect to the real energy in the emitting nucleus rest frame, due to the Doppler effect, and the width of the corresponding full-energy peak is enlarged. This shift increases with the half-life of the decaying state. Simulations with different lifetimes for the decaying states were carried out to best reproduce the experimental spectra. The precision of this method depends on the energy resolution of the $\gamma$-ray detectors. Consequently, using the DALI2 array made of scintillators (which had a low resolution of $\sigma$= 45 keV at 1 MeV), only an upper limit of the order of 100 ps was estimated for the half-lives of both the 656 keV and the 855 keV transitions [5]. Such large error bars did not allow any conclusion. Nevertheless, if half-life effects could induce an energy shift of a few percent, it would not affect the placement of the transitions in the level scheme.

### 1.5.3 Study proposed in this work

To solve the remaining ambiguities from the results of the SEASTAR campaign, where the low energy resolution DALI2 scintillator was used for the detection of the $\gamma$ rays, a similar experimental program was driven by the HiCARI collaboration. This led to a campaign with several experiments aimed at the spectroscopy of nuclei in different exotic regions of the nuclear chart, including the vicinity of $^{78}$Ni. This time, high energy resolution germanium detectors were used to be able to identify some of the previously unresolved $\gamma$ transitions and reach a better constraint on the lifetimes of the decaying states. These lifetimes help to evaluate the single particle character of the states, as detailed further in the next section. In the experiment described in the next chapter, we are dealing with inverse kinematics, and the $^{79}$Cu nucleus of interest is produced through knockout reactions. The $\gamma$ rays emitted by the latter are detected with the HiCARI germanium array. The next chapter provides all the details about the experimental setup.

# 2

# Experimental setup

## Contents

As a part of the HiCARI campaign [52], an experimental program aimed at investigating the properties of exotic nuclei produced in-flight, the NP1912-RIBF181 experiment [53] was conducted over seven days in April 2021, as the last experiment of the campaign, at RIKEN[1]'s Radioactive Isotope Beam Factory (RIBF) in Japan. Its objective was the $\gamma$-ray spectroscopy and the measurement of the lifetimes of neutron-rich nuclei in the vicinity of $^{78}$Ni. The experiment involved the BigRIPS and ZeroDegree spectrometers for the identification of nuclear species and the HiCARI germanium array surrounding the secondary beryllium target for the detection of the $\gamma$ rays. This chapter provides a detailed description of the components of the experimental setup we used to study the $^{80}$Zn($^{9}$Be, X)$^{79}$Cu reaction channel.

## 2.1 Beam production

To produce the beam, the experiment relied on the in-flight separation technique. Specifically, a beam of $^{238}$U was sent onto a primary 4mm-thick rotating target made of $^{9}$Be for in-flight fission. This generated a mixture of exotic nuclei. The latter were then separated in-flight by a magnetic spectrometer, which produced the secondary beam that was used for the experiment.

### 2.1.1 Heavy-ion accelerating system

The RIBF heavy-ion accelerator system [54] employed to generate a high-energy $^{238}$U primary beam is illustrated in figure 2.1. Its exact configuration depends on the mass and charge of the nuclei to be accelerated. There are three possible operational modes in total. In our case, the fixed-energy mode was used. To begin with, the $^{238}$U ions are produced using an Electron Cyclotron Resonance Ion Source (ECRIS) and then directed to the RILAC linear accelerator, serving as the first injector for the four-cyclotron sequence comprising of RRC (RIKEN Ring Cyclotron), fRC (Fixed-frequency Ring Cyclotron), IRC (Intermediate-stage Ring Cyclotron) and SRC (Superconduction Ring Cyclotron), with the SRC driving the beam up to 345 MeV/nucleon. Two strippers are located upstream and downstream fRC ensuring a highly charged state for the primary beam. Following the SRC, the beam is directed towards the primary target located at the entrance of the BigRIPS separator. The intensity of the $^{238}$U beam was 90 pnA, equating to $5.6 \times 10^{11}$ particles per second (pps).

---

[1] Rikagaku Kenkyusho, which means Physical and Chemical Research Institute in Japanese.

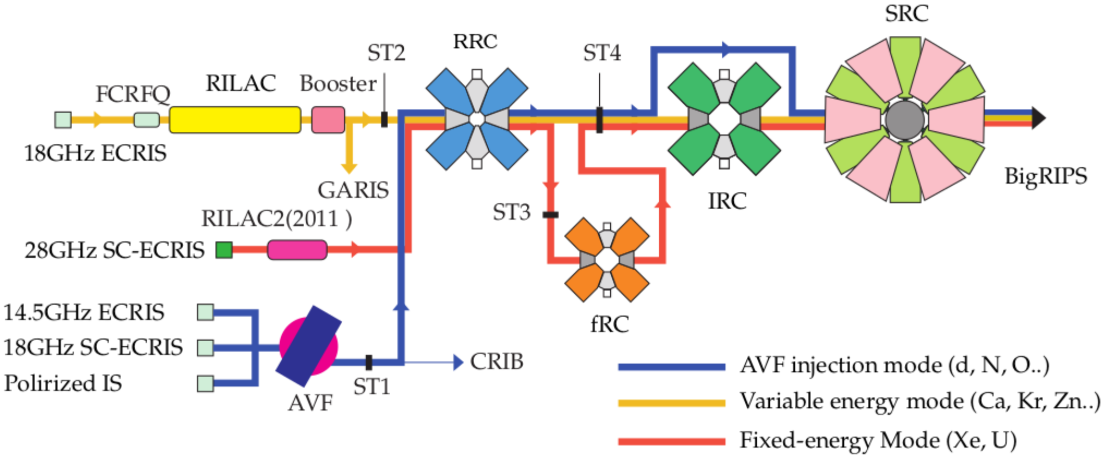

Figure 2.1: Overview of the RIBF heavy-ion acceleration system. Image taken from [54].

### 2.1.2 BigRIPS

After the accelerator system, the two-stage BigRIPS fragment separator is employed for radioactive ion beam separation [55]. It spans a length of 78.2 m and comprises 14 superconducting triplet quadrupoles (STQs) for beam focusing, and 6 room-temperature dipoles with a bending angle of 30°, distributed between eight foci (F0 to F7). Its momentum acceptance is ±3%, while its horizontal and vertical angular acceptances are ±40 mrad and ±50 mrad, respectively. The first stage of BigRIPS, from F0 to F2, is configured as a two-bend achromatic separator. It comprises a set of 4 STQs and 2 dipoles, with sextupoles integrated into several STQs to introduce higher order corrections aimed at achieving an enhanced resolution. This part is involved in producing the secondary RI-beam and selecting the desired nuclei using the B$\rho$-$\Delta$E-B$\rho$ method. This way, the momentum-loss achromat technique [56, 57] is made possible thanks to a wedge-shaped energy degrader at F1, as explained in 2.1.2.a.

This first stage does not allow to produce isotopically pure beams. Therefore, in the second stage, from F3 to F7, the isotopes are identified using the so called TOF-$B\rho$-$\Delta E$ method [2]. Following this, the secondary beam is directed into the different experimental beam-lines of the RIBF, such as SAMURAI [3] or ZeroDegree in the case of our experiment, as demonstrated in figure 2.2.

---

[2] Time of flight, magnetic rigidity and energy loss.

[3] Superconducting Analyzer for Multi-particles from Radioisotope beams.

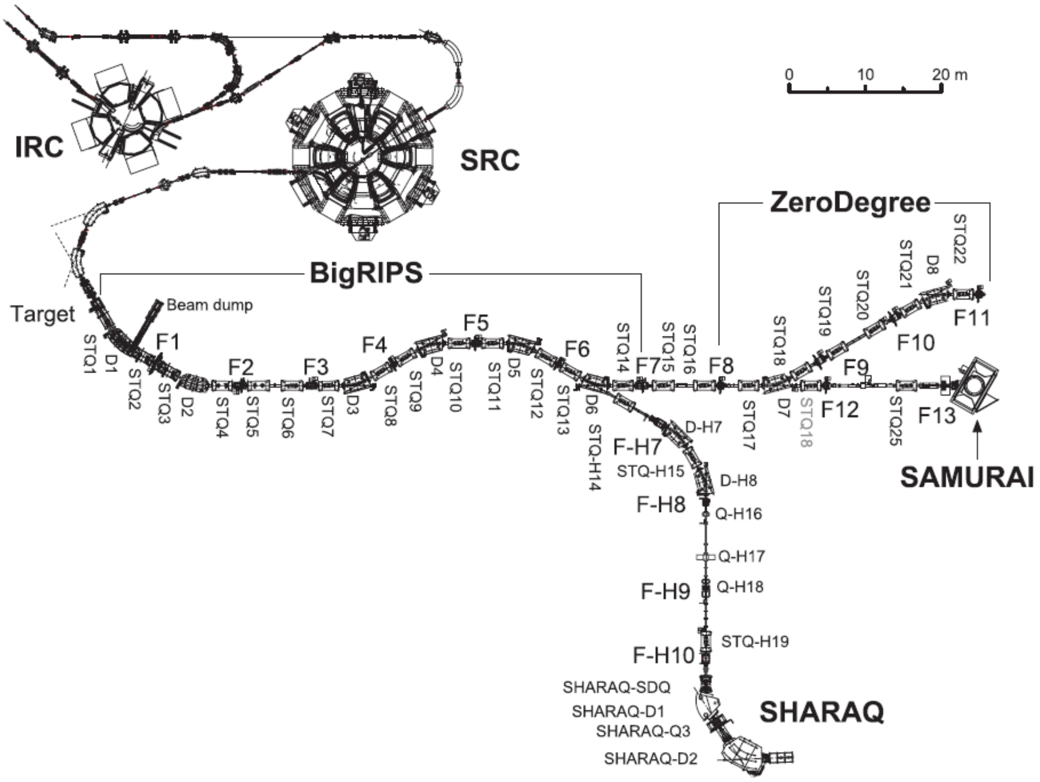

Figure 2.2: Schematic layout of the RI Beam Factory (RIBF) at RIKEN Nishina Center. Image taken from [55].

### a/ Production and selection of the secondary beam

At the entrance of BigRIPS (F0), a rotating 4-mm thick $^9$Be primary target was employed to induce the in-flight fission of the $^{238}$U primary beam, resulting in the production of a wide range of nuclei. These nuclei are fully stripped, indicating that their charge is identical to their proton number $Z$. To select the nuclei of interest, the momentum-loss achromat method is employed [57]. This technique utilizes a B$\rho$-$\Delta$E-B$\rho$ selection method employing two dipoles (D1 and D2) separated by an aluminium wedge-shaped 8mm-thick degrader, placed at F1. A schematic representation of this technique is shown in figure 2.3.

The motion of an ion with a mass number $A$ and charge $Q = Ze$, in a uniform magnetic field $\overrightarrow{B}$, is determined by its magnetic rigidity $B\rho$ defined as :

$$B\rho = \frac{P}{Q} = \frac{\gamma m v}{Ze} = \frac{uc\beta\gamma A}{Ze}, \tag{2.1}$$

where the ion's curvature radius $\rho$, the velocity ($v = \beta c$), the mass ($m \approx Au$), the atomic mass unit ($u \approx 931.5$ MeV), the speed of light in vacuum ($c$), and the Lorentz factor ($\gamma$ = (1 - $\beta^2)^{-1/2}$) are all related by the given equation. The first dipole (D1) separates the beam based on $\beta\gamma A/Z$ selection, but this selection in $B\rho$ is insufficient since multiple nuclei can have similar $\beta\gamma A/Z$ values. Thus, an aluminum degrader is positioned in F1, where the beam loses energy in accordance with the relativistic Bethe-Bloch formula:

$$\Delta E = \frac{4\pi e^4 nzZ^2}{m_e\beta^2c^2}[\ln\frac{2m_e\beta^2c^2}{I} - \ln(1-\beta^2) - \beta^2], \tag{2.2}$$

where $z$, $n$ and $I$ are respectively the atomic number, atomic density and mean excitation potential of the crossed medium which is the aluminium degrader in this case. As seen from equation 2.2, the dissipation of energy by the fragments within the degrader is approximately proportional to $Z^2/\beta^2$. This is a distinct dependency on factors ($A$, $Z$, $\beta$) compared to $B\rho$. Consequently, the degrader enables discrimination between two distinct isotopes possessing identical $B\rho$ values, as their energy losses differ. Subsequently, another selection based on $B\rho$ is carried out after the degrader, using the dipole (D2). The degrader's thickness varies in correspondence with the horizontal position at F1, ensuring a complete achromatism in the D1-degrader-D2 arrangement. This design guarantees that the isotopes' positioning within the F2 focal plane remains unaffected by their momentum, it depends solely on their nature. Then, the adjustment of the slits within F2 serves to purify the beam.

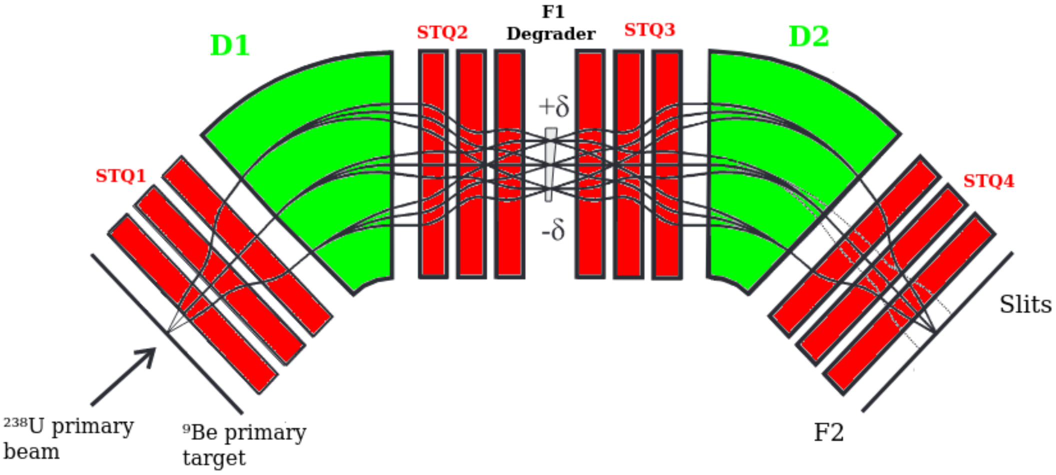

Figure 2.3: Schematic representation of the momentum-loss achromat technique. The beam can be purified by stopping the contaminants (dashed lines) with the F2 slits after B$\rho$-$\Delta$E-B$\rho$ selection. Image taken from reference [58] and modified.

### b/ Identification of the secondary beam

The second stage of BigRIPS, spanning from F3 to F7, aims to detect the fragments that have exited the first stage. An additional wedge-shaped 2mm-thick aluminium degrader is positioned at F5 to enhance the separation of the secondary beam. In order to identify the isotopes, the TOF-$B\rho$-$\Delta E$ method is employed, where the time of flight, magnetic rigidity, and energy loss of the nuclei are measured to determine their mass-to-charge ratio ($A/Q$) and atomic number ($Z$). A detailed explanation of this method is provided in section 3.1.2. The time of flight is measured by two plastic scintillators positioned at F3 and F7, which provide a flight path of 46.6 m, and have a time resolution of approximately 40 picoseconds [59], which results in a relative time-of-flight resolution of 0.016% for the $^{80}$Zn secondary beam at 265 MeV/nucleon. To determine the horizontal angle $\theta$ and the vertical angle $\phi$ of the ion trajectory with respect to the optical axis (z-axis) in the ($xz$) and ($yz$) planes, respectively, two sets of double position-sensitive parallel plate avalanche counters (PPACs) measure the positions $(x, y)$ of the fragments in F3, F5, and F7 focal planes [60, 61]. These ($x$, $\theta$, $y$, $\phi$) coordinates are needed to calculate the $B\rho$ of the ions, as explained in section 3.1.1. The energy loss of the isotopes is measured with a tilted electrode gas ionization chamber [62] situated at F7. Following the second stage of BigRIPS, the nuclei are directed towards the secondary target located in F8, at the entrance of the ZeroDegree spectrometer. This target is an assembly of two beryllium targets with an identical area of 5 x 5 cm$^2$ and thicknesses of 3 mm and 3.8 mm, both with a material density of 1.848 g/cm$^3$. These two parts have been placed into one target holder making a total thickness of 6.8 mm, as shown in Figure 2.4.

The total secondary beam rate was about $4 \times 10^4$ pps at F7, and about 1500 pps for $^{80}$Zn isotopes at the same focal plane.

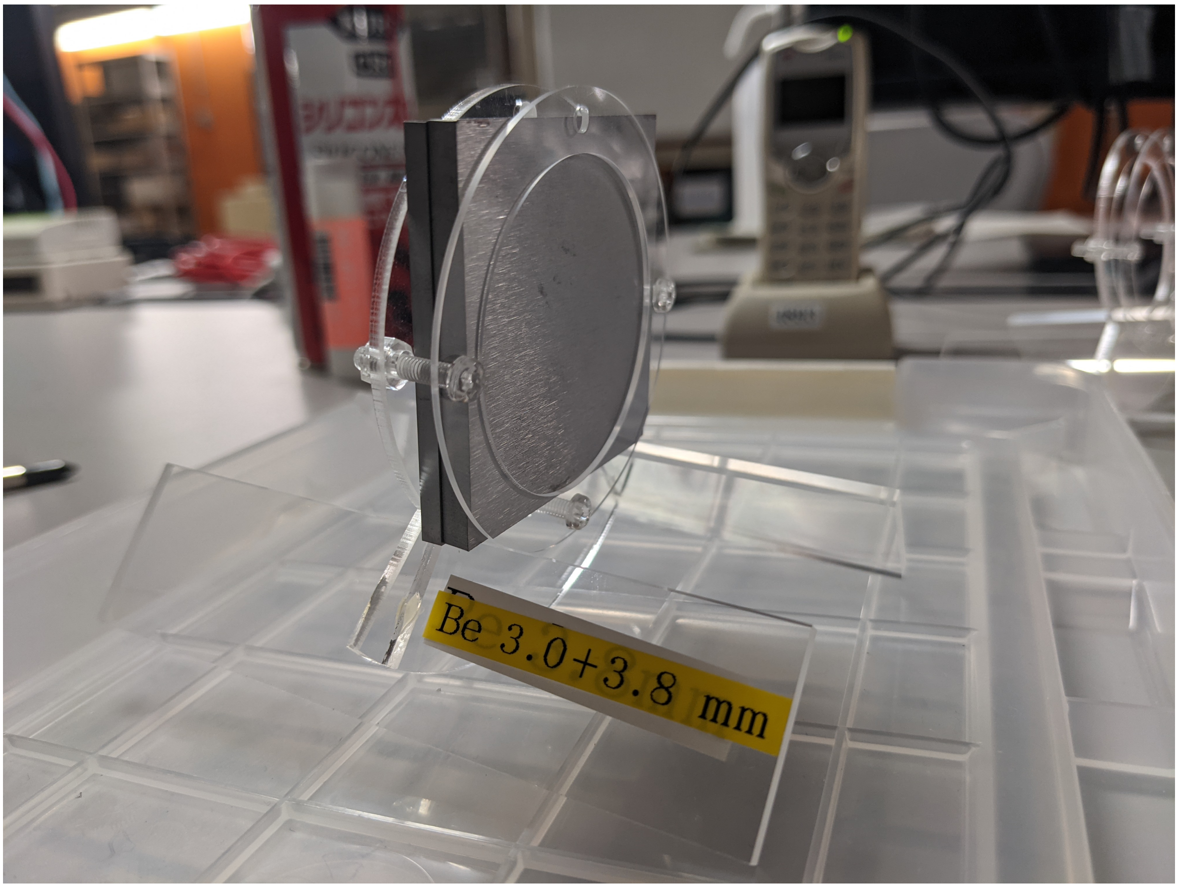

Figure 2.4: Image of the secondary $^{9}$Be target.

## 2.2 BigRIPS and ZeroDegree beamline detectors

To achieve an event-by-event identification of beam particles within the BigRIPS and ZeroDegree spectrometers, three main types of detectors are employed for the TOF-$B\rho$-$\Delta E$ method. These include the PPAC tracking detectors (discussed in section 2.2.1) to determine the ion's position and trajectory, MUSIC ionization chambers (detailed in section 2.2.3) to measure the energy loss, and the plastic scintillators (described in section 2.2.2) to measure the time of flight. Additionally, in the specific case of absolute calibration for the separator and spectrometer, a high-purity germanium (HPGe) detector can be introduced to identify well-known isomer transitions [63].

### 2.2.1 Parallel plate avalanche counters - PPAC

The two-dimensional Parallel Plate Avalanche Counters (PPACs) are gaseous detectors which offer position and trajectory reconstruction at focal planes, serving dual purposes: aiding beam diagnostics and tuning, as well as facilitating event-by-event particle identification in experiments via $B\rho$ determination. The initial PPACs employed at RIKEN's RIPS separator [64] utilized the charge-division method for position determination. However, they have been succeeded by delay-line read-out PPACs, predominantly due to the issue of signal pile-up (approximately 3 µs), which imposed limitations on the maximum counting rates, capping at a few thousand per second. The adoption of the delay-line read-out approach resulted in achieving peak rates of $10^6$ Hz [60].

Utilizing position-sensitive detectors at dispersive focal planes mandates a considerable sensitive area to effectively measure substantial beam momentum and phase space. In the context of beamline detectors for the BigRIPS and ZeroDegree spectrometers, the PPACs' sensitive areas typically measure 240 mm by 100 mm and 240 mm by 150 mm, in the horizontal and vertical dimensions [65]. A single PPAC incorporates two layers for two-dimensional particle measurement, covering both horizontal and vertical aspects. The standard PPAC configuration consists of dual PPAC detectors, earning it the designation "double PPAC." This design enhances efficiency, diminishes event losses attributed to $\delta$-rays[4], and additionally provides a redundant particle tracking capability. At focal planes F3, F5, F7, F9, and F11, two double PPACs are placed to reconstruct particle trajectories. At F8, three double PPACs are employed for a more accurate determination of the ion's trajectory at the point of the $\gamma$ ray. A schematic representation of a RIKEN PPAC is shown in figure 2.5.

The operational principle of PPACs centers on recording energy loss within gases, commonly $C_4H_{10}$ (isobutane) or $C_3F_8$ (perfluoropropane), resulting in the creation of charge (electrons and ionized gas). The presence of a strong electric field between electrode films prompts newly generated electrons to initiate a Townsend discharge, swiftly producing a measurable charge quantity. Due to the high mobility of electrons within the gas at standard pressures, the resulting charge exhibits a distinctive rapid rise and fall time.

Position reconstruction is achieved by capturing the induced charge on cathode electrode strips, which are subsequently linked to multitap delay lines. The delay line maintains a constant characteristic impedance (50 Ω), ensuring a constant signal propagation speed. As a consequence, the time difference between the two extremities of the delay line is proportional to the position of charge accumulation. With an electrode pitch of 2 mm (equivalent to half the width of the charge distribution), this arrangement yields time delay increments of 2 ns.

---

[4] $\delta$-rays arise as secondary electrons possessing enough energy to trigger additional ionization at a distance from the initial particle they were released from. In the context of implementing PPACs, undesired $\delta$-rays initiate multiple avalanche regions, leading to an inaccurate reconstruction of the ion's position.

The time-delayed signals are measured using a time-to-digital converter (TDC), where the start and stop signals are given respectively by the anode and the cathode. The position is then computed with the following expression:

$$x = 0.5\ K_x(T_{x1} - T_{x2}) + x_{offset} \tag{2.3}$$

Here, $K_x$ represents the propagation speed in millimeters per nanosecond (approximately 1.2 mm/ns). $T_{x1}$ and $T_{x2}$ denote the stop times, while $x_{offset}$ is a time offset to take into account the differences in signal propagation time between the extremities of the delay lines and the TDC. With the delay line's dimensions fixed, the sum of the stop signals, $T_{sum} = T_{x1} + T_{x2}$, is a constant and does not depend on the discharge's location. Additional processes, such as the generation of $\delta$-rays and particle multiple hits, lead to reduced $T_{x1}$ or $T_{x2}$ values. This phenomenon results from the enlargement of the avalanche region. All particles produce $\delta$-rays as they traverse and decelerate within a medium. The signals originating from the PPAC experience local amplification, and an optical transmitter dispatches these optical signals through a 100-meter-long fiber optic cable to the data acquisition (DAQ) zone. The high-speed signals are preserved and picked up by photodiodes. Temporal cues are conveyed to a multifunctional time-to-digital converter (TDC) for multiple-hit events.

The final $X, Y$, $\theta$ and $\phi$ values in a given focal plane at a position $Z$, are obtained by combining the measurements of the 2 sets of double PPACs, using the following formulae:

$$\begin{cases} X = X_1 + \dfrac{X_1 - X_2}{Z_1 - Z_2}(Z - Z_1) & (2.4) \\ Y = Y_1 + \dfrac{Y_1 - Y_2}{Y_1 - Y_2}(Z - Y_1) & (2.5) \\ \theta = \arctan\left(\dfrac{X_1 - X_2}{Z_1 - Z_2}\right) & (2.6) \\ \phi = \arctan\left(\dfrac{Y_1 - Y_2}{Z_1 - Z_2}\right), & (2.7) \end{cases}$$

where $X_i$ and $Y_i$ are the measured coordinates in the double PPACs that are located at $Z_i$.

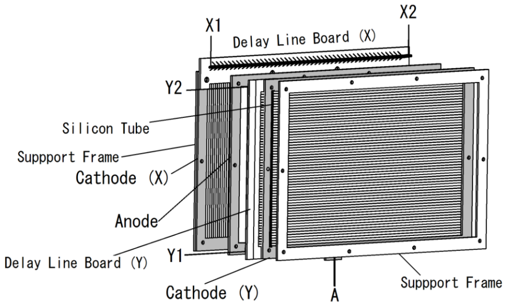

(a) Main components of a 240 mm × 150 mm PPAC detector at RIKEN.

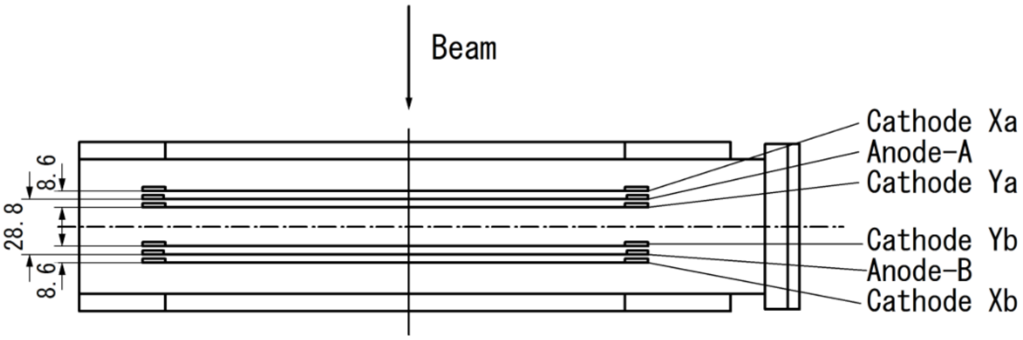

(b) Side view of double PPAC layers

Figure 2.5: Schematic views of RIKEN PPACs for BigRIPS and ZeroDegree. Images taken from [65].

### 2.2.2 Plastic scintillator detectors

For determining the time-of-flight (ToF) between focal planes within the spectrometers, fast timing plastic scintillators are utilized (possessing decay constants of the order of 2 ns). With this fast timing properties and their very high efficiency (close to 100%), these detectors at F7 and F11 are used for triggering the BigRIPS and ZeroDegree acquisitions, respectively, when they are hit. The ones used in this experiment had a thickness of 200 µm, and their active area typically measures 120 mm by 100 mm.

The readout of the scintillation generated by the energy deposition of the beam ions as they traverse the plastic material is achieved using a pair of photomultiplier tubes (PMTs). These PMTs are positioned on opposing edges (right and left) of the plastic material, allowing for dual-sided light collection. The correlation of signals in terms of charge and timing between the two PMTs enables the identification and rejection of spurious events, such as background noise or events involving multiple particles. By examining the difference in the charges collected from the two PMTs (which correspond to the quantities of detected photons), one can deduce the point of interaction of the ions in the plastic sheet. The cumulative charges captured by the two PMTs can be expressed using the following relationship:

$$Q_{left} = Q_{total} \exp\left\{\frac{-L/2 + x}{\lambda}\right\} \tag{2.8}$$

$$Q_{right} = Q_{total} \exp\left\{\frac{-L/2 - x}{\lambda}\right\}, \tag{2.9}$$

where $Q_{left}$ and $Q_{right}$ represent the charges collected by the left and right PMTs, respectively. $Q_{total}$ is the total accumulated charge, $L$ denotes the distance between the two PMTs across the scintillator, $x$ indicates the position along the scintillator's length, and $\lambda$ is the light attenuation length[5].

The combination of the two previous equations leads to the relation between the charges and the ion's interaction position:

$$x = \frac{\lambda}{2} \ln\left(\frac{Q_{left}}{Q_{right}}\right) \tag{2.10}$$

Similarly to PPACs, the position of the interaction can be obtained using the time difference between the two PMTs:

$$x = (T_{left} - T_{right})\frac{c}{n}, \tag{2.11}$$

where $c$ is the speed of light in vacuum, and $n$ is the refraction index of the scintillator medium. $T_{left}$ and $T_{right}$ are the observed time flashes in the left and right PMTs, respectively. Combining the equations 2.10 and 2.11, one gets the following relationship:

$$(T_{left} - T_{right})\frac{c}{n} = \frac{\lambda}{2} \ln\left(\frac{Q_{left}}{Q_{right}}\right) \tag{2.12}$$

$c$, $\lambda$ and $n$ being constant, they can be gathered into one single factor, leading to a linear relation between the time difference and the logarithm of the charges ratio. The events which do not satisfy this equality can be removed as it will be detailed in section 3.2.1.d.

---

[5] The light attenuation length refers to the distance over which light intensity decreases to about 1/e (approximately 37%) of its initial value as it travels through a medium. In the context of scintillators or other materials, it quantifies how far light can propagate before its intensity diminishes significantly due to absorption and scattering processes within the material. It is expressed in units of inverse distance

For the calculation of the time of flight between two focal planes, an average time between the left and right PMTs is used in each focal plane. Then, the time of flight is calculated as the difference between these two averages. For instance, for the flight path between F3 and F7, the following formula is used:

$$ToF_{F3F7} = \frac{T_{F7left} + T_{F7right}}{2} - \frac{T_{F3left} + T_{F3right}}{2} + ToF_{F3F7offset} \tag{2.13}$$

where $ToF_{F3F7offset}$ is a time offset that is introduced to take into account the sum of all propagation delays within the cables. This parameter is determined experimentally as explained in section 3.1.4. An equation similar to equation 2.13 is used to determine the time of flight between F8 and F11, in ZeroDegree.

### 2.2.3 Ionization chambers (MUSIC)

The Beth-Bloch equation 2.2 allows to deduce the atomic charge from the energy loss. For the measurement of the energy deposit, one ionization chamber (MUSIC [6]) is employed at F7 and another one is at F11. A specialized MUSIC detector designed for high-rate applications has been successfully developed and put into operation at RIKEN, taking the form of a Tilted-Electrode Gas Ionization Chamber (TEGIC) [62]. The maximum sustainable particle count per second for the RIKEN TEGIC has been demonstrated to reach levels as high as $10^6$ particles [62].

Illustrated in figure 2.6 is an overview of the RIKEN TEGIC. Similar to a conventional MUSIC detector, the gas volume is subdivided into discrete sections (24 in total), utilizing a configuration of 12 anode electrodes and 13 cathode electrodes (with a pitch of 20 mm), constructed from thin layers of aluminized mylar. As beam particles traverse the gas-filled chamber, the energy deposition results in the release of electrons and ions. The tilted orientation of the electrodes causes these generated electrons and positive ions to travel in opposite directions along the electric field lines, away from the trajectory of the beam ions. This way, their paths do not intersect, and this enables the effective operation under high-intensity beam conditions with the minimization of electron-ion recombination, a phenomenon that decreases the charge collection efficiency. Since electrons exhibit a greater mobility in a gas compared to ions, the charge collected by the anode (which captures electrons) is registered more rapidly than that collected by the cathode. Therefore, only the anode signal is read out. The cathodes are interconnected, and pairs of anodes are linked as well, resulting in a total number of outputs that is reduced to six. Each of these outputs is subjected to amplification using a charge-sensitive amplifier, and a subsequent amplification is carried out using

---

[6] MUlti-Sampling Ionization Chamber

a spectroscopy amplifier, before the signal is digitized by a peak-sensitive ADC. The geometric mean of these signals is proportional to the energy loss, thus allowing for the determination of the atomic charge, using the following expression:

$$Z = c_3\beta\sqrt{\frac{(c_1\Delta E + c_2)_{MeV}}{\ln(I\beta^2) - \ln(1-\beta^2) - \beta^2}} + c_4 \tag{2.14}$$

where $I$ represents the ionization energy required for the creation of an electron-ion pair, and $\Delta E$ the raw non-calibrated geometric mean of the amplified six anode signals. The energy deposition is first calibrated to MeV units using coefficients $c_1$ and $c_2$, while the remaining coefficients, $c_3$ and $c_4$, are optimized to accurately reproduce atomic numbers. The velocity $\beta$ that is used is either the one in the F5-F7 region for the identification in BigRIPS, or the one in the F9-F11 region in ZeroDegree. These are obtained with the two-fold $B\rho$ measurements as explained in section 3.1.3.

For operational purposes, a typical gas mixture of 90% Ar and 10% $CH_4$ is employed, with the bias voltage set at 500 V. The ion chamber's entrance is designed to be sufficiently large, enabling the capture of the complete phase space of the beam at both F7 and F11 positions.

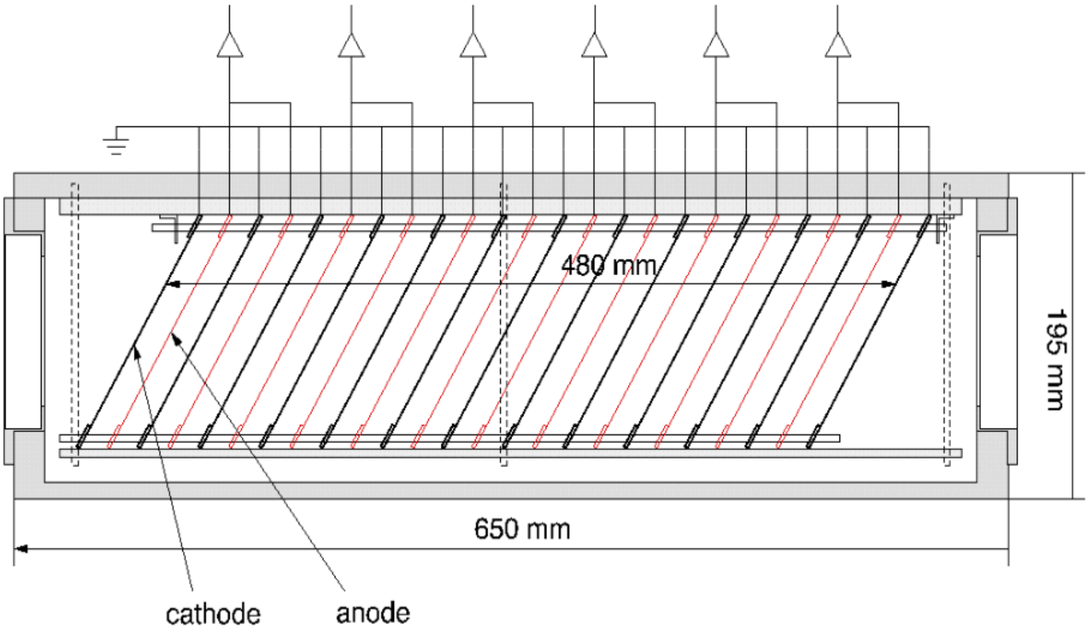

Figure 2.6: Side view of a TEGIC at RIKEN. Image taken from [62].

## 2.3 HiCARI germanium array

HiCARI (High-resolution Cluster Array at RIBF) is a germanium multi-detector developed by the SUNFLOWER[7] collaboration, aiming at a better energy resolution than the previous scintillators that were used at RIBF. This $\gamma$-ray spectrometer is made of different types of high-purity germanium clusters, gathered from different laboratories in the world. These clusters comprise highly segmented crystals, thus improving both the intrinsic energy resolution and the position resolution on the $\gamma$-ray hits. In the RIBF181 experiment, we had:

- 4 Miniball triple clusters[8](labeled as MB0, MB2, MB4 and MB5 in the data analysis) from ISOLDE (CERN). Each cluster comprises 3 hexagonal crystals that are 6-fold segmented [66]. One crystal in MB0 was no longer working correctly.
- 4 clover detectors from IMP (China), also referred to as SuperClovers (with labels from SC6 to SC9 in the data). Each clover is made of 4 crystals, and each crystal is 4-fold segmented.
- One GRETINA [67] P3 from LBNL (Berkeley), made of 3 crystals[9] (labeled from 0 to 2) that are 36-fold segmented. For the second crystal (labeled CRYST1), due to an issue with its signal analysis, there was no recorded mode2 data (defined in section 2.5) in the second half of the experiment.
- One GRETINA QUAD from RCNP (Osaka), made of 4 crystals with a similar 36-fold segmentation. Unfortunately, 2 out of the 4 crystals were not operational during the experiment.

  Geometrical representations of the crystals with their segmentation for each detector type are shown in figure 2.7.

---

[7] Spectroscopy of Unstable Nuclei with Fast and sLOW beam Experiments at RIBF.

[8] Initially, in the first experiments of the HiCARI campaign, there were 6 MB modules (with labels from MB0 to MB5 in the data). Since our experiment was the last in the campaign, one of the Miniball detectors (MB1) was damaged before the beginning of our experiment. Consequently, it was not mounted in our setup. In addition, since the beginning of our experiment, it was noticed that MB3 was having large gain instabilities. This prevented us from using its data. Therefore, we ended up with only 4 operational MB clusters.

[9] There are 3 crystals labeled CRYST0, CRYST1 and CRYST2 and they were at average $\theta$ angles of 57°, 69°and 80°, respectively.

Figure 2.7: Geometrical representations of the crystals for each detector-type [68]

### 2.3.1 Geometry

Due to the high beam velocities ($\beta \approx 0.6$), there is a Lorentz boost that reduces the angle between the trajectories of the $\gamma$ rays and the beam axis. Therefore, the germanium clusters were placed downstream the target, at forward angles to maximize the detection efficiency. To have a better constraint on the lifetime measurements, the different detector types were arranged into different rings (different $\theta$ angles with respect to the beam axis). The GEANT4 visualization of the geometry of the HiCARI array located at the F8 focus is shown in Figure 2.10. In this picture, all the detectors are represented, whether they were operational or not. The forward ring ($\theta$≈22–55°) comprises the Miniball detector modules (MB). The tracking detectors (P3 and QUAD) are located in the horizontal plane, with the clover detectors (SC) arranged on top and bottom of the $\theta$≈60–85° ring. These angles are summarized in table 2.1 for each detector. The mentioned details can be seen on figures 2.8 and 2.9 that show the angles in spherical coordinates and the positions in Cartesian coordinates, respectively, for only the functional crystals. In both figures, the segment centers are shown for Miniball and clover detectors, while the reconstructed hit positions are represented for the GRETINA-type ones.

The method employed to determine the centers of all segments relative to the target involved the use of the photogrammetry technique. The latter consists in taking, from different angles, several images of the detectors on which small markers were attached. With a minimization algorithm, each capsule was positioned within the laboratory frame, and the coordinates of the segment centers were derived using the provided detector designs from the manufacturer.

| Detector | $\theta$ (degrees) |
|---|---|
| MB0 | 44 |
| MB2 | 30 |
| MB3 | 30 |
| MB4 | 43 |
| MB5 | 44 |
| SC6 | 77 |
| SC7 | 75 |
| SC8 | 79 |
| SC9 | 78 |
| P3 | 71 |
| QUAD | 75 |

Table 2.1: Summary of the $\theta$ angles for each cluster in the HiCARI array, as derived from the photogrammetry technique. The MB3 cluster was not used in our analysis.

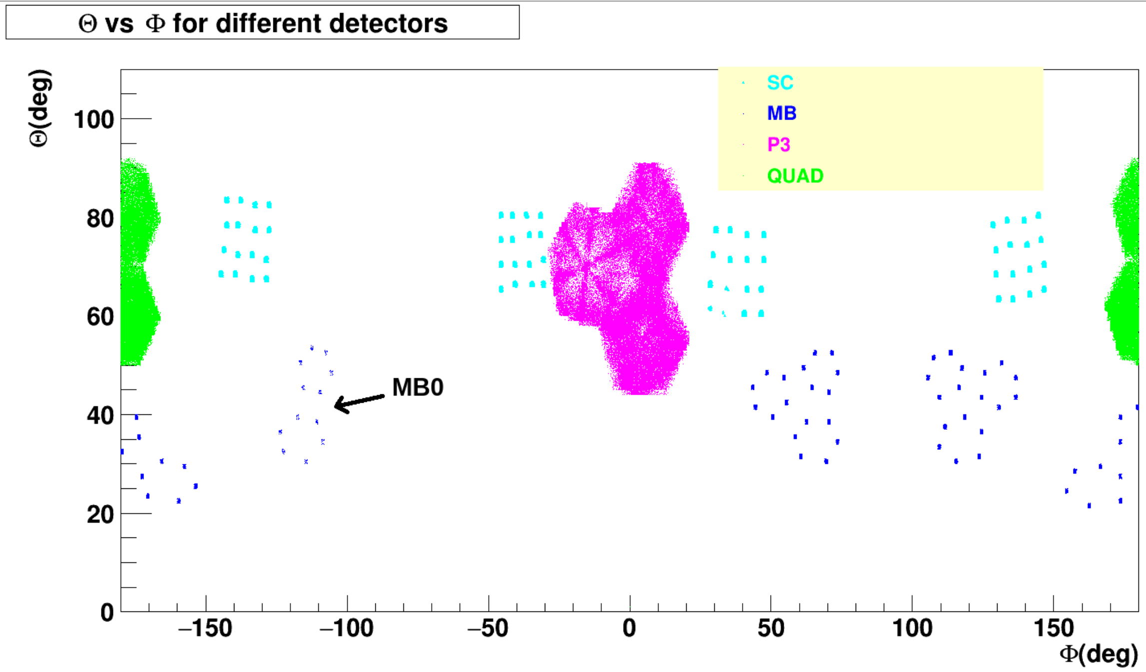

Figure 2.8: Angular positions for the HiCARI array clusters in spherical coordinates. The MB3 detector and the missing crystals (one in MB0 and two in QUAD) are not represented.

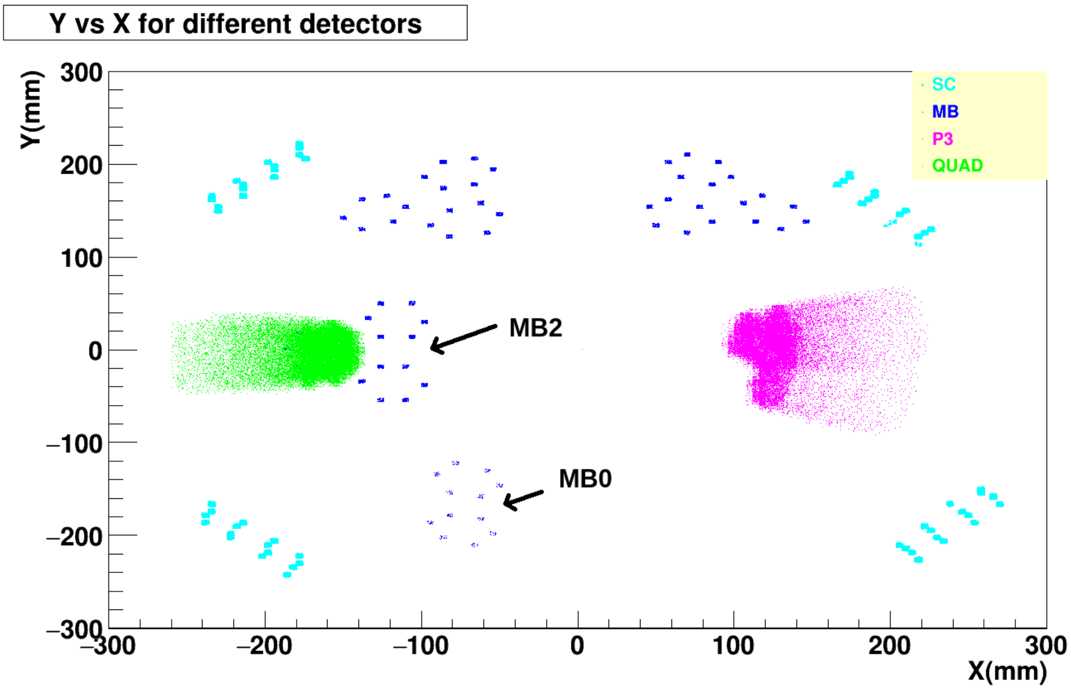

Figure 2.9: Cartesian coordinates for the HiCARI array clusters. The MB3 module and the missing crystals (one in MB0 and two in QUAD) are not represented. One crystal of MB2 is hidden by the QUAD module.

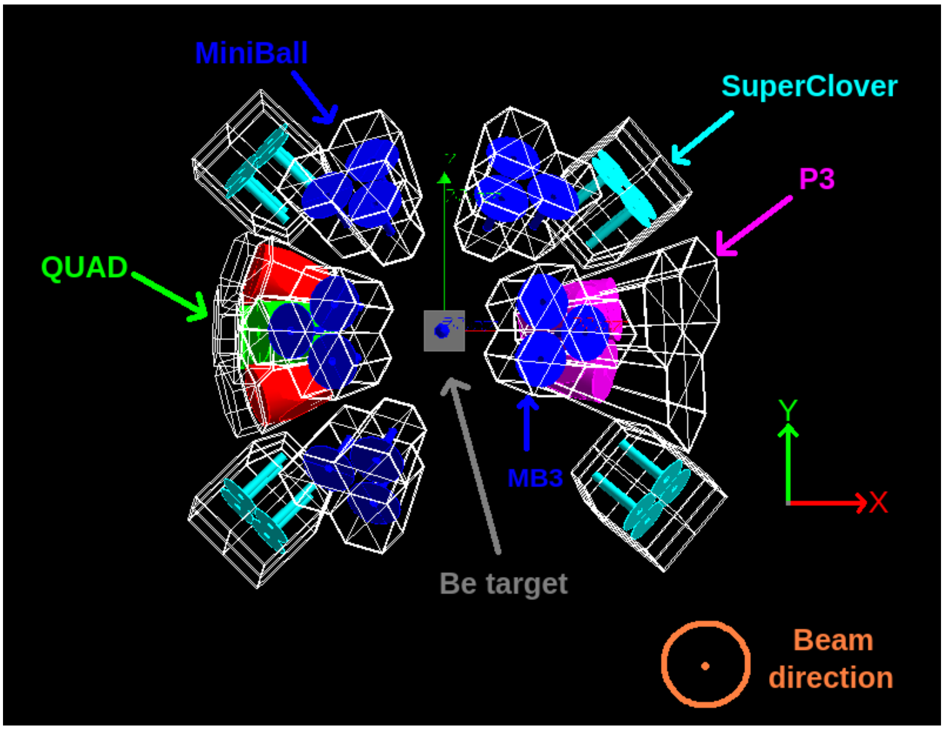

Figure 2.10: Image of the HiCARI geometry using GEANT4 simulation.

### 2.3.2 Pulse shape decomposition

The GRETINA-type detectors are highly segmented (36 segments per crystal). For each segment, the pulse shape (trace) is recorded, and then compared to a library (basis) that links the pulse shape with the position of the hit in the detector. To establish a robust basis, a "superpulse" is collected from the crystal segments, typically by employing a $^{60}$Co source to generate a typical signal in a given segment and induced signals in the neighbouring segments. A superpulse is a concatenation of averaged signals (traces) from numerous single-segment events, exemplified in Fig 2.11, where each trace segment spans 500 ns. Monte Carlo simulations are used to reproduce the measured superpulse, employing a function with nearly a thousand fit parameters that consider cross-talks, signal delays, rise times, and other correction factors such as those for crystal impurity distribution, electron and hole mobilities, neutron damage, electronics non-linearities, crystal temperatures, and charge cloud dimensions [69]. The fitted parameters allow for the generation of the final basis, computed across all grid points, forming the cornerstone of the GRETINA decomposition. Typically, a superpulse fit is conducted before each campaign or experiment to accommodate changing conditions, such as crystal neutron damage. Thanks to this method, the coordinates of the hits in the detectors are determined with a precision of about 2 mm, better than the size of a segment [70].

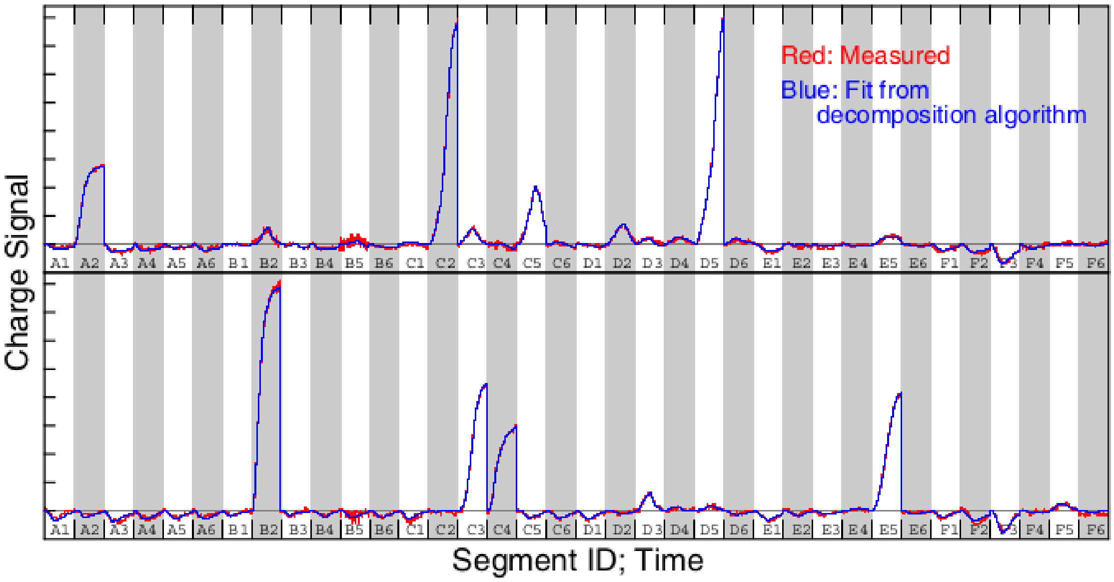

Figure 2.11: Two examples of measured superpulses (red) with the fits of the pulses (blue). Image taken from [71].

## 2.4 ZeroDegree

### 2.4.1 Identification of the outgoing beam

The products resulting from the fragmentation on the secondary target are identified using the ZeroDegree spectrometer [55], as depicted in figure 2.2, with the same TOF-$B\rho$-$\Delta E$ method as in BigRIPS. Comprising 6 STQs and 2 dipoles similar to those found in BigRIPS, ZeroDegree spans a total length of 36.5 m and features 4 foci (F8 to F11). The plastic scintillators were positioned at F8 and F11 for the time of flight measurement. The MUSIC Ionization chamber was at F11 for the recording of the energy loss, and the PPAC detectors were localized at the F8, F9 and F11 focal planes for the reconstruction of the beam trajectory. During the HiCARI campaign, ZeroDegree operated in its large acceptance mode, with an angular acceptance of ±45 mrad horizontally and ±30 mrad vertically, along with a momentum acceptance of ±3%. The settings of ZeroDegree were specifically adjusted for $^{79}$Cu isotopes. The average rate of $^{79}$Cu nuclei from the $^{80}$Zn($^{9}$Be, X)$^{79}$Cu reaction channel at F11 was of the order of 6 pps, with an average kinetic energy of 210 MeV/nucleon.

### 2.4.2 Doppler correction of the $\gamma$-ray energies

As the beam travels with relativistic speeds when emitting the $\gamma$ rays, the energy $E_\gamma$ observed by the HiCARI detectors deviates from the energy $E_0$ in the nucleus reference frame, due to the Doppler effect. This effect depends on the velocity $\beta$ of the nucleus and the $\theta_\gamma$ angle between the $\gamma$-ray direction and the velocity vector of the emitting isotope. This shift can be corrected with the following formula:

$$E_0 = E_\gamma \frac{1 - \beta \cos\theta_\gamma}{\sqrt{1 - \beta^2}} \tag{2.15}$$

An accurate calculation of $E_0$ requires the measurement of the $\theta_\gamma$ angle and the velocity at the emission point. When a nucleus with an incoming velocity $\overrightarrow{\mathbf{V}}_{\text{in}}$ traverses the target, the nucleus itself or the reaction residue are scattered with an angle $\theta_s$ with respect to z-axis that can be different from the incident angle $\theta_{in}$. This scattering angle (the direction of the outgoing velocity vector $\overrightarrow{\mathbf{V}}_{\text{s}}$) is measured thanks to 2 sets of double PPAC detectors upstream the target and a third one downstream from the target, as illustrated in fig 2.12.

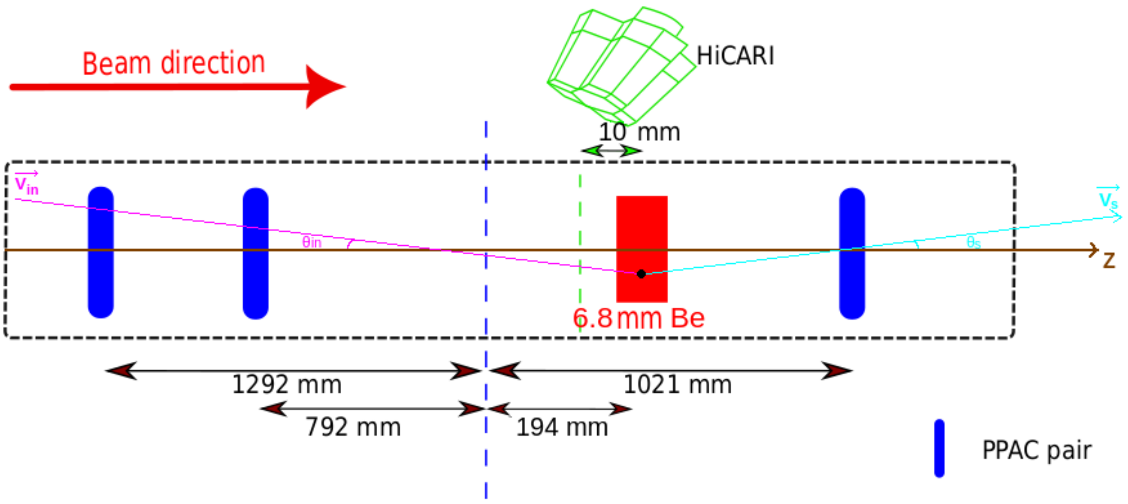

Figure 2.12: Schematic view of the configuration of the PPAC detectors at F8. The blue dashed line is in the F8 focus while the green one shows the Z-axis origin of the reference frame of HiCARI.

As regards the direction of the $\gamma$ ray, it is taken as the direction of the straight line that links the position of the hit (known from HiCARI data) and the emission point. As there is no knowledge about the position at which the reaction and the emission occur, both are assumed to happen at the middle of the target, after crossing a distance $d = 3.4$ mm / $\cos(\theta_{in})$ (half its total thickness). Having these two processes at the same point is correct only if the lifetimes of the decaying states in the residue are neglected. However, if these states have a significant lifetime (of the order of picoseconds or more), this assumption is not valid anymore, since the angle that is used for the Doppler correction is smaller than the real angle and the velocity that is used is higher than the real one. This effect is discussed in section 3.7.1.

## 2.5 Data acquisition

Event recording is accomplished through the RIBF data-acquisition system [72]. To enhance efficiency, minimize dead time, and conserve disk space, it is imperative to fine-tune the data acquisition process, by keeping only the relevant events.
When a nucleus traverses the F7 plastic scintillator, it generates an F7-trigger signal. If this nucleus, or the product of a reaction in the target, reaches the F11 plastic scintillator, it initiates an F11-trigger signal. These two signals, F7-trigger and F11-trigger, are combined to form the F7×F11 signal. In the HiCARI acquisition, a $\gamma$-detector signal serves as a trigger signal if its energy is above a specified threshold. This $\gamma$ trigger is then combined with the F7xF11 trigger. Finally, the data acquisition starts if at least one of the following conditions is satisfied:

- The F7 plastic scintillator is hit, disregarding if the nucleus reaches the end of ZeroDegree or not, and if there is any $\gamma$ ray that triggered the HiCARI acquisition or not. This is the F7DS trigger, downscaled (DS) by a factor of 100 for avoiding to record too many events.

- Both scintillators at F7 and F11 are hit, without necessarily requesting a $\gamma$-ray hit in HiCARI. Also for this case, the event goes through a downscale window of 1/7, and thus giving the downscaled F7xF11 trigger.

- The plastics in F7 and F11 are hit, and a $\gamma$ ray is detected. This is the F7xF11x$\gamma$ trigger.

As regards the acquisition in the HiCARI spectrometer, the data was written into disk in two different formats (modes):

- Mode 3 : For all detectors, this is the raw data that is directly taken from the acquisition, and it contains the traces.

- Mode 2 : This is written only for the case of the Gretina-like detectors. To do so, the raw data is sent to a software that applies the pulse shape decomposition allowing to reconstruct the positions of the $\gamma$-ray hits in the resulting files.

Timestamps are kept in all the recorded data. By comparing to the reference timestamp of the BigRIPS acquisition, the 3 types of data files (mode2, mode3, and BigRIPS/ZeroDegree) are merged into a single one, allowing to gate on the reaction channels of interest and obtain and analyze the corresponding $\gamma$-ray spectra. An overview of the data flow can be seen in fig 2.13.

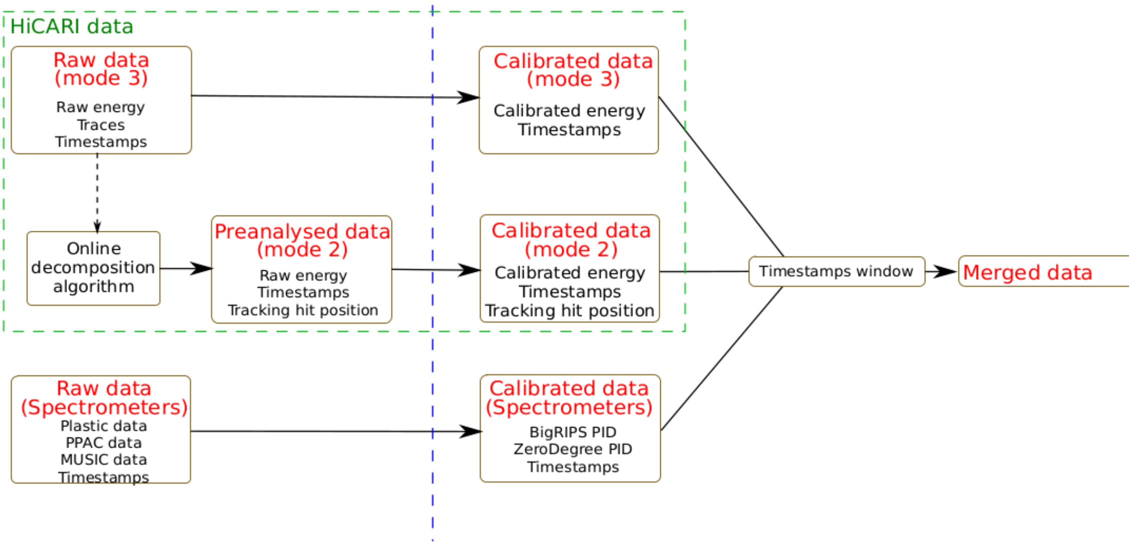

Figure 2.13: Schematic view of the data analysis framework. Image taken from [68]

# 3

# Data analysis

## Contents

The data analysis can be divided into three major parts. The first part deals with the identification of the nuclei in both BigRIPS and ZeroDegree, whereas the second part deals with the energy calibration of the HiCARI germanium detectors and the Doppler correction of $\gamma$-energy spectra. Finally, GEANT4 simulations are performed for the extraction of lifetimes from the shapes of the peaks in the $\gamma$ spectra.

## 3.1 Particle identification

To begin the analysis process, the BigRIPS and ZeroDegree spectrometers are utilized to identify the produced isotopes. This is accomplished through an event-by-event analysis, where the trajectory of particles is reconstructed and the TOF-$B\rho$-$\Delta E$ and the two-fold $B\rho$ methods are applied.

### 3.1.1 Trajectory reconstruction

The trajectory reconstruction is needed to determine the $B\rho$. The ion's path within a spectrometer is characterized by an ion-optical transfer matrix, which connects the input and output coordinates in two consecutive focal planes. For instance, the following matrix equation is used between F3 and F5:

$$\begin{pmatrix} x_5 \\ \theta_5 \\ y_5 \\ \phi_5 \\ \delta_{35} \end{pmatrix} = \begin{pmatrix} (x|x) & (x|\theta) & (x|y) & (x|\phi) & (x|\delta) \\ (\theta|x) & (\theta|\theta) & (\theta|y) & (\theta|\phi) & (\theta|\delta) \\ (y|x) & (y|\theta) & (y|y) & (y|\phi) & (y|\delta) \\ (\phi|x) & (\phi|\theta) & (\phi|y) & (\phi|\phi) & (\phi|\delta) \\ (\delta|x) & (\delta|\theta) & (\delta|y) & (\delta|\phi) & (\delta|\delta) \end{pmatrix} \begin{pmatrix} x_3 \\ \theta_3 \\ y_3 \\ \phi_3 \\ \delta_{35} \end{pmatrix} \tag{3.1}$$

Here, $x$ and $\theta$ are the horizontal position and angle, $y$ and $\phi$ are the vertical position and angle, and $\delta_{35}$ is the relative deviation of the $B\rho_{35}$ between the two foci from the central value B$\rho_0$ , and it is defined as:

$$\delta_{35} = \frac{B\rho_{35} - B\rho_0}{B\rho_{35}} \tag{3.2}$$

The central value B$\rho_0$ is obtained by the magnetic field measurements within the dipole magnets. High accuracy and precise Nuclear Magnetic Resonance (NMR) probes are employed for this purpose.

For example, the horizontal position coordinate $x_5$ is linked to $x_3$, $\theta_3$, $y_3$, $\phi_3$ and $\delta_{35}$ through the coefficients in the matrix. These coefficients are known at first order from previous experiments, and higher order corrections are needed as discussed in section 3.3, to achieve a better $A/Q$ resolution.

Thanks to PPAC detectors, $x_3$, $x_5$, $\theta_3$, $y_3$, and $\phi_3$ are measured, and their values are used to deduce $\delta_{35}$. After that, $B\rho_{35}$ is calculated using equation 3.2. The same calculation is used in the F5-F7, F8-F9 and F9-F11 regions.

### 3.1.2 TOF-$B\rho$-$\Delta E$

The identification of particles in BigRIPS and ZeroDegree relies on the TOF-$B\rho$-$\Delta E$ method [59]. The latter allows to deduce, on an event-by-event basis, both the atomic number ($Z$) and the mass-to-charge ratio ($A/Q$) of the nuclei through measurements of their time of flight (TOF), magnetic rigidity ($B\rho$), and energy loss ($\Delta E$). These quantities are determined using the following relations:

$$TOF = \frac{L}{\beta c} \tag{3.3}$$

$$B\rho = \frac{uc\beta\gamma A}{Q} \tag{3.4}$$

$$\Delta E = \frac{4\pi e^4 nzZ^2}{m_e\beta^2c^2}[\ln\frac{2m_e\beta^2c^2}{I} - \ln{(1-\beta^2)} - \beta^2] \tag{3.5}$$

In these equations, $L$ is the flight path length, $\beta$ is the velocity of the particle relative to the speed of light in vacuum ($c$), $\gamma$ is the Lorentz factor calculated as $(1-\beta^2)^{-1/2}$, $u$ is the atomic mass unit, with a value of 931.5 MeV, $m_e$ is the mass of the electron and $e$ is the elementary charge. Concerning the remaining parameters, $z$, $n$ and $I$ are respectively the atomic number, the atomic density and the mean excitation potential of the material that the particle is penetrating.

### 3.1.3 Two-fold $B\rho$ method

Incorporating the wedge energy degrader at F5 in BigRIPS results in two distinct ion beam velocities between the TOF detectors at F3 and F7, one before and one after passing through F5. Consequently, in order to accurately consider the energy loss for the determination of $A/Q$ and the reconstruction of the nuclei velocities in the target (for the Doppler correction of the $\gamma$-ray energies), it is necessary to perform a dual $B\rho$ determination. Then, from equations 3.3 and 3.4, we have:

$$TOF = \frac{L_{35}}{\beta_{35}c} + \frac{L_{57}}{\beta_{57}c} \tag{3.6}$$

$$(\frac{A}{Q})_{35} = \frac{c(B\rho)_{35}}{m_u\gamma_{35}\beta_{35}} \tag{3.7}$$

$$(\frac{A}{Q})_{57} = \frac{c(B\rho)_{57}}{m_u \gamma_{57} \beta_{57}} \tag{3.8}$$

In the case where there is no charge state change when passing through F5, the two values of $A/Q$ in the F3-F5 and the F5-F7 regions are equal. Therefore, the following relation is obtained by combining equations 3.7 and 3.8:

$$\frac{(B\rho)_{35}}{(B\rho)_{57}} = \frac{\gamma_{35}\beta_{35}}{\gamma_{57}\beta_{57}} \tag{3.9}$$

Using equations 3.6 and 3.9, it is possible to calculate the velocities $\beta_{35}$ and $\beta_{57}$ of the ions before and after passing through F5 materials. These calculations are based on the measured $(B\rho)_{35}$, $(B\rho)_{57}$, and the time of flight values that were measured with the F3 and F7 scintillators. Subsequently, the $A/Q$ value is determined utilizing equation 3.4, along with the atomic number ($Z$) obtained from equation 3.5 (equivalently eq 2.14), using the measured $\Delta E$ and $\beta_{57}$ values. These two variables, $A/Q$ and $Z$, provide a means for unambiguously identifying the incoming nuclei. For the identification in ZeroDegree, a similar set of equations is used within F8, F9 and F11 focal planes.

### 3.1.4 Calibration of time of flight offsets

As mentioned in section 2.2.2, to obtain a reliable value for the time of flight along the F3-F7 and F8-F11 paths, it is necessary to account for the delays in the propagation signals within the cables of the scintillator PMTs. This is done using equation 2.13 by adding an offset. This offset is adjusted both in BigRIPS and ZeroDegree, so that the final reconstructed $A/Q$ value for a given nuclear species equals the real ratio. These calibrations were optimized on the nuclei of interest which are $^{80}$Zn in BigRIPS and $^{79}$Cu in ZeroDegree, for a proper selection of the $^{80}$Zn($^{9}$Be, X)$^{79}$Cu reaction channel and for which the spectrometers were tuned. In order to correctly identify these isotopes, the expected rates from LISE++ simulations were used [73]. For instance, the estimated beam purity for $^{80}$Zn with the simulation was around 5.3% at F7. This was indeed matching with the 5.5% experimental purity that was attained. In this calibration procedure, we produced several Particle identification plots ($Z$ vs $A/Q$) similar to the ones in 3.8a, but with the addition of different values for the time of flight offset. In each plot, a gate was set on the nucleus of interest ($^{80}$Zn in BigRIPS and $^{79}$Cu in ZeroDegree), and the resulting average ($A/Q$) value is taken. This produced a diagram of the mass-to-charge ratio as a function of the time offset, as illustrated in figure 3.1 for the example of zinc. Finally, this curve is fitted with a first order polynomial. This allowed to find the values of $ToF_{offset}$ that reproduce the correct theoretical values of $A/Q$ (2.666 for $^{80}$Zn in BigRIPS and 2.724 for $^{79}$Cu in ZeroDegree), as shown with blue dashed lines. The final values of the offsets were found at $292.27 \pm 0.02$ ns in BigRIPS and $-135.75 \pm 0.02$ ns in ZeroDegree.

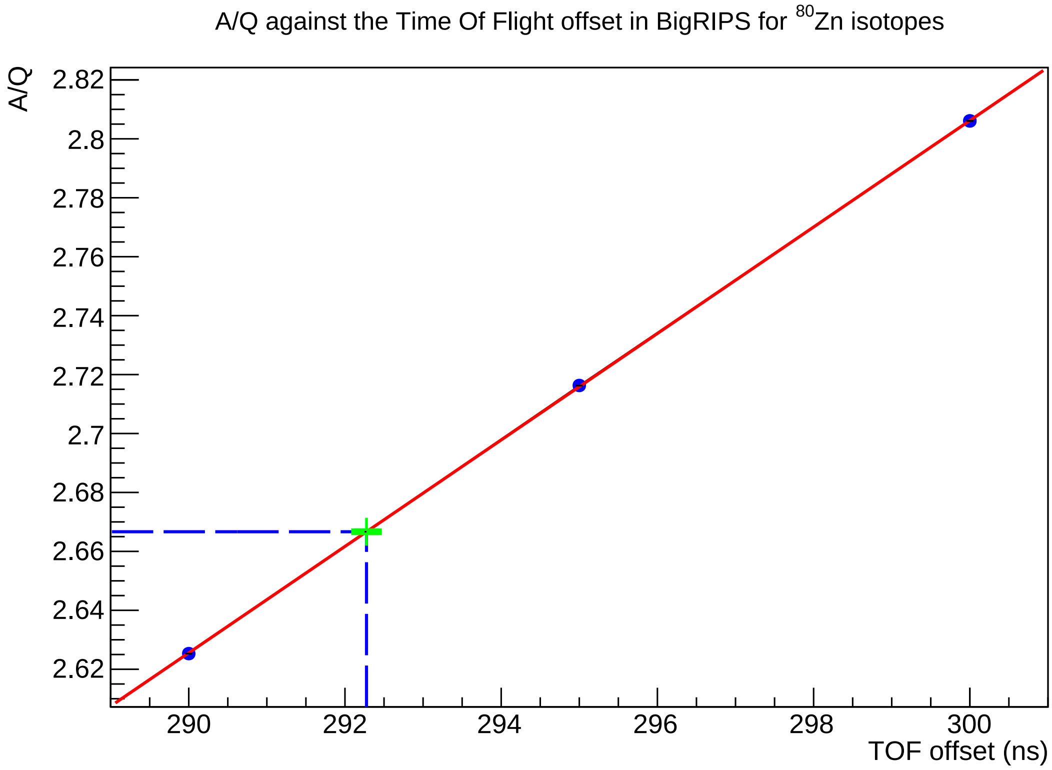

Figure 3.1: Example of a correlation between the time of flight offset and the mass-to-charge ratio for $^{80}$Zn in BigRIPS. The abscissa of the point highlighted in green color represents the final value that was taken for the offset.

## 3.2 Background removal

### 3.2.1 Description of the procedure for background removal

The appearance of background events on the identification diagram can be attributed to various factors, such as reactions occurring in the materials along the beam line or incorrect detector responses. The process of eliminating these background events is discussed in the following sections.

#### a/ PPAC detectors

In order to achieve a precise position reconstruction for the determination of $A/Q$, it is important to eliminate unwanted events recorded by the PPACs such as $\delta$-rays or multiple ions on an event-by-event basis. As explained in section 2.2.1, the inherent properties of finite delay lines result in a constant sum of stop signals from the two ends of the delay lines, denoted as $T_{sum} = T_{x1} + T_{x2} =$ constant. Figure 3.2 illustrates a histogram of $T_{sum}$ for the events of an experimental run. To filter out the undesired events, a rejection process is applied beyond the central value of $T_{sum}$. The central position is determined through a fitting procedure employing a Gaussian function in a reduced range around the maximum of the distribution, and the width of the acceptance window is set as $3\sigma$ around the central value. In total, 52 time windows are established, corresponding to 52 individual PPAC layers. Due to the high beam rate in BigRIPS, the PPAC detectors at F3 and F7 were frequently tripping. Consequently, they had to be replaced in the middle of the experiment after two days and 10 hours of beam time, due to their efficiency decrease. Therefore, new values of the $T_{sum}$ gates were correspondingly adjusted. The typical window widths for all the PPACs were found to be of the order of 10 ns. This procedure allowed to reject 3% of the events in the total BigRIPS PID.

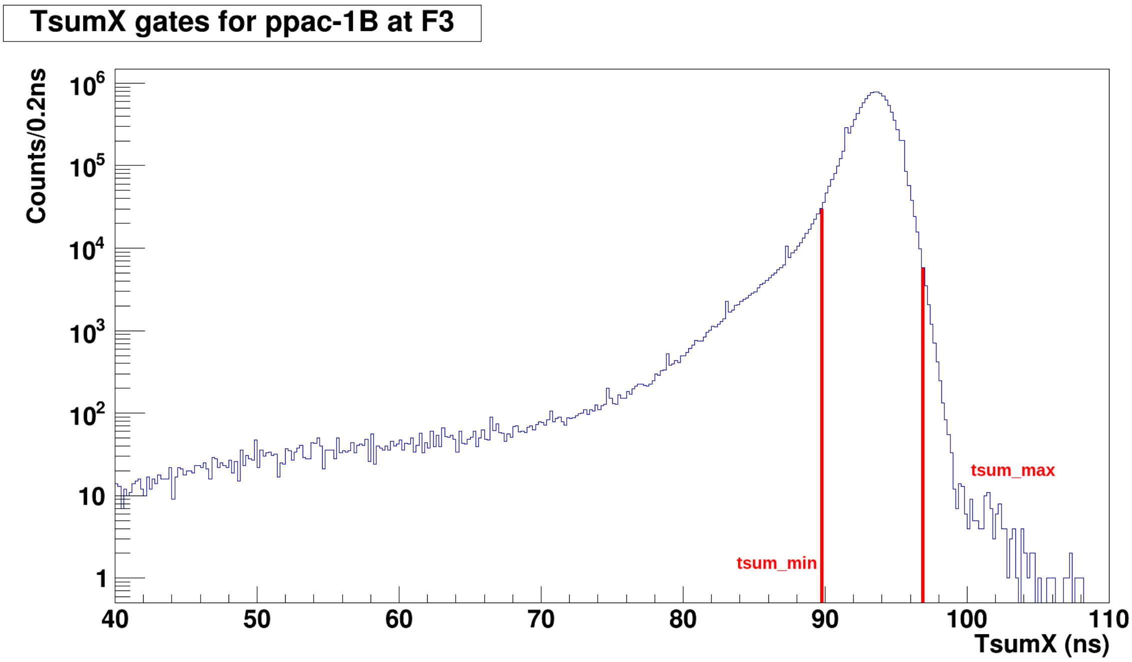

Figure 3.2: Example of a $T_{sum}$ distribution in the horizontal plane for the PPAC at the focal plane F3, for one data run. The chosen gates are highlighted with red lines.

### b/ Correlation between the energy loss in MUSIC and the charge in the plastic scintillation counters

Another approach to reject background events involves examining the correlation between the energy loss recorded in the ionization chamber and the charge-integrated signal from the plastic scintillator counter in F7 and F11. Figures 3.3 and 3.4 illustrate such a correlation at F7 and F11, respectively, in one data run, where pileup events in the ionization chamber are evident. This correlation can be used as a tool to identify and subsequently reject these events. By taking the remaining events after using PPAC $T_{sum}$ gates, and applying these two additional selections, 2% of the remaining events were rejected[1].

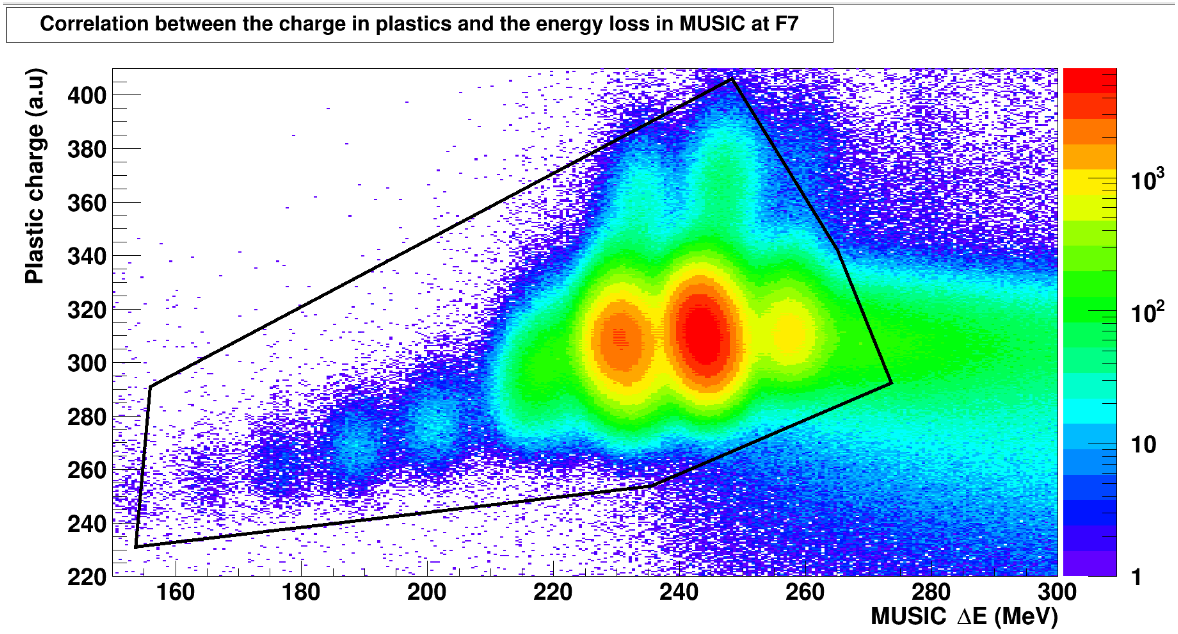

Figure 3.3: Correlation between the energy loss in MUSIC and the charge in plastics at F7. Only the events inside the cut in black are kept.

---

[1] About 1% for each correlation

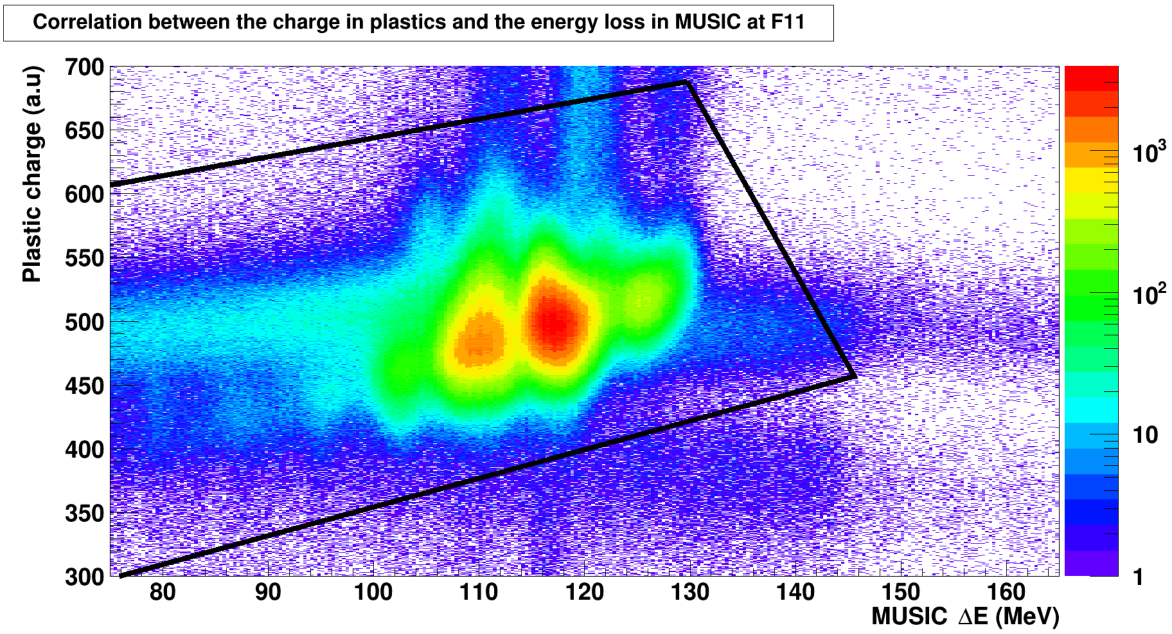

Figure 3.4: Correlation between the energy loss in MUSIC and the charge in plastics at F11. Only the events inside the cut in black are kept.

### c/ Charge states

To avoid inaccuracies in the reconstruction of $\beta_{35}$ and $\beta_{57}$ values resulting from changes in the charge state within the F5 materials such as the wedge degrader, the validity of equation 3.9 is a necessary condition. When a change in the charge state occurs, the relation is not valid anymore, and $\beta_{35}$ and $\beta_{57}$ are no longer correctly reconstructed. To eliminate such events, the correlation between $B\rho_{35}$ and $B\rho_{57}$ is carefully examined. The same issue needs to be addressed in ZeroDegree, at F9, using $B\rho_{89}$ and $B\rho_{911}$. When there is no change in the charge state when crossing some medium, alterations in particle $B\rho$ only arise from a decrease in velocity. Consequently, for a given isotope, the ratio of $B\rho$ values before and after the medium should remain constant. Events that exhibit different ratios can be identified and removed as they indicate potential issues with charge state changes. Figures 3.5 and 3.6 illustrate the correlation plots in BigRIPS and ZeroDegree, respectively, together with the applied gates. As seen from figure 3.5, no clear changes in the charge states were observed in BigRIPS. This is due to the adjustment of the slits at F5 in the experiment. Therefore, no gate was applied using this plot.

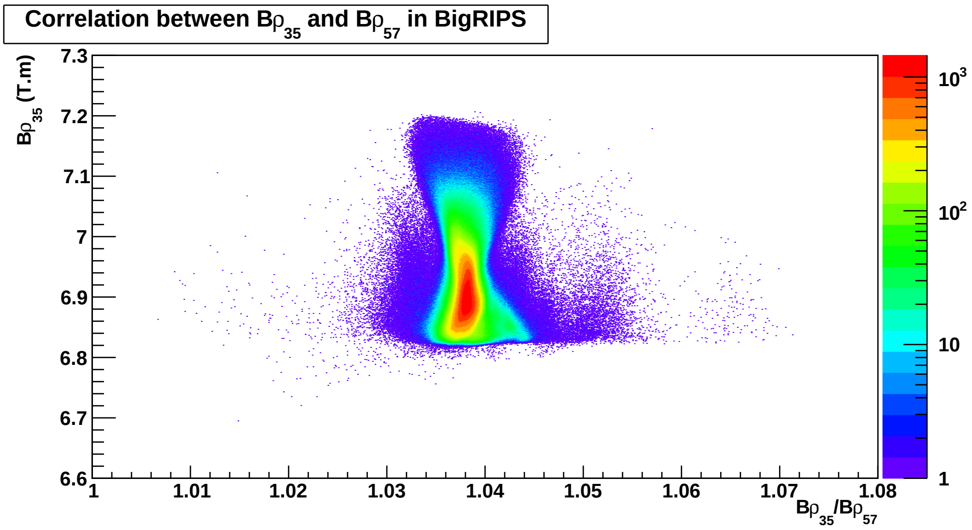

Figure 3.5: Correlation between the magnetic rigidities before and after F5. No clear presence of charge states was observed.

In ZeroDegree, however, the events where there was a change in the charge state are clearer and these were removed by applying the selection as displayed in figure 3.6. This additional selection of the charge states in ZeroDegree allowed to remove less than 0.5% of the remaining events of the Particle Identification diagrams in BigRIPS and ZeroDegree.

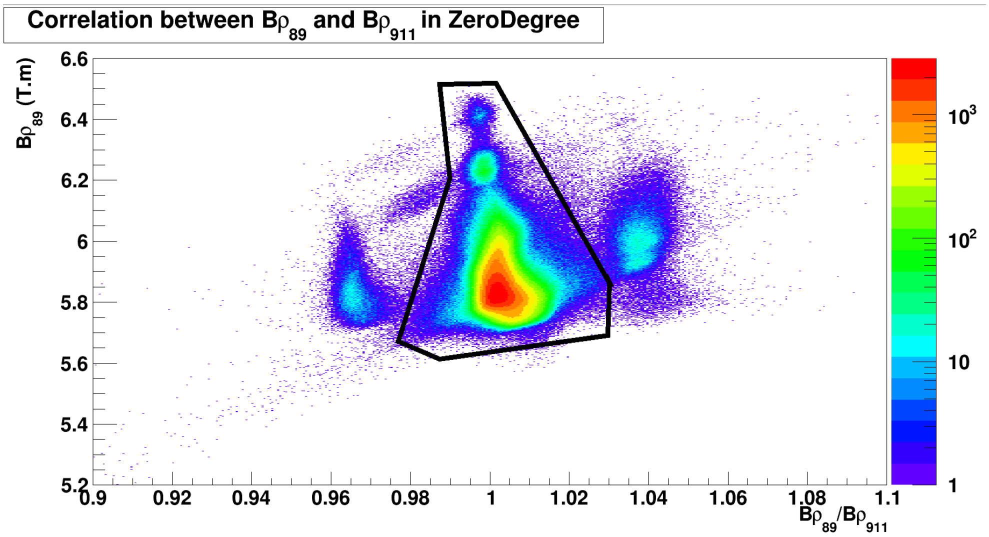

Figure 3.6: Correlation between the magnetic rigidities before and after F9. All events outside the cut in black are rejected.

### d/ Plastic scintillators

As previously discussed in section 2.2.2 and outlined in equation 2.12, the relationship between the time difference and the logarithm of the fractional charge difference between the left and right PMTs in the scintillators can be used to remove background events. An example of this removal process is demonstrated in figure 3.7 for the F7 plastic scintillator.

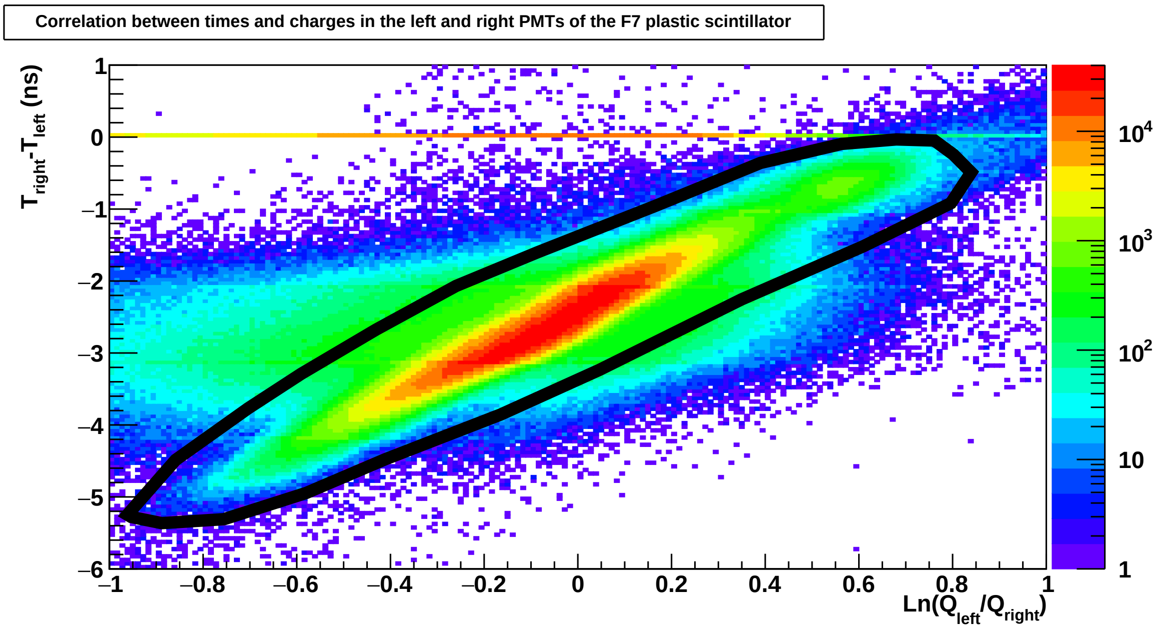

Figure 3.7: Example of background removal with the plastic scintillator at F7. The events outside the black cut are discarded.

## 3.2.2 Result of the background suppression

The simultaneous application of all the mentioned gates allowed to reject the contaminating events in the Particle Identification diagram (PID). Figures 3.8a and 3.8b show the PID plots before and after the background rejection, respectively, in one experimental data run. The proportion of the contaminants was found to be 12% in the total diagram and 9% in the region corresponding to $^{80}$Zn isotopes in BigRIPS.

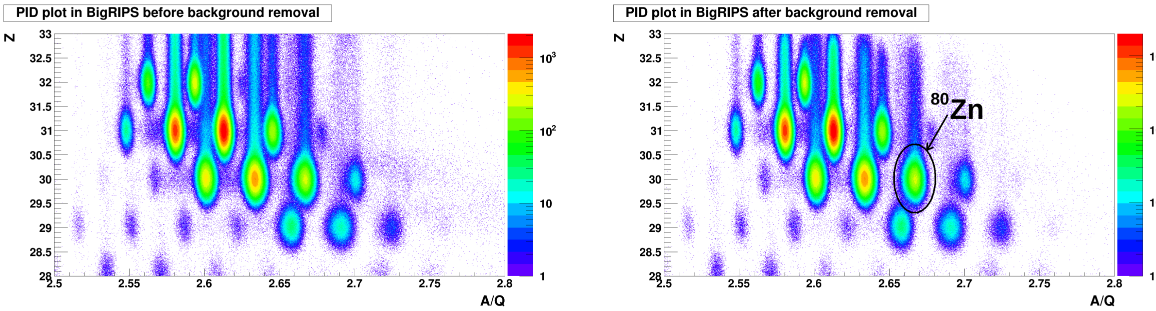

(a) PID in BigRIPS before background removal.

(b) PID in BigRIPS after background removal.

Figure 3.8: Comparison of the PID diagrams before and after background suppression in BigRIPS. The $^{80}$Zn nucleus is circled in black.

As regards the PID in ZeroDegree, a similar comparison is shown in figure 3.9. After applying all the suppressions, the percentage of the deleted events in the part corresponding to the $^{80}$Zn($^{9}$Be, X)$^{79}$Cu reaction channel was found to be at 5%.

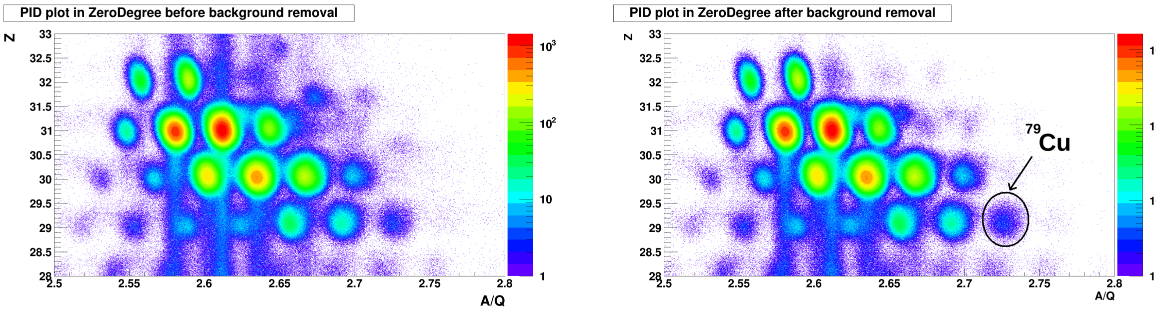

(a) PID in ZeroDegree before background removal.

(b) PID in ZeroDegree after background removal.

Figure 3.9: Comparison of the PID diagrams before and after background suppression in ZeroDegree. The $^{79}$Cu nucleus is circled in black.

## 3.3 Optical corrections

### 3.3.1 Identification in BigRIPS

As mentioned in section 3.1.1, the transfer matrix 3.1 allows to determine the beam trajectory only at first order. Higher order corrections can be empirically added for a more precise determination of the ion paths and thus a better $A/Q$ resolution in the final PID. When the trajectory is accurately reconstructed, the $A/Q$ value of an isotope should not exhibit any dependence on its position or the angle of its trajectory in any of the focal planes. For instance, the obtained $A/Q$ in BigRIPS should not depend on the $x$, $y$, $\theta$ and $\phi$ variables at F3, F5 and F7. However, in practice, small deviations are possible, and such dependencies occur as shown in figure 3.10a for the relation between the horizontal angle $\theta$ at F5 and the $A/Q$. In this context, this mass-to-charge ratio can be expressed as a power series of the position and angle variables at F3, F5 and F7. To address this issue, the coefficients of the polynomials in the power series expansion were determined using a multidimensional fit. The corrections were applied with a specific focus on the nuclei for which the beam tuning was optimized. For this particular case, a selection was made on the $^{80}$Zn events and an algorithm was used to fit the dependencies[2]. This allowed for the calculation of correction terms up to the third order, as well as the inclusion of cross terms, which consider possible correlations between various parameters. This approach is akin to applying a higher-order optical transport matrix, as opposed to the initial first-order matrix used to solve for $\delta$, the relative deviation from the central value $B\rho_0$ of the magnetic rigidity. The result of this method is illustrated in figure 3.10b where the relationship between the $\theta$ angle at the momentum dispersive plane F5 and the $A/Q$ value after the application of these corrections is shown. As it can be seen, the $A/Q$ dependency on the angle is minimized, especially for $^{80}$Zn isotopes (located at $A/Q = 80/30 = 2.666$) since the procedure was optimized on the latter.

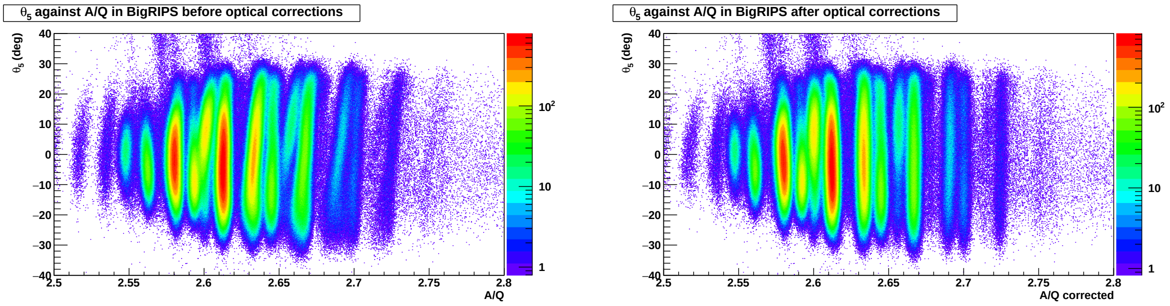

(a) $A/Q$ dependency on the $\theta_5$ angle before optical corrections.

(b) $A/Q$ dependency on the $\theta_5$ angle after optical corrections.

Figure 3.10: Comparison of the dependencies of the reconstructed $A/Q$ in BigRIPS on the F5 horizontal angle before and after applying the optical corrections.

The impact of this procedure on the $A/Q$ resolution in the total PID is shown in figure 3.11, where a better separation of the isotopes can be noticed.

---

[2] The multidimensional fitting was carried out using the ROOT TMultiDimFit class

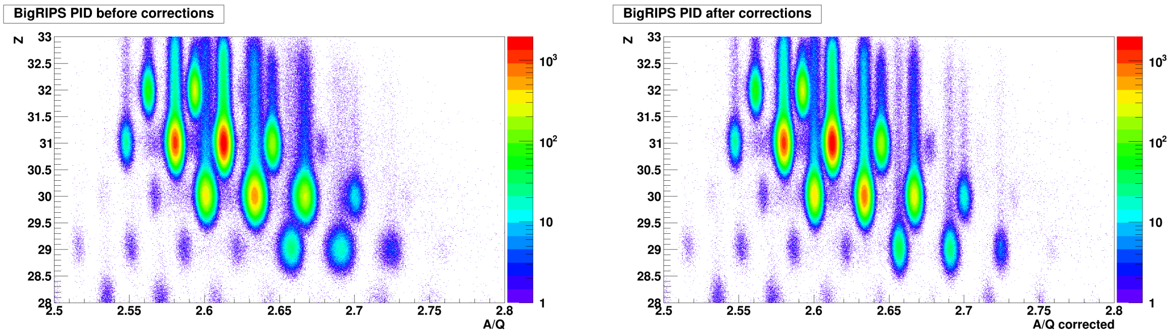

(a) PID diagram in BigRIPS before optical corrections.

(b) PID diagram in BigRIPS after optical corrections.

Figure 3.11: Comparison of the particle identification diagrams in BigRIPS before and after optical corrections. The background events have been removed in both diagrams.

In order to quantify the enhancement in the resolution, a projection was made on zinc isotopes before and after the corrections as depicted in figure 3.12. The peaks were fitted using Gaussians. For the $^{80}$Zn particles, the $A/Q$ resolution was improved from 0.11% to 0.08%, which was enough to separate them from the other nuclear species.

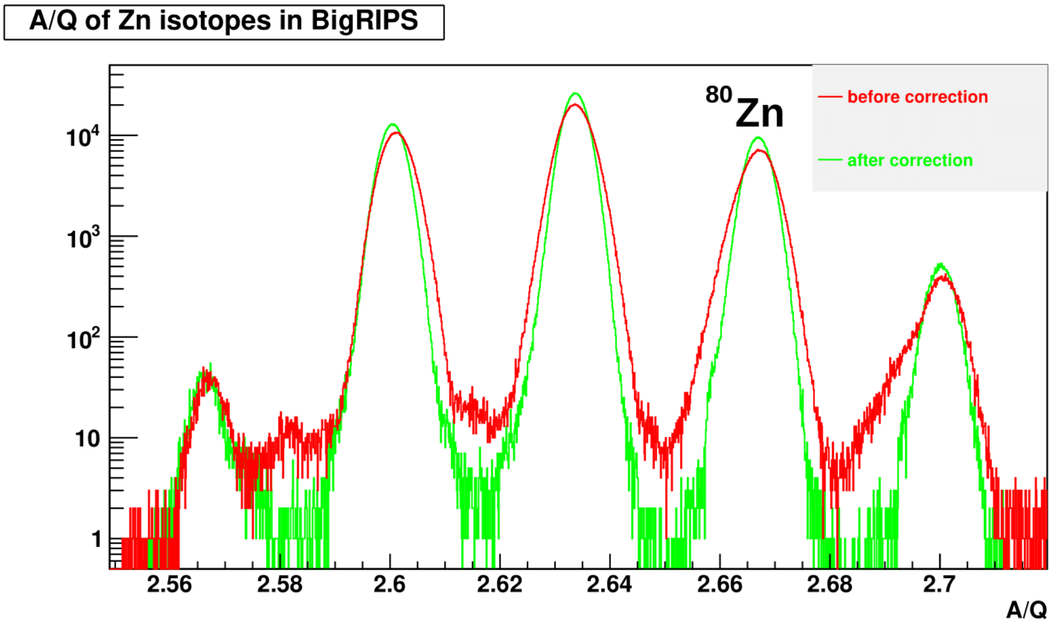

Figure 3.12: Comparison of the $A/Q$ resolutions for the Zn isotopic chain before and after the optical corrections.

### 3.3.2 Identification in ZeroDegree

In ZeroDegree, the procedure was applied in a similar fashion by fitting the behavior of the $A/Q$ as a function of the position and angle variables at F8, F9 and F11. This time, the events corresponding to $^{79}$Cu were selected. For instance, the relation between $A/Q$ and the horizontal position at F11 is shown before and after the corrections in fig 3.13. Here, also one can see a dependence between the two variables.

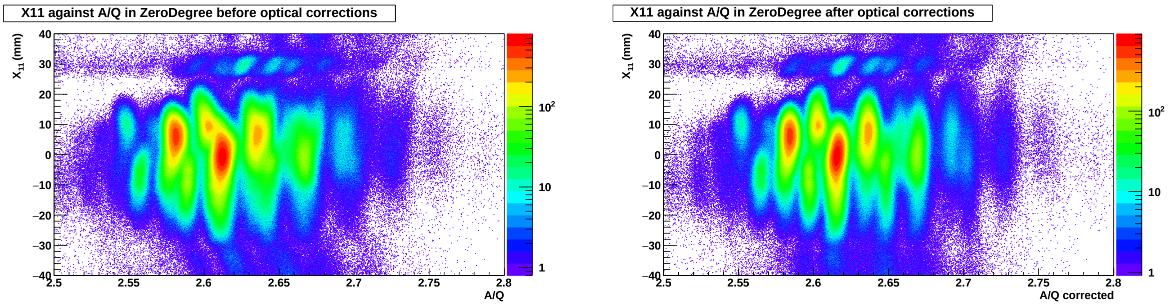

(a) $A/Q$ dependency on the $X_{11}$ coordinate before optical corrections.

(b) $A/Q$ dependency on the $X_{11}$ coordinate after optical corrections.

Figure 3.13: Comparison of dependencies of the reconstructed $A/Q$ in ZeroDegree on the F11 horizontal position before and after applying the optical corrections.

The same exercise was repeated for the comparison of the total PID diagrams in

ZeroDegree. This is depicted in figure 3.14 where the separation of isotopes is better in figure 3.14b.

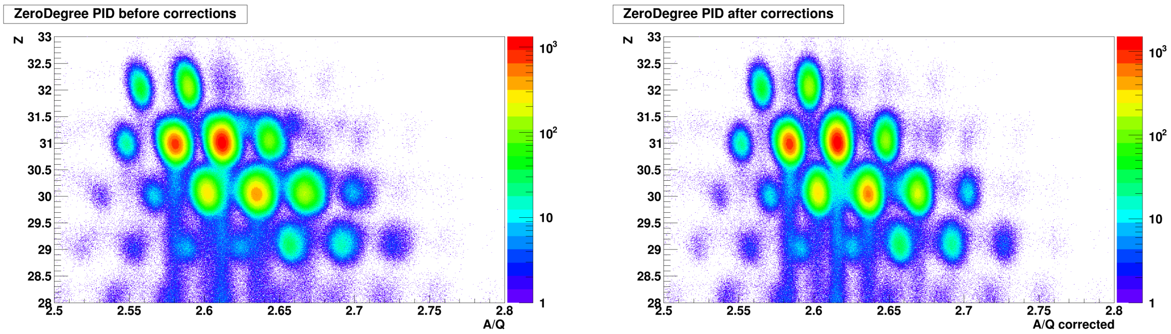

(a) PID diagram in ZeroDegree before optical corrections.

(b) PID diagram in ZeroDegree after optical corrections.

Figure 3.14: Comparison of the particle identification diagrams in ZeroDegree before and after optical corrections. The background events have been removed in both diagrams.

These histograms were projected on the copper isotopic chain, and these projections are illustrated in figure 3.15. The resolution for the $^{79}$Cu isotopes was improved from 0.22% to 0.15%. This was enough to separate these nuclei from the other ones, for a proper selection of the $^{80}$Zn($^{9}$Be, X)$^{79}$Cu reaction channel of interest.

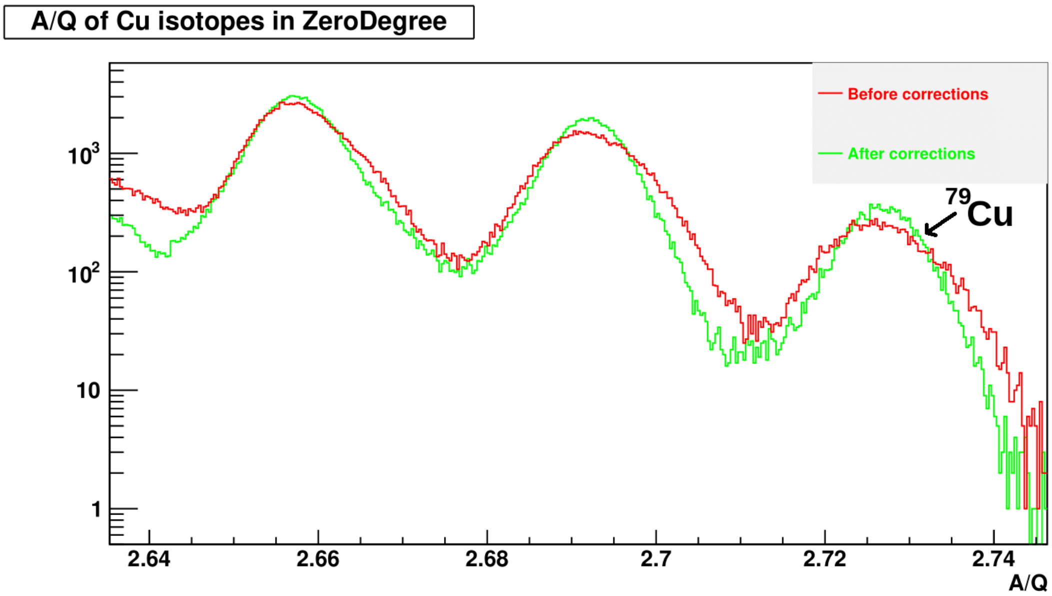

Figure 3.15: Comparison of the $A/Q$ resolutions for the Cu isotopic chain before and after the optical corrections.

### 3.3.3 Alignment of the F8 third PPAC

As already mentioned in section 2.4.2, the scattering angle $\theta_s$ (or equivalently the direction of the outgoing velocity $\overrightarrow{\mathbf{V}}_{\mathrm{s}}$) of the emitting nucleus is needed for the Doppler correction of the $\gamma$-ray energies. In order to determine this angle, the three sets of double PPACs at F8 are employed. The two sets before the target are used to extrapolate the trajectory of the incoming nucleus as a straight line (which is the direction of the incoming velocity vector $\overrightarrow{\mathbf{V}}_{\mathrm{in}}$) until the middle of the target where the reaction is assumed to occur. This allows to obtain the $X_t$ and $Y_t$ coordinates on the target for the reaction point at $Z_t$. After that, the position of the outgoing nucleus is measured in the third set after the target, and the direction of the velocity $\overrightarrow{\mathbf{V}}_{\mathrm{s}}$ is then taken as the line that links the reaction point and this measured position, as shown in figure 2.12. To accurately measure the latter, it was needed to align the position of the third set of double PPACs. Indeed, this set was not a standard one at RIKEN, and it was only added in our specific experiment to achieve this beam tracking. Therefore, some possible offsets had to be taken into account because of its positioning procedure. To do so, some empty target experimental data runs were recorded. In this configuration, the direction of the velocity $\overrightarrow{\mathbf{V}}_{\mathrm{in}}$ of the incoming nucleus is directly extrapolated until the third PPAC to deduce the real expected position of the beam on the last pair, as illustrated in figure 3.16. The final offset values are then deduced with the following equations:

$$X_{offset} = X_{extrapolated} - X_{measured} \tag{3.10}$$

$$Y_{offset} = Y_{extrapolated} - Y_{measured} \tag{3.11}$$

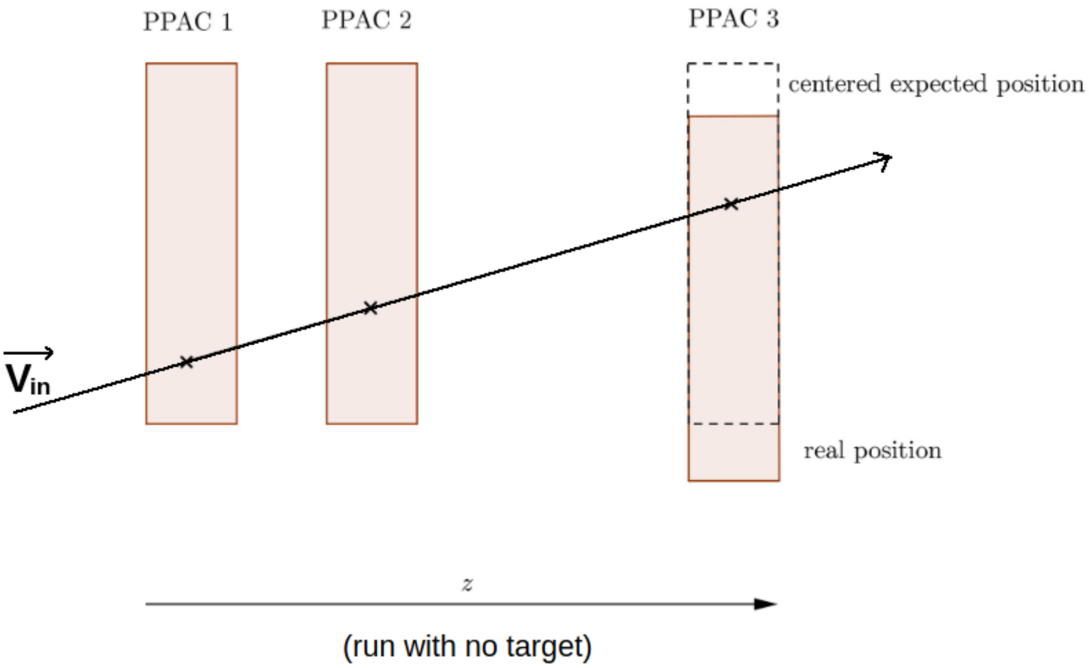

Figure 3.16: Illustration of the procedure for the alignment of the third PPAC at F8.

With this calculation, the final values of the shifts we ended up with are summarized in table 3.1.

| Double PPAC label | $X_{offset}$ (mm) | $Y_{offset}$ (mm) |
|---|---|---|
| F8PPAC-3A | 0.185 | -1.202 |
| F8PPAC-3B | 1.868 | -0.341 |

Table 3.1: Summary of the final position offsets for the F8 third PPAC.

## 3.4 HiCARI calibration

Energy calibration of the HiCARI array was accomplished for a correct reconstruction of the $\gamma$-ray energies. After that, the add-back procedure was applied in order to increase the peak over total ratio as explained further in section 3.6. Finally, the reconstructed $\gamma$-ray energies in the lab frame were Doppler-corrected for the determination of the energies in the rest frames of the emitting nuclei.

### 3.4.1 Energy calibration

The germanium detectors were calibrated in energy both before and after the beam time using reference $\gamma$-ray energies spanning from 121 keV to 1836 keV. These reference energies were generated by four calibration sources: $^{60}$Co, $^{88}$Y, $^{152}$Eu and $^{133}$Ba, as outlined in table 3.2. These sources were positioned at the $^{9}$Be secondary target location, with 0.5 mm of beam pipe shielding made of lead.

| Source | Transition energies (keV) |
|---|---|
| $^{60}$Co | 1173, 1333 |
| $^{152}$Eu | 122, 245, 344, 779, 867, 964, 1086, 1112, 1408 |
| $^{133}$Ba | 898, 1836 |
| $^{88}$Y | 276, 303, 356, 384 |

Table 3.2: Transition energies of the calibration sources.

For every segment and crystal core, the full-energy peaks of the calibration transitions were fitted with a sum of a Gaussian and a background modeled as a first order polynomial. The obtained centroids were then associated to their corresponding energy and a linear fit was performed to determine the calibration relation between ADC channel and energy. An example of the procedure is shown in figure 3.17 for one crystal core contact in a Miniball cluster.

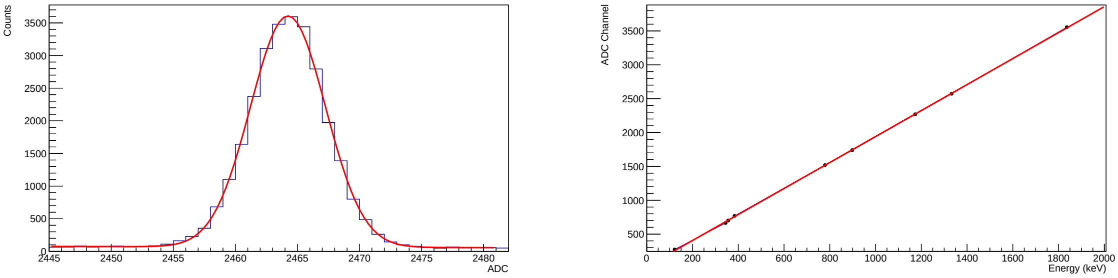

(a) Raw spectrum of $^{60}$Co, the energy peak at 1173 keV is fitted with a Gaussian and a first order polynomial background.

(b) Linear relation between ADC channel and energy obtained from the transitions of the four calibration sources.

Figure 3.17: HiCARI energy calibration procedure.

After applying the energy calibration to all crystal segments and cores, the full-energy peaks of the calibrated spectra were fitted using the same function of a Gaussian with a linear background. To assess the quality of the calibration, a comparison was made between the measured energies of the transitions and their known values from literature, i.e. the residuals. Figure 3.18 shows an example of a residue plot for one Miniball segment. For this particular case, the residues are less than 2 keV. More generally, in all the detectors, these residues were not more than 4 keV.

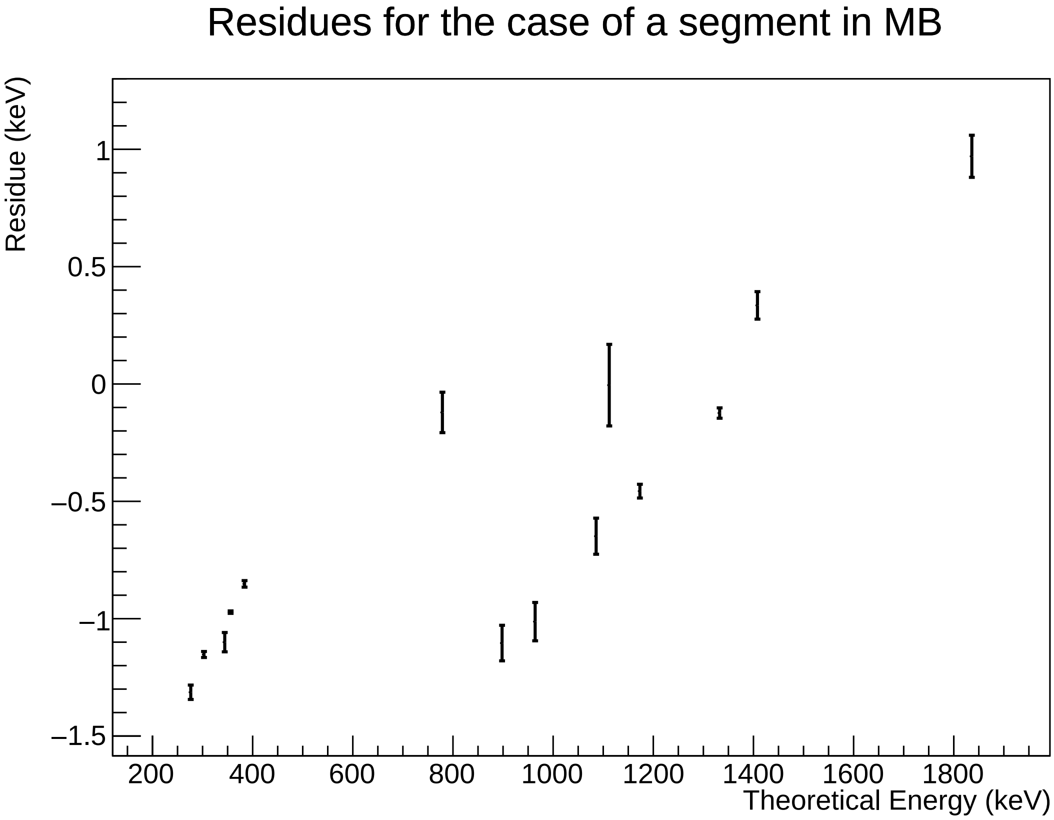

Figure 3.18: Difference between the measured and literature energies of the calibration transitions for one Miniball segment. The uncertainty of each point is less than 0.2 keV.

Lastly, some crystal segments had to be either removed from the analysis or treated with a particular procedure (described in section 3.5.1) because they exhibited either significant nonlinear behavior or gain instabilities. These are summarized in table 3.3.

| Cluster | Crystal | Segments |
|---|---|---|
| MB0 | 2 | All |
| MB2 | 0 | 2 |
|  | 1 | 2 |
| MB4 | 2 | 3 |
| MB5 | 2 | 4 |
| SC6 | 3 | 3 |
| SC8 | 0 | 1 |
|  | 2 | 2 |
| SC9 | 0 | 2 |
|  | 1 | 0, 1 and 2 |
| QUAD | 1 and 3 | All |

Table 3.3: Summary of the segments and crystals that were not functional during the whole experiment.

### 3.4.2 Energy resolution

In the fitting process for the calibration in energy, detailed in section 3.4.1, the resolutions of the peaks were also extracted. As explained in [74], the resolution is proportional to the square-root of the energy, with a proportionality constant that depends on the average energy required to create an electron/hole pair in the semi-conductor material. We nevertheless slightly modified this dependence by introducing additional terms to account for other effects. Then, the behavior of the resolution as a function of the energy was fitted with the following function:

$$\sigma(E) = A\sqrt{1 + BE} + CE \tag{3.12}$$

where $A$ is the constant noise from the electronics readout, $B$ is a factor for the stochastic term incorporating fluctuations in the number of collected electrons from the electron-hole pairs on the electrodes, and $C$ parametrizes the linear growth of the width due to systematic effects such as detector response non-uniformity or energy losses in dead materials. Figure 3.19 shows an example of this fitting procedure in one Miniball crystal from the experimental resolutions.

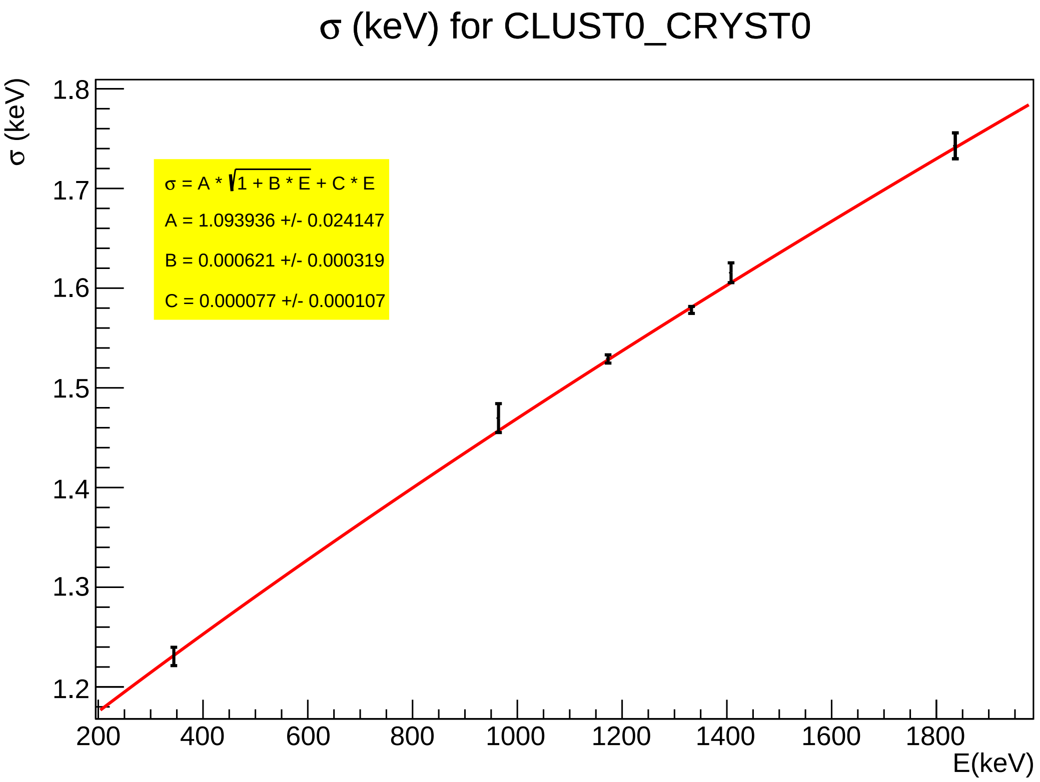

Figure 3.19: Experimental resolutions for one Miniball crystal. The data points are fitted with the red curve of which the formula is given by equation 3.12

The previous procedure was repeated to determine the 3 parameters of the modeling function for each crystal. The obtained coefficients were subsequently used in the simulation to take into account the differences in the widths of all the modules and reproduce the experimental resolutions.

The resulting modeling curves for each crystal are shown in figure 3.20 for Miniball and SuperClover detectors, while those of the tracking detectors are shown in figure 3.21.

In the case of clovers, one can notice a particularly worse resolution of one crystal in the SC7[3] cluster. As regards Miniball, MB4 has a resolution that is twice worse than those of the other Miniball modules.

---

[3] A given SuperClover cluster is made of 4 crystals, labeled from CRYST0 to CRYST3. In SC7, it is CRYST1 that had a worse resolution as compared to the other crystals.

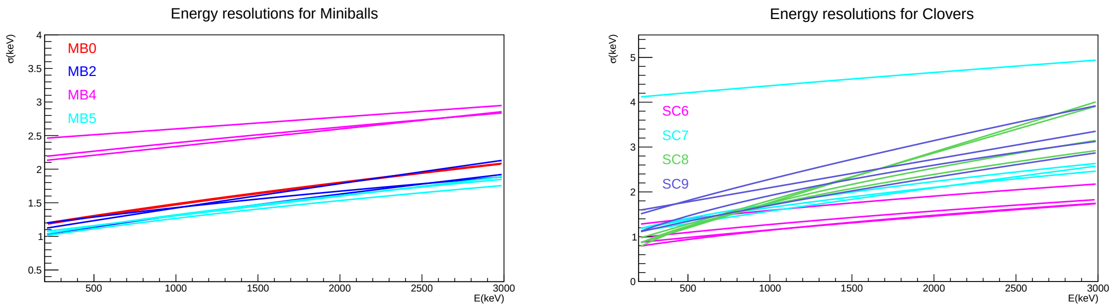

(a) Energy resolution of the Miniball crystals. Each color represents the crystals within one cluster.

(b) Energy resolution of the clover crystals. Each color represents the crystals within one cluster.

Figure 3.20: Energy resolution modeling functions for Miniball and Clover detectors.

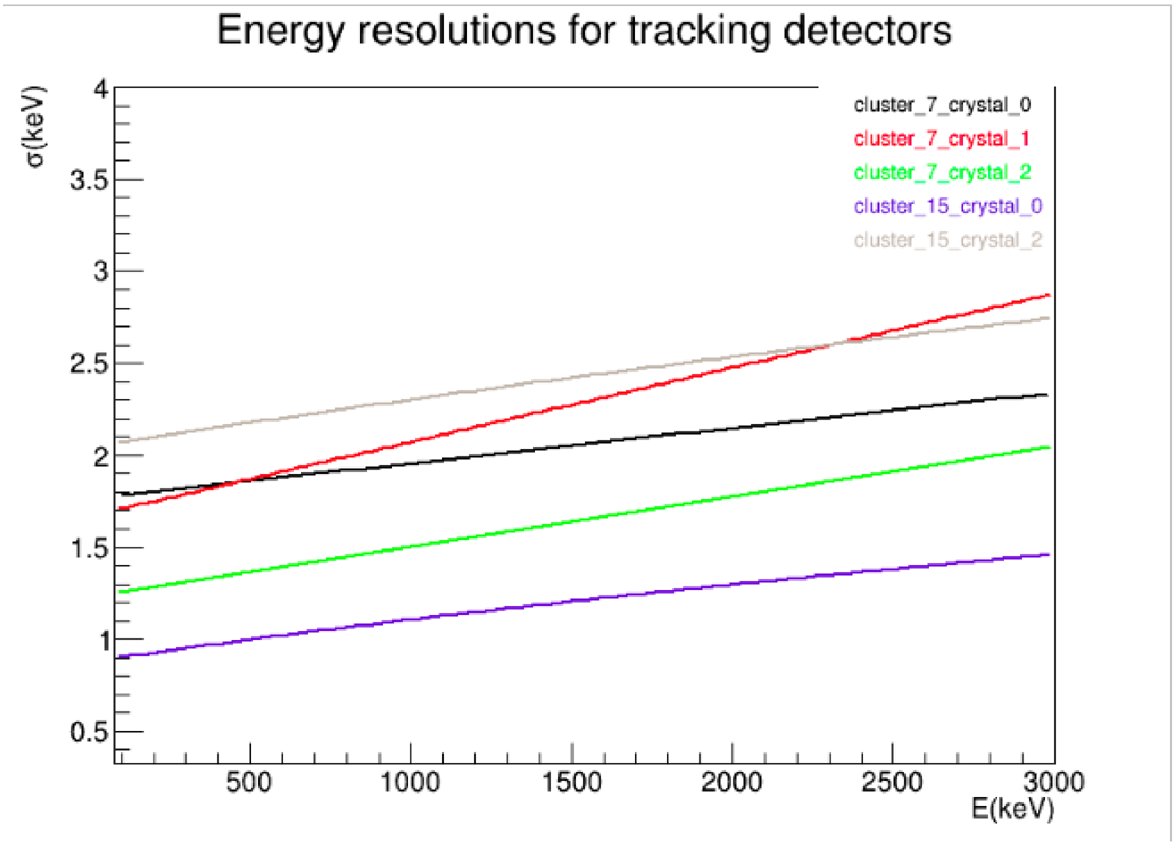

Figure 3.21: Energy resolution modeling functions for P3 (cluster 7) and QUAD (cluster 15) crystals.

### 3.4.3 Energy thresholds

In the experiment, ADC thresholds were applied for each crystal. The generated pulses that fall below the established threshold values are disregarded and do not contribute to the experimental dataset. These individualized thresholds serve the purpose of ensuring efficient detection of in-flight $\gamma$ rays while preventing excessive sensitivity to atomic background and minimizing false triggers from dark counts in individual detectors. The accurate determination of these individual thresholds is more particularly important to replicate the correct intensity at low energy during data fitting with the generated response functions[4]. These thresholds were then incorporated into the HiCARI detectors response functions in the GEANT4 simulation. Their values were deduced individually from the spectra of the calibration runs. To do so, we took the $^{60}$Co $\gamma$ spectrum, and the distribution was fitted in a reduced range at low energies with the following function:

$$f(E) = C[1 + tanh(\frac{E-A}{B})] + D \tag{3.13}$$

where $A$ is the established threshold value in keV, and $B$ characterizes the sharpness of the energy cut. The larger its value, the smoother the increase of the counts around the $A$ parameter. As regards the remaining coefficients, $C$ and $D$ represent, respectively, a scaling factor and an offset that are adjusted based on the number of counts in the spectra. An example of this fitting procedure is shown in figure 3.22, where the experimental spectrum obtained with one crystal of MB4 is fitted with the mentioned model function in red. The final threshold values were found at around 100 keV for all detectors, with the exception of MB0 crystals which had thresholds of the order of 250 keV. These were increased on purpose during the experiment since this particular detector had a high level of noise.

---

[4] For the case studied in this work, the transition of interest in $^{79}$Cu is at 656 keV. The established thresholds being below 250 keV, the impact of these threshold choices on the peak shape in the simulated response functions is marginal.

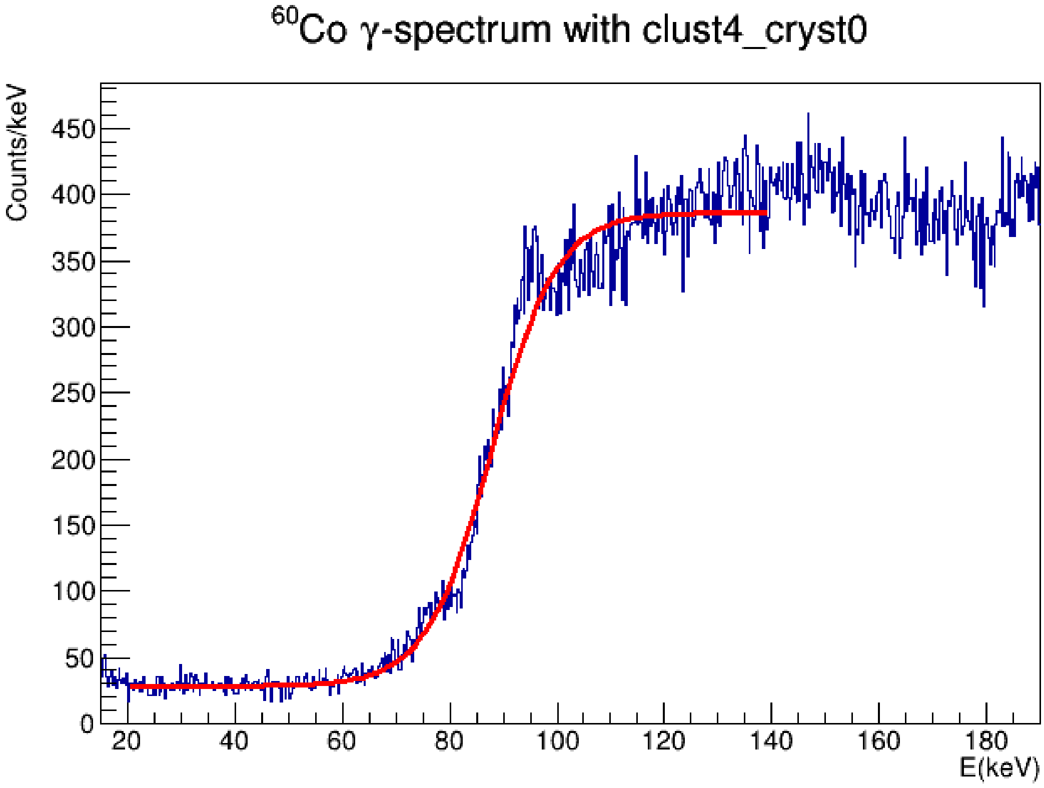

Figure 3.22: Example of an energy threshold determination with one crystal in MB4.

### 3.4.4 Time correlation between the beam and the $\gamma$ rays

In this section, the time correlation between beam and $\gamma$-ray events is verified. The timestamp for the BigRIPS event $T_{BR}$ is recorded when the ion passes through the plastic scintillator at focal plane F7. This timestamp is compared to the recorded $\gamma$-ray event timestamp $T_\gamma$:

$$\Delta T = T_{BR} - T_\gamma \tag{3.14}$$

$\gamma$ rays detected in HiCARI that are emitted from the beam should show a consistent timestamp difference $T_{BR} - T_\gamma$. An example of this time distribution is shown in figure 3.23 for one QUAD crystal, where the distribution was realigned around zero for convenience. For every crystal, gates were applied between $\Delta T = -100$ ns and $\Delta T=$ 10 ns, in order to keep only the events where the beam and the $\gamma$ rays are correlated, and remove the background from random coincidences. Such a treatment removes about 1% of the counts in the final Doppler-corrected $\gamma$ spectrum corresponding to the $^{80}$Zn($^{9}$Be, X)$^{79}$Cu reaction channel.

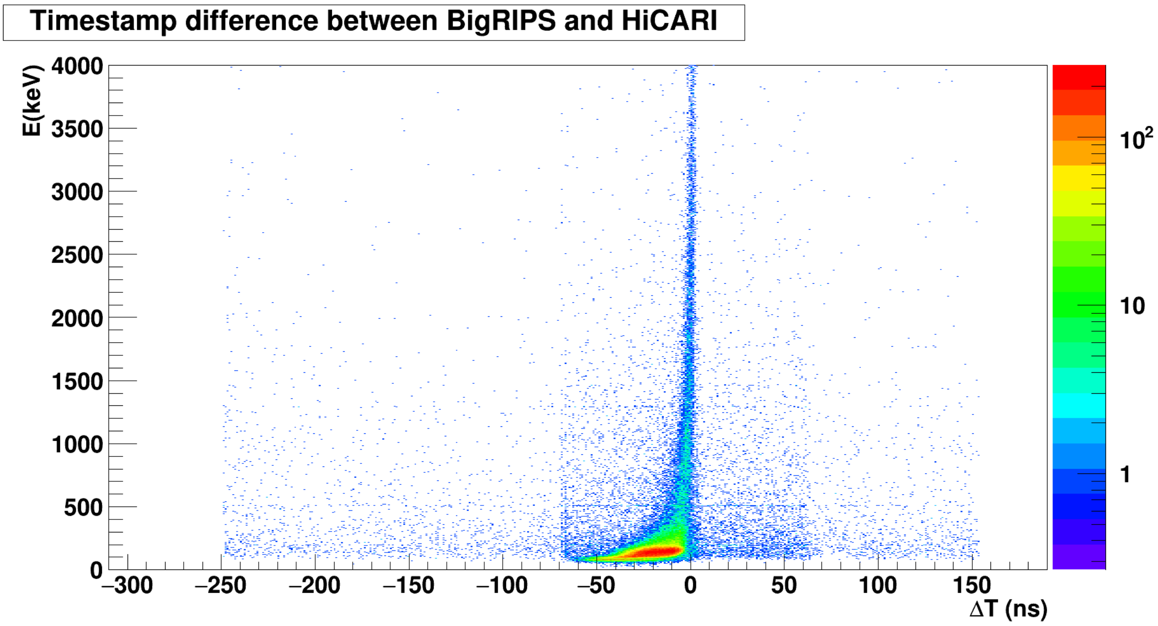

Figure 3.23: Example of timestamp difference between BigRIPS and the first crystal of the QUAD module.

### 3.4.5 Efficiency calibration

The efficiency of the HiCARI array as a function of the energy can be evaluated using the known initial activity $A_0$ (in Bq) of each source with its manufacture date [75], and $\Delta t$ which is the duration of each calibration run. The total number of the emitted $\gamma$ rays during one run is calculated using the following formula:

$$N_{emitted} = A \times \Delta t \tag{3.15}$$

In this calculation, $A$ represents the activity of the source once half of the total run duration has passed, and was taken as a constant[5]. All these details are summarized in table 3.4.

---

[5] The decrease of the activity between the beginning and the end of one data run is neglected given that the longest run had a total duration that was less than one hour and the minimal half-life of the calibration sources was 106 days (for $^{88}$Y).

| Source | Run duration (s) | $A$ (Bq) |
|---|---|---|
| $^{60}$Co | 1802 | 20480.2 |
| $^{152}$Eu | 2059 | 6019.1 |
| $^{133}$Ba | 1798 | 47399.4 |

Table 3.4: Summary of the activities of the calibration sources and the duration of the recorded data runs.

The efficiency was then separately calculated for each detector group. At a given $\gamma$-ray energy, the number of counts under the peak is obtained with a Gaussian fit[6], and the branching ratio $I_\gamma$ which corresponds to the average number of $\gamma$ rays following 100 $\beta$ decays of the nuclei is used to calculate the absolute efficiency as follows:

$$\epsilon = \frac{N_{counts}}{N_{emitted} \times I_\gamma} \tag{3.16}$$

The results of this calculation are illustrated in figure 3.24. It can be seen that the Miniball and clover detector groups have a higher total efficiency since both have 4 clusters, and that the Miniball detectors have a slightly better efficiency than the clovers, particularly at higher energies, where the high thresholds of the former do not have any impact on the detection. On the other hand, for the GRETINA-type detectors, there were only the two separate P3 and QUAD clusters. Therefore, their total individual efficiencies are lower than those of the Miniball and clover groups. One can also notice that the P3 module has a slightly better efficiency than the QUAD cluster. This is due to the fact that the former was closer to the target position.

---

[6] Using the ROOT analysis tool, the "gausn" predefined function was used. The first fitted parameter of the latter is the integral $N_{counts}$ under the peak (the background was taken into account as a first order polynomial).

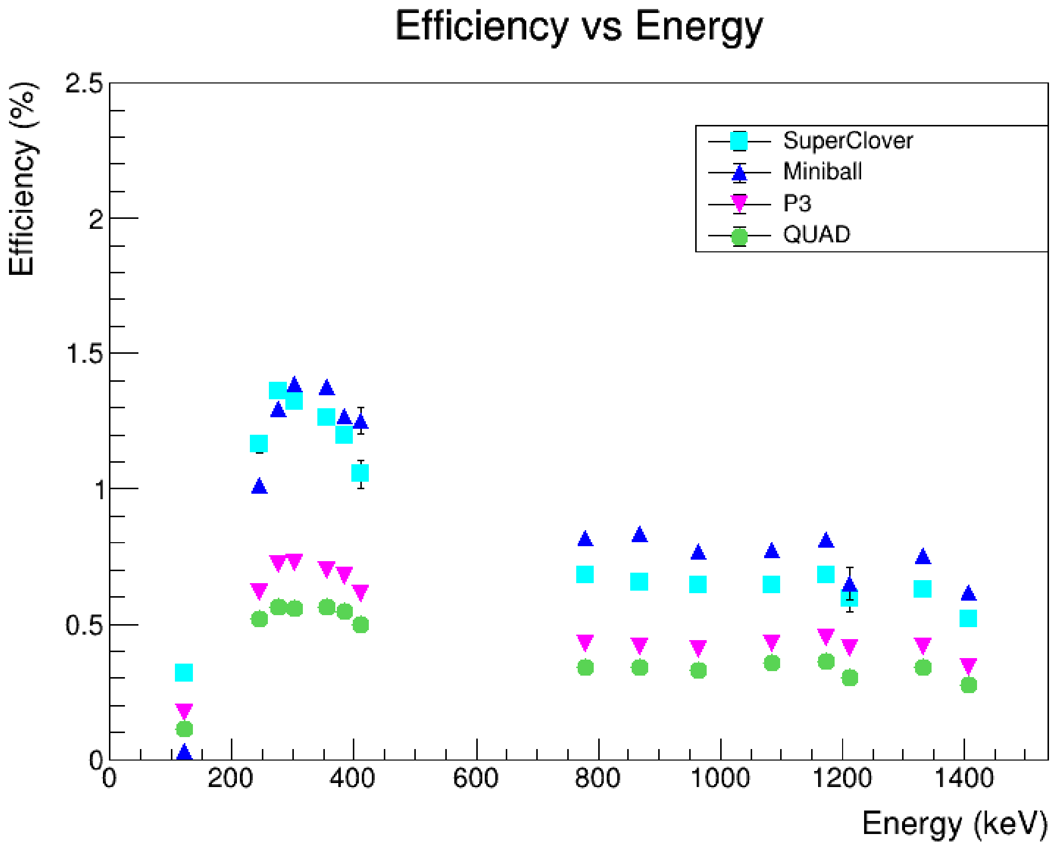

Figure 3.24: Comparison between the experimental efficiencies of the different detector groups.

## 3.5 Procedure for Doppler correction

### 3.5.1 Determination of the angle for Doppler correction

As it was previously mentioned, the $\theta_\gamma$ angle between the residue velocity vector and the $\gamma$-ray trajectory is needed for the Doppler correction of the energies. This trajectory is taken as the straight line that links the reaction point at the middle of the target and the hit position in the HiCARI detectors. The employed method to ascertain the latter depends on the detector type:

- In the case of Miniball and Clover crystals, a comparison is made between the signals in each segment. The first interaction point of the $\gamma$ ray is then taken as the geometrical center of the segment in which there was the highest energy deposit. Among the crystals highlighted in table 3.3, for those containing exactly one non-operational segment, the sum of the energies of all the functional segments is subtracted from the total energy of the crystal central contact to deduce the missing energy that would be measured by the lost segment if it properly worked. This missing energy is then

assigned to it, and the comparison is made again between all the segments to obtain the position of the $\gamma$ ray.
- With GRETINA-like detectors, the pulse shape decomposition explained in section 2.3.2 is employed.

## 3.5.2 Determination of the velocity for Doppler correction

### a/ Simulation of the average velocity at the reaction point

The other crucial parameter intervening in equation 2.15 is the speed of the reaction residue when it undergoes a $\gamma$ decay. As already mentioned in section 2.4.2, the reaction and emission points are assumed to be in the transverse plane at half of the target thickness. Therefore, the $\beta$ velocity that is used in equation 2.15 must be the one in the middle of the target. However, there was no way to directly measure this quantity in the experiment since the only available measurements were the average velocities between F3 and F7 (before the target), and between F8 and F11 (after the target), through the time of flights given by the plastic scintillators at these focal planes. With the use of the two-fold $B\rho$ method, detailed in section 3.1.3, it was possible to calculate the velocities $\beta_{57}$ and $\beta_{89}$ in F5-F7 and F8-F9 regions, respectively. These values are closer to the required one at the target but they are still different from it since there are some intermediate materials[7] between the different focal planes, as illustrated in figure 3.25. For this purpose, the energy losses of the particles in these materials are estimated with LISE++ simulations. There are two possible ways to evaluate the velocity at the target:
- The forward propagation method:
With this first approach, in the experimental data set, a gate on the $^{80}$Zn($^{9}$Be, X)$^{79}$Cu reaction channel is set and the mean of the $\beta_{57}$ distribution is determined as $\beta_{in}$. The latter is taken as a velocity input value for a beam of $^{80}$Zn in the simulation. The LISE++ physics calculator is used to evaluate the energy loss of nuclei with this incoming velocity when they reach half of the target thickness (3.4 mm depth). The final speed value after this calculation is then used to Doppler-correct the $\gamma$-ray energies.
- The backward propagation method:
In this approach, several simulations are run with different values around the previously determined $\beta_{in}$, as inputs for the incoming velocity of $^{80}$Zn isotopes. In each case, the velocity at the target center is evaluated. Furthermore, at this same point, the $^{80}$Zn($^{9}$Be, X)$^{79}$Cu reaction is simulated. This allows for the calculation of the energy losses of $^{79}$Cu isotopes through the second half of the target and the remaining materials

---

[7] These materials include the double PPAC detectors, the ionization chambers (MUSIC) and the plastic scintillators at both F7 and F8.

until they reach the F8-F9 region, where the decreased velocity is evaluated as $\beta_{out}$. This procedure is repeated until $\beta_{out}$ coincides with the average of the $\beta_{89}$ experimental distribution for the same reaction channel.

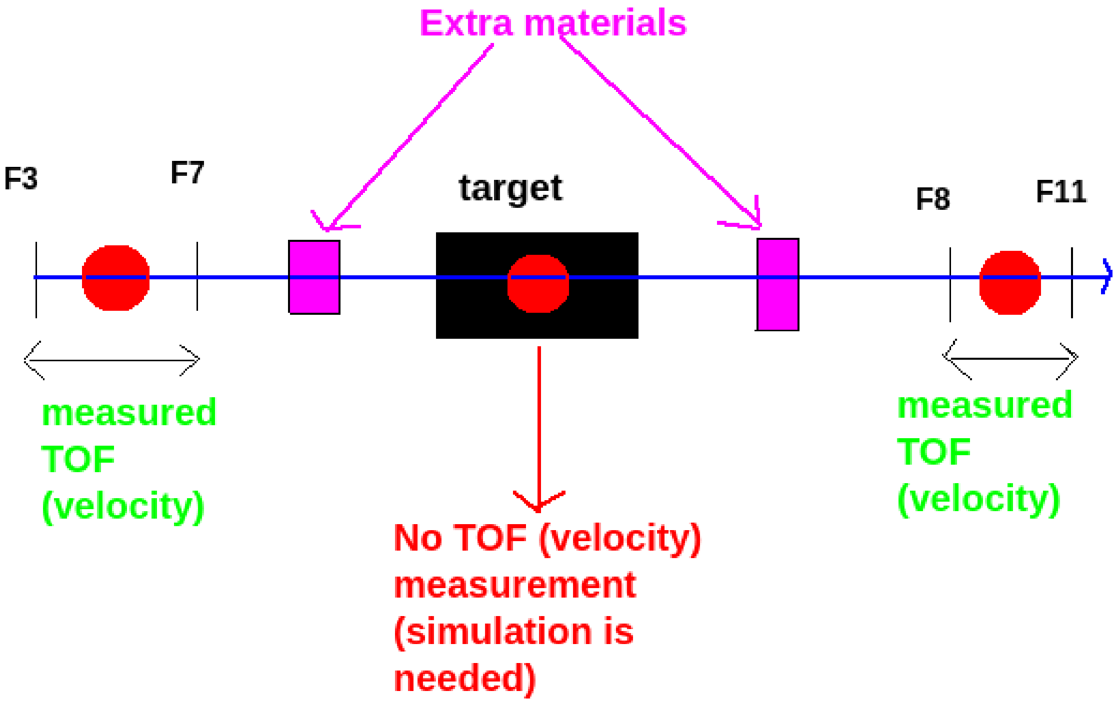

Figure 3.25: Illustration of the available velocity measurements.

As there is an energy degrader at F5 in BigRIPS, the calculated $\beta_{57}$ with the two-fold $B\rho$ method is less reliable than the calculated $\beta_{89}$ using the same method in ZeroDegree. Indeed, when the isotopes in BigRIPS cross the degrader, their energy is continuously and significantly decreased throughout its thickness. This implies that the equation 3.6 would require a third term to take into account this additional energy loss at F5. In ZeroDegree, however, there was no energy degrader and such a term is not required. This leads to less uncertainty on the calculated $\beta_{89}$ as compared to $\beta_{57}$. Consequently, we chose to use the backward propagation approach to determine the Doppler-correction velocities. This procedure was applied for several reaction channels. We particularly put our focus on two cases, which are the $^{80}$Zn($^{9}$Be, X)$^{79}$Cu (the case of interest for the thesis) and the $^{80}$Zn($^{9}$Be, X)$^{78}$Zn (used as a benchmark for the lifetime analysis). The final values we obtained are summarized in table 3.5.

| Method | Incoming beam | Residue | Simulated mid-target $\beta_R$ | Required $\beta_{in}$ |
|---|---|---|---|---|
| Backward | $^{80}$Zn | $^{79}$Cu | 0.6017 | 0.6276 |
| Forward | $^{80}$Zn | $^{79}$Cu | 0.6028 | 0.6285 |
| Backward | $^{80}$Zn | $^{78}$Zn | 0.6091 | 0.6337 |
| Forward | $^{80}$Zn | $^{78}$Zn | 0.6084 | 0.6331 |

Table 3.5: Summary of the final Doppler correction average velocities. The values obtained with the backward method were used to correct for the $\gamma$-ray energies.

### b/ Event-by-event velocity for Doppler-correction

The procedure described in the previous section allows to determine the average velocity $\beta_R$ at the reaction point (third column of table 3.5). However, for an event-by-event approach, it is necessary to take into account the differences in kinetic energies between the nuclei. To do so, the $\beta_{89}$ distribution in ZeroDegree is shifted to a new distribution that is centered on the simulated mid-target velocity $\beta_R$, and the final value that is employed in equation 2.15 is obtained using the following formula:

$$\beta_{doppler} = \beta_R \times [1 + \frac{\beta_{89} - < \beta_{89} >}{< \beta_{89} >}] \tag{3.17}$$

where $<\beta_{89}>$ is the average over all the events of the $\beta_{89}$ experimentally measured distribution and $\beta_{89}$ is the measured velocity for the event of interest. An example of the difference between the measured $\beta_{89}$ and the resulting $\beta_{doppler}$ for our reaction of interest is shown in figure 3.26.

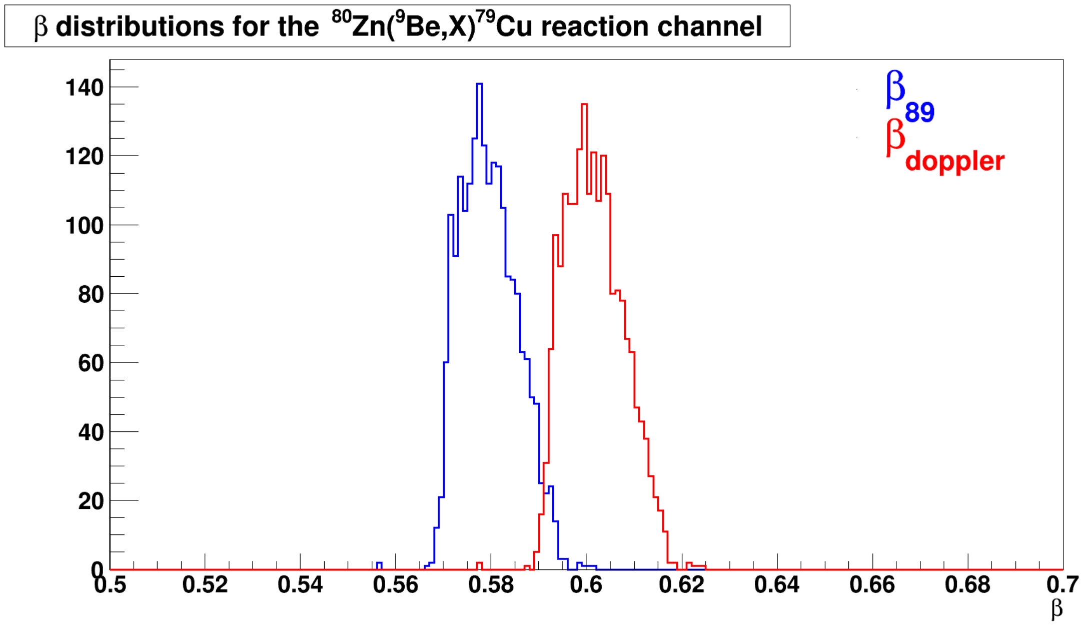

Figure 3.26: Comparison between the experimentally measured $\beta_{89}$ in ZeroDegree and $\beta_{doppler}$ used for the Doppler correction of the $\gamma$-ray energies.

## 3.6 Add-back procedure

In the energy range we are looking at, from 100 keV to 2-3 MeV, the dominant process for the interaction of $\gamma$ rays with matter is the Compton scattering. Some of the $\gamma$ rays do not deposit their full energy in one single crystal. In order to increase the peak-to-Compton ratio, the add-back procedure can be employed. To do so, the energies of the hits within crystals of the same cluster are added together before applying any Doppler correction. The hit position is still determined with the method described in section 3.5.1. An example of the effect of this add-back procedure is shown in figure 3.27. In the latter, a comparison is made between the Doppler-corrected spectra obtained with MB detectors, with and without employing the add-back. It can be seen that thanks to this procedure, the number of counts at low energy is reduced, and the peak-to-background ratio for the transition at 656 keV is enhanced. In this particular spectrum, the number of counts under the photo-peak after subtracting the background (modeled for instance with an exponential decay), increases by 10%. Although this method successfully enhances the peak-to Compton ratio, we did not use it for the lifetime determination due to eventual incomplete reconstruction of the total energy before applying the Doppler correction. Indeed, it may happen that the scattered $\gamma$ ray escapes from the detector after depositing different amounts of energy in the different crystals. In this case, the sum of these deposits does not reach the real total energy of the $\gamma$ ray. Then, when this lower total energy is Doppler-corrected, it will end at a value that is smaller than the correct one, thus contributing to an increase of the counts in the low energy tail. In addition, the first interaction point is taken as the center of the segment in which the highest energy deposit occurs. This assumption is not always true, particularly for $\gamma$-ray energies below 500 keV. In this case, a wrong angle is taken for the Doppler correction, thus inducing counts on both sides of the energy peak. As the half-life determination is based on the analysis of the peak shape, these additional counts can skew the results.

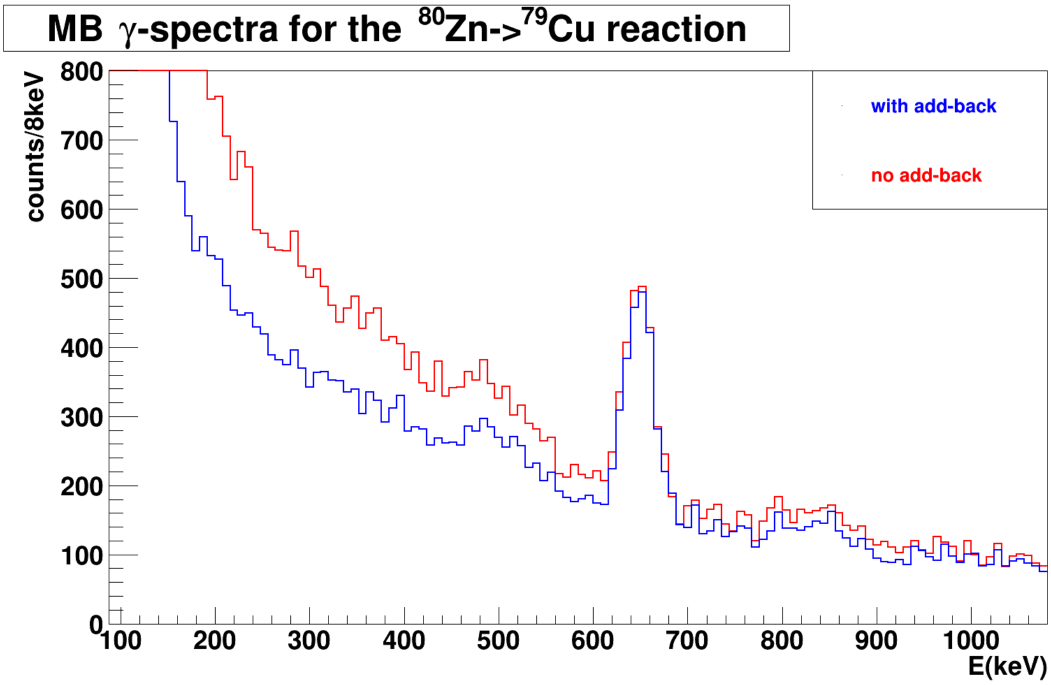

Figure 3.27: Comparison between the Doppler corrected $\gamma$ spectra obtained with MB with and without applying the add-back procedure.

## 3.7 GEANT4 simulation of the experimental setup

The HiCARI spectrometer simulations with GEANT4 are conducted in order to obtain the response functions of its components. These functions will be used to fit the experimental $\gamma$-ray spectra and extract the lifetimes of the decaying states of interest. The simulation code has been developed by K. Wimmer [76]. It incorporates factors such as detector geometry, target thickness, beam energy, beam pipe shielding material and thickness, the lifetimes of the excited states and the anisotropy of $\gamma$ rays emitted by moving nuclei, due to the Lorentz boost. The code operates in two main steps:

- First, it simulates the interaction between the ion beam and the beryllium target. It calculates the energy loss in the target before (for $^{80}$Zn) and after (for $^{79}$Cu) the knockout reaction, and takes into account the half-life of the excited states before the $\gamma$ decay. Inputs for this step include the number of ions in the incoming beam, their velocities before the target, taken as a distribution that is centered on the values from the last column of table 3.5, $\gamma$ transition energies, and the half-life of de-exciting states.

- In the second step, the code simulates the interaction of $\gamma$ rays from the first step with HiCARI, employing the geometry that was derived from the photogrammetry. This step requires other inputs which include the experimental resolution of each crystal, determined through calibration sources at rest (as detailed in section 3.4.2) and their thresholds (as explained in section 3.4.3). Subsequently, the simulated events undergo an analysis that is similar to the one used for the treatment of the experimental data. In this procedure, the speed at the reaction point in the target is obtained with GEANT4 energy loss calculations for each simulated event. Then, the average of the resulting velocity distribution for the total number of beam ions is used for the Doppler correction of the $\gamma$-ray energies. The difference between this parameter obtained with GEANT4 and the mid-target velocity simulated with LISE++ (used for the Doppler correction in the analysis of the experimental data) is negligible compared to the width of the experimental velocity distribution [8], as summarized in table 3.6.

| Incoming beam | Residue | LISE++ mid-target $\beta$ | GEANT4 $\beta$ at reaction |
|---|---|---|---|
| $^{80}$Zn | $^{79}$Cu | 0.6017 | 0.6014 |
| $^{80}$Zn | $^{78}$Zn | 0.6091 | 0.6089 |

Table 3.6: Velocities used for the Doppler correction for the experimental data (using the backward method) and the simulation.

### 3.7.1 $\gamma$-decay lifetimes in the simulation

As already mentioned in section 2.4.2, the positions at which the reaction of the beam and the $\gamma$-ray emission occur are both assumed to coincide with the middle of the target, after crossing half its total thickness. This assumption is valid only if the

---

[8] For instance, the width of the velocity distribution for the $^{80}$Zn($^{9}$Be, X)$^{79}$Cu reaction channel in the experimental data (shown in figure 3.26) is of the order of 0.0050.

lifetimes of the decaying states in the residue are neglected. If instead these states have a significant lifetime, this is not valid anymore. Indeed, the velocity that is used for the Doppler correction is higher than the real one and the angle that is employed is smaller than the real angle[9] and . These differences are schematically illustrated in figure 3.28.

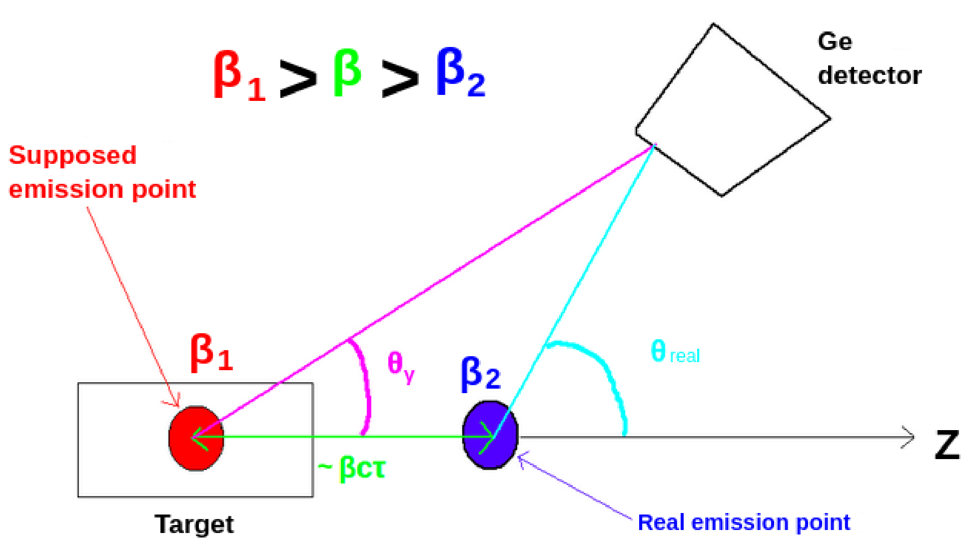

Figure 3.28: Illustration of the lifetime effect on the angle and velocity that are used for the Doppler correction.

These two effects on the angle and velocity will change the position and the shape of the Doppler-corrected energy peaks. The peak is shifted to lower energies and a tail appears on its left. These effects can be seen with GEANT4 simulations of a transition with different lifetimes. An example is illustrated in figure 3.29 for MB, figure 3.30 for SC, figure 3.31 for P3 and figure 3.32 for QUAD, where the $^{80}$Zn($^{9}$Be, X)$^{79}$Cu reaction is simulated and the outgoing copper isotope decays by emitting a 656 keV $\gamma$ ray. The $\gamma$ spectra obtained after Doppler correction are shown. One can notice that Miniball, clover and Gretina-type detectors do not exhibit the same sensitivity to the lifetimes. For the case of Miniball and clover detectors, the dominant effect is the shift of the energy peak position to lower values. This shift is higher with MB as compared to SC, since the latter were placed at an angle where the sensitivity to lifetime effects is reduced. On the other hand, for the case of the GRETINA-type modules, the low energy tail is more visible. Later on, as detailed in the next chapter, in our analysis,

---

[9] For instance, with a velocity $\beta$ of the order of 0.6, with a state having a half-life $T_{1/2} = 10$ ps, the nuclei would travel a distance of about 2 mm.

these simulated response functions with different lifetimes will be compared to the final Doppler-corrected spectra that we obtained from the experimental data, in order to determine the half-lives of the decaying states of interest. In short, simulations are conducted with various half-life values, and for each value, the simulated response function is used to fit the experimental distribution. The quality of the fit for each half-life value, i.e. the agreement between the shapes of the experimental and simulated spectra, is assessed using the $\chi^2$. A minimization of the latter allows to measure the half-life of interest. This procedure must be separately repeated for each type of detector due to their different lifetime sensitivities.

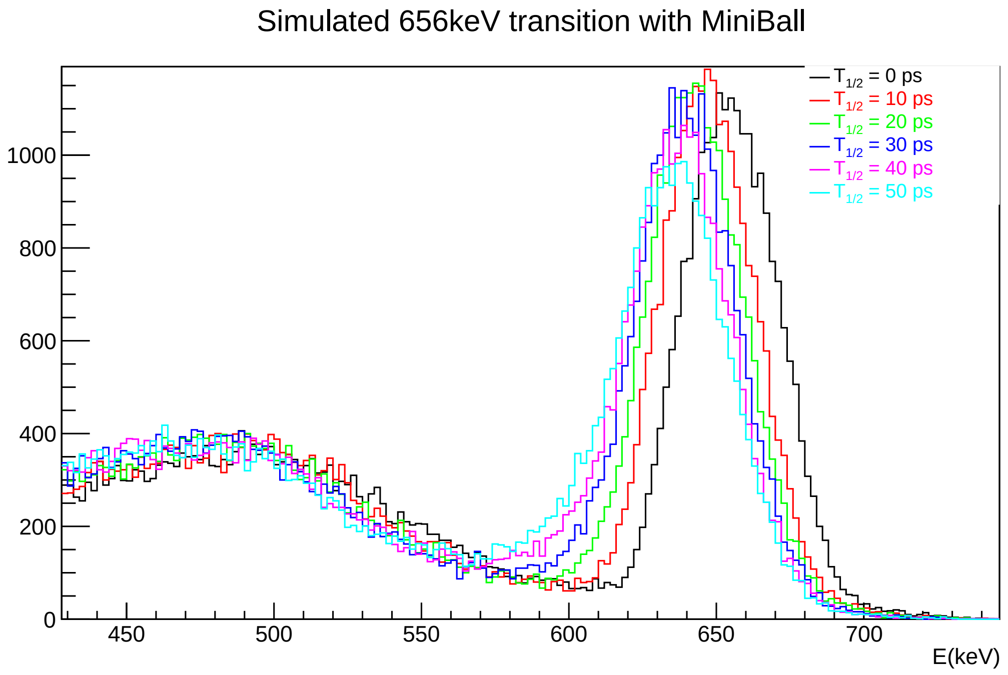

Figure 3.29: Illustration of the lifetime effect on the Doppler-corrected energy for a 656 keV $\gamma$ ray emitted by a $^{79}$Cu nucleus and detected with MB.

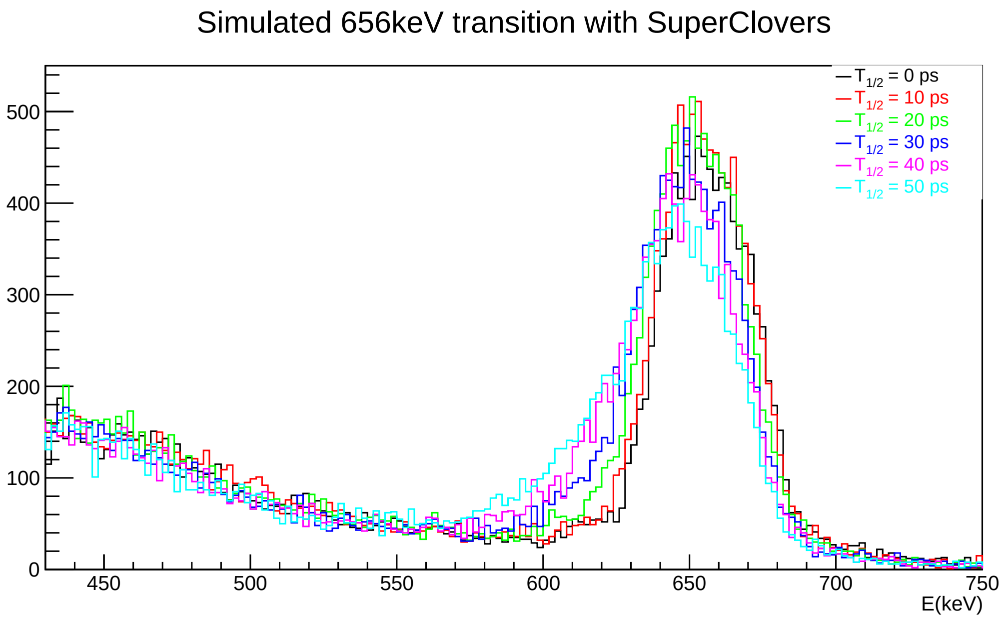

Figure 3.30: Illustration of the lifetime effect on the Doppler-corrected energy for a 656 keV $\gamma$ ray emitted by a $^{79}$Cu nucleus and detected with SC.

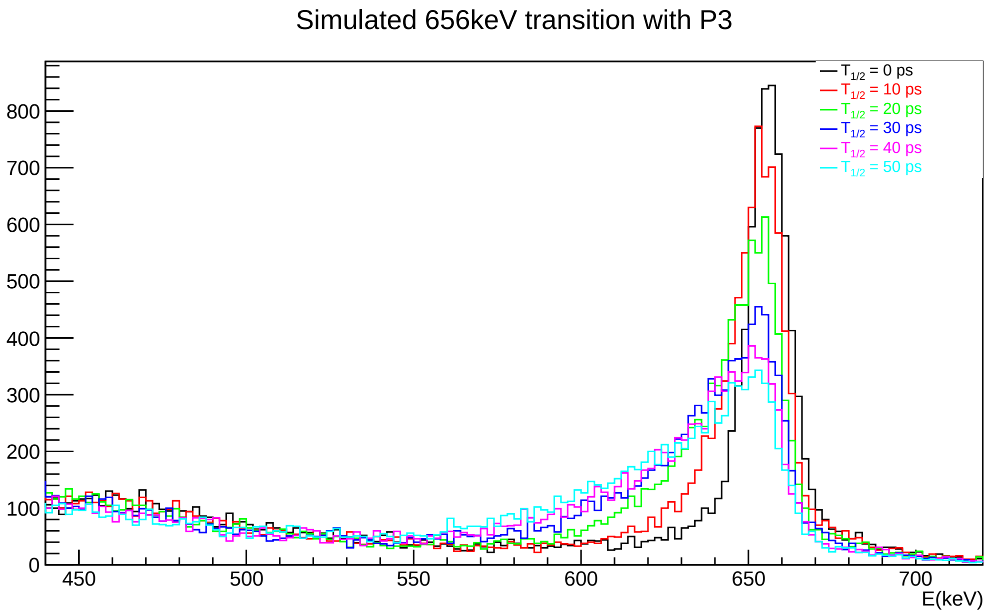

Figure 3.31: Illustration of the lifetime effect on the Doppler-corrected energy for a 656 keV $\gamma$ ray emitted by a $^{79}$Cu nucleus and detected with P3.

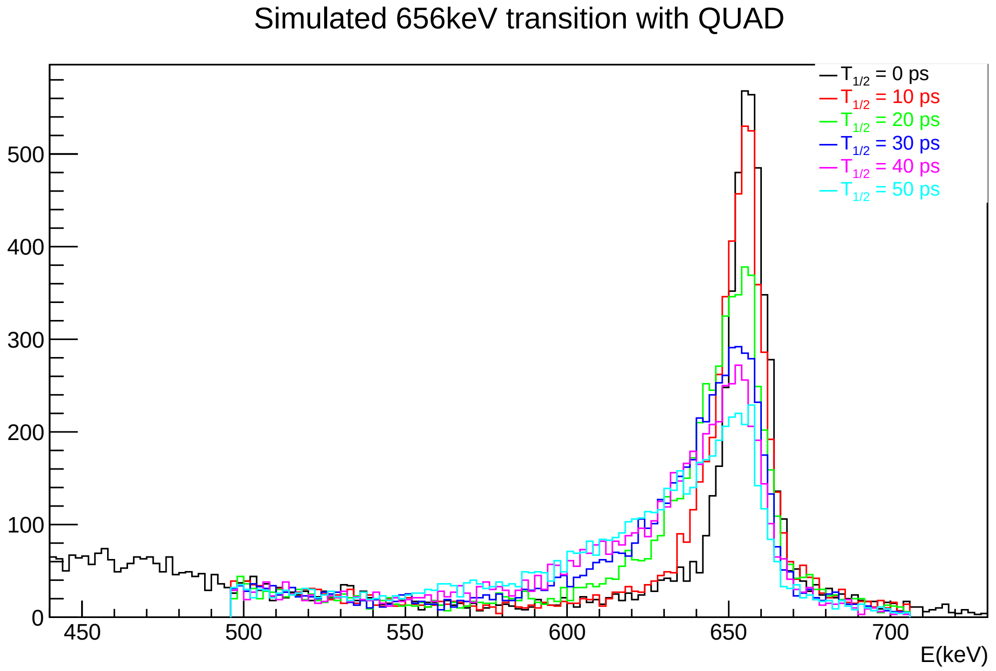

Figure 3.32: Illustration of the lifetime effect on the Doppler-corrected energy for a 656 keV $\gamma$ ray emitted by a $^{79}$Cu nucleus and detected with QUAD.

### 3.7.2 Comparison with the expected detector response from the experiment's proposal

In the original proposal for the HiCARI campaign [77], the GEANT4 simulation we described was employed to estimate and compare the expected performances of the HiCARI germanium spectrometer and the DALI2 scintillator array. This included the evaluation of the total energy resolution after the Doppler correction of the $\gamma$-ray spectra. Using the formula in equation 2.15, the overall energy resolution is the result of 3 contributions:

$$\left(\frac{\Delta E_0}{E_0}\right)^2 = \left(\frac{\Delta E_\gamma}{E_\gamma}\right)^2 + \left(\frac{\beta - \cos\theta_\gamma}{(1-\beta^2)(1-\beta\cos\theta_\gamma)}\right)^2 (\Delta\beta)^2 + \left(\frac{\beta\sin\theta_\gamma}{1-\beta\cos\theta_\gamma}\right)^2 (\Delta\theta_\gamma)^2 \tag{3.18}$$

- The first one is the intrinsic resolution $\Delta E_\gamma$ of the crystals. In our case, the latter has been determined using the calibration source data, as explained in section 3.4.2.
- The second contribution originates from the velocity uncertainty $\Delta\beta$. This is

mainly due to the inaccurate knowledge of the emission point, which was assumed to coincide with the middle of the $^9$Be target.

- The last error $\Delta\theta_\gamma$ comes from the imprecise determination of both the emission point in the target and the hit position of the $\gamma$ photon in the germanium detectors.

The comparison between the energy resolution in DALI2 and HiCARI is shown in figure 3.33, for a transition at 1 MeV, with a zero lifetime and a nucleus speed $\beta \approx 0.6$. Clearly, the most evident gain using germanium detectors is in the intrinsic energy resolution. With HiCARI, the latter remains below 5 keV for all the angles, contrary to DALI2 for which it is always above 45 keV. As regards the velocity uncertainties, these are the same in the two cases since the same target was employed in both simulations. Finally, the angle uncertainties which are the dominant effect at $\theta \approx 45$ °, are lower with HiCARI and more particularly with the tracking detectors thanks to the pulse shape decomposition algorithm that retrieves the hit position with a higher precision (as explained in section 2.3.2).

.

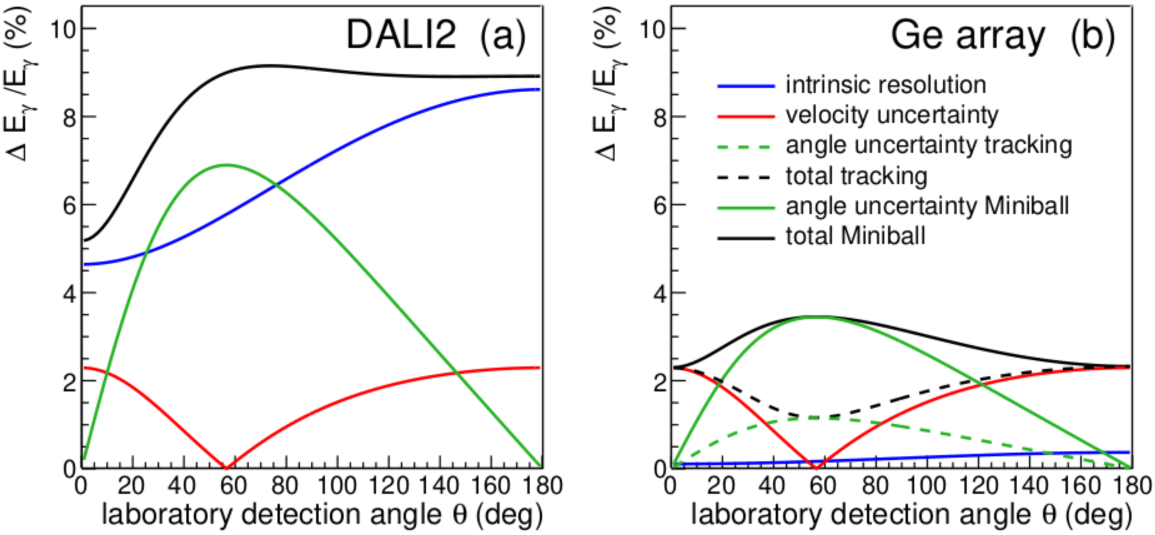

Figure 3.33: Comparison between the energy resolutions after Doppler correction using DALI2 (a) and HiCARI (b).

In order to compare the expected energy resolutions of the HiCARI components with those obtained in our experimental conditions, we similarly simulated a transition at 1 MeV. The results are shown for GRETINA-type detectors and high angle Miniball with two separated $\gamma$ spectra in figure 3.34. Fitting these spectra with Gaussian functions around the peaks leads to final energy resolutions of $\sigma \approx 25$ keV with Miniball and $\sigma \approx 13$ keV. The latter is comparable with the resolution of $\sigma \approx 12$ keV obtained with the tracking detectors from figure 3.33 at $\theta \approx 73$ °(Average angle between P3 and QUAD). However, for Miniball, the resolution of $\sigma \approx 25$ keV we obtained is a bit better than the value of $\sigma \approx 33$ keV that is expected from figure 3.33. This difference is likely due to an overestimated intrinsic resolution for the Miniball crystals in the proposal and other parameters that were not tuned at that time. Therefore, this comparison has not be taken too seriously, and what we experimentally obtained remains more important.

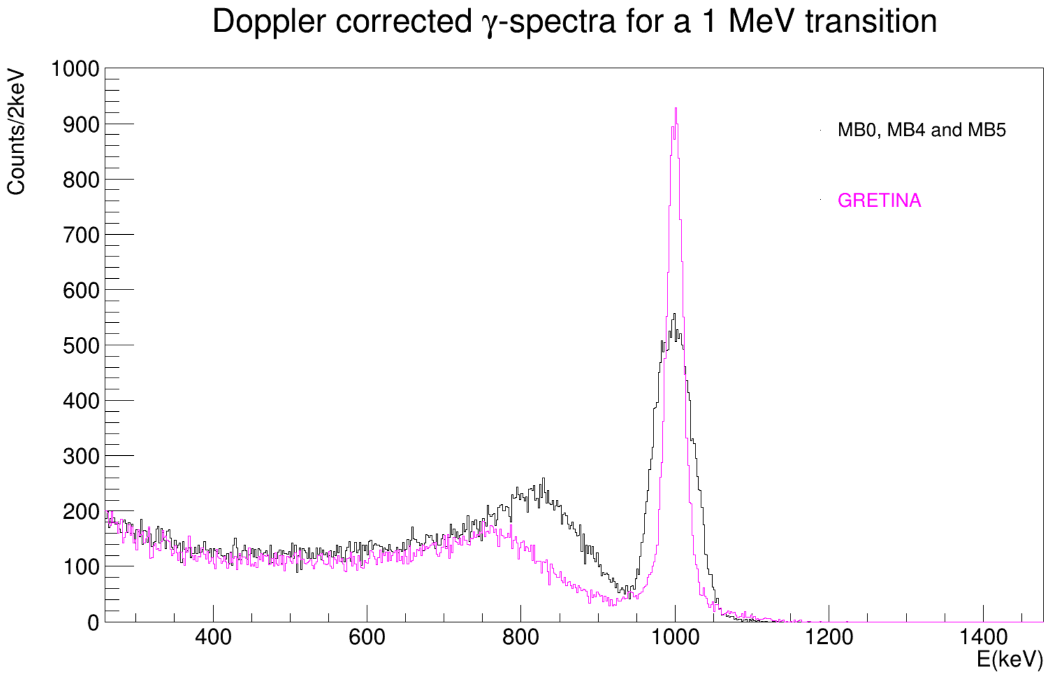

Figure 3.34: Comparison between the $\gamma$ spectra obtained for a 1 MeV transition resolutions after Doppler correction using GRETINA and high-angle ($\theta \approx 45$ °) Miniball detectors.

### 3.7.3 Comparison between the experimental and simulated detection efficiencies for HiCARI

For a complete verification of the consistency between the experimental and simulated data, it is worth to compare between the measured detection efficiencies that were discussed in section 3.4.5 and the simulated ones for the HiCARI array. The results of such a comparison are shown in figure 3.35. It can be seen that the simulated efficiencies are better than the experimental ones by some factor. This factor is similar for the Miniball and the tracking detectors, and slightly higher for clovers, as illustrated in figure 3.36 where the ratio between the simulated and the experimental efficiencies is represented for each detector group. It can be noticed that this ratio is closer to unity for the transitions in $^{60}$Co (at 1173 keV and 1332 keV). The exact reason for the discrepancy between the simulated and experimental efficiencies for the other $\gamma$ sources is still under investigation. Nevertheless, the impact of this incoherence on the lifetime analysis in this work is marginal. Indeed, as it will be discussed further in chapters 4 and 5, since the different detectors exhibit different sensitivities to the lifetime effects, the analysis is performed separately for each detector group, and the modules that will provide the most reliable and accurate results are the GRETINA-type ones, which suffer from the same discrepancy factor in efficiencies.

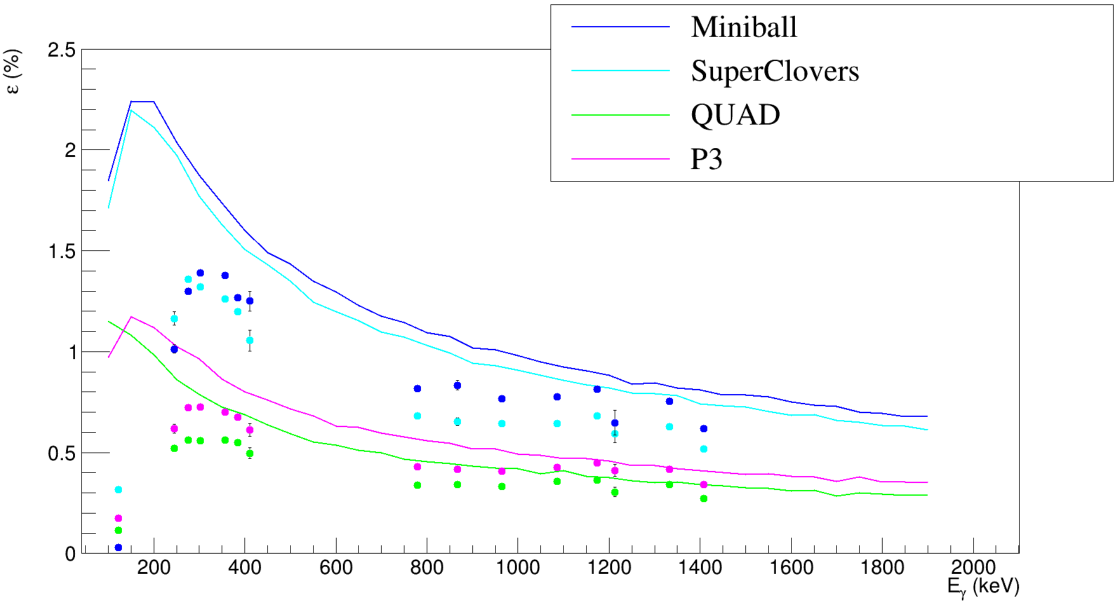

Figure 3.35: Comparison between the simulated (solid lines) and experimental (data points) efficiencies for the HiCARI spectrometer.

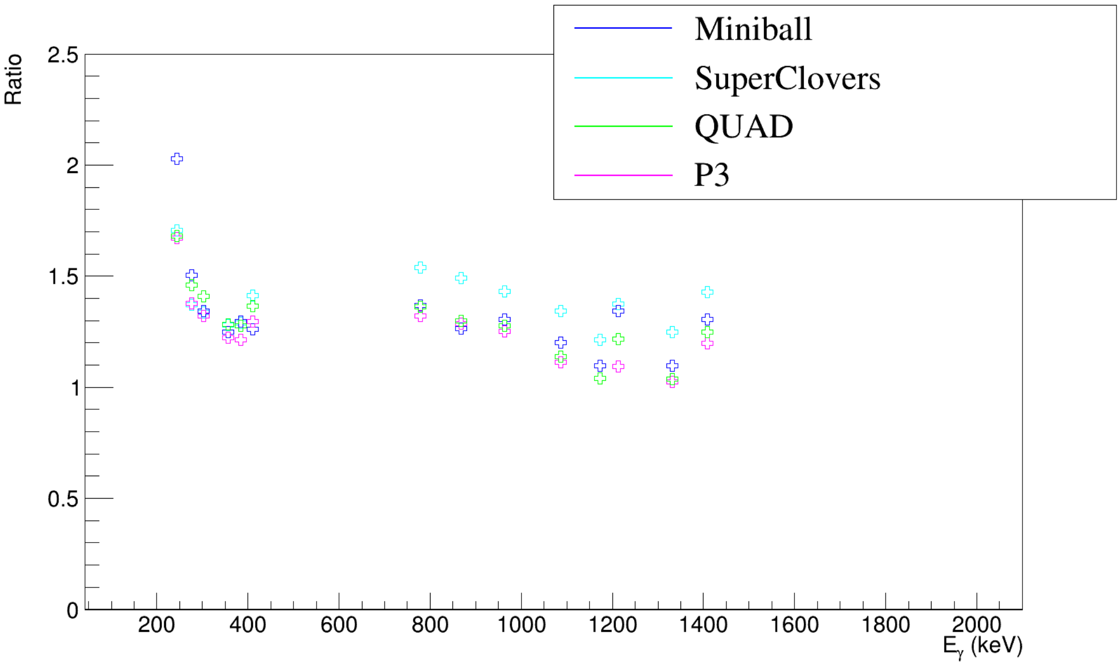

Figure 3.36: Ratio between the simulated and experimental efficiencies for each detector group in the HiCARI spectrometer.

# 4

# Benchmark case

## Contents

The $\gamma$ spectra in the center of mass frame of the emitting nuclei are derived through the steps outlined in the preceding chapter. Before analysing the reaction channel of interest, a substantial portion of this thesis focused on benchmarking the Doppler correction and lifetime extraction procedures using a known case within our dataset.

The benchmark analysis was conducted on the $^{80}$Zn→$^{78}$Zn reaction. We particularly focused on the lifetime of the first excited state in $^{78}$Zn. There were many reasons that led to this choice of benchmark. First, the energies of the $\gamma$ transitions in this nucleus are already known from literature with a precision that is below 1 keV, and their values are in the same range (between 500 keV and 1 MeV) as the ones we obtained from the decay of $^{79}$Cu in our experiment. Furthermore, in this channel, the incoming beam, which is $^{80}$Zn, is the same as for our case of interest. Therefore, the validity of the velocities determined for Doppler correction should be similar for the two cases. Additionally, this channel had a rather high statistics as compared to the other cases in the data set. Finally, the first excited state in $^{78}$Zn has a known lifetime value, of the order of a few picoseconds. This is in the same order of magnitude as for the lifetimes we expected from the decay of $^{79}$Cu after some preliminary analysis, and for which the HiCARI array is sensitive.

## 4.1 Presentation of the benchmark case

The level scheme of $^{78}$Zn has already been studied in previous experiments with different methods, including isomer spectroscopy after fragmentation at GANIL [78] and Coulomb excitation at REX-ISOLDE (CERN) [79], and the lifetimes for some of the states have been determined. This level scheme is presented in figure 4.1, where we focused our analysis on the $2^+ \rightarrow 0^+$ transition at 730 keV. Its corresponding half-life was deduced from $B(E2)$ measurements in the Coulomb excitation experiment at ISOLDE and the resulting value was $18 \pm 4$ ps.

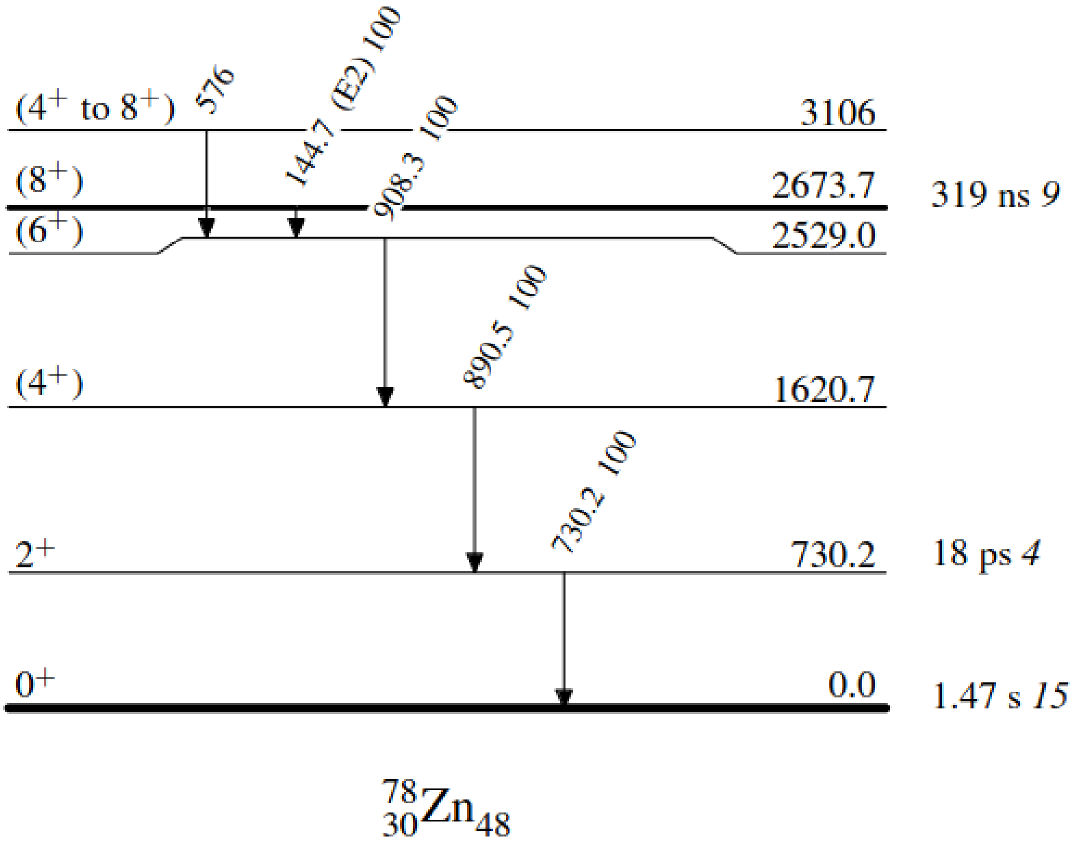

Figure 4.1: Nuclear level scheme of $^{78}$Zn isotope [80].

Before going through the lifetime determination procedure, we show the full $\gamma$-ray spectra that we obtained after Doppler correction for the $^{80}$Zn→$^{78}$Zn case. These were reconstructed separately for the different detector groups. Those corresponding to MB and SC are displayed in figure 4.2, while those from GRETINA-like modules are illustrated in figure 4.3, both in the [200 keV: 2 MeV] range. With all types of detectors, all the rays in the level scheme of figure 4.1 are present. The range below 200 keV was not included for clarity purposes, and since we did not see the 144.7 keV peak. Indeed, the lifetime of the decaying ($8^+$) state is of the order of 300 ns. If this isomeric state is populated in the reaction, it will decay far after the target (more than 50 meters farther) and will not be detected. One can notice a higher statistics with MB modules. This is mainly due to the geometry of the HiCARI array. The Miniball rings were placed at low angles (20° to 50°), contrary to the other clusters being at higher angles (above 60°). Due to the Lorentz boost at relativistic speeds, the emitted $\gamma$ rays are focused at low angles, leading to a higher number of counts with Miniball[1].

---

[1] For instance, the ratio between the number of counts under the 730 keV peak in MB and SC is expected to be of the order of 2.4 when using GEANT4 simulations. In the experimental data, this

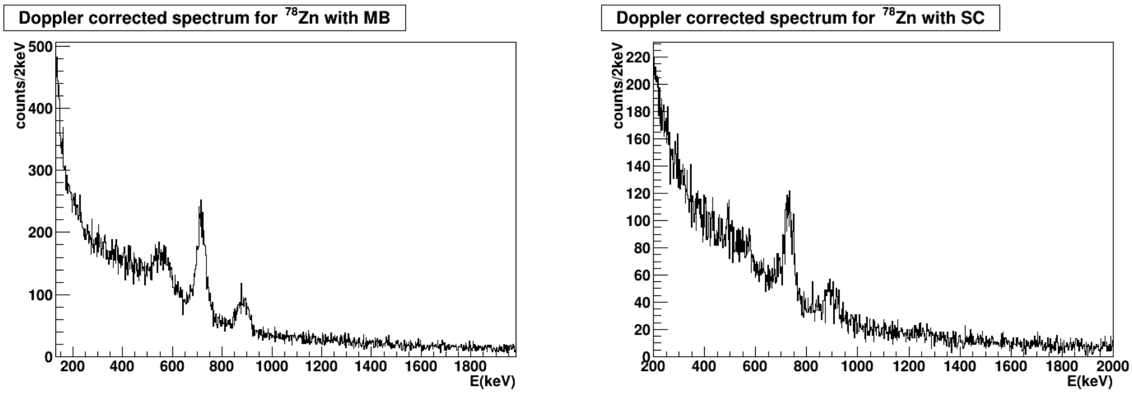
Doppler corrected spectrum for $^{78}$Zn with MB

Doppler corrected spectrum for $^{78}$Zn with SC

(a) $\gamma$ spectrum for $^{78}$Zn after Doppler correction with MB detectors

(b) $\gamma$ spectrum for $^{78}$Zn after Doppler correction with SC detectors

Figure 4.2: Doppler corrected $\gamma$ spectra for the $^{80}$Zn$\rightarrow$$^{78}$Zn case with MB (left) and SC (right) detector groups.

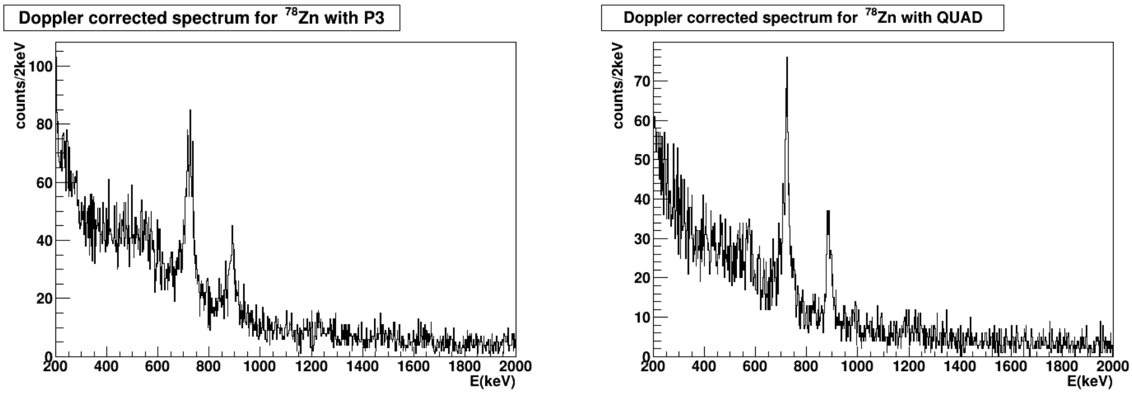
Doppler corrected spectrum for $^{78}$Zn with P3

Doppler corrected spectrum for $^{78}$Zn with QUAD


(a) $\gamma$ spectrum for $^{78}$Zn after Doppler correction with P3 detector

(b) $\gamma$ spectrum for $^{78}$Zn after Doppler correction with QUAD detector

Figure 4.3: Doppler corrected $\gamma$ spectra for the $^{80}$Zn$\rightarrow$$^{78}$Zn case with P3 (left) and QUAD (right) detectors.

As regards the observed transitions, the following can be noticed:
- The 576 keV ray is not fed by any other decay according to the level scheme. Consequently, it is expected to be the least intense transition among all those observed. Furthermore, it is situated 200 keV below the most intense transition at 730 keV. Therefore, the Compton edge of the latter disrupts the 576 peak, and its resolution is enlarged. For these reasons, it is clearly visible only in the spectrum obtained with Miniball.
- The 908 keV and the 890 keV $\gamma$ rays could not be separated in our spectra. This

---

ratio is about 2.6.

is mainly due to the fast deterioration of the energy resolution[2] of the germanium detectors as the energy grows. Additionally, there is no lifetime information about the involved ($6^+$) and ($4^+$) decaying states[3]. If these half-lives were long enough, they would enlarge and shift the corresponding peaks as explained in section 3.7.1.
- The main peak of interest at 730 keV is the only one that is unambiguously observed with all types of clusters. The half-life of 18(4) ps for the decaying state has an impact on the shape and position of the peaks that is already visible without comparing to simulations. For instance, just with a preliminary approach, by fitting each spectrum with a sum of Gaussian functions and an exponential background, the peak centroids are not at the same position in terms of energy for all the detectors. An example of this fitting procedure is illustrated in figure 4.5 with MB. In addition, since the Miniball detectors had a higher statistics as compared to the other detector groups, we tried to separate them into angular groups, to see if these different angular rings could be affected differently by the lifetimes. As it was mentioned in table 2.1, MB2 was placed at a lower angle (around 30°) than the three other Miniball modules (around 45°). Therefore, we separated the $\gamma$ spectra for the two cases, as shown in figure 4.4. All the resulting values are summarized in table 4.1 for the different groups. It can be noticed that the peak centroid is shifted between the high angle and low angle Miniball clusters. The energy for MB2 was at 713 keV while it was found at 718 for the other modules, leading to an average of 717 keV when summing all Miniball spectra. Additionally, It can be seen that the average energy measured with clovers coincides with the literature value of 730 keV. These detectors were indeed placed at $\approx 75$ °which is the angle found when solving the equation 2.15 for $E_\gamma = E_0$, with a velocity $\beta \approx 0.6$. Given their worse energy resolution after Doppler correction as compared to the tracking detectors, they are not sensitive to the shifts caused by lifetime effects (as it can be observed from figure 3.30).

---

[2] Using GEANT4 simulations, the expected energy resolution (FWHM) at 908 keV after Doppler correction is 20 keV for GRETINA-type detectors and 50 keV for Miniball.

[3] These two states belong to the same band structure as the $2^+$ level. Their lifetimes can thus be expected to be of the same order (a few picoseconds to a few tens of picoseconds).

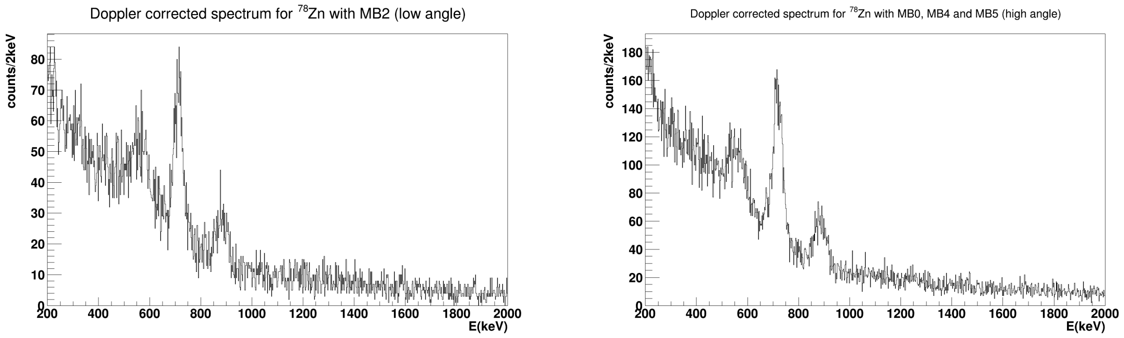

(a) $\gamma$ spectrum for $^{78}$Zn after Doppler correction with MB at low angle.

(b) $\gamma$ spectrum for $^{78}$Zn after Doppler correction with at high angle.

Figure 4.4: Doppler corrected $\gamma$ spectra for the $^{80}$Zn$\rightarrow$$^{78}$Zn case with MB2 (left) and MB0, MB4 and MB5 (right).

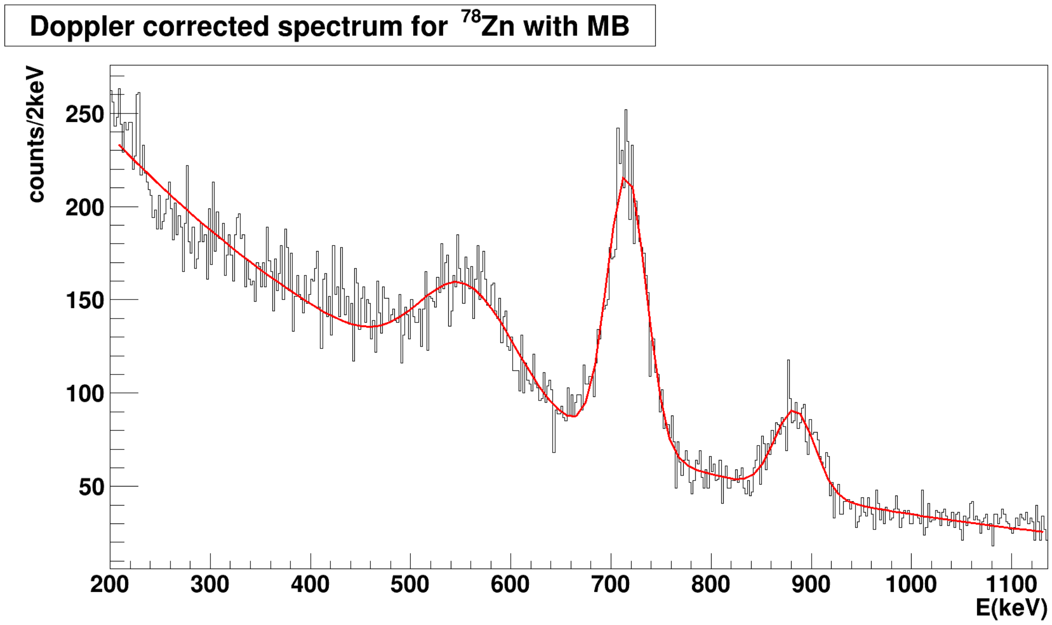

Figure 4.5: Example of the fitting procedure employed to evaluate the mean energy of the $2^+ \rightarrow 0^+$ transition. The fitting function in red line is a sum of Gaussians and an exponential background.

| Detector(s) | Energy(keV) |
|---|---|
| All MB | 717 ±2 |
| MB2 (low angle) | 713 ±2 |
| MB0, MB4 and MB5 (high angle) | 718 ±1 |
| SC | 730 ±2 |
| P3 | 721 ±2 |
| QUAD | 721 ±1 |

Table 4.1: Summary of the average energies for the $2^+ \rightarrow 0^+$ transition, for the different detector groups, as obtained with the fitting procedure displayed in figure 4.5.

## 4.2 Procedure for fitting the $\gamma$-ray spectra

In order to determine the lifetime of the first excited state in the $^{78}$Zn isotope, GEANT4 simulations were carried out with different inputs for the half-life of this state, to compare the shape of the $\gamma$ peaks in the experimental data with the outcome of the simulated response functions. To produce realistic response functions, all the transitions present in the experimental spectra were simulated and a background function $f_{bg}$ was added. Here are the steps through which the final total fitting function was obtained for each simulated response function:

- In our experimental spectra, background components essentially originate from atomic processes generating low-energy $\gamma$ rays, such as bremsstrahlung and radiative electron capture, or from unresolved transitions and Compton scattering or pair creation. The precise proportions and origins of these contributions cannot be accurately anticipated or simulated. Instead, we assume an effective and analytical representation of this background as an exponential decay of the form :

$$f_{bg}(E) = A\ e^{-BE} \tag{4.1}$$

where the $A$ and $B$ parameters are the usual amplitude and decay rate of the exponential function, respectively, and $E$ is the energy in keV units. In the fitting process, these $A$ and $B$ coefficients were left as free parameters after initializing them with the values obtained from the results of the procedure illustrated in figure 4.5.

- After that, the response functions for the transitions at 576 keV, 890 keV and 908 keV were simulated, as $f_{576}$, $f_{890}$ and $f_{908}$. The lifetimes of the latter have been assumed to be zero. Each $f_i$ function (where $i$ is either 576, 890 or 908) is shifted by an offset

$\Delta_i$ to take into account possible shape changes caused by lifetime effects. After that, the shifted functions were multiplied by scaling factors $S_i$ to match the intensities of the peaks in the data. The sum of the three resulting functions is written as follows:

$$f_{sum}(E) = S_{576} \times f_{576}(E - \Delta_{576}) + S_{890} \times f_{890}(E - \Delta_{890}) + S_{908} \times f_{908}(E - \Delta_{908}) \quad (4.2)$$

- Finally the transition of interest is simulated with an energy $E_{sim}$ in the neighborhood of 730 keV and a half-life $T_{1/2}$ of choice to generate a response function $f_{E_{sim}}^{T_{1/2}}(E)$. The latter is then multiplied by a scaling coefficient $S_{E_{sim}}^{T_{1/2}}$.

The total response function employed to fit the experimental spectrum is written as follows:

$$F_{total}(E) = f_{bg}(E) + f_{sum}(E) + S_{E_{sim}}^{T_{1/2}} \times f_{E_{sim}}^{T_{1/2}}(E) \quad (4.3)$$

In this formula, the $A$ and $B$ parameters of the background are left as free parameters around the initial values. This is to adjust for the contribution of the Compton events originating from all the simulated $\gamma$ rays, that could affect the shape of the exponential function. So, for a given single fitting function, where the corresponding two simulation inputs $E_{sim}$ and $T_{1/2}$ are imposed, there are 9 fitting parameters that are adjusted in the process[4]. An example of this fitting procedure is depicted in figure 4.6 in the case of P3 detector with a choice of $E_{sim} = 731$ keV and $T_{1/2} = 20$ ps for the simulation inputs. The energy range in which the fit was performed was chosen to be in a reduced zone where the lower and upper limits were at around 200 keV and 1400 keV (the exact values are given in the next section in table 4.2), respectively. This was to ensure that the quality of the $\chi^2$ indicator is controlled only by the transitions present in the range of interest.

---

[4] These 9 parameters of the total fitting function are the scaling factors $S_{576}$, $S_{890}$, $S_{908}$, $S_{E_{sim}}^{T_{1/2}}$, the offsets $\Delta_{576}$, $\Delta_{890}$, $\Delta_{908}$ and the $A$ and $B$ coefficients of the exponential background.

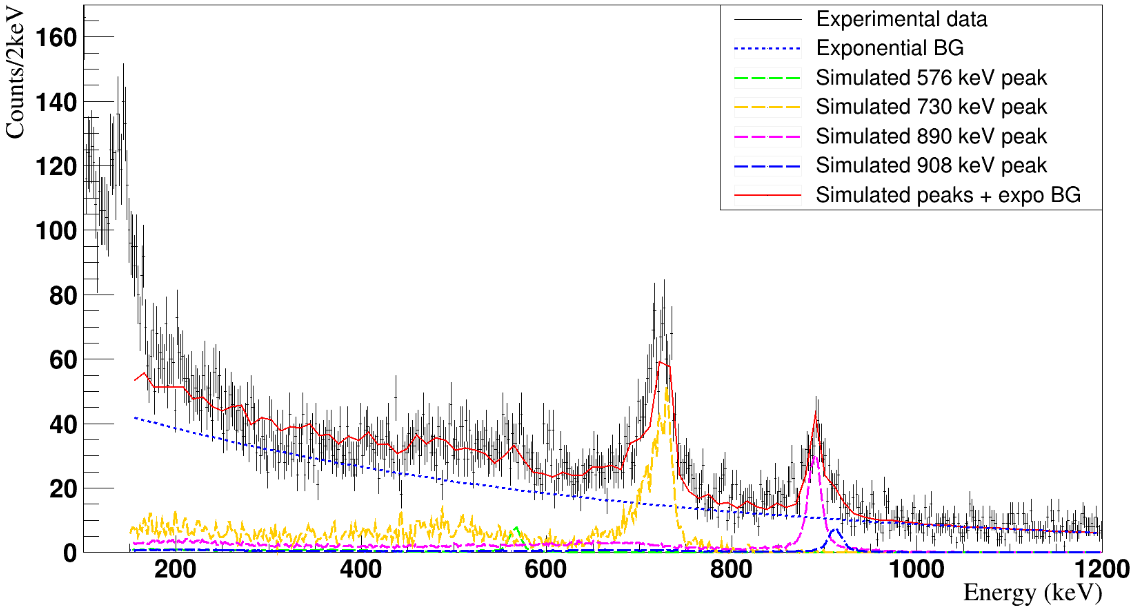

Figure 4.6: Example of the $\gamma$ spectrum obtained with P3, fitted with the total response function to evaluate the $\chi^2$

## 4.3 Determination of the lifetime for the $2^+$ state

The method described in the previous section was used to simulate[5] several total response functions $F_{total}(E)$. Each function was generated with a different couple of input values $(E_{sim},\, T_{1/2})$. For each couple, the experimental $\gamma$ spectra were fitted with the obtained response. For each detector group, when the $\gamma$ spectra were fitted, several fit ranges were tested. For each test, two-dimensional distributions of both $\chi^2$ and $\chi^2_{ndf}$ (the $\chi^2$ divided by the number of degrees of freedom) were obtained. In each $\chi^2_{ndf}$ plot, a global minimum for the reduced $\chi^2$ was evaluated. The final choice of the $\gamma$-spectra energy range for the fit was taken as the one leading to the lowest value among the evaluated global minima of $\chi^2_{ndf}$ [6]. The intervals that were finally chosen for the fitting of the $\gamma$-ray spectra are summarized in table 4.2.

---

[5] Each simulation was performed with $10^6$ events. This was chosen as a compromise between a sufficient statistics for the reliability of the shapes of the peaks on one hand and the running time on the other hand.

[6] It turned out that changing the lower and upper limits for these intervals by few tens of keV around the final choices in table 4.2 did not significantly change the results on the half-lives and energies, since the main effect is a global shift of the absolute $\chi^2$ value. This means that the established procedure is robust.

| Detector(s) | Energy(keV) |
|---|---|
| All MB | [150:1300] |
| MB2 (low angle) | [150:1300] |
| MB0, MB4 and MB5 (high angle) | [150:1300] |
| SC | [300:1300] |
| P3 | [300:1300] |
| QUAD | [300:1300] |

Table 4.2: Summary of the energy intervals where the total response functions in equation 4.3 were used to fit the experimental $^{78}$Zn $\gamma$ spectra, for the different detector groups.

This allowed to produce two-dimensional histograms of the $\chi^2$ as a function of $E_{sim}$ and $T_{1/2}$. These are represented separately for each detector group, with bin sizes of 1 keV and 1 ps for the energy and the half-life, respectively. Those obtained with MB and SC are illustrated in figure 4.7, while those of GRETINA are shown in figure 4.8. Similarly, those corresponding to the different Miniball rings are shown in figure 4.9. A detailed explanation of the method used to deduce the half-life from these plots is provided in the next paragraphs.

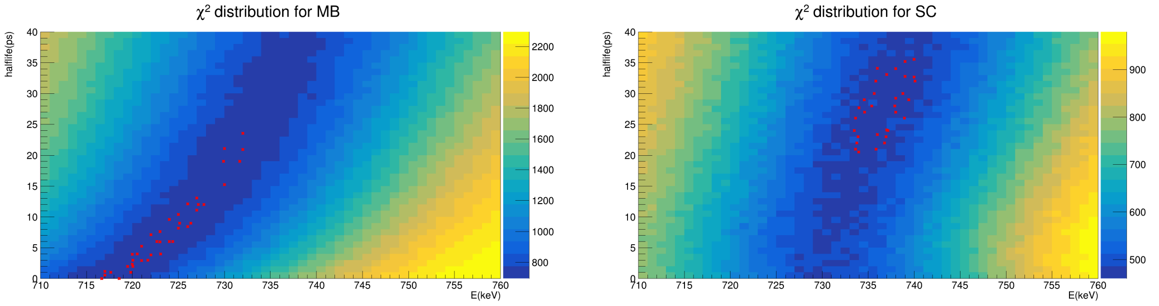

(a) (b)

Figure 4.7: $\chi^2$ distributions as a function of the energy and the half-life of the $2^+$ state in $^{78}$Zn with MB (a) and SC (b). The red dots show the limits found with the condition in equation 4.4

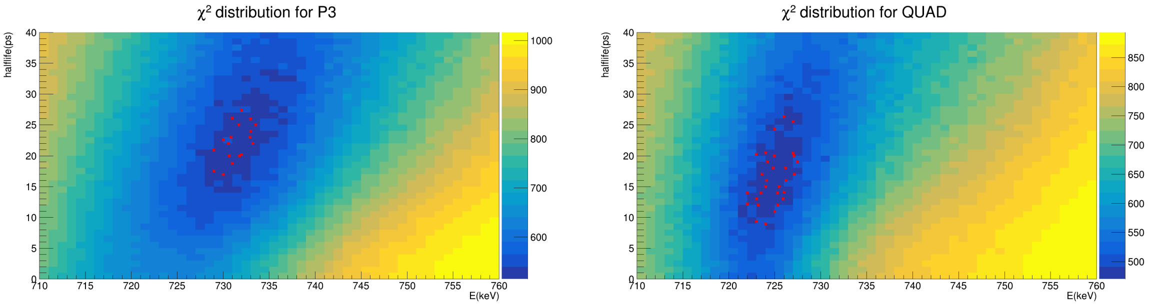

(a) (b)

Figure 4.8: $\chi^2$ distributions as a function of the energy and the half-life of the $2^+$ state in $^{78}$Zn with P3 (a) and QUAD (b). The red dots show the limits found with the condition in equation 4.4

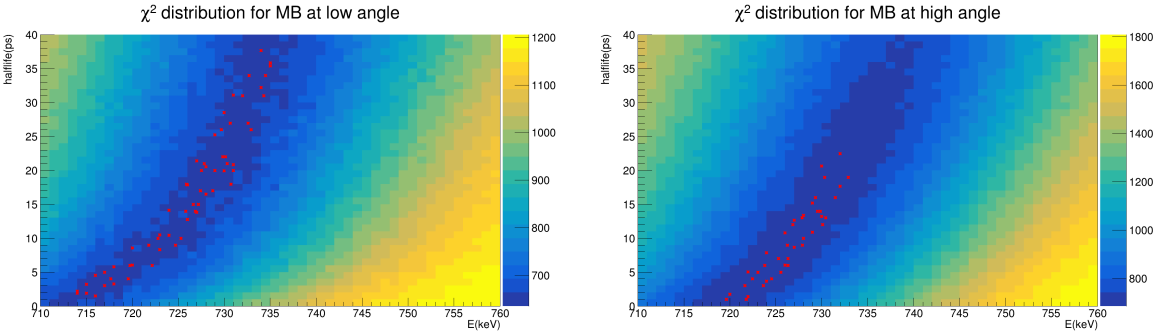

(a) (b)

Figure 4.9: $\chi^2$ distributions as a function of the energy and the half-life of the $2^+$ state in $^{78}$Zn with low angle MB (a) and high angle MB (b). The red dots show the limits found with the condition in equation 4.4

### 4.3.1 One-dimensional approach with a fixed energy

As the energy of the $2^+$ state is already known with a precision that is below 1 keV, the first approach was to look only at the behavior of the $\chi^2$ as a function of the lifetime, while the energy is fixed at 730 keV. This allows to check whether the half-life corresponding to the minimal $\chi^2$ coincides with the value of 18(4)ps from the past studies. The resulting one-dimensional histograms are shown in figure 4.10 for Miniball and SuperClovers, whereas those obtained with the tracking detectors are displayed in figure 4.11. For a more accurate determination of the minimal $\chi^2$, polynomial fits were performed in a reduced range around the bin of the minimum. The $1\sigma$-statistical uncertainty on the half-life is obtained by varying it until the $\chi^2$ reaches a value of $\chi^2_{min}+1$. This corresponds to 68% confidence level for one single parameter [81] since the energy is fixed. With this method, the minimum for MB was found at $18^{+1}_{-1}$ ps, which is in agreement with the tabulated value. For the case of clovers, the statistical fluctuations and their insensitivity to the lifetimes prevent us from finding a clear minimum as it can be seen in figure 4.10b. As regards the P3 cluster, the $\chi^2$ showed a minimum at $T_{1/2} = 20^{+2}_{-2}$ ps, also coinciding with the literature value. With the QUAD module, however, the range of the minima is not as clear as in P3, the minimum is obtained at $T_{1/2} = 31^{+2}_{-11}$ ps. The uncertainty is large enough to match with the 18(4) ps value from literature, but the measured value of 31 ps is much further than the highest value of 22 ps suggested by the previous studies. This discrepancy is discussed in the next paragraph, where the energy of the peak is also varied to find the couple $(E_{sim}, T_{1/2})$ corresponding to $\chi^2_{min}$.

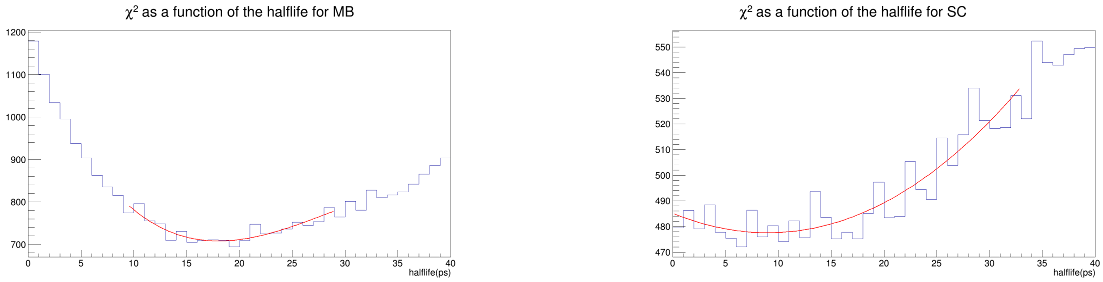

(a) (b)

Figure 4.10: $\chi^2$ distributions as a function of the half-life of the $2^+$ state with an energy fixed at 730 keV in $^{78}$Zn with MB (a) and SC (b)

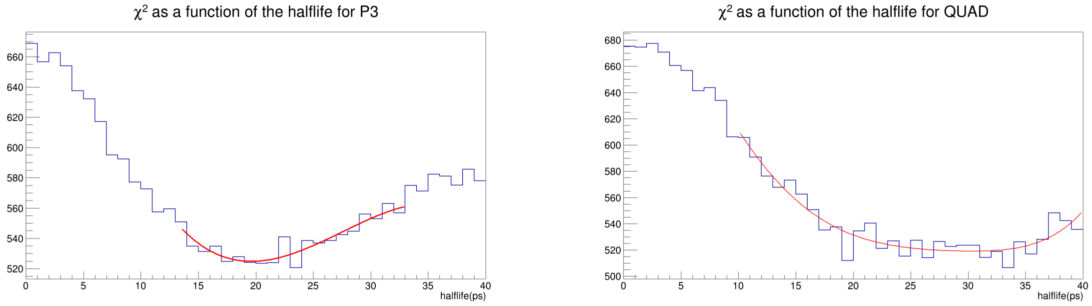

(a) (b)

Figure 4.11: $\chi^2$ distributions as a function of the half-life of the $2^+$ state with an energy fixed at 730 keV in $^{78}$Zn with P3 (a) and QUAD (b)

### 4.3.2 Two-dimensional approach

The $\chi^2$ surfaces in figures 4.7 and 4.8 can be used without fixing the energy of the $2^+$ state at 730 keV. This is important given that for the case of interest in the thesis, the excitation energies of the decaying states in $^{79}$Cu are known with an uncertainty that is larger than 5 keV [49], contrary to those in $^{78}$Zn. This method allows to find both the energy and the lifetime that minimize the $\chi^2$, together with their uncertainties. These are obtained with the following steps:
- The one-dimensional approach described in the previous paragraph is used for each value of $E_{sim}$ in the [710 keV: 760 keV] range. For each energy in this interval, the $\chi^2$ distribution as a function of the half-life is fitted, and the minimum is evaluated with the fitting function[7]. This allows to find the half-life that minimizes the $\chi^2$ for each energy value.
- All the minima obtained from these fits are compared to find a global minimum ${\chi^2_{min}}^{global}$, with the corresponding couple ($E_{sim}$, $T_{1/2}$).
- A graph representing all the minima against their corresponding half-lives is obtained and fitted with a polynomial function in a reduced range around the $T_{1/2}$ value that is given by ${\chi^2_{min}}^{global}$. The abscissa of the fitted minimum in this graph gives the final measurement for the half-life of the $2^+$ state. These graphs are shown for MB and SC in figure 4.12. Those we obtained with the tracking detectors are displayed in figure 4.13. From these plots, it can be noticed that for Miniball and clover detectors, there is no clear minimum that appears. This can be expected from the behavior of the $\chi^2$ in the two-dimensional plots of figure 4.7. In these plots, there is a continuous valley where the $\chi^2$ values are the lowest, and this valley follows a correlation curve having a positive slope. For instance, this slope is of the order of 2 ps/keV for Miniball. This means that if a simulation is run with a choice of ($E_{sim}$, $T_{1/2}$), the resulting response function will be similar to the one generated by a choice of ($E_{sim}$+1 keV, $T_{1/2}$+2 ps). This is indeed related to the fact that the half-life effect on the peaks was only shifting the centroid as explained in section 3.7.1 and no low energy tail appears for MB and SC. Therefore, there are several choices of the ($E_{sim}$, $T_{1/2}$) situated along the correlation line that lead to $\chi^2$ values close to the minimum, and the half-life can be determined only with a very large uncertainty. The lowest half-life and energy values for Miniball, for which the $\chi^2$ is close to ${\chi^2_{min}}^{global}$, are thus expected to correspond to $T_{1/2} = 0$ ps and $E_{sim} = 717$ keV, that is the position of the energy centroid as determined in table 4.1. The same conclusion is made when looking at the separated Miniball rings. From figure 4.9a, the lowest energy value is found at 714 keV for the low angle Miniball while it is at 719

---

[7] Due to statistical fluctuations, the $\chi^2$ minimum obtained using a fit is larger than the height of the minimum bin, with typical differences of 6 units.

keV for the high angle Miniball. Indeed, these values coincide with those in table 4.1.

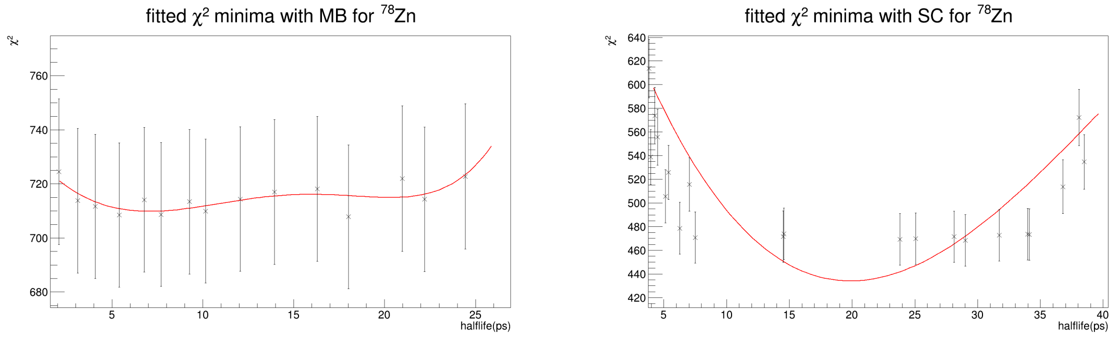

(a)

(b)

Figure 4.12: $\chi^2$ minima as a function of the half-life of the $2^+$ state in $^{78}$Zn with MB (a) and SC (b)

On the other hand, with the tracking detectors, the effect of the lifetime on the shape of the $\gamma$ peaks includes the appearance of a significant low energy tail (as discussed in section 3.7.1). Therefore, in the 2D-surfaces of figure 4.8, the valleys where the $\chi^2$ is close to ${\chi^2_{min}}^{global}$ are situated in a more reduced range around this minimum. This implies that the graphs displayed in figure 4.13 show clear minima at 22 ps with P3 and 18 ps with QUAD. The errors on these values are discussed later in this section.

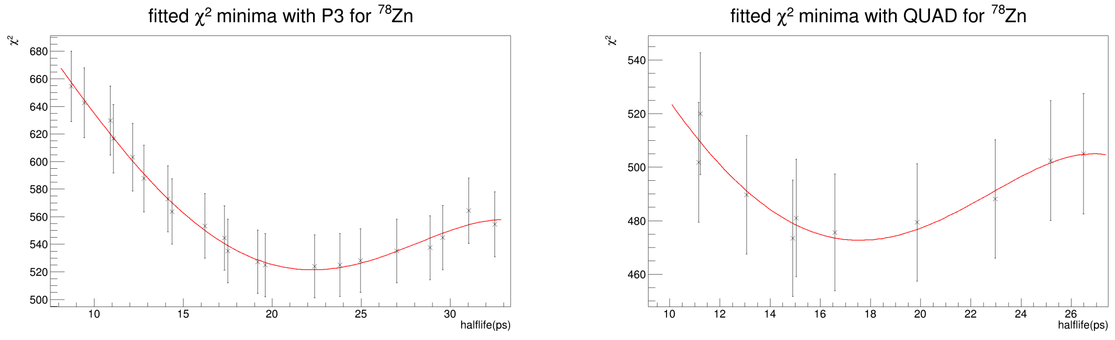

(a)

(b)

Figure 4.13: $\chi^2$ minima as a function of the half-life of the $2^+$ state in $^{78}$Zn with P3 (a) and QUAD (b)

These same steps are used to look for the energy that minimizes the $\chi^2$ for each fixed half-life value, and a graph representing all the minima against their corresponding energies is obtained and fitted to evaluate the final energy value for the decaying state. These graphs are shown in figure 4.14 for Miniball and clovers, and in figure 4.15 for the GRETINA-like detectors. The same conclusions are made on the shapes of the valleys in the neighborhood of ${\chi^2_{min}}^{global}$. No clear minima can be found for the energy with MB and SC, while these minima showed up at 731 keV for P3 and 726 keV for QUAD.

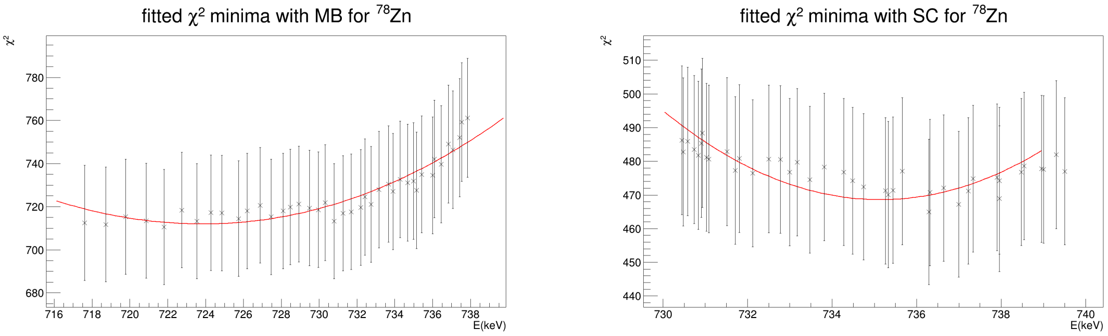

(a) (b)

Figure 4.14: $\chi^2$ minima as a function of the energy of the $2^+$ state in $^{78}$Zn with MB (a) and SC (b)

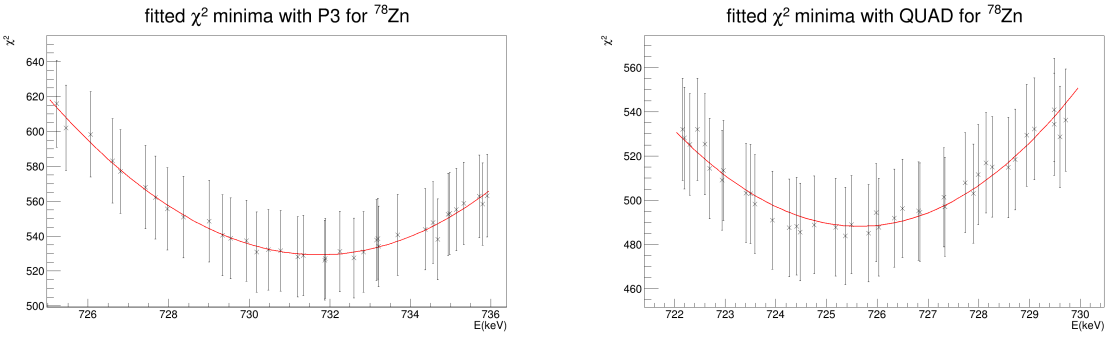

(a) (b)

Figure 4.15: $\chi^2$ minima as a function of the energy of the $2^+$ state in $^{78}$Zn with P3 (a) and QUAD (b)

To evaluate the statistical errors on the lifetimes and energies, only the ranges of half-lives and energies satisfying the following condition are kept:

$$\chi^2 < {\chi^2_{min}}^{global} + 2.3 \tag{4.4}$$

This allows to draw a contour around the minimum and obtain the $1\sigma$-uncertainties in the case of a simultaneous minimisation of the $\chi^2$ for two parameters [81]. These contours are shown with red dots in figure 4.7 for Miniball and clovers, and in figure 4.8 for the tracking detectors. The finally measured energy and lifetime values with their uncertainties are summarized in table 4.3 as obtained with GRETINA-like detectors[8]. As regards Miniball and clovers, we decided to disregard them since their corresponding $\chi^2$ distributions did not show clear minima.

| Detector(s) | Energy(keV) | half-life (ps) |
|---|---|---|
| P3 | $731^{+3}_{-2}$ | $22^{+6}_{-5}$ |
| QUAD | $726^{+2}_{-4}$ | $18^{+8}_{-9}$ |

Table 4.3: Measured energy and half-life of the $^{78}$Zn first excited state with the tracking detectors.

## 4.4 Preliminary conclusions

From the results shown in the previous section, the behavior of the different detectors and the way they can be exploited for the study of the $^{80}\text{Zn}\rightarrow^{79}\text{Cu}$ case can be anticipated. From table 4.3, it can be noticed that the only detector for which both lifetime and energy values coincide with the literature values of 730 keV and 18(4) ps is the P3 cluster. For the QUAD module, the half-life is well reproduced but its energy is lower than the required value. Therefore, for the study of the $^{79}$Cu decay in the next chapter, the QUAD module will be considered for the lifetime only whereas the P3 will be considered for both the energy and the lifetime. With SuperClover detectors, the two-dimensional $\chi^2$ minimization methodology will not be used. Instead, the fitted energy values from their experimental spectra with the procedure illustrated in figure 4.5 will be considered as the measured energy of the decaying states in the rest frame of the $^{79}$Cu nucleus, given their insensitivity to the lifetime effects. The consistency of this energy value obtained with the clovers can be checked with the energy that is determined using the two-dimensional $\chi^2$ minimization procedure with P3. As regards the Miniball detectors, large uncertainties on the energy and half-life measurements are expected with the two-dimensional analysis procedure. For these modules, however, the one-dimensional $\chi^2$ minimization described in section 4.3.1 can be used. In this approach, the validated energy measured by clovers and P3 is fixed, and the $\chi^2$ is minimized to check if the resulting half-life coincides with the one obtained with P3.

---

[8] With P3 and QUAD, if one fixes the energy to the measured value in table 4.3 and searches the half-life for which the $\chi^2$ is minimal, the resulting half-life is the same as the one that is reported in this same table (with a difference that is below 1 ps, which can be attributed to statistical fluctuations). The same agreement is found when fixing the half-life to the value in the table and looking for the corresponding energy.

# 5

# Case of interest

## Contents

In this chapter, we present the results of the procedures that were explained in chapter 3. Firstly, we show the full Doppler corrected $\gamma$ spectrum for each detector group. After that, we compare the outcomes of our $\gamma$-$\gamma$ coincidences with those of the SEASTAR campaign. Finally, we show the results that we obtained from our lifetime determination procedure.

## 5.1 Full Doppler-corrected $\gamma$-ray spectra

The full $\gamma$-ray spectra obtained after applying the add-back and Doppler correction procedures for the $^{80}$Zn($^{9}$Be,X)$^{79}$Cu reaction channel are shown in figure 5.1 for MB and SC, and in figure 5.2 for GRETINA. The separated spectra for the two Miniball rings are displayed in figure 5.3. With all detector groups, one can see the two peaks that were previously identified in the SEASTAR campaign as the 656(5) keV and the 855(6) keV transitions. A wide structure at energies above 2 MeV can also be noticed, but the fast decrease of the detection efficiency prevents us from seeing clear peaks. Another increase of the statistics between 450 keV and 550 keV is visible. These are events corresponding to some Compton-scattered $\gamma$ rays that are Doppler corrected with an angle that is not relevant. Indeed, they can already be seen with the GEANT4 simulation of the main transition at 656 keV, as illustrated in figure 3.29 with Miniball for instance.

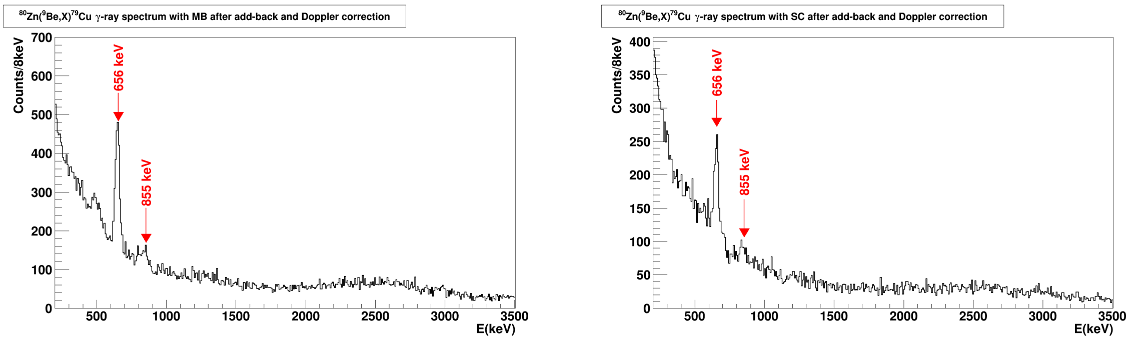

(a) (b)

Figure 5.1: $^{79}$Cu $\gamma$ spectra after add-back and Doppler correction with MB (a) and SC (b)

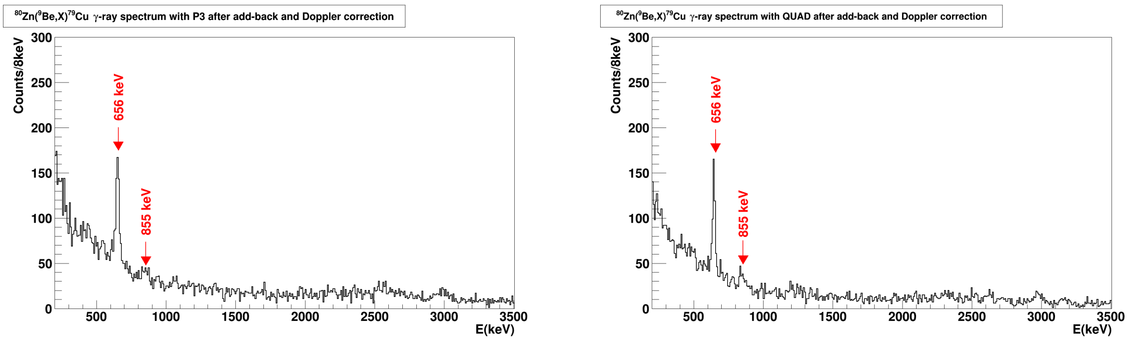

(a) (b)

Figure 5.2: $^{79}$Cu $\gamma$ spectra after add-back and Doppler correction with P3 (a) and QUAD (b)

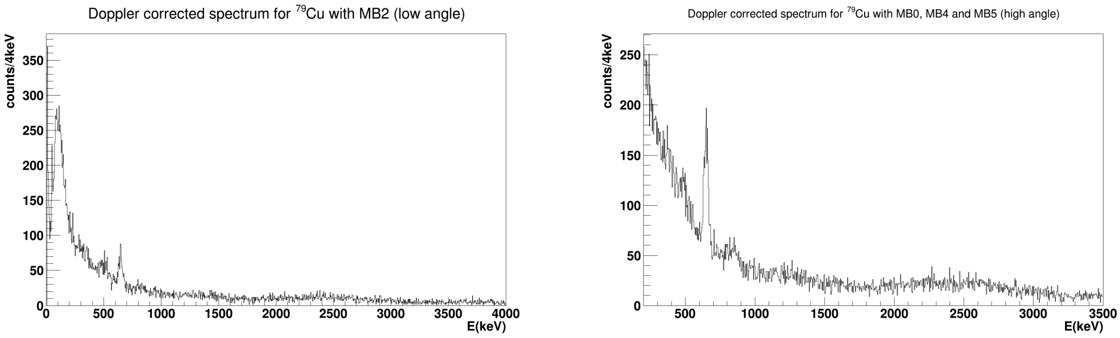

(a) (b)

Figure 5.3: $^{79}$Cu Doppler corrected $\gamma$ spectra with MB2 (a) and MB0, MB4 and MB5 (b)

## 5.2 Energy centroids fitting

As already mentioned, a more precise analysis showed that the shapes and positions of the energy peaks depend on the detector group, since they do not exhibit the same sensitivities to lifetimes. By looking separately at the Doppler corrected spectra for each detector group, and a using a gaussian fit with an exponential background, different mean values are obtained. The results of this fitting process are summarized in table 5.1.

| Detectors | Energy (keV) | Uncertainty (keV) |
|---|---|---|
| All MB | 648 | 1 |
| MB2 | 646 | 2 |
| MB0 MB4 and MB5 | 649 | 1 |
| Clovers | 656 | 2 |
| P3 | 651 | 2 |
| QUAD | 645 | 2 |

Table 5.1: Mean energy values after Doppler correction

## 5.3 $\gamma$-$\gamma$ coincidences

From the full $\gamma$ spectra shown in figure 5.1 and figure 5.2, the most intense visible transition is the 656 keV one. Therefore, we tried to apply the $\gamma$-$\gamma$ coincidences method without background subtraction by setting a gate around this peak. As already mentioned, the energy of this peak depends on the detector of interest. So, we built 4 coincidence spectra (one for Miniball, one for clovers, one for P3 and one for QUAD). For instance, here are the steps for the reconstruction of the coincidence spectrum of Miniball:

- Build a $\gamma$-$\gamma$ matrix where the first axis represents the energy in the Miniball detectors and the other axis is the energy in any detector. The detector of the second axis is labeled "X" where X can refer to all Miniball modules, all clovers, P3 or QUAD. So, there are 4 matrices in total.

- In each matrix, project the full spectrum to obtain the energy in the "X" detector, regardless of the energy in the Miniball. The resulting spectrum shows the energy in the "X" detector.

- In each projected energy spectrum of the "X" detector, look at the shape of the peak around 656 keV to determine the width of the gate to be applied later.

- Get back to the non-projected spectrum and apply each chosen gate condition on each corresponding matrix, by projecting on the first axis (axis of Miniball). This is to obtain 4 Miniball energy spectra. The first one is the coincidence spectrum of Miniball with Miniball, the second one is for Miniball in coincidence with Clovers, the third one is for Miniball in coincidence with P3 and the last one is for the coincidence with QUAD.

- Sum all the 4 resulting Miniball energy spectra into one total spectrum.

Following these steps, the reconstructed energy spectrum in Miniball using gates within all detectors is shown in figure 5.4. As it can be seen, the statistics is not sufficient to be able to retrieve all the transitions obtained in SEASTAR.

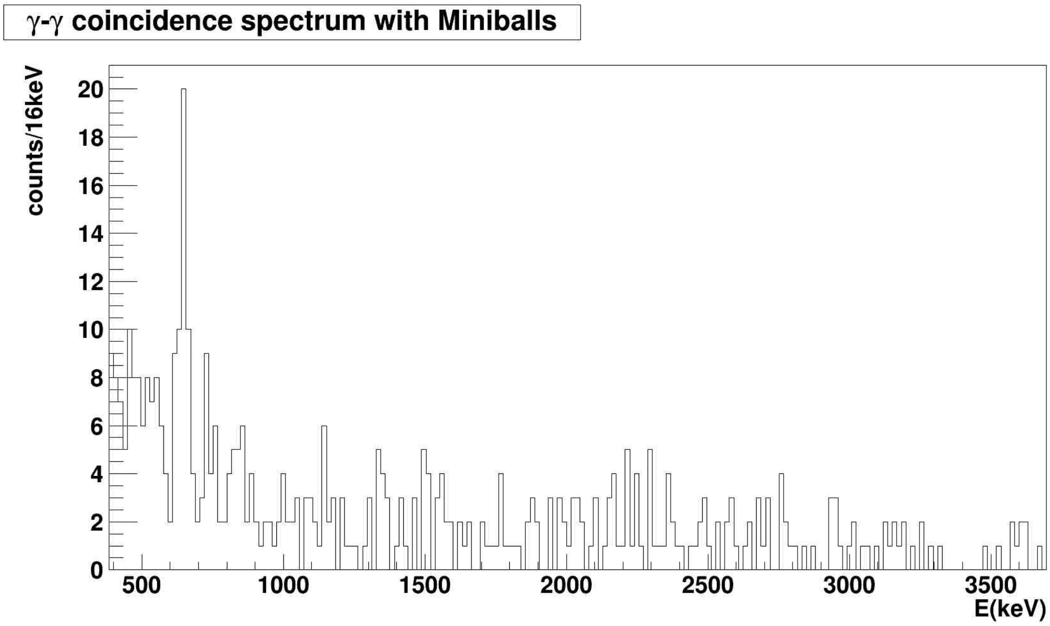

Figure 5.4: $\gamma$-$\gamma$ coincidence spectrum using Miniball detectors (gated on the 656 keV transition).

As it can be noticed from figure 5.1 and figure 5.2, the Miniball detectors have the highest amount of statistics. This is due to their placement at average angles of 40° which allowed them to intercept the Lorentz-boosted $\gamma$ rays, contrary to clovers and tracking detectors which were at more than 60°. However, due to the lack of statistics (as illustrated in figure 5.4), even in Miniball detectors, no $\gamma$-$\gamma$ coincidences could be analyzed in this work. Therefore, the coincidence spectra that were built for the other detectors are even more difficult to exploit for the identification of the transitions than in the case of figure 5.4.

## 5.4 Lifetime measurement of the $(3/2^-)$ state

### 5.4.1 Fitting algorithm

As already mentioned, the transition that was observed in our experiment with the highest amount of statistics is the decay from the $(3/2^-)$ first excited state to the $(5/2^-)$ ground state. Therefore, we employed the procedures explained in the previous chapter to measure the lifetime of this state. As the level schemes of the benchmark

case and our reaction of interest are different, some adjustments were made in the formula of the final simulated response function. Here are the steps we followed to generate each total response function:
- The background components are modeled in the same way as in the previous chapter, with an exponential decay law as in equation 4.1.
- As we also identified the transition at 855 keV from the $(1/2^-)$ state to the $(3/2^-)$, we simulated its response function. Since the statistics we obtained for this peak was significantly low, it is difficult to apply the $\chi^2$ analysis to the decaying state at 1511 keV to determine its lifetime. Instead, we assumed the latter to be zero when simulating the corresponding response function $f_{855}$. To account for the uncertainty on the energy value, an offset $\Delta_{855}$ was added and the final shifted function was multiplied by a scaling factor $S_{855}$ to match with the number of counts in the experimental spectra.
- Finally, the transition of interest is simulated with a choice of energy $E_{sim}$ in the [640 keV : 670 keV] range and a half-life $T_{1/2}$ in the [0 ps : 50 ps] range, with steps of 1 keV and 1 ps, respectively, for the simulation inputs. The obtained response function $f_{E_{sim}}^{T_{1/2}}(E)$ is scaled with a $S_{E_{sim}}^{T_{1/2}}$ coefficient.

The total function employed to fit the experimental $\gamma$ spectra is written as follows:

$$F_{total}(E) = f_{bg}(E) + S_{855} \times f_{855}(E - \Delta_{855}) + S_{E_{sim}}^{T_{1/2}} \times f_{E_{sim}}^{T_{1/2}}(E) \qquad (5.1)$$

In this fashion, when the two simulation inputs $E_{sim}$ and $T_{1/2}$ are chosen, there are 5 parameters that are fitted[1]. An example of this fitting procedure with the QUAD detector is illustrated in figure 5.5 for a choice of $E_{sim} = 649$ keV and $T_{1/2} = 13$ ps in the simulation[2]. Similarly to the $^{78}$Zn case, the energy interval where the total response function was employed to fit the experimental $\gamma$ spectra is chosen as the one leading to the lowest value of $\chi^2_{ndf}$. These intervals are summarized in table 5.2.

---

[1] These 5 parameters of the total fitting function are the $S_{855}$ and $S_{E_{sim}}^{T_{1/2}}$ scaling factors, the $\Delta_{855}$ offset and the $A$ and $B$ coefficients of the exponential background.

[2] Each simulation was run with $10^6$ events

| Detector(s) | Energy(keV) |
|---|---|
| All MB | [390:1150] |
| MB2 (low angle) | [390:1150] |
| MB0, MB4 and MB5 (high angle) | [390:1150] |
| SC | [330:950] |
| P3 | [290:1050] |
| QUAD | [290:1150] |

Table 5.2: Summary of the energy intervals where the total response functions in equation 5.1 were used to fit the experimental $^{79}$Cu $\gamma$ spectra, for the different detector groups.

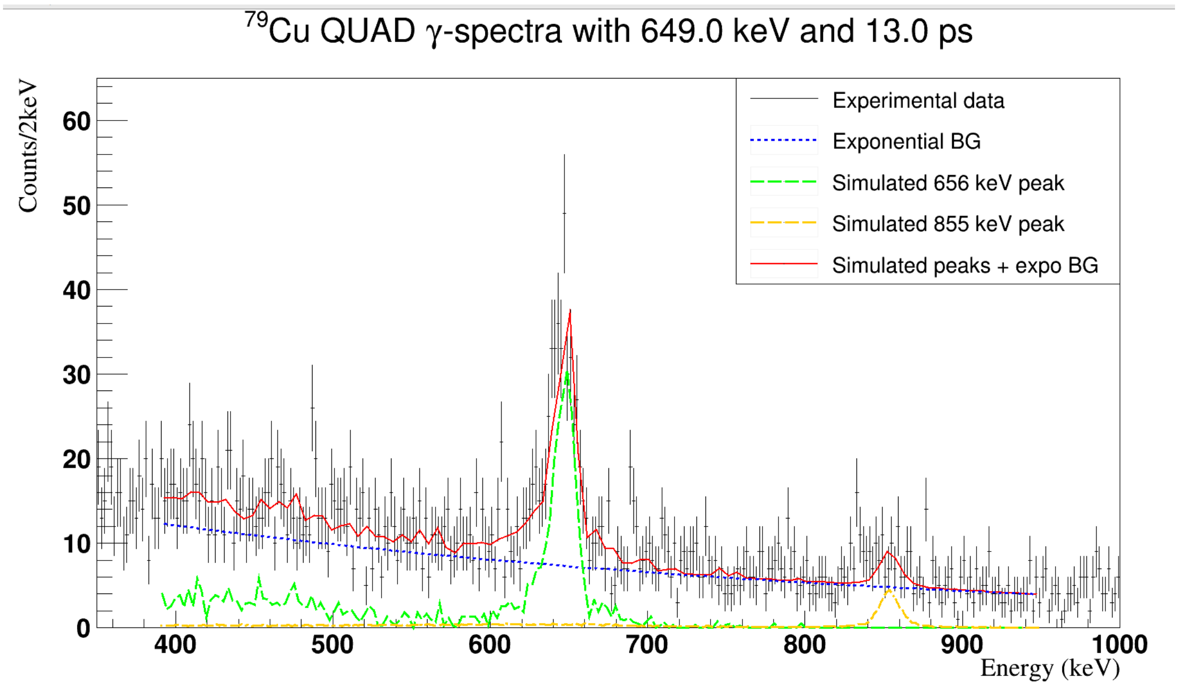

Figure 5.5: Example of the $\gamma$ spectrum obtained with QUAD, fitted with the total response function to evaluate the $\chi^2$

### 5.4.2 Results

The $\chi^2$ surfaces obtained with the different detector groups are represented in figure 5.6 for Miniball and clovers, and in figure 5.7 for the tracking detectors. The separated distributions for the Miniball angular groups are illustrated in figure 5.8. As already mentioned in the previous chapter, the uncertainties on the lifetimes and energies obtained with Miniball and clovers are larger than with GRETINA. These uncertainties are the worst in the case of SuperClovers, as it can be seen in figure 5.6b, where the valley of the minimal $\chi^2$ values goes beyond the range of the two-dimensional histogram, and the contour in red color does not close. This leads to upper limits that are higher than 670 keV for the energy and 34 ps for the half-life. Furthermore, the graph representing the $\chi^2$ minima as a function of the half-life for each fixed energy does not show a minimum. This can be seen in figure 5.9b, where the distribution is flat. The same behavior is noticed for the energy as illustrated in figure 5.11b. Therefore, the two-dimensional $\chi^2$ analysis is not considered for these detectors, as expected from the conclusions in section 4.4. In the case of Miniball, the contour limits were found in the [0 ps : 12 ps] range for the half-life and [648 keV : 657 keV] for the energy. Again, the lower limit for the energy (correlated to a zero lifetime) is nothing but the central position of the $\gamma$ peak in table 5.1. A similar conclusion is made when looking at the different Miniball rings. The lower limit for the energy found with the low angle MB2 was at 645 keV, while this value was found at 648 keV for the higher angle MB clusters (MB0, MB4 and MB5). These limits do indeed correspond to the values in table 5.1. With P3, the contour obtained with equation 4.4 leads to the accepted ranges of [7 ps : 24 ps] for the half-life and [653 keV : 659 keV] for the energy, as depicted in figure 5.7a. As regards the determination of the final values, these were found at 656 keV (from the graph in figure 5.12a) and 15 ps (from the graph in figure 5.10a). Finally, using the QUAD module, the contour in the 2D-surface delimits the ranges of [646 keV : 651 keV] and [3 ps : 18 ps], as it can be seen in figure 5.7b. The optimal energy was found at 648 keV (from the fit of the graph in figure 5.12b) and 10 ps for $T_{1/2}$ (from the graph in figure 5.10b). All these measured values with GRETINA-like detectors and their uncertainties are summarized in table 5.3.

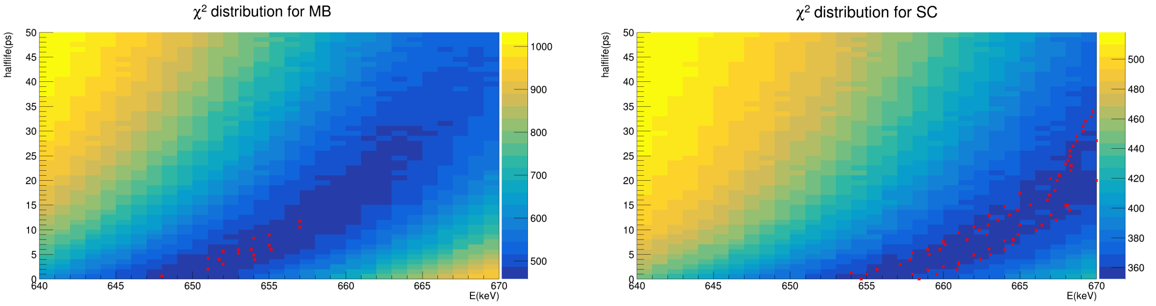

(a) (b)

Figure 5.6: $\chi^2$ distributions as a function of the energy and the half-life of the $(3/2^-)$ state in $^{79}$Cu with MB (a) and SC (b). The red dots show the limits found with the condition in equation 4.4

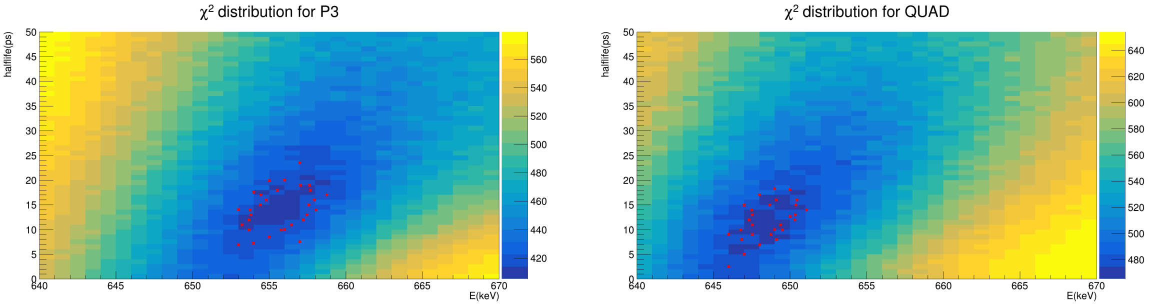

(a) (b)

Figure 5.7: $\chi^2$ distributions as a function of the energy and the half-life of the $(3/2^-)$ state in $^{79}$Cu with P3 (a) and QUAD (b). The red dots show the limits found with the condition in equation 4.4

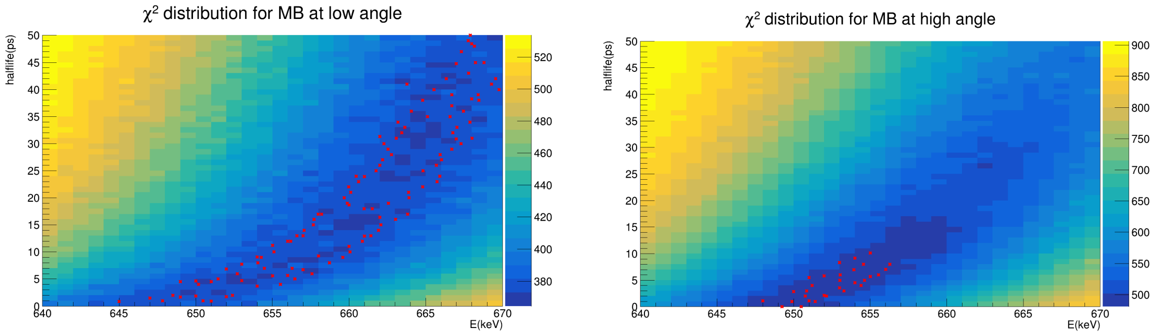

(a)

(b)

Figure 5.8: $\chi^2$ distributions as a function of the energy and the half-life of the $(3/2^-)$ state in $^{79}$Cu with low angle MB (a) and high angle MB (b). The red dots show the limits found with the condition in equation 4.4

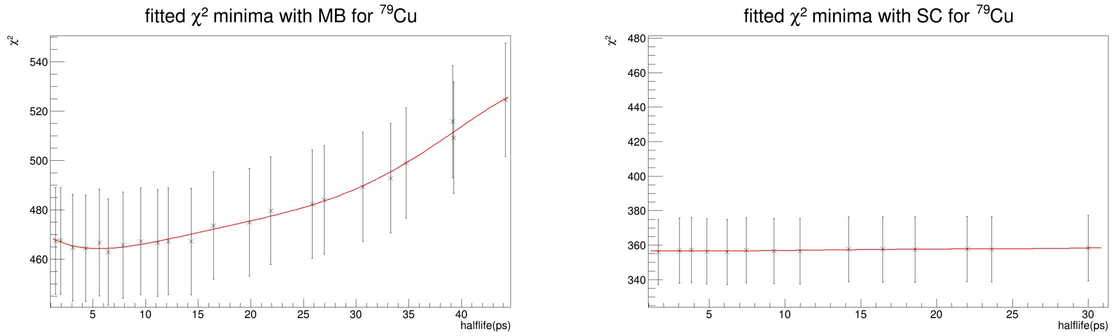

(a)

(b)

Figure 5.9: $\chi^2$ minima as a function of the half-life of the $(3/2^-)$ state in $^{79}$Cu with MB (a) and SC (b)

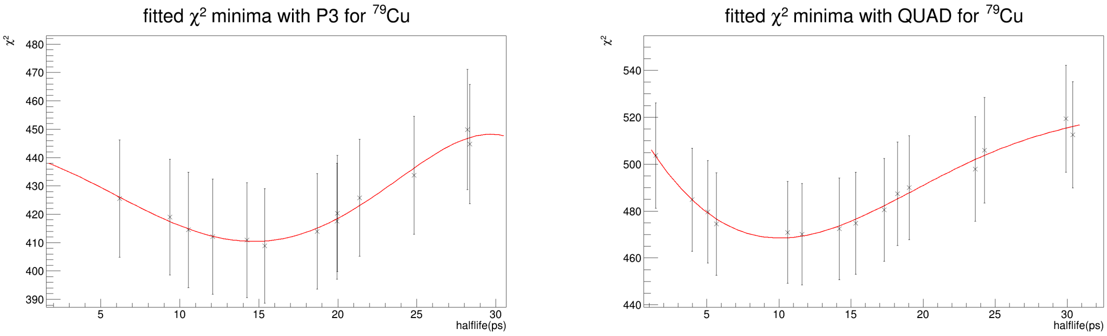

(a)

(b)

Figure 5.10: $\chi^2$ minima as a function of the half-life of the $(3/2^-)$ state in $^{79}$Cu with P3 (a) and QUAD (b)

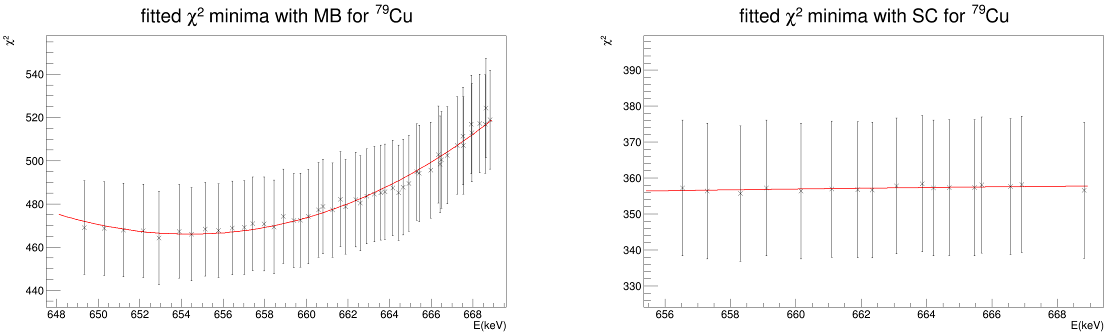

(a)

(b)

Figure 5.11: $\chi^2$ minima as a function of the energy of the $(3/2^-)$ state in $^{79}$Cu with MB (a) and SC (b)

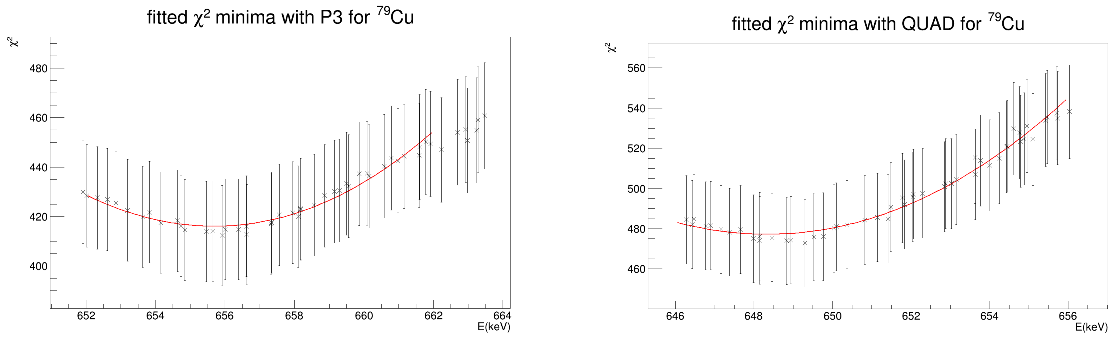

(a)

(b)

Figure 5.12: $\chi^2$ minima as a function of the energy of the $(3/2^-)$ state in $^{79}$Cu with P3 (a) and QUAD (b)

| Detector(s) | Energy(keV) | half-life (ps) |
|---|---|---|
| P3 | $656^{+3}_{-3}$ | $15^{+9}_{-8}$ |
| QUAD | $648^{+3}_{-2}$ | $10^{+8}_{-7}$ |

Table 5.3: Measured energy and half-life of the $^{79}$Cu first excited state with the tracking detectors.

### 5.4.3 Discussion of the differences in the results between the detectors

As seen from table 5.3, the lifetimes measured by QUAD and P3 modules are $1\sigma$-compatible but with a large relative difference of about 30%. Furthermore, the discrepancy between the final energy values is worse since they are not $1\sigma$-compatible. To address this issue, we slightly modified the fitting algorithm to check if the final results can be impacted. The validity of the $\chi^2$ minimization procedure depends on the range of energies and response function that are chosen for the fitting of the $\gamma$ spectra. In the previous discussion, only the absolute $\chi^2$ value was considered. However, it is possible to evaluate the agreement between the data and the simulation using an equivalent parameter which is the reduced $\chi^2$, i.e. the $\chi^2$ divided by the number of degrees of freedom. This is particularly useful when different modeling functions or different fit ranges are used. If the interval of the fit is too large, the $\gamma$ spectrum will include additional peaks such as the one at 855 keV which has less counts, which make more difficult the convergence of the fitting process. Particularly, the lifetime of the latter was assumed to be zero. If it turned out that its half-life was significant, the shape of its full-energy peak would not be correctly represented, leading to a distortion of the $\chi^2$ indicator that would become less relevant.

To overcome this problem, we fitted the $\gamma$ spectra in a more restricted range around the peak of interest, between 200 keV and 800 keV, thus excluding the 855 keV peak. The final formula of the total response function[3] is written as follows:

$$F_{total}(E) = f_{bg}(E) + S^{T_{1/2}}_{E_{sim}} \times f^{T_{1/2}}_{E_{sim}}(E) \qquad (5.2)$$

An example of a $\gamma$ spectrum fitted using this function is shown in figure 5.13 for the QUAD detector with a choice of $E_{sim} = 649$ keV and $T_{1/2}$= 11 ps. The final energy intervals in which the $\gamma$-ray spectra wre fitted are summarized in table 5.4.

| Detector(s) | Energy(keV) |
|---|---|
| All MB | [290:700] |
| MB2 (low angle) | [290:700] |
| MB0, MB4 and MB5 (high angle) | [290:700] |
| SC | [330:740] |
| P3 | [290:740] |
| QUAD | [390:800] |

Table 5.4: Summary of the energy intervals where the total response functions in equation 5.2 were used to fit the experimental $^{79}$Cu $\gamma$ spectra, for the different detector groups, when the 855 keV peak was excluded.

---

[3] In this fashion, when $E_{sim}$ and $T_{1/2}$ are imposed as the inputs in the simulation, in each fitting process, only 3 parameters are adjusted, which are $A$ and $B$ of the exponential background and $\mathrm{S}^{T_{1/2}}_{E_{sim}}$.

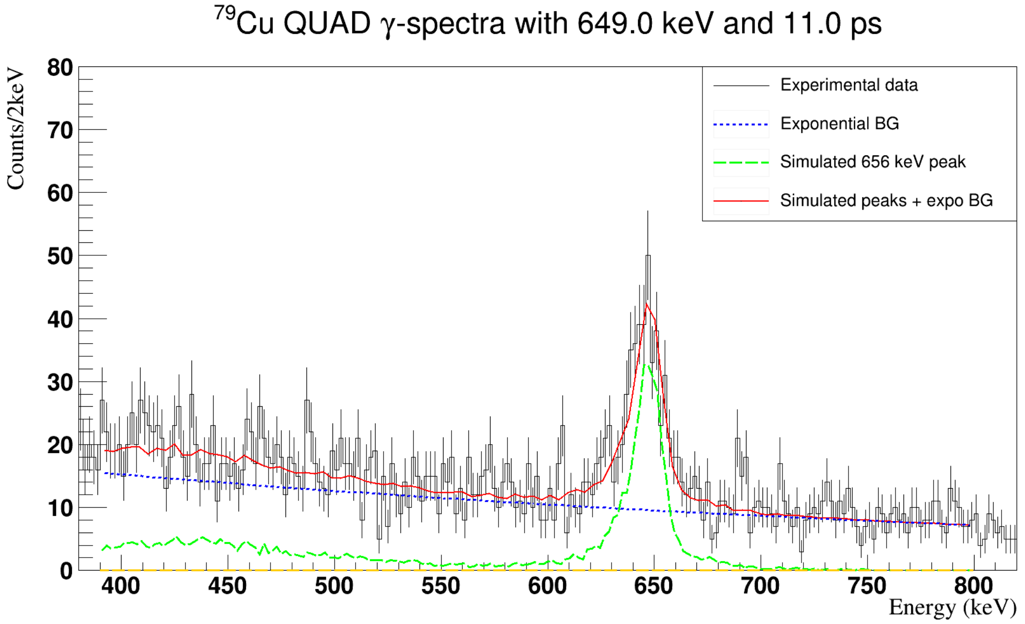

Figure 5.13: Example of the $\gamma$ spectrum obtained with QUAD, fitted with the total response function to evaluate the $\chi^2$. The energy range of the fit does not include 855 keV transition.

The two-dimensional $\chi^2$ analysis was repeated and the resulting 2D-surfaces are shown in figure 5.14 for Miniball and clovers, and in figure 5.15 for GRETINA-like modules. To evaluate the improvement of the agreement between the experimental and simulated $\gamma$ spectra, the minimal reduced $\chi^2$ values obtained with and without including the 855 keV transition in the fitting process are summarized in table 5.5. In the latter, it can be noticed that the reduced $\chi^2$ values are smaller when the transition at 855 keV is not taken into account. Furthermore, the final energy and half-life measurements obtained with P3 and QUAD from the two-dimensional analysis got closer. These values are summarized in table 5.6.

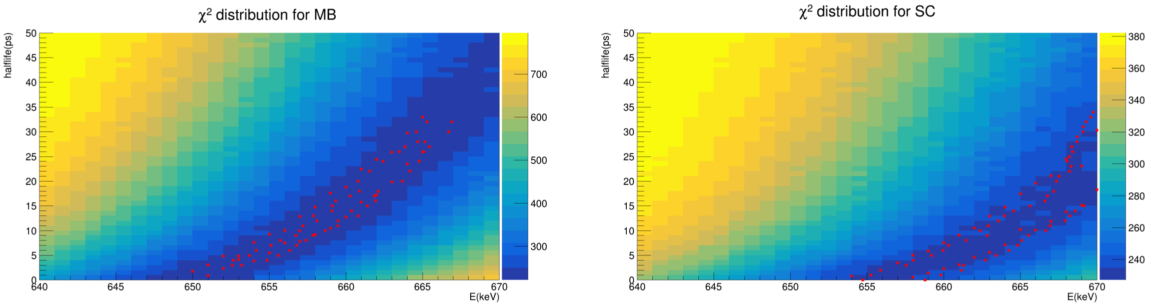
$\chi^2$ distribution for MB

$\chi^2$ distribution for SC

(a)

(b)

Figure 5.14: $\chi^2$ distributions as a function of the energy and the half-life of the $(3/2^-)$ state in $^{79}$Cu with MB (a) and SC (b), when the 855 keV transition is not included in the fitting process. The red dots show the limits found with the condition in equation 4.4

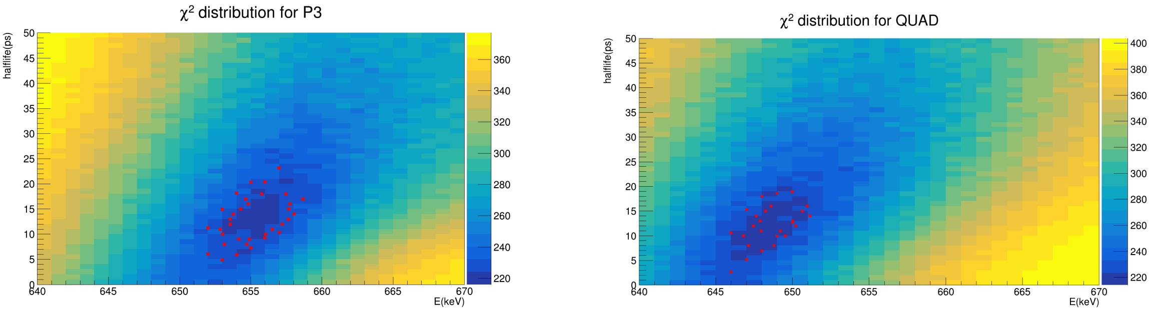
$\chi^2$ distribution for P3

$\chi^2$ distribution for QUAD

(a)

(b)

Figure 5.15: $\chi^2$ distributions as a function of the energy and the half-life of the $(3/2^-)$ state in $^{79}$Cu with P3 (a) and QUAD (b), when the 855 keV transition is not included in the fitting process. The red dots show the limits found with the condition in equation 4.4

| Detector(s) | Large fit range | Restricted fit range |
|---|---|---|
| MB | 1.22 | 1.07 |
| SC | 1.16 | 1.12 |
| P3 | 1.08 | 0.96 |
| QUAD | 1.09 | 1.05 |

Table 5.5: Summary of the minimal reduced $\chi^2$ values obtained with and without including the 855 keV transition in the fitting process.

| Detector(s) | Energy(keV) | half-life (ps) |
|---|---|---|
| P3 | $655^{+4}_{-3}$ | $14^{+9}_{-9}$ |
| QUAD | $649^{+2}_{-3}$ | $11^{+8}_{-8}$ |

Table 5.6: Measured energy and half-life of the $^{79}$Cu first excited state with the tracking detectors, when the 855 keV transition is excluded from the fitting process.

Even with this better agreement, the energy values are still not $1\sigma$-compatible. We therefore tried to improve the quality of the P3 result. As previously mentioned in section 2.3, there was an issue with the signal analysis of one of its crystals (CRYST1). Consequently, we repeated the lifetime analysis when this crystal is not taken into account. The corresponding 2D-surface is shown in figure 5.16. The results of the new measurements are written in table 5.7. This time, both the energy and the half-life are $1\sigma$-compatible, and the relative difference in lifetimes is less than 10%.

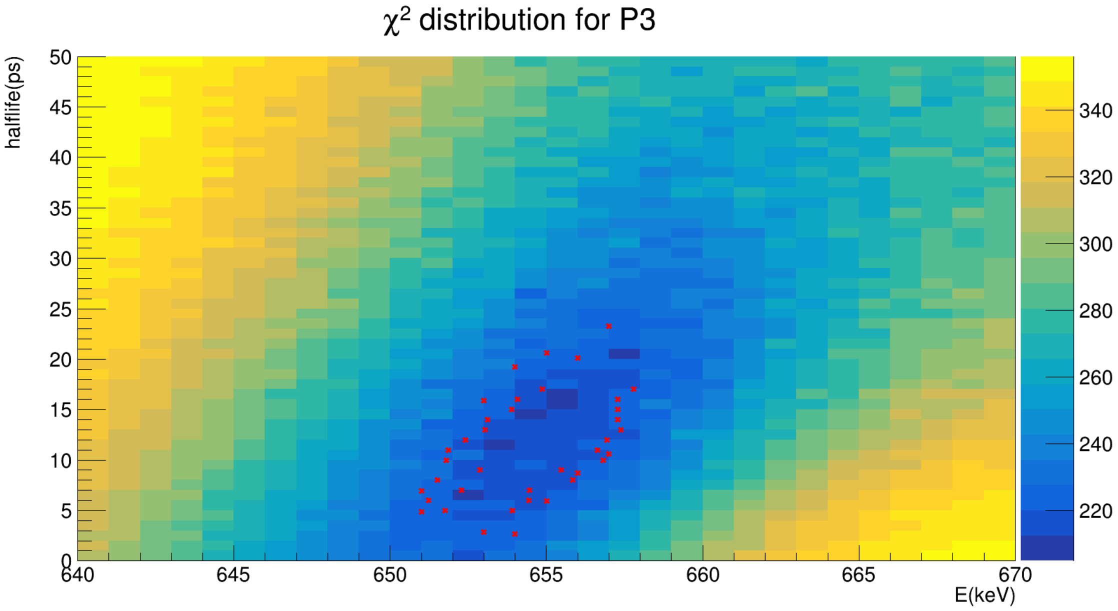

Figure 5.16: $\chi^2$ distribution as a function of the energy and the half-life of the $(3/2^-)$ state in $^{79}$Cu with P3 when both the 855 keV transition and CRYST1 are not included. The red dots show the limits found with the condition in equation 4.4

| Detector(s) | Energy(keV) | half-life (ps) |
|---|---|---|
| P3 (without CRYST1) | $654^{+4}_{-3}$ | $12^{+11}_{-9}$ |
| QUAD | $649^{+2}_{-3}$ | $11^{+8}_{-8}$ |

Table 5.7: Measured energy and half-life of the $^{79}$Cu first excited state with the tracking detectors, when the 855 keV transition is excluded from the fitting process. The result for P3 is obtained when its second crystal was removed.

In order to double check if the removal of the mentioned crystal is justified, we also repeated the analysis of the $^{78}$Zn benchmark case. Previously (see table 4.3), a value of $T_{1/2} = 22^{+6}_{-5}$ ps was measured with P3. This time, when we removed the defective crystal, we ended up with a value of $T_{1/2} = 20^{+7}_{-7}$ ps, as it can be seen with the contour in figure 5.17 and the one-dimensional $\chi^2$ distribution as a function of the half-life in figure 5.18. This is closer to the value obtained with QUAD, which was $T_{1/2} = 18^{+8}_{-9}$ ps and which equals the literature value. As regards the energy, the new value of $731^{+3}_{-3}$ obtained from figure 5.19, does not differ from the one in table 4.3, if one forgets about the slight difference in the errors. Table 5.8 summarizes all the measurements with the tracking detectors. Since a better agreement between P3, QUAD and the literature is found for $^{78}$Zn, when the specific crystal is removed, the hypothesis that its removal leads to better results also in copper is strengthened. Therefore, the results we obtained for $^{79}$Cu when CRYST1 of P3 is excluded are the ones that are taken into account[4], discussed and compared with theoretical calculations in the next chapter.

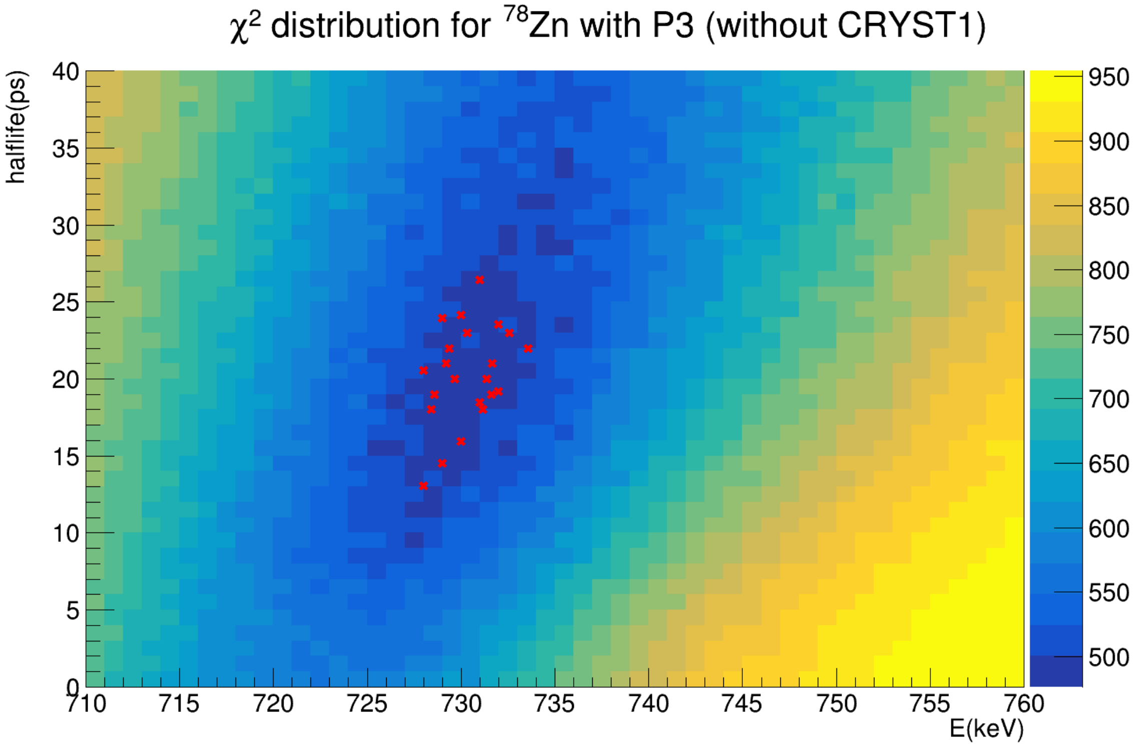

Figure 5.17: $\chi^2$ distribution as a function of the energy and the half-life of the $2^+$ state in $^{78}$Zn with P3 when CRYST1 is excluded. The red dots show the limits found with the condition in equation 4.4

---

[4] In the next chapter, the $12^{+11}_{-9}$ ps half-life obtained with P3 when the deficient crystal is excluded is used to calculate the reduced transition probabilities. Although an agreement within less than 10% is found for the lifetimes between QUAD and P3, the energy values measured with the former for both $^{79}$Cu and $^{78}$Zn are rather low. This hints that there is still some possible non-trivial issue with this module. Since for P3, both energy and lifetime agree with the literature for the $^{78}$Zn case, we took only the half-life provided by this detector for $^{79}$Cu, even if the difference with QUAD is below 10%.

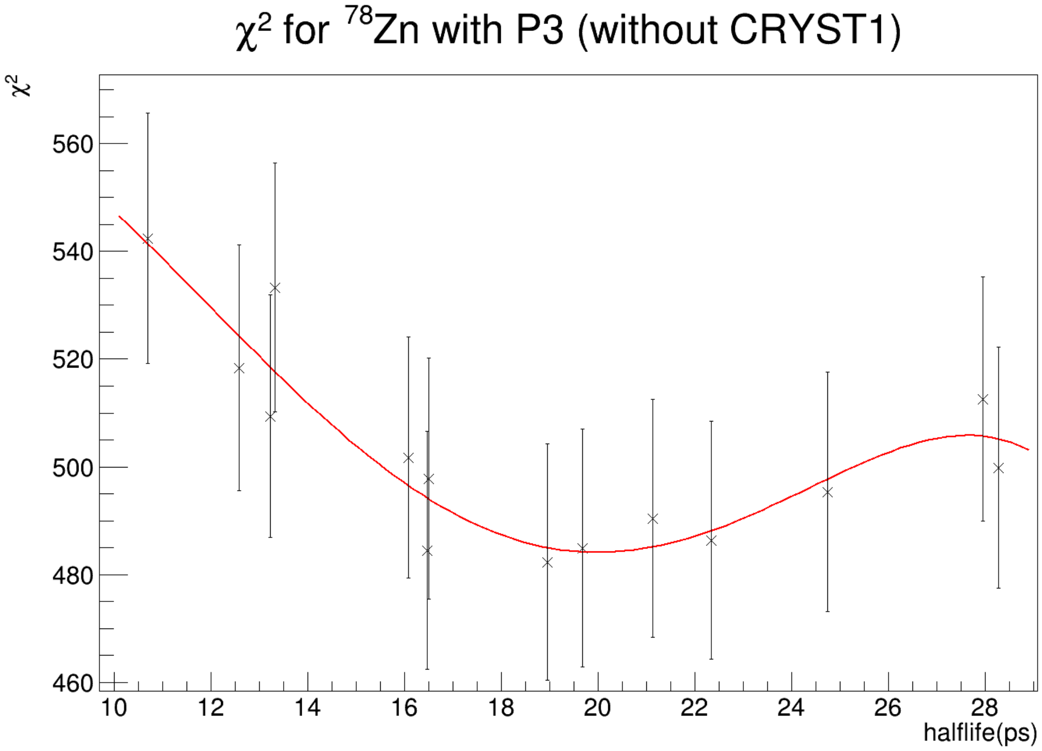

Figure 5.18: $\chi^2$ distribution as a function the half-life of the $2^+$ state in $^{78}$Zn with P3 when CRYST1 is excluded.

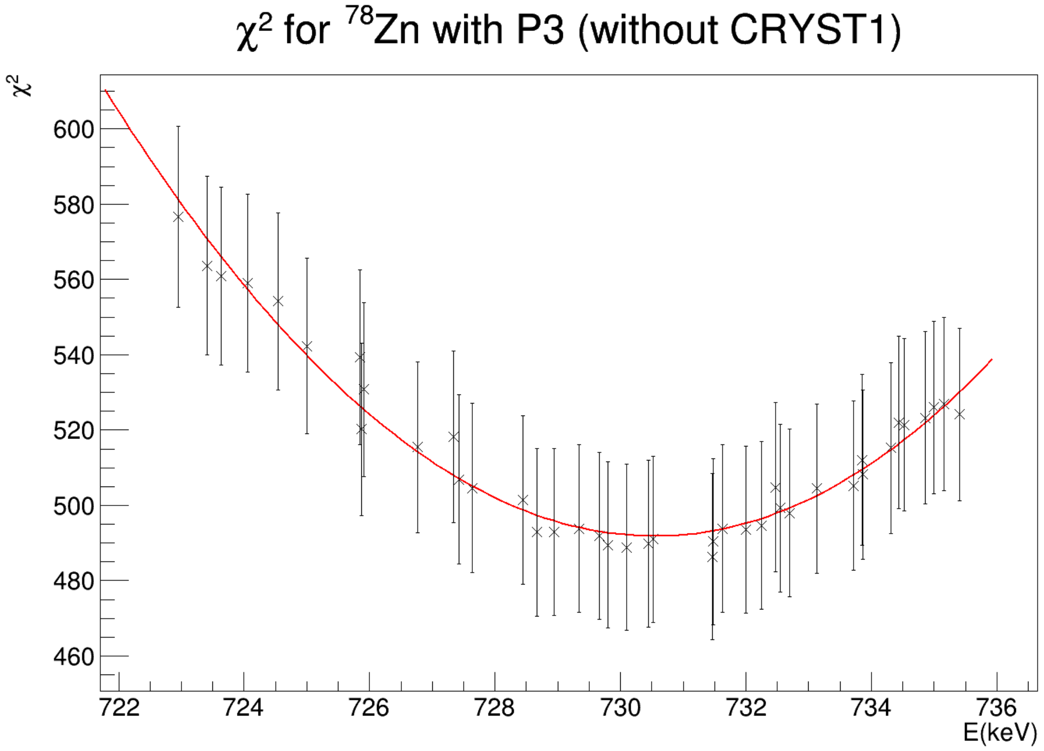

Figure 5.19: $\chi^2$ distribution as a function the energy of the $2^+$ state in $^{78}$Zn with P3 when CRYST1 is excluded.

| Detector(s) | Energy(keV) | half-life (ps) |
|---|---|---|
| P3 | $731^{+3}_{-2}$ | $22^{+6}_{-5}$ |
| P3 (without CRYST1) | $731^{+3}_{-3}$ | $20^{+7}_{-7}$ |
| QUAD | $726^{+2}_{-4}$ | $18^{+8}_{-9}$ |

Table 5.8: Measured energy and half-life of the $^{78}$Zn first excited state with the tracking detectors.

## 5.5 Limits of the analysis

In summary, the methodology we established for the lifetime determination was tested on the $^{78}$Zn benchmark case and allowed us to retrieve a good enough agreement with the literature. This procedure was then applied for our $^{79}$Cu case of interest. Although this technique was reasonably successful, it is still worth to remind of and summarize its main weak points and the possible improvements that can be made.

- When the $2^+$ state in $^{78}$Zn was studied, the lifetimes of the states above the latter were neglected. A non-zero lifetime could affect the results and impact the effective lifetime of the $2^+$ level. A more rigorous analysis would require to first determine the half-lives of the $(4^+)$ and $(6^+)$ states above and fix them in the level scheme. One of the main difficulties arises from the fact that the $(4^+)\rightarrow 2^+$ and the $(6^+)\rightarrow(4^+)$ transitions, at 890 keV and 908 keV, respectively, are not resolved in our experimental spectra. This makes more difficult the evaluation of their respective weights in the total spectrum.

- In the $\chi^2$ analysis, due to the low statistics, there is an ambiguity in the choice of the value for ${\chi^2_{min}}^{global}$ when looking for the contours using equation 4.4. In each two-dimensional plot, there were two possible values. The first one is the minimum obtained by fitting the one-dimensional $\chi^2$ distribution as a function of the energy, while the second one is obtained as the minimum in the one-dimensional $\chi^2$ distribution as a function of the half-life. In general, these two possible values are different. In order to get results that are inclusive, we systematically chose the highest values. This leads to larger uncertainties but is more likely to include the correct lifetimes and energies. One possible way to overcome this issue is to increase the number of events in the simulation to generate more representative response functions. This, however rapidly increases the required computation time and the disk space, and we are also limited by the low statistics in the experimental $\gamma$ spectra. Another possibility is to utilize the "Smooth" method provided by ROOT. This modifies the bin contents of the histogram by averaging each bin's content with its neighboring bins' contents. This process reduces statistical fluctuations and makes the histogram appear less noisy, providing a smoother representation of the underlying data. However, this method biases the results since it modifies the measurements in an uncontrolled way.

- Also in the case of $^{79}$Cu, the lifetime of the $(1/2^-)$ state at 1511 keV that decays to the $(3/2^-)$ first excited level at 656 keV by emitting a 855 keV $\gamma$ ray was neglected. If this half-life was significant (a few tens to a few hundreds of picoseconds), it would affect the effective lifetime of the 656 keV state. For a more complete analysis, it would be necessary to first determine the half-life of the 1511 keV level and fix it before analyzing the first excited state. The main difficulty with this procedure is the much lower statistics of the 855 keV transition in our experimental spectra.
- Other parameters in the simulation were not entirely fixed to the right value. One of the most important parameters is the resolution on the position of $\gamma$-ray hits in the tracking detectors. In all this work, the adopted value was 2.35 mm (FWHM) and might be underestimated with respect to the real value. If a larger value is used in the simulation, the resulting response functions get larger widths for the Doppler-corrected $\gamma$-ray energy peaks. In this fashion, the obtained lifetimes are also shortened. For instance, some preliminary calculations using the double of the adopted resolution for the P3 module showed a decrease of the half-life by $\approx$ 25% for the first excited state in $^{79}$Cu. The optimal position resolution can be determined by varying it until finding the value that leads to the overall lowest $\chi^2_{ndf}$.

# 6

# Discussion and interpretation

## Contents

As mentioned in the end of the introduction chapter, the lifetimes of the excited states can be related to the reduced transition probabilities to shed light on the collectivity of the transitions of interest. In $^{79}$Cu, we measured the half-life of the deexcitation from the $(3/2^-)$ state to the $(5/2^-)$ ground state. From the parity and angular momentum conservation rules highlighted in section 1.3.2, the allowed multipolarity for the $\gamma$ photon is either even-electric ($E2$, $E4$, $E6$ ...) or odd-magnetic ($M1$, $M3$, $M5$ ...). Due to the higher probability of the lower multipolarities, only $M1$ (magnetic dipole) and $E2$ (electric quadrupole) are to be considered.

With an assumption of a single-particle transition between pure states, the initial level is described by the valence proton in the $\pi p_{3/2}$ orbit, meaning that $J_i = L_i + S_i$ $= 1 + 1/2 = 3/2$. Similarly, the final state is described by the same proton occupying the $\pi f_{5/2}$ level with $J_f = L_f + S_f$ $=$ 3 - 1/2 $=$ 5/2. Therefore, such a decay consists in a change of orbital angular momentum $\Delta L = L_f - L_i = 3 - 1 = 2$ and a spin flip $\Delta S = S_f - S_i = (-1/2) - (1/2) = -1$, the magnetic dipole operator being responsible for this spin inversion. In principle, a decay of $M1$ type is $L$-forbidden since it only induces a change in the spin and does not act on the orbital angular momentum. This means that the only allowed final state is the one in which $L$ is unchanged. This corresponds to a proton in a $\pi p_{1/2}$ orbital. However, $M1$ transitions have been observed in different cases where not only the spin changes but also the orbital angular momentum. This anomaly is either explained by an incomplete description of the magnetic dipole moment operator, where the addition of some terms could allow the change in $L$, or by the fact that the states are not pure and configuration mixing is present. The first hypothesis was discussed since the 1950s and was not successful to explain the observed transitions in medium and heavy nuclei [82, 83] . We, therefore, favor the second assumption.

The $B(M1)$ and $B(E2)$ systematics for neutron-rich copper isotopes as well as for other isotopic/isotonic chains are discussed in the next sections, for comparison. More particularly, we focus on the transitions involving a change of total angular momentum $\Delta J = 1$ as for the transition in $^{79}$Cu. But before that, we start by evaluating the Weisskopf single particle estimates for the reduced transition probabilities, by supposing either pure $E2$ or pure $M1$ transitions.

- For the case of a pure $E2$ hypothesis, putting an excitation energy of 656 keV, in equation 1.19, results in a half-life of 231 ps (lifetime of 333 ps), which is a few orders of magnitude higher than the measured value. This suggests the presence of an $M1$ component for the transition.
- For the case of a pure $M1$ hypothesis, the calculation results in a half-life of 79 fs (lifetime of 114 fs), which is a few orders of magnitude less than the measured

value.

From these two calculations, one can estimate the contribution for each component with the following relation:

$$\lambda_{tot} = a\lambda_{E2} + b\lambda_{M1} \tag{6.1}$$

where $\lambda_{tot}$ is the total transition rate corresponding to the measured half-life of 12 ps, while $a$ and $b$, are the weights of $E2$ and $M1$ components, respectively. Such a calculation leads to $a = 99.4\%$ and $b = 0.6\%$, meaning that the transition is to a larger extent likely to be of an electric quadrupole nature. However, with a small $M1$ contribution, it is enough to accelerate the transition and reduce the lifetime. This question about the competition between $E2$ and $M1$ contributions is discussed in the next paragraph.

## 6.1 Systematics of B(E2) and B(M1) in odd-A copper isotopes

As already detailed in section 1.5.1, the addition of neutrons above the $N = 40$ subshell lowers the energy of the first $5/2^-$ excited state with respect to the $3/2^-$ ground state, until the spins of these states are inverted at and above $N = 46$. Here, we are interested in the transition rates between these two states, through the measured reduced transition probabilities $B(E2)$ and $B(M1)$. Starting with $^{69}$Cu, the collective properties of its low-lying levels were investigated in the Coulomb excitation experiment at REX-ISOLDE [84]. The measurement led to a $B(E2; 5/2^- \rightarrow 3/2^-_{gs})$ value of 3.0(3) W.u., which is much smaller than those of lighter copper isotopes ($N < 40$) which are more than 10 W.u. [84, 85]. This small $B(E2)$ value suggested a single-particle character for the $5/2^-$ level. In the same experiment, $^{71}$Cu and $^{73}$Cu isotopes were also produced and their $B(E2)$ values were found at 3.9(5) W.u. and 4.4(5) W.u., respectively, thus slightly increasing the collectivity with the filling of the $\nu g_{9/2}$ orbital. After that, in $^{75}$Cu, where the ground state inversion occurs, the lifetime measurement performed at GANIL for the two nearly degenerate first $3/2^-$ and $1/2^-$ excited isomeric states allowed to deduce two possible $B(E2)$ values[1] (16.4(6) W.u. and 22.5(8) W.u.) for both $3/2^- \rightarrow 5/2^-_{gs}$ and $1/2^- \rightarrow 5/2^-_{gs}$ transitions [46]. Although these values are

---

[1] From that experiment in GANIL, two possible scenarios were suggested for the level scheme of $^{75}$Cu. In both cases, the ground state was the same ($5/2^-$), but the order between the $3/2^-$ and $1/2^-$ excited states was different. Later on, a magnetic moment measurement at RIKEN [86] allowed to firmly confirm one of the two possible scenarios (the one leading to a value of 16.4(6) W.u.).

much larger than those of $^{69}$Cu, $^{71}$Cu and $^{73}$Cu, the authors concluded that collective and single-particle properties of the excited states of $^{75}$Cu were similar to those in the three lighter isotopes. The isomerism which is there for $^{75}$Cu and absent for the other isotopes was attributed to the small energy differences between the $(1/2^-)$, $(3/2^-)$ and $(5/2^-)$ levels. Furthermore, these $B(E2)$ values were calculated assuming a pure $E2$ multipolarity for the transition. A non-known non-zero $M1$ component would decrease the real $B(E2)$ values. This means that the adopted 16.4(6) W.u. has to be seen as an upper limit. In that work, the authors also theoretically evaluated the transition rates that can be obtained with different interactions [87]. The best agreement between the measured lifetime and the theoretical predictions was found for a mixing ratio $\delta \approx 0.47$. With this choice, the value of $B(E2)$ falls to $\approx 3.3$ W.u. In this fashion, one can preserve the single-particle nature of the states in $^{75}$Cu. The general effect of the mixing ratio on the transition rates and its link with collectivity will be discussed in section 6.5. All the excitation energies and spin configurations as well as the methods used to determine $B(E2)$ rates are summarized in table 6.1, while the total systematics of $B(E2)$ values for copper odd-A isotopes is depicted in figure 6.1. In this graph, the systematics of $B(M1)$ is also illustrated, where the values were multiplied by a factor of 3000 for clarity purposes. All these $B(M1)$ values were deduced from the lifetimes of the decaying states, assuming pure $M1$ transitions. These lifetimes were either taken from direct measurements ($^{75}$Cu and $^{79}$Cu) or deduced from $B(E2)$ values (all the other isotopes). From the observed trend, one can expect a decrease beyond the mid-shell for $N > 46$ with a smaller value in $^{77}$Cu, before reaching a minimum at $N = 50$, like in the case of the sub-shell closure at $N = 40$. However, from the $12^{+11}_{-9}$ ps half-life obtained for $^{79}$Cu, the deduced values are found at $19^{+58}_{-9}$ W.u. and $0.0065^{+0.0194}_{-0.0031}$ W.u. for $B(E2)$ and $B(M1)$, respectively, thus showing an increase of $B(E2)$ at $N = 50$, contrary to $^{69}$Cu. The lifetime of 12 ps from which the transition probabilities were deduced is smaller than it should be if a minimum in $B(E2)$ is expected. Nevertheless, the small half-life can be attributed to the presence of the $M1$ component that accelerates the deexcitation, and not to a collective character and a weakening in the magicity at $N = 50$. This leads us to study the systematics of $B(E2)$ and $B(M1)$ in other neutron-rich isotopic and isotonic chains in the vicinity of $^{78}$Ni with transitions involving a change of total angular momentum $\Delta J = 1$, and investigate if a similar effect is observed when reaching shell or sub-shell closures.

| Nucleus | N | Excitation energy (keV) | Excited state configuration | Ground state configuration | $B(E2)$ measurement |
|---|---|---|---|---|---|
| $^{65}$Cu | 36 | 1115 | $5/2^-$ | $3/2^-$ | From Coulomb excitation |
| $^{67}$Cu | 38 | 1115 | $5/2^-$ | $3/2^-$ | From Coulomb excitation |
| $^{69}$Cu | 40 | 1214 | $5/2^-$ | $3/2^-$ | From Coulomb excitation |
| $^{71}$Cu | 42 | 534 | $5/2^-$ | $3/2^-$ | From Coulomb excitation |
| $^{73}$Cu | 44 | 166 | $5/2^-$ | $3/2^-$ | From Coulomb excitation |
| $^{75}$Cu | 46 | 66 | $3/2^-$ | $5/2^-$ | From a lifetime supposing a pure $E2$ transition |
| $^{77}$Cu | 48 | 293 | $3/2^-$ | $5/2^-$ | No available information |
| $^{79}$Cu | 50 | 656 | $3/2^-$ | $5/2^-$ | From a lifetime supposing a pure $E2$ transition |

Table 6.1: Summary of the excitation energies, spin configurations and the methods and assumptions used to evaluate the $B(E2)$ rates shown in figure 6.1 for copper isotopes.

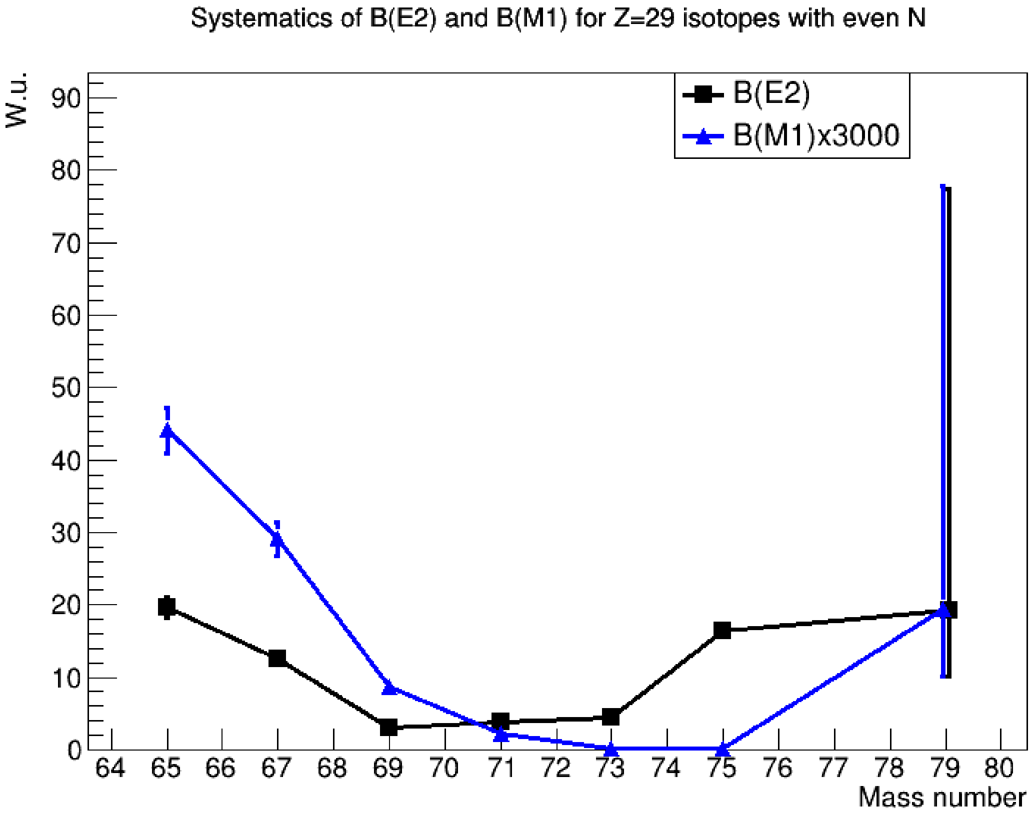

Figure 6.1: Systematics of $B(E2, M1; 5/2^- \rightarrow 3/2^-_{gs})$ for $A < 75$ and $B(E2, M1; 3/2^- \rightarrow 5/2^-_{gs})$ for $A \geq 75$, in copper neutron-rich isotopes. Data taken from [46, 84, 85]. The result for $^{79}$Cu is from this work.

## 6.2 Systematics of B(E2) and B(M1) in N=49 isotones with even-Z

One possible way to study the effects highlighted in the previous section is to look at the systematics of $B(M1)$ and $B(E2)$ in the neutron-rich $N = 49$ isotones, with an even number of protons. In these nuclei, a $9/2^+$ spin-parity is assigned to the ground state. This is resulting from the presence of 9 neutrons in the $\nu g_{9/2}$ sub-shell, that leads to a $\nu g_{9/2}^{-1}$ hole configuration. The transition of interest is the deexcitation from the $7/2_1^+$ levels to the ground state. The lightest nucleus for which relevant data is available is $^{85}$Kr. In the latter, the $(7/2^+)$ state was found at 1847 keV with a half-life of $0.08^{+0.03}_{-0.02}$ ps [50]. The corresponding $B(E2)$ and $B(M1)$ values were established at $10^{+5}_{-6}$ W.u. and $0.010^{+0.012}_{-0.010}$ W.u., respectively, with a multipolarity mixing ratio $\delta = 1.7 \pm 1.3$ obtained from the angular distribution of the $\gamma$ rays. The next isotone in the chain is $^{87}$Sr, with $Z = 38$, where the decay from the $7/2^+$ state at 1920 keV to the ground state was measured within experiments involving different reactions [88, 89]. The $7/2^+$ was interpreted as a member in the multiplet involving the $2^+$ core of $^{88}$Sr with the hole in the $\nu g_{9/2}$ orbital. Particularly, an in-beam $\gamma$-ray spectroscopy was performed together with a lifetime measurement employing DSAM [89]. A half-life of 0.14(3) ps was obtained, with a value of 1.9(5) W.u. for $B(E2)$ and 0.013(3) W.u. for $B(M1)$, with a mixing $\delta = 0.70 \pm 0.05$. Given the large uncertainty for the $M1$ transition strength in $^{85}$Kr, no clear conclusion can be made on its evolution between $Z = 36$ and $Z = 38$, but a significant decrease in $B(E2)$ can be noticed, as one approaches the semi-magicity at $Z = 40$. Finally, the last nucleus when reaching the $Z = 40$ harmonic oscillator magic number, corresponds to $^{89}$Zr. Its lowest $(7/2^+)$ state was measured at 2102 keV and was interpreted as a coupling between the $2^+$ core of $^{90}$Zr and a hole in the $\nu g_{9/2}$ orbit. Its level scheme was studied in an experiment through the $^{86}$Sr$(\alpha,\mathrm{n}\gamma)^{89}$Zr reaction, employing DSAM to measure the lifetimes of the deexciting levels [90], where a half-life of 104(14) fs was obtained. Assuming a pure $M1$ transition, the authors deduced a value of 0.023(3) W.u. for $B(M1)$, whereas a pure $E2$ transition leads to a value of 5.6(8) W.u. for $B(E2)$. This time, an increase[2] in the electric quadrupole transition rate can be observed relative to $^{87}$Sr. At the same time, the magnetic dipole transition strength is also increased, as illustrated in the total systematics of the reduced transition rates in figure 6.2 (the excitation energies, spin configurations and methods used to evaluate the transition rates are summarized

---

[2] This comparison between $Z = 38$ and $Z = 40$ is not trivial since the mixing ratio is not known for $Z = 40$ for which the adopted $B(E2)$ can thus be seen as an upper limit. We nevertheless do not exclude a rise in $B(E2)$ between Sr and Zr.

in table 6.2), leading to a small lifetime value of 0.104 ps. Therefore, this simultaneous rise in both $B(M1)$ and $B(E2)$ at $Z = 40$ sub-shell closure in the $N = 49$ isotones is comparable to the one that was discussed in $Z = 29$ isotopes in section 6.1. However, one should keep in mind that the excited states we described are mainly multiplet members, which are the result of the coupling between the neutron hole configuration and the $2^+$ excitation of the core. The decaying states are not pure single particle states[3] and such a comparison between these cases and the copper isotopic chain does not have to be taken as an absolute reference. In order to evaluate the systematics of this behavior towards closed shells or sub-shells, other cases shall be studied. The next section focuses on another case where one can analyze the $E2$ and $M1$ strengths in the $N = 51$ isotonic chain.

| Nucleus | Z | Excitation energy (keV) | Excited state configuration | Ground state configuration | $B(E2)$ measurement |
|---|---|---|---|---|---|
| $^{85}$Kr | 36 | 1847 | $7/2^+$ | $9/2^+$ | From a lifetime measurement and a $\delta$ mixing ratio |
| $^{87}$Sr | 38 | 1920 | $7/2^+$ as a member of the $2^+(^{88}\mathrm{Sr}) \otimes \nu 1g_{9/2}^{-1}$ multiplet | $9/2^+$ | From a lifetime measurement and a $\delta$ mixing ratio |
| $^{89}$Zr | 40 | 2102 | $7/2^+$ as a member of the $2^+(^{90}\mathrm{Zr}) \otimes \nu 1g_{9/2}^{-1}$ multiplet | $9/2^+$ | From a lifetime measurement supposing a pure $E2$ transition |

Table 6.2: Summary of the excitation energies, spin configurations and the methods and assumptions used to evaluate the $B(E2)$ rates shown in figure 6.2 for even-Z $N = 49$ isotones.

---

[3] The only possible single particle levels would require the promotion of the odd neutron from the $1g_{9/2}$ orbital to a level that is above the $N = 50$ shell gap. Furthermore, to be in the same conditions as for the decay in $^{79}$Cu, one has to look for a final state where the total angular momentum changes by one unit, the orbital angular momentum changes by two units and the spin is inverted with respect to the $1g_{9/2}$ configuration of the ground state, keeping the same positive parity. The lowest level satisfying all these criteria is the $1i_{11/2}$, which is above $N = 126$ and thus energetically too far.

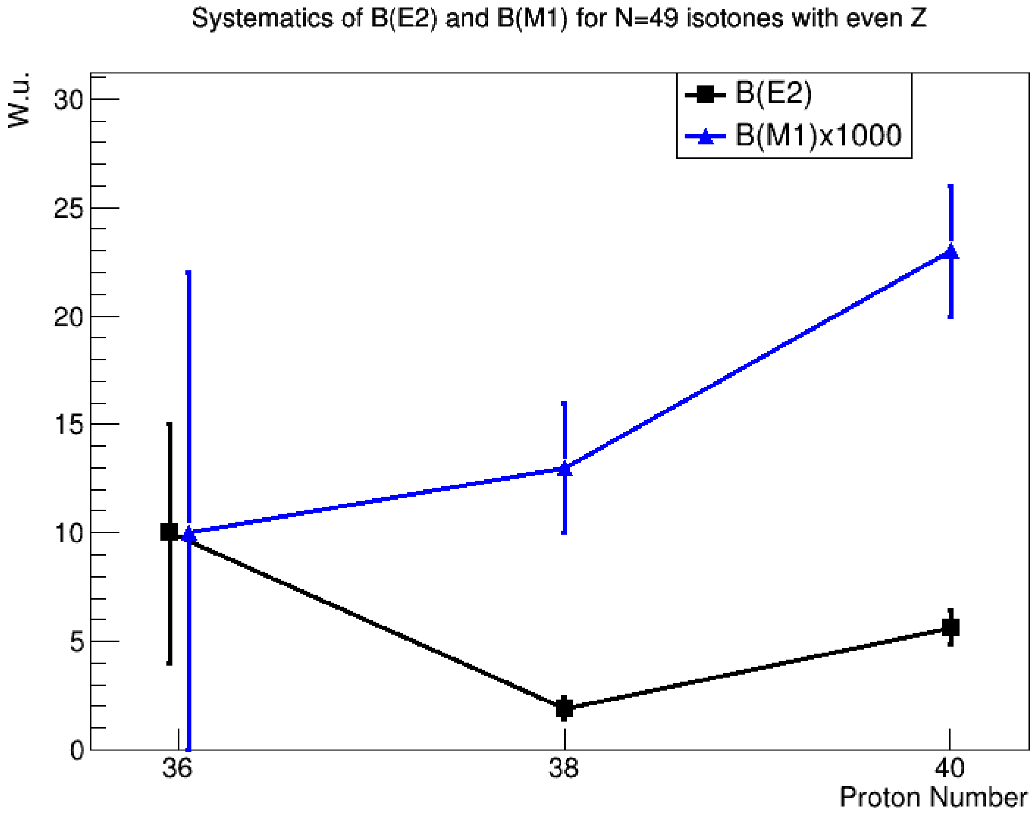

Figure 6.2: Systematics of $B(E2, M1; (7/2^+) \rightarrow 9/2^+_{gs})$ for $N = 49$ isotones with an even number of protons.

## 6.3 Systematics of B(E2) and B(M1) in N=51 isotones with even-Z

In the $N = 51$ isotonic chain with an even number of protons, the ground state configuration is determined by the odd neutron present above the shell gap at $N = 50$. According to the order of the orbits illustrated in figure 1.1, the next level above this gap corresponds to the $2d_{5/2}$ orbital. Consequently, a $5/2^+$ spin-parity is assigned to the ground state. When the valence neutron is promoted to the next orbit which is the $1g_{7/2}$ one, the nucleus reaches a $7/2^+$ excited state. Here, we are interested in the evolution of $B(E2)$ and $B(M1)$ for the transition between the two states we just mentioned. The lightest isotone in which information on the latter is available is $^{85}$Se, with $Z = 34$. The excited states in this nucleus were previously studied in $\beta$-decay works [91, 92], in prompt-$\gamma$ measurements [93, 94], and in transfer reactions [95]. In the latter, the ground state of $^{85}$Se was firmly assigned a $5/2^+$ spin-parity. In all these experiments, an excited level was observed at 1115 keV to which a $(7/2^+)$ spin-parity was assigned.

This assumption was later strengthened in an experiment performed at the high-flux reactor of the Institut Laue-Langevin in Grenoble, where the authors suggested a $\nu g_{7/2}$ single-particle nature for this state [96]. Recently, an experiment was performed at the LNL[4] tandem-ALPI accelerator complex. The $^{85}$Se nuclei were produced by multinucleon transfer reactions induced by a $^{82}$Se beam [97]. Lifetime measurements were performed using the recoil distance Doppler shift (RDDS) technique. This allowed to obtain an upper limit of $2.08 \pm 1.39$ ps for the half-life of the $7/2^+_1$ level. This result can be used to deduce lower limits of 7 W.u. for $B(E2)$ and $8.10^{-3}$ W.u. for $B(M1)$. The authors concluded that such a low upper limit for the lifetime was an indication of a very small contribution of the $\nu 1g_{7/2}$ configuration to the wavefunction of the state. In this same experiment, $^{87}$Kr which is the next $N = 51$ isotone (with $Z = 36$) was also produced. In this nucleus, a lifetime of $0.4^{+1.6}_{-0.4}$ ps, corresponding to a half-life of $0.3^{+1.1}_{-0.3}$ ps was measured for the $7/2^+$ state at 1420 keV. This allows to deduce a value of 14 W.u. for $B(E2)$ and $26.10^{-3}$ W.u. for $B(M1)$, with lower limits at 3 W.u. and $5.10^{-3}$ W.u., respectively. Similarly, the measured $(7/2^+_1)$ lifetime was consistent with a core-coupled $2^+ \otimes \nu 2d_{5/2}$ configuration for this state. The next element in the chain is $^{89}$Sr, with 38 protons and its lowest $(7/2)^+$ excited state lies at 1473 keV, understood as a multiplet member resulting from the coupling of the $\nu d_{5/2}$ odd neutron with the vibrational $2^+_1$ of the $^{88}$Sr core. Indeed, in the previously mentioned work [97], the authors also compared the 0.38(14) ps lifetime of the 1473 keV level (known from a DSAM measurement [98] that followed a $^{86}$Kr($\alpha$, $n$)$^{89}$Sr reaction) to theoretical predictions and the result was in agreement with a core coupling configuration for 95% of the wavefunction. In addition, the lifetime that would be obtained if the main configuration was a single neutron in the $1g_{7/2}$ was estimated and it was found to be of the order of 15 ps (or 10 ps for the half-life), which is of the same order as for the 656 keV level in our $^{79}$Cu case. Assuming similar behaviors for protons in Cu and neutrons in Sr, this comparison would suggest that the latter 656 keV state can be described with a wavefunction in which the dominant part is the $\pi 2p_{3/2}$ single particle configuration. The decay of $^{89}$Sr was also investigated through the $^{88}$Sr($d$, p$\gamma$)$^{89}$Sr reaction [99], where angular correlations of the $\gamma$ rays allowed to obtain an $E2/M1$ multipolarity mixing ratio $\delta{=}-0.32 \pm 0.05$, with a value of $4.8 \pm 2.0$ W.u. for $E2$ and $0.017 \pm 0.007$ W.u. for $M1$ rates, which are therefore decreased when approaching $Z = 40$ shell closure. Finally, the $^{91}$Zr level scheme was investigated in several experiments, where a $7/2^+$ level at 1882 keV was observed, for which a half-life of $72.8^{+4.9}_{-4.2}$ fs was measured using Doppler Shift Attenuation Method, following an $(n,n'\gamma)$ reaction [100]. The resulting decay rates were found at $0.017 \pm 0.004$ W.u. for magnetic dipole and $7.7 \pm 1.3$ W.u. for electric quadrupole transitions, with a mixing $\delta = 1.25(15)$. Clearly, there is an

---

[4] Laboratori Nazionali di Legnaro

increase of $B(E2)$ at the harmonic oscillator $Z = 40$ magic number, like in the $N = 49$ isotonic chain for $^{89}$Zr, as illustrated in figure 6.3, in the systematics of the transition rates of the $N = 51$ isotonic chain (the excitation energies, spin configurations and methods used to evaluate the transition rates are summarized in table 6.3). No clear change can be noticed on $M1$ rates between $Z = 38$ and $Z = 40$, but such a value of the order of 0.02 W.u. is sufficient to account for the 73 fs small half-life of the deexciting $7/2^+$ level in zirconium. As for the $N = 49$ isotonic chain, this comparison has to be kept as an approximate indicator of the behaviors of $B(E2)$ and $B(M1)$ reduced transition probabilities, since the decaying states are not pure single particle states.

| Nucleus | Z | Excitation energy (keV) | Excited state configuration | Ground state configuration | $B(E2)$ measurement |
|---|---|---|---|---|---|
| $^{85}$Se | 34 | 1115 | $7/2^+$ | $5/2^+$ | Lower limit for $B(E2)$ from a lifetime upper limit measurement |
| $^{87}$Kr | 36 | 1420 | $7/2^+$ as a member of the $2^+(^{86}\text{Kr}) \otimes \nu 2d_{5/2}$ multiplet | $5/2^+$ | Lower limit for $B(E2)$ from a lifetime upper limit measurement |
| $^{89}$Sr | 38 | 1473 | $7/2^+$ as a member of the $2^+(^{88}\text{Sr}) \otimes \nu 2d_{5/2}$ multiplet | $5/2^+$ | From a lifetime measurement and a $\delta$ mixing ratio |
| $^{91}$Zr | 40 | 1882 | $7/2^+$ | $5/2^+$ | From a lifetime measurement and a $\delta$ mixing ratio |

Table 6.3: Summary of the excitation energies, spin configurations and the methods and assumptions used to evaluate the $B(E2)$ rates shown in figure 6.3 for even-Z $N = 51$ isotones.

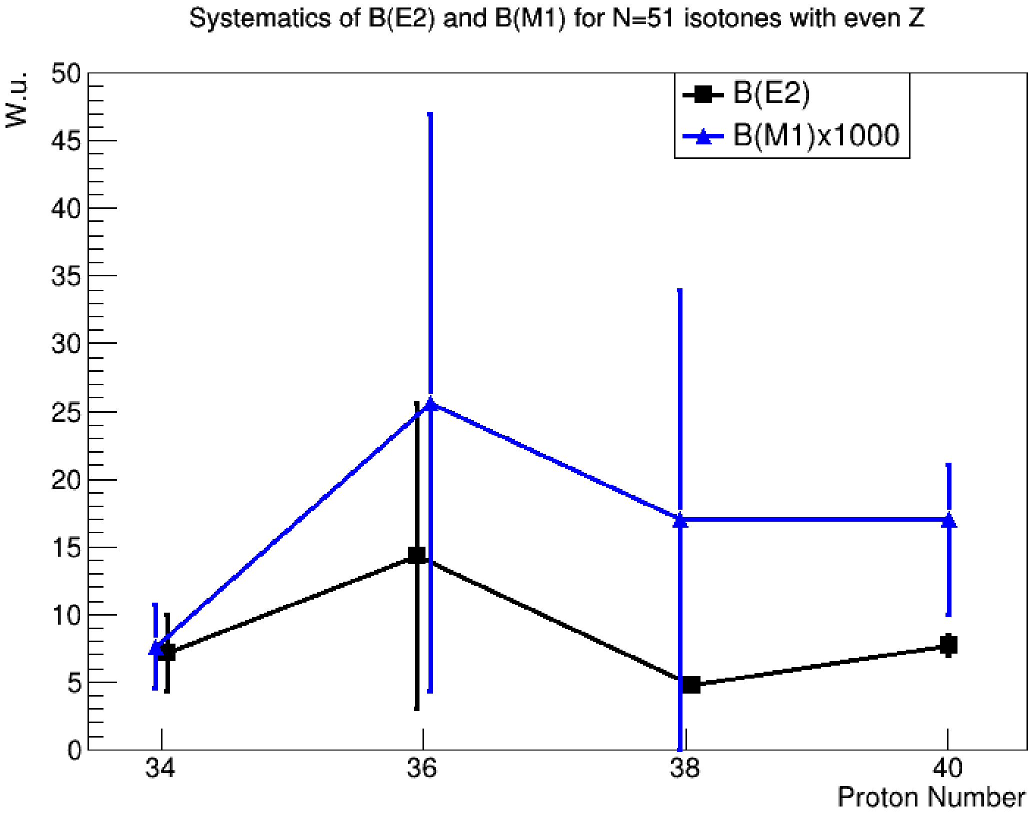

Figure 6.3: Systematics of $B(E2, M1; (7/2^+) \rightarrow 5/2^+_{gs})$ for $N = 51$ isotones with an even number of protons. For $Z = 34$, and $Z = 36$, the drawn data points represent the lower limits for $B(E2)$ and $B(M1)$ and not the absolute measurements.

## 6.4 Systematics of B(E2) and B(M1) in N=50 isotones with odd-Z

The last chain at which one can look and which includes $^{79}$Cu is the $N = 50$ isotonic chain. The transition of interest is between the $3/2^-$ and $5/2^-$ single particle states. We previously described the ground state in $^{79}$Cu with an odd proton in the $\pi 1f_{5/2}$ level, and the first excited state is obtained when this proton is promoted to the $\pi 2p_{3/2}$ orbit. For lighter $N = 50$ isotones ($Z \leq 27$), no information is available about the level schemes since the latter are too exotic. Therefore, we only study the heavier isotones above $Z = 29$. The systematics of $E2$ and $M1$ decay strengths are illustrated in figure 6.4, while the excitation energies, spin configurations and methods used to evaluate the transition rates are summarized in table 6.4. The first target in the chain is $^{81}$Ga, with $Z = 31$. With 3 valence protons in the $\pi 1f_{5/2}$ orbital, the ground state remains with a $5/2^-$ spin-parity. The promotion of one of these three particles into the $\pi 2p_{3/2}$ level induces a $3/2^-$ first excited state, in a similar fashion as for $^{79}$Cu. This excited level was observed at 351 keV. In a paper following an experiment at GANIL [101], the experimental level scheme was compared with state-of-the-art large-scale shell model (LSSM) calculations. The wavefunction of the ground state was found to be in agreement with the configurations we described. In a recent work [102], the half-life of the 351 keV level was determined at 60(10) ps and values of 85(14) W.u. and 8.5(14).$10^{-3}$ W.u. for $B(E2)$ and $B(M1)$, respectively, assuming either pure $E2$ or pure $M1$ multipolarities. Recalling the results for $^{79}$Cu ($19^{+58}_{-9}$ W.u. for $E2$ and $0.0065^{+0.0194}_{-0.0031}$ W.u. for $M1$), it seems that $B(E2)$ increases in $^{81}$Ga but no absolute conclusion can be made on the evolution of the decay strengths between copper and gallium given the larger uncertainties for $^{79}$Cu. The next isotone in the chain is $^{83}$As, with 5 valence protons which are all in $\pi 1f_{5/2}$ sub-shell, leading to a $5/2^-$ ground state. Also in this nucleus, a $3/2^-$ excited state can be created if one of the 5 nucleons reaches the $\pi 2p_{3/2}$ level. The energy of such a state was measured at 307 keV. So far, there is no published result on probability transition rates for this isotope. There is only an ongoing work [103], where the lifetime of the 307 keV level is being estimated at 255(20)ps as a preliminary result. Supposing either pure $E2$ or pure $M1$ multipolarities, values of 38(3) W.u. and 3.0(2).$10^{-3}$ W.u. are obtained for $B(E2)$ and $B(M1)$, respectively. The next element in the chain is $^{85}$Br with 35 protons, of which 7 are above the $Z = 28$ shell gap. The ground state configuration is described with a fully occupied $\pi 1f_{5/2}$ with 6 particles, and an individual $\pi 2p_{3/2}$ proton, leading to a $3/2^-$ spin-parity. A $5/2^-$ excited state can be generated if one of the 6 inner valence protons leaves its counterparts and pairs with the outer one, leaving a hole in the $\pi 1f_{5/2}$ level. Such an excited state was measured at 345 keV. For the time being, no official result can be found for the transition rates of this state. There is only an ongoing work at ILL in which a half-life of the order of 100 ps is expected [103]. The next nuclear species of the chain is $^{87}$Rb, with $Z = 37$, having 9 protons above the $Z = 28$ gap. With 6 protons in the $\pi 1f_{5/2}$ orbit and 3 in the $\pi 2p_{3/2}$ one, the $3/2^-$ and $5/2^-$ spin-parities are still assigned to the ground state and to the excited state, respectively, the latter being at 403 keV. The lifetime and the multipolarity mixing ratio of the latter were measured [104–106]. With a half-life of $78^{+11}_{-60}$ ps and $\delta = -0.24^{+0.09}_{-0.12}$, $B(E2) = 1.63(15)$ and $B(M1) = 0.0042^{+0.0061}_{-0.0023}$ could be deduced [5]. Such a low $B(E2)$ value hints to a low collectivity in the transition. The half-life of this state being about at least $78/12 \approx 7$ times larger than for the 656 keV transition in $^{79}$Cu, the $B(E2)$ value will be lower than the one of $\approx 19$ W.u. obtained for copper assuming a pure $E2$ multipolarity (an infinite value of $\delta$). However, if instead, one puts the hypothesis of a mixing ratio of the same order for $^{79}$Cu ($\delta \approx 0.24$), the previously evaluated $B(E2) \approx 19$ W.u. would

---

[5] If a pure $E2$ is assumed, a value of $\approx 30$ W.u. would be obtained for $B(E2)$.

also decrease. This question on the behavior of the transition strengths as a function of the multipolarity mixing ratio in $^{79}$Cu is discussed in the next section.

| Nucleus | Z | Excitation energy (keV) | Excited state configuration | Ground state configuration | $B(E2)$ measurement |
|---|---|---|---|---|---|
| $^{79}$Cu | 29 | 656 | $3/2^-$ | $5/2^-$ | From the $12^{+11}_{-9}$ ps half-life assuming a pure $E2$ decay |
| $^{81}$Ga | 31 | 351 | $3/2^-$ | $5/2^-$ | From the 60(10) ps half-life assuming a pure $E2$ decay |
| $^{83}$As | 33 | 307 | $3/2^-$ | $5/2^-$ | From the 255(20) ps half-life assuming a pure $E2$ decay |
| $^{87}$Rb | 37 | 407 | $5/2^-$ | $3/2^-$ | From the $78^{+11}_{-60}$ ps half-life and a $\delta$ mixing ratio |

Table 6.4: Summary of the excitation energies, spin configurations and the methods and assumptions used to evaluate the $B(E2)$ rates shown in figure 6.4 for odd-Z $N = 50$ isotones.

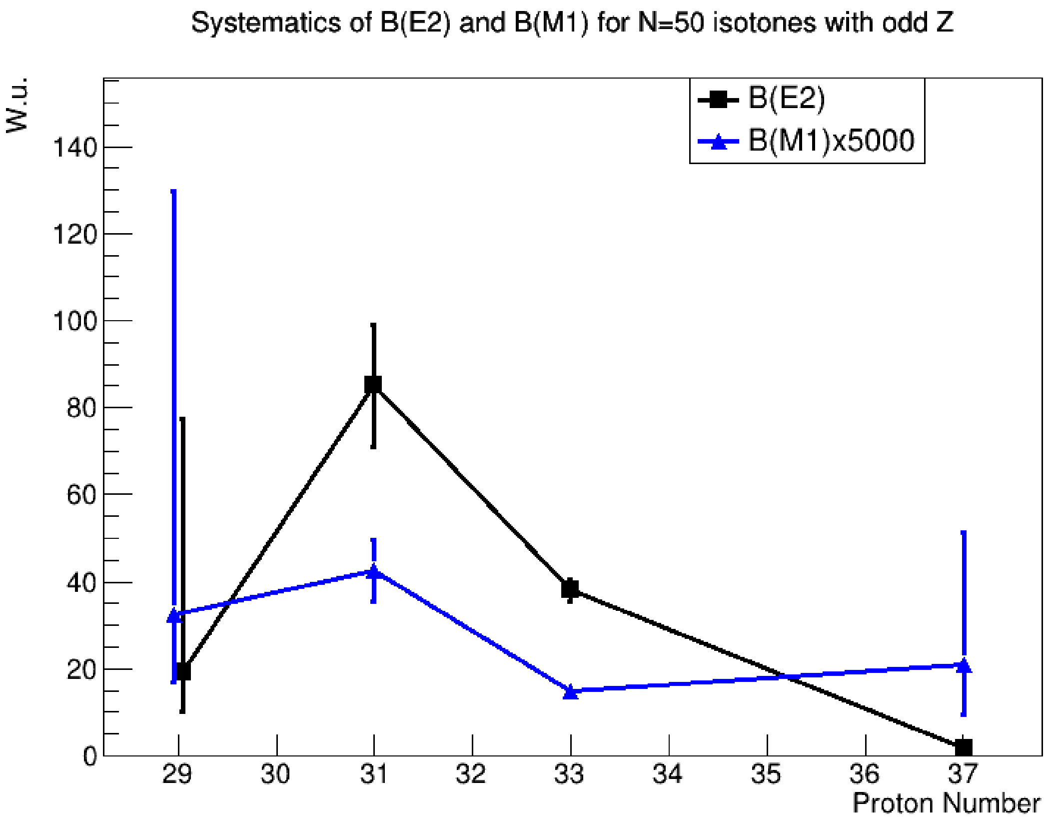

Figure 6.4: Systematics of $B(E2, M1; 3/2^- \rightarrow 5/2^-_{gs})$ for $Z < 34$ and $B(E2, M1; 5/2^- \rightarrow 3/2^-_{gs})$ for $Z = 37$, in $N = 50$ odd-Z isotones. The result for $^{79}$Cu is from this work.

# 6.5 Implementation of the mixing ratio in $^{79}$Cu

## 6.5.1 Choices of the mixing ratio

As already mentioned, the measured half-life of $12^{+11}_{-9}$ ps in $^{79}$Cu results in a large value of $B(E2) = 19^{+58}_{-9}$ W.u. if the transition is of a pure $E2$ nature. The presence of the $M1$ component in the decay can however lower the electric quadrupole component. In the competition between the latter and the magnetic dipole component, the evaluation of the importance of each contribution requires the knowledge of the multipolarity mixing ratio $\delta$ as highlighted in equation 6.1. The measurement of this parameter can be obtained with the angular distributions of the 855 keV and the 656 keV $\gamma$ rays when these two transitions are in coincidence. Unfortunately, the statistics in our $\gamma\gamma$ coincidence spectra is insufficient for this purpose. Consequently, we looked for typical values in the neighborhood of the $^{79}$Cu nucleus when we studied the $(3/2)^- \leftrightarrow (5/2)^-$ transitions in isotopic and isotonic chains in the previous sections.

The first case to be considered is the $^{75}$Cu isotope where the use of a mixing ratio $\delta \approx 0.47$ lowers the $B(E2)$ rate from 16.4(6) W.u. to about 3.3 W.u., thus retrieving a value that is comparable to those of lighter copper isotopes. Assuming this same $\delta$ for the 656 keV transition in $^{79}$Cu would also lower the electric decay strength from $\approx$ 19 W.u. to $\approx$ 3.5 W.u., which is similar to the one in the other copper nuclei. With this assumption of a same mixing for $A = 75$ and $A = 79$, no clear evolution can be noticed when reaching the shell closure at $N = 50$ (as it can be seen in figure 6.5 where the $B(E2)$ rates obtained with $\delta = 0.47$ for these two heaviest isotopes are illustrated [6]), and the single particle nature of the states involved in the transition can not be excluded.

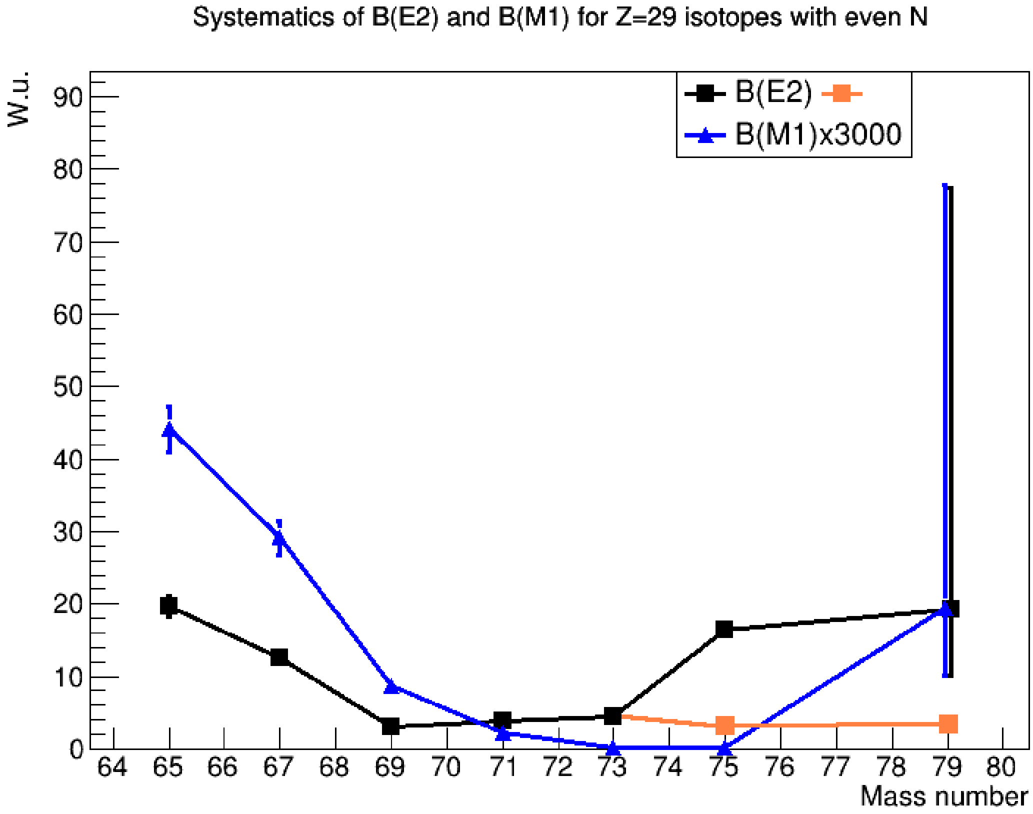

Figure 6.5: Systematics of $B(E2, M1; 5/2^- \rightarrow 3/2^-_{gs})$ for $A < 75$ and $B(E2, M1; 3/2^- \rightarrow 5/2^-_{gs})$ for $A \geq 75$, in copper neutron-rich isotopes. Data taken from [46, 84, 85]. The results for $^{75}$Cu and $^{79}$Cu were deduced from lifetimes supposing either a pure $E2$ decay (black) or $\delta = 0.47$ (orange).

The other case where a multipolarity ratio was found is in $^{87}$Rb. As already mentioned in the previous section, a $\delta = -0.24^{+0.09}_{-0.12}$ ratio was measured with the angular

---

[6] The error bars are not represented for clarity purposes.

distributions of the $\gamma$ rays [106]. If one uses this same mixing in $^{79}$Cu, the deduced $B(E2)$ decreases from $\approx 30$ W.u. to $\approx 1$ W.u., thus leading to values that are comparable with the $^{87}$Rb case. This value is even smaller than the $\approx 3.3$ W.u. obtained for $^{75}$Cu, suggesting a minimum when reaching the $N = 50$ shell closure.

### 6.5.2 Relation between the mixing ratio and collectivity

In the previous paragraph, the behavior of the reduced transition probabilities as a function of the multipolarity mixing ratio was discussed. In this section, we present how this can be interpreted in terms of the wavefunctions of the states that are involved in the $\gamma$ deexcitation. The composition of these functions is schematized in figure 6.6. In the single-particle picture, the decay in $^{79}$Cu involves the transition of the odd proton from the $\pi 2p_{3/2}$ level to the $\pi 1f_{5/2}$ orbital (this corresponds to a transition between the red parts of the wavefunctions in figure 6.6). Since this involves a change in orbital angular momentum $|\Delta L|= 2$, it can only take place by an electric quadrupole transition. To be able to see the $L$-forbidden $M1$ decay, the mentioned wavefunctions must contain components that allow to flip the spin between the initial state and the final state while keeping the same orbital angular momentum. The most probable configurations for such a decay include either a $2^+(^{78}\mathrm{Ni}) \otimes \pi 1f_{7/2}$ part in the initial wavefunction $\Psi_i$ to allow the $M1$ transition to the $1f_{5/2}$ component in the ground state, or a $2^+(^{78}\mathrm{Ni}) \otimes \pi 2p_{1/2}$ portion in the final wavefunction $\Psi_f$ to permit the overlap with $2p_{3/2}$ part of the excited state. The importance of these additional components (represented with a blue color in figure 6.6) depends on the mixing ratio. The smaller the absolute value of the latter, the larger the percentage of this contaminating parts, the higher the $M1$ contribution. In other words, the knowledge of $\delta$ is a measurement of the importance of the mentioned additional components and does not provide information on the composition of the remaining part that includes the single-particle components (represented in red color), since other contaminants may be present.

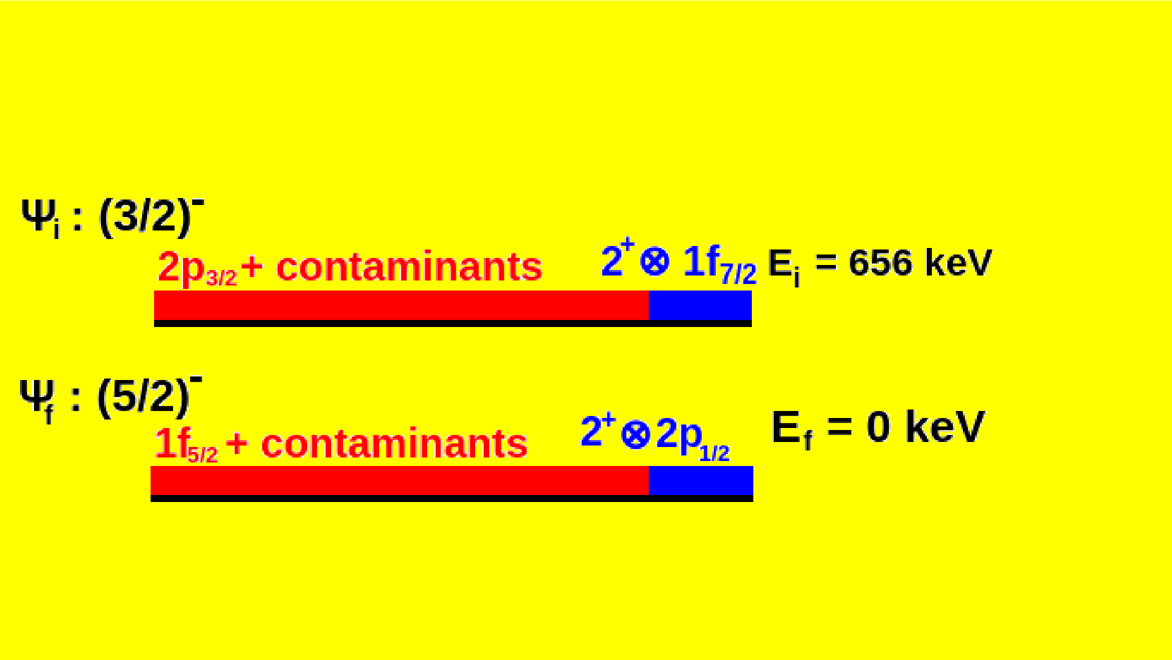

Figure 6.6: Illustration of the composition of the wavefunctions that are involved in the 656 keV transition in $^{79}$Cu.

# Conclusion

In this work, we performed the in-beam $\gamma$-ray spectroscopy of the $^{79}$Cu exotic isotope, with one more proton than $^{78}$Ni. The former was produced at RIBF after the fragmentation of a high energy $^{80}$Zn beam on a $^{9}$Be target. The $\gamma$ rays emitted by copper isotopes were detected with the HiCARI hybrid germanium array, made of Miniball, clover and GRETINA-type detectors. The analysis procedure we followed allowed us to confirm two of the previously known transitions in $^{79}$Cu, at 656 keV and 855 keV, the latter being less intense than the former. The $\chi^2$ minimization method was employed to evaluate for the first time the lifetime of the $(3/2^-)$ level at 656 keV. The use of different detector groups led to different values for the energy and the half-life, the latter being found at $12^{+11}_{-9}$ ps, using the P3 module. Nevertheless, these measurements allowed to get more insight on the single-particle and collective character of the $(3/2^-)$ and $(5/2^-_{gs})$ states involved in the deexcitation, as well as the multipolarity of the corresponding transition, through the probability transition rates we deduced. It was found that a small $M1$ contribution in the transition is sufficient to account for the short half-life. Such a contribution, that increases the total decay rate, is allowed with the presence of other components than the single-particle configurations in the total wavefunctions. The importance of these additional parts depends on the mixing ratio that can be measured using angular distributions of the $\gamma$ rays (which could not be done due to the low statistics). Therefore, no definitive conclusion can be made on the single-particle and collective behaviors for the states in $^{79}$Cu. For a more comprehensive study of the collectivity in this nucleus, theoretical shell-model calculations shall be performed to evaluate the electric and magnetic transition rates.

In order to get the full systematics of $B(M1)$ and $B(E2)$, a measurement of half-lives of the excited states in $^{77}$Cu will be necessary, by looking at the transition between the $3/2^-$ level at 293 keV and the $5/2^-_{gs}$ ground state. In our data set, this isotope was also produced and we could identify it in our PID plots. For instance, the $\gamma$ spectra we obtained, after gating on the $^{79}$Zn($^{9}$Be,X)$^{77}$Cu reaction channel are illustrated in figure 6.7. The main transition that can be seen is the one at 946 keV, and for which a lifetime measurement can be done using the methodology we described. Unfortunately, the 293 keV $\gamma$ ray is dominated by the background at low energy and a half-life measurement is not possible using our data.

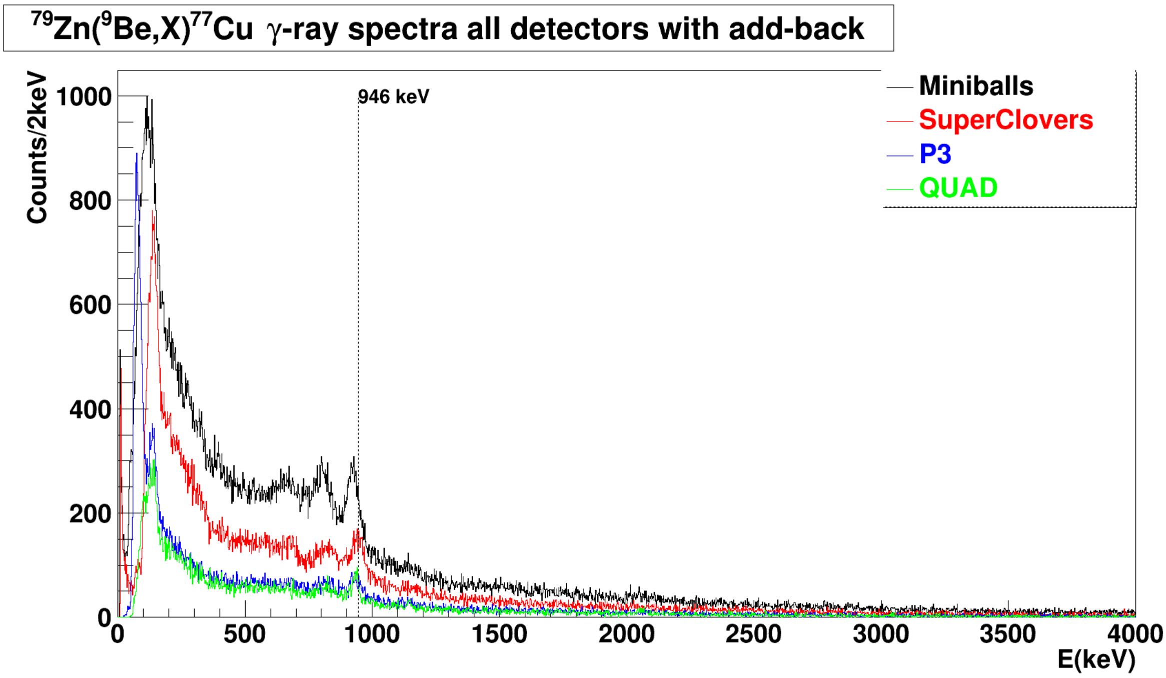

Figure 6.7: Doppler corrected $\gamma$ spectra for the $^{79}$Zn($^{9}$Be,X)$^{77}$Cu reaction channel, as obtained with the different detector groups.

To overcome this issue, a new experiment was proposed and approved at the RIKEN facility for 2025, where fast timing LaBr$_3$(Ce) scintillators can be employed to measure the lifetimes of the deexciting states in neutron-rich copper isotopes, including $^{75}$Cu and $^{77}$Cu, as a part of the IDATEN project[7]. This project was made possible through partnerships with FATIMA (FAst TIMing Array) in the UK and KHALA (Korea High-resolution Array of LaBr$_3$(Ce)) in South Korea. The main structure of the IDATEN detector assembly comprises 84 cerium-doped lanthanum bromide (LaBr$_3$(Ce)) scintillators, combining 36 FATIMA detectors and 48 KHALA-type detectors. A geometrical representation from GEANT4 simualtions is illustrated in figure 6.8.

---

[7] International Detector Assembly for fast-Timing measurements of Exotic Nuclei

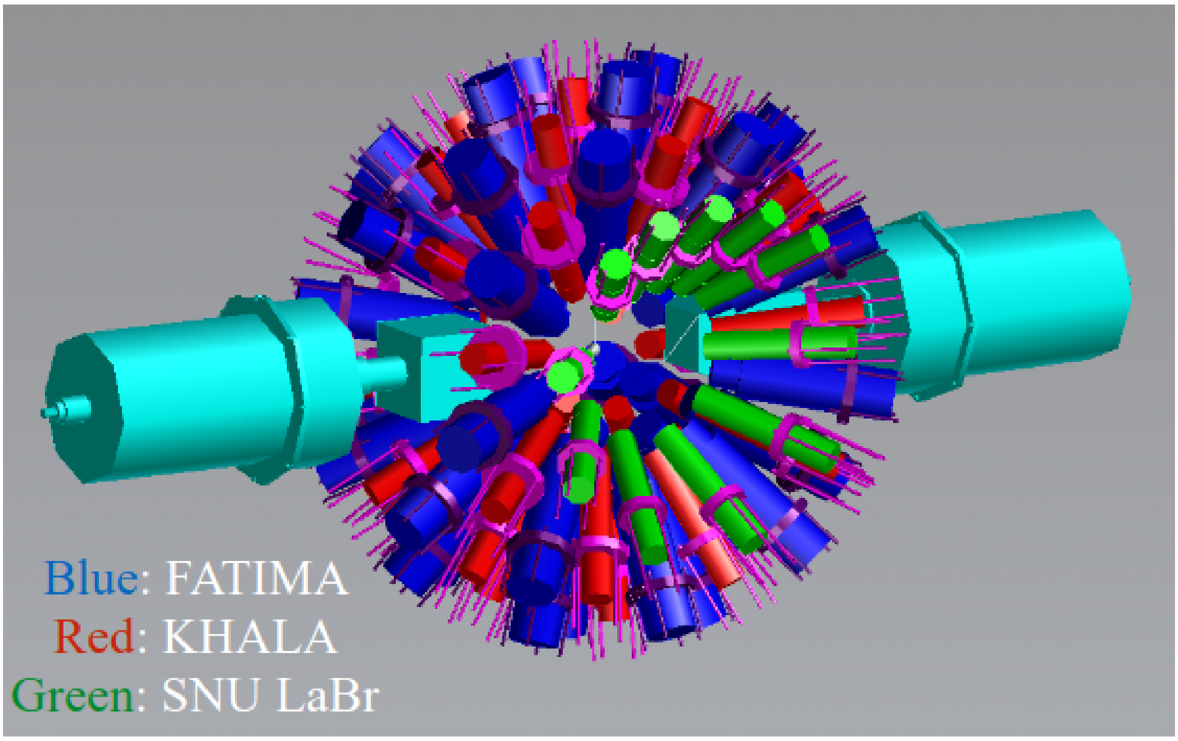

Figure 6.8: GEANT4 geometrical representation of the IDATEN $\gamma$ spectrometer.

This configuration is expected to achieve $\gamma$-ray full energy-peak efficiencies of approximately 20%, 9%, and 5% for 100 keV, 500 keV, and 1000 keV $\gamma$ rays, respectively. Additionally, two clover-type HPGe detectors will be installed to monitor $\gamma$-ray energy spectra with high resolution and to simplify complex decay spectra by gating on specific $\gamma$ rays measured in coincidence with the $LaBr_3$(Ce) detectors. These $\gamma$-ray detectors will be positioned around a modified version of the WAS3ABi (Wide-range Active Silicon-Strip Stopper Array for Beta and ion detection) system, which includes several layers of double-sided silicon-strip detectors and fast-timing plastic scintillator detectors in a compact geometry, at the end of the BigRIPS-ZeroDegree spectrometer (F11). The new IDATEN array is capable of measuring the lifetimes of excited states in the picosecond range using electronic fast-timing $\beta$-$\gamma$ and $\gamma$-$\gamma$ coincidence methods. Some of the characteristics and expected performances of the $LaBr_3$(Ce) components of the array are summarized in the following table.

| | **FATIMA** | **KHALA** |
|---|---|---|
| Number of detectors | 36 | 36+12 |
| Energy resolution | 3.4% at 779 keV | 3.3% at 662 keV |
| Time resolution | 334.3(4) ps at 1332-1173 keV | 335(1) ps at 511-511 keV |

# Résumé en Français

Le noyau atomique représente l'un des systèmes physiques les plus complexes et captivants, manifestant une grande diversité de comportements tels que la déformation, les excitations collectives, l'émission de particules, la décroissance $\beta$, la fusion ou la fission. Depuis sa découverte il y a plus d'un siècle, de nombreuses études expérimentales et théoriques ont été menées pour tenter d'élucider ses nombreuses propriétés. Cependant, à ce jour, il n'existe toujours pas de théorie unifiée capable d'expliquer tous les phénomènes nucléaires, et de nombreuses questions demeurent partiellement résolues. L'un des défis majeurs est de comprendre le comportement de la matière nucléaire loin de la vallée de stabilité.

Au début du siècle précédent, il a été observé que certains noyaux possédant un nombre spécifique de protons et/ou de neutrons présentent une stabilité accrue. Ces nombres, connus aujourd'hui sous le nom de "nombres magiques", sont 2, 8, 20, 28, 50, 82, 126. Cette observation a été interprétée comme une indication que le noyau pourrait être décrit en termes d'orbitales et de couches, de manière analogue aux électrons dans l'atome. Divers modèles de particules individuelles ont rapidement été proposés, mais tous ne pouvaient que reproduire les 3 premiers nombres magiques (2, 8 et 20). Ce problème n'a été résolu qu'en 1949, quand Goeppert Mayer [2] et Haxel, Jensen et Suess [3] avaient indépendamment introduit un terme empirique de spin-orbite dans le potentiel nucléaire. Néanmoins, avec le développement des faisceaux radioactifs au cours des dernières décennies, des noyaux de plus en plus exotiques sont devenus expérimentalement accessibles. Pour ces derniers, il a été observé que des réarrangements significatifs de la structure nucléaire peuvent se produire. Les nombres magiques mentionnés ci-dessus, valides près de la vallée de stabilité, ne sont pas universels : loin de cette stabilité, certains peuvent disparaître et de nouveaux nombres magiques peuvent émerger. Cela conduit naturellement à une autre question majeure, celle des forces impliquées dans l'évolution des couches loin de la stabilité.

Dans cette thèse, nous nous concentrons sur l'évolution de la structure nucléaire du côté des protons en direction du noyau de $^{78}$Ni ($Z = 28$, $N = 50$), l'un des noyaux les plus exotiques (avec un nombre important de neutrons) avec deux nombres magiques conventionnels. L'évolution du gap $Z = 28$ vers $N = 50$ peut être étudiée en sondant le caractère de particule individuelle des niveaux d'énergie dans la chaîne isotopique du cuivre, qui a un proton de plus que le nickel. Ce travail porte sur $^{79}$Cu, à $N = 50$, produit par la réaction de fragmentation sur une cible de $^{9}$Be et étudié par spectroscopie $\gamma$ en vol.

## Motivation physique

Pour le moment, il n'y a pas eu d'observation d'une disparition des fermetures de couche à $Z = 28$ et $N = 50$. Toutefois, certaines études ont suggéré un possible affaiblissement de ces gaps autour du $^{78}$Ni [28, 29]. Comme expliqué dans le chapitre 1, certaines données expérimentales existent sur le $^{78}$Ni, à savoir son temps de demi-vie pour la décroissance $\beta$ [30] et son schéma de niveaux [41] proposé suite à une récente étude de spectroscopie $\gamma$ en vol, les deux indiquant la robsustesse de la double magicité de ce noyau. Il demeure néanmoins intéressant d'étudier les isotopes de cuivre qui permettent d'explorer la structure nucléaire du côté des protons dans cette région, notamment en caractérisant leur caractère de particule individuelle. Les orbitales d'intérêt pour les protons incluent $1f_{7/2}$, supposément remplie, ainsi que $2p_{3/2}$ et $1f_{5/2}$. Pour les neutrons, l'orbitale concernée est $1g_{9/2}$, pleine à $N = 50$.

La taille du gap à $Z = 28$ peut être influencée par des dérives monopolaires. Lorsque des neutrons sont ajoutés dans l'orbitale $\nu g_{9/2}$ au-delà de $N = 40$, l'énergie du premier état excité $5/2^-$ diminue significativement par rapport à l'état fondamental $3/2^-$ dans les noyaux $^{71,73}$Cu [43, 44]. L'inversion de ces deux états a ensuite été observée dans le $^{75}$Cu, où le spin de l'état fondamental est $5/2^-$, et celui de l'état excité à 66 keV est $3/2^-$ [45]. Théoriquement, ces niveaux $3/2^-$ et $5/2^-$ correspondent principalement aux états de particule individuelle $2p_{3/2}$ et $1f_{5/2}$ respectivement. Cette tendance continue dans le $^{77}$Cu où on a observé que l'état excité $3/2^-$ atteignait une énergie de 293 keV [48]. Puis, très récemment, la toute première spectroscopie du $^{79}$Cu a été réalisée à RIKEN [5, 49]. Cette étude avait permis de proposer pour la première fois un schéma de niveaux pour cet isotope. La dérive monopolaire continuait d'augmenter l'énergie de l'état excité $3/2^-$, atteignant une valeur de 656 keV. Cette étude avait permis d'avoir une indication que les états dans $^{79}$Cu pouvaient bien être décrits par une particule individuelle autour d'un noyau doublement magique de $^{78}$Ni. Toutefois, la résolution du scintillateur DALI2 employé pour la détection des rayons $\gamma$ était un facteur limitant. Il y avait des transitions susceptibles d'exister, mais qui ne pouvaient pas être séparées des autres. De plus, il n'était pas possible de mesurer les temps de vie des états qui décroissent. En effet, ces demi-vies sont liées à la nature collective ou de particule individuelle des états impliqués dans les transitions et leurs mesures permettraient d'éclaircir la siuation sur ces questions, pour confirmer ou non la possibilité de décrire le noyau de $^{79}$Cu avec une particule individuelle autour d'un coeur magique de $^{78}$Ni.

# Dispositif expérimental

Afin de résoudre les ambiguités de l'éxpérience précédente, une nouvelle mesure a été proposée, prévoyant d'exploiter des détecteurs au germanium de haute résolution. L'expérience étudiée ici faisait partie de la campagne HiCARI (signifiant en anglais *High-resolution Cluster Array at RIBF*), un programme expérimental visant à étudier par spectroscopie $\gamma$ en ligne des noyaux riches en neutrons produits par fragmentation sur cibles. Notre expérience s'est déroulée pendant 1 semaine au laboratoire RIKEN, au Japon. Le dispositif expérimental est décrit dans le chapitre 2.

Un faisceau primaire de $^{238}$U, accéléré à une énergie de 345 MeV/nucléon et d'une intensité de 90 pnA, fut envoyé sur une cible primaire de $^{9}$Be. La fission en vol des noyaux d'uranium engendra un cocktail d'isotopes radioactifs, identifiés et sélectionnés en vol par le spectromètre BigRIPS [55] pour former le faisceau secondaire. Les noyaux d'intérêt furent ensuite envoyés avec une vitesse $\beta \sim 0.6$ sur une cible secondaire de $^{9}$Be d'une épaisseur de 6.8 mm. Des détecteurs PPAC [60, 107] étaient placés avant et après cette cible pour permette de déterminer la trajectoire des noyaux et corriger le plus efficacement possible l'important effet Doppler affectant les rayons $\gamma$ prompts émis par le résidu et détectés par le spectromètre $\gamma$ HiCARI, composé de plusieurs types de détecteurs au germanium [52]. Il y avait 4 clovers, 4 Miniball, 1 GRETINA P3 et un GRETINA QUAD. Ces deux derniers offraient une meilleure résolution en enérgie après correction Doppler grâce une meilleure segmentation et à l'algorithme de décomposition de signal qui permettait de déduire la position de l'interaction des rayons $\gamma$ de manière plus précise. Les résidus furent identifiés par le spectromètre ZeroDegree [55] situé en sortie de la cible secondaire.

L'intensité moyenne du faisceau secondaire de $^{80}$Zn était de l'ordre de 1500 particules par seconde (pps) tandis que le nombre d'événements correspondant à la réaction $^{80}$Zn($^{9}$Be,X)$^{79}$Cu valait environ 6 pps.

# Analyse de données

Afin d'obtenir les spectres $\gamma$ du $^{79}$Cu ou tout autre noyau, nous avons principalement suivi les étapes suivantes, détaillées dans le chapitre 3:

+ Nous avons commencé par supprimer les évènements de bruit de fond, en nous basant sur les caractéristiques des différents détecteurs présents le long de la ligne de faisceau et leurs corrélations. Les mauvais évènements ont été rejetés à l'aide des PPACs dans tous les plans focaux où il étaient présents, la corrélation entre les charges et les temps dans les scintillateurs plastiques, ainsi que la corrélation entre l'énergie déposée dans les chambres d'ionisation (MUSIC) et la charge déposée dans les scintillateurs plastiques. Enfin, les états de charge ont été enlevés en comparant les rigidités magnétiques $B\rho$ mesurées dans les portions successives du spectromètre. L'application simultanée de toutes ces procédures a permis de retirer environ 5% des évènements correspondant à la voie de réaction $^{80}$Zn($^{9}$Be,X)$^{79}$Cu.

+ Suite à cela, nous avons procédé à des corrections empiriques dans le but d'améliorer l'identification des isotopes dans les spectromètres BigRIPS et ZeroDegree. Cette procédure dite correction optique consiste à corriger les dépendances entre les variables de positions et angles des noyaux et le ratio entre leurs masse et charge $A/Q$, dans les différents plans focaux. Ceci est équivalent au rajout de termes d'ordre supérieur dans les matrices de transport du faisceau.

+ Ensuite, il fallait calibrer les temps de vol dans les scintillateurs plastiques. En effet, il y a un délai entre les temps d'enregistrement des évènements dans les plastiques et le vrai instant de passage des ions à travers ces derniers. Ce délai dépend entre autres de la longueur des cables utilisés, et induit un décalage de la valeur du temps de vol des noyaux entre les plans focaux où ces scintillateurs sont placés. Ce temps de vol ($ToF$ pour Time of Flight en anglais) est utilisé pour calculer le rapport entre la masse et la charge des isotopes $A/Q$. Un décalage en temps de vol engendre donc un décalage en $A/Q$. Cette différence est ensuite corrigée en rajoutant un offset global au temps de vol, ajusté de manière à retomber sur la valeur théorique de $A/Q$ pour une espèce nucléaire donnée.

+ Une fois l'identification du faisceau finalisée, il fallait calibrer les détecteurs $\gamma$ constituant le spectromètre HiCARI. Pour ce faire, des données ont été enregistrées avec des sources de calibration permettant de couvrir une gamme d'énergies entre 100 keV et 3 MeV. Les sources utilisées sont celles du $^{60}$Co, $^{152}$Eu, $^{88}$Y et $^{133}$Ba. L'étalonnage a été effectué pour tous les cristaux et segements de tous les détecteurs. Par la même occasion, ces données ont permis d'extraire les résolutions en énergie de chaque cristal pour les implémenter ultérieurement dans les simulations et les rendre plus réalistes.

+ Afin d'obtenir la bonne valeur de l'énergie, la correction de l'effet Doppler nécessite une valeur précise de la vitesse des noyaux au moment de l'émission des photons $\gamma$. Le dispositif expérimental permettait d'obtenir cette vitesse uniquement avant la cible et après celle-ci. De ce fait, nous avions réalisé des simulations avec LISE++ afin d'extrapoler les vitesses mesurées jusqu'au milieu de la cible supposé comme étant le point d'émission des rayons $\gamma$.

+ Enfin, nous avons simulé, avec GEANT4, des fonctions de réponse pour des transitions $\gamma$ d'intérêt, dans les conditions expérimentales avec différentes demi-vies pour les états excités. Ces fonctions ont été ensuite utilisées pour ajuster les spectres $\gamma$ expérimentaux et en extraire les temps de vie de ces états.

# Étude d'un cas de référence

Avant de déterminer les temps de vie des états excités dans le $^{79}$Cu, il fallait d'abord valider la procédure sur un cas connu avec une statistique suffisante. Dans nos données, nous avions choisi d'étudier la voie de réaction $^{80}$Zn($^{9}$Be,X)$^{78}$Zn. En effet, dans le noyau de $^{78}$Zn, la demi-vie du premier état excité $2^+$ à 730 keV avait déjà été mesurée, et la valeur de 18(4) ps avait été retenue [79]. Afin de retrouver cette valeur, nous avions réalisé des simulations avec GEANT4, en utilisant des valeurs différentes de l'énergie (entre 710 keV et 760 keV) et de la demi-vie de l'état excité (entre 0 ps et 40 ps), pour générer des fonctions de réponse. Nous avons ensuite, pour chaque couple de valeurs de l'énergie et du temps de vie, utilisé la fonction de réponse correspondante pour ajuster le spectre $\gamma$ expérimental et extrait une valeur du paramètre $\chi^2$. Ce dernier est un indicateur de la qualité de l'ajustement et donc de l'accord entre les spectres expérimentaux et simulés. Nous avions donc cherché le couple de valeurs pour lequel ce paramètre est minimal. Du fait que le spectromètre HiCARI était consitué de détecteurs différents et disposés à des angles différents, les sous-parties de HiCARI n'avaient pas la même sensibilité aux effets de temps de vie. Ainsi, il fallait effectuer des analyses séparées pour chaque groupe de détecteurs. Nous avions donc séparé dans un premier temps les composantes de détection en 4 parties: Miniball, clovers, P3 et QUAD. Du fait de la meilleure résolution en énergie de ces deux derniers, des minimas de $\chi^2$ ont pu être obtenus, contrairement aux clovers et Miniball. Nous avions une légère différence entre les énergies obtenues avec QUAD et P3, mais les deux nous ont permis de mesurer la bonne valeur pour le temps de vie. Ceci nous a ensuite conduit à privilégier les détecteurs de type GRETINA pour l'analyse du $^{79}$Cu.

# Étude du cas d'intérêt

Après avoir testé la validité de la méthodologie de reconstruction des spectres $\gamma$ et celle de la détermination de la demi-vie, sur le cas du $^{78}$Zn, nous sommes passés au cas du $^{79}$Cu. Les spectres $\gamma$ obtenus après correction Doppler nous avaient permis de confirmer la présence de deux raies qui étaient déjà observées dans la première expérience SEASTAR [5, 49]. Il s'agit des transitions à 656 keV et à 855 keV. Nous avions également tenté une analyse des coïncidences $\gamma\gamma$, mais les faibles statistique et efficacité de HiCARI ne permettaient pas d'observer de raies supplémentaires. Après cela, nous avons appliqué la procédure de minimisation du $\chi^2$ pour déterminer la demi-vie de l'état à 656 keV car sa transition vers le fondamental était la plus intense. Comme l'avait suggéré l'étude du cas de référence du $^{78}$Zn, les seuls détecteurs exploitables étaient ceux de type GRETINA (QUAD et P3). Nous avons ainsi mesuré une énergie $E = 654^{+4}_{-3}$ keV et une période $T_{1/2} = 12^{+11}_{-9}$ ps avec P3, puis $E = 649^{+2}_{-3}$ keV et $T_{1/2} = 11^{+8}_{-8}$ ps avec QUAD. Là aussi, nous avons mesuré deux énergies différentes mais deux valeurs compatibles pour le temps de vie. Vu les faibles valeurs des énergies obtenues par le QUAD vis-à-vis de la littérature, nous avons par la suite retenu la valeur de $T_{1/2} = 12^{+11}_{-9}$ ps obtenue avec P3 pour la discussion et l'interprétation théorique dans le dernier chapitre.

## Discussion et interprétation

N'ayant pas eu le temps de réaliser des calculs théoriques de modèles en couches poussés, nous nous sommes limités à l'étude de systématiques des demi-vies et des probabilités de transitions dans les noyaux riches en neutrons. La courte demi-vie de 12 ps qu'on a obtenue nous a permis de déduire une valeur de $B(E2)$= 19 W.u. qui semble large et qui suggérereait une collectivité importante dans les états du $^{79}$Cu. Cependant, cette valeur est obtenue dans l'hypothèse d'une transition ayant une multipolarité $E2$ pure. Un cas analogue dans la littérature qui est celui de la transition à 403 keV dans le $^{87}$Rb nous a permis de choisir une hypothèse d'une valeur $\delta = 0.24$ qui décrit le rapport de probabilités entre les composantes de type $E2$ et $M1$. En utilisant ces mêmes poids pour la raie à 656 keV dans le cuivre, une valeur de $B(E2)$ de l'ordre de 1 W.u. est obtenue. Ceci suggère que la courte demi-vie n'est pas due à une collectivité accrue des états mais plutôt à la présence de la composante magnétique $M1$ dans la transition, préservant ainsi la possibilité de décrire les états dans le $^{79}$Cu avec une particule individuelle autour d'un coeur doublement magique de $^{78}$Ni.

## Conclusion

Dans cette étude, nous avons pu mesurer la demi-vie du premier état excité dans le $^{79}$Cu, puis nous avons suggéré que les états dans cet élément pouvaient être décrits par un proton de valence autour d'un coeur doublement magique de $^{78}$Ni. Afin d'avoir une image complète sur l'évolution de la collectivité ou du caractère de particule individuelle le long de l'intégralité de la chaine isotopique du cuivre, une mesure des temps de vie des états excités dans le noyau de $^{77}$Cu est requise. À cet effet, l'expérience IDATEN a été proposée et acceptée pour 2025 à RIKEN. L'idée de la collaboration est d'utiliser les scintillateurs $LaBr_3$ pour mesurer les demi-vies des états dans les isotopes de $^{75}$Cu et $^{77}$Cu. On s'intéressera en particulier à la transition à 293 keV dans $^{77}$Cu qui contient juste deux neutrons en moins avant la fermeture de couche à $N = 50$.

# Bibliography

[1] E. Rutherford. The scattering of $\alpha$ and $\beta$ particles by matter and the structure of the atom. *The London, Edinburgh, and Dublin Philosophical Magazine and Journal of Science*, 21(125):669–688, 1911.

[2] M. Goeppert Mayer. On Closed Shells In Nuclei ii. *Physical Review*, 75:1969–1970, June 1949.

[3] O. Haxel, J. H. D. Jensen, and H. E. Suess. On the "magic numbers" in nuclear structure. *Physical Review*, 75:1766, June 1949.

[4] P. Cottle. Doubly magic tin. *Nature*, 465(430-431), 2010.

[5] L. Olivier. *Nuclear structure in the vicinity of* $^{78}Ni$ *: In-beam gamma-ray spectroscopy of* $^{79}Cu$ *through proton knockout.* PhD thesis, Université Paris-Saclay, 2017.

[6] O. Sorlin and M.-G. Porquet. Nuclear magic numbers: New features far from stability. *Progress in Particle and Nuclear Physics*, 61(2):602–673, October 2008.

[7] Wienholtz et al. Masses of exotic calcium isotopes pin down nuclear forces. *Nature*, 498:346–349, October 2013.

[8] C. R. Hoffman et al. Evidence for a doubly magic $^{24}O. Phys.Lett.B, 672 : 17 - -21, 2009$.

[9] K. Tshoo, Y. Satou, H. Bhang, S. Choi, T. Nakamura, Y. Kondo, S. Deguchi, Y. Kawada, N. Kobayashi, Y. Nakayama, K. N. Tanaka, N. Tanaka, N. Aoi, M. Ishihara, T. Motobayashi, H. Otsu, H. Sakurai, S. Takeuchi, Y. Togano, K. Yoneda, Z. H. Li, F. Delaunay, J. Gibelin, F. M. Marqués, N. A. Orr, T. Honda, M. Matsushita, T. Kobayashi, Y. Miyashita, T. Sumikama, K. Yoshinaga, S. Shimoura, D. Sohler, T. Zheng, and Z. X. Cao. $N = 16$ Spherical Shell Closure in $^{24}\mathbf{O}$. *Phys. Rev. Lett.*, 109:022501, Jul 2012.

[10] D. Steppenbeck et al. Evidence for a new nuclear ‘magic number’ from the level structure of $^{54}Ca. Nature, 502 : 207\breve{}210, October$ 2013.

[11] B. Bastin, S. Grévy, D. Sohler, O. Sorlin, Zs. Dombrádi, N. L. Achouri, J. C. Angélique, F. Azaiez, D. Baiborodin, R. Borcea, C. Bourgeois, A. Buta, A. Bürger, R. Chapman, J. C. Dalouzy, Z. Dlouhy, A. Drouard, Z. Elekes, S. Franchoo, S. Iacob, B. Laurent, M. Lazar, X. Liang, E. Liénard, J. Mrazek, L. Nalpas, F. Negoita, N. A. Orr, Y. Penionzhkevich, Zs. Podolyák, F. Pougheon, P. Roussel-Chomaz, M. G. Saint-Laurent, M. Stanoiu, I. Stefan, F. Nowacki, and A. Poves. Collapse of the N=28 Shell Closure in $^{42}$Si. *Phys. Rev. Lett.*, 99:022503, Jul 2007.

[12] O. Sorlin and M-G. Porquet. Evolution of the N= 28 shell closure: a test bench for nuclear forces. *Physica Scripta*, T152:014003, January 2013.

[13] I. Murray. *Mapping the Big Island of Deformation around N=20 and 28.* PhD thesis, Université Paris-Saclay, 2019.

[14] N. A. Smirnova, K. Heyde, B. Bally, F. Nowacki, and K. Sieja. Nuclear shell evolution and in-medium *N\$interaction.Phys.Rev.C*, 86 : 034314, *Sep*2012.

[15] L. Coraggio, G. De Gregorio, T. Fukui, A. Gargano, Y. Z. Ma, Z. H. Cheng, and F. R. Xu. The role of three-nucleon potentials within the shell model: Past and present, 2023.

[16] A. P. Zuker. Three-Body Monopole Corrections to Realistic Interactions. *Phys. Rev. Lett.*, 90:042502, Jan 2003.

[17] G. Hagen, M. Hjorth-Jensen, G. R. Jansen, R. Machleidt, and T. Papenbrock. Continuum effects and three-nucleon forces in neutron-rich oxygen isotopes. *Phys. Rev. Lett.*, 108:242501, Jun 2012.

[18] Takaharu Otsuka, Toshio Suzuki, Jason D. Holt, Achim Schwenk, and Yoshinori Akaishi. Three-body forces and the limit of oxygen isotopes. *Phys. Rev. Lett.*, 105:032501, Jul 2010.

[19] N. A. Smirnova, K. Heyde, B. Bally, F. Nowacki, and K. Sieja. Nuclear shell evolution and in-medium *nn* interaction. *Phys. Rev. C*, 86:034314, Sep 2012.

[20] A. Poves and A. Zuker. Theoretical spectroscopy and the fp shell. *Physics Reports*, 70(4):235–314, 1981.

[21] Yutaka Utsuno, Takaharu Otsuka, Takahiro Mizusaki, and Michio Honma. Varying shell gap and deformation in $N \sim 20$ unstable nuclei studied by the Monte Carlo shell model. *Phys. Rev. C*, 60:054315, Oct 1999.

[22] A. Ozawa, T. Kobayashi, T. Suzuki, K. Yoshida, and I. Tanihata. New magic number, $N = 16$, near the neutron drip line. *Phys. Rev. Lett.*, 84:5493–5495, Jun 2000.

[23] Takaharu Otsuka, Rintaro Fujimoto, Yutaka Utsuno, B. Alex Brown, Michio Honma, and Takahiro Mizusaki. Magic numbers in exotic nuclei and spin-isospin properties of the *NN* interaction. *Phys. Rev. Lett.*, 87:082502, Aug 2001.

[24] Kenneth S. Krane. *Introductory Nuclear Physics.* John Wiley & Sons, New York, 1987.

[25] K.E.G. Löbner, M. Vetter, and V. Hönig. Nuclear intrinsic quadrupole moments and deformation parameters. *Atomic Data and Nuclear Data Tables*, 7(5):495–564, 1970.

[26] Kris L. G. Heyde. *The Nuclear Shell Model.* Springer-Verlag, Berlin, 2nd edition, 1994.

[27] T. Kibédi, T.W. Burrows, M.B. Trzhaskovskaya, P.M. Davidson, and C.W. Nestor. Evaluation of theoretical conversion coefficients using BrIcc. *Nuclear Instruments and Methods in Physics Research Section A: Accelerators, Spectrometers, Detectors and Associated Equipment*, 589(2):202–229, 2008.

[28] F. Nowacki, A. Poves, E. Caurier, and B. Bounthong. Shape coexistence in $^{78}$Ni as the portal to the fifth island of inversion. *Phys. Rev. Lett.*, 117:272501, Dec 2016.

[29] C. Santamaria, C. Louchart, A. Obertelli, V. Werner, P. Doornenbal, F. Nowacki, G. Authelet, H. Baba, D. Calvet, F. Château, A. Corsi, A. Delbart, J.-M. Gheller, A. Gillibert, T. Isobe, V. Lapoux, M. Matsushita, S. Momiyama, T. Motobayashi, M. Niikura, H. Otsu, C. Péron, A. Peyaud, E. C. Pollacco, J.-Y. Roussé, H. Sakurai, M. Sasano, Y. Shiga, S. Takeuchi, R. Taniuchi, T. Uesaka, H. Wang, K. Yoneda, F. Browne, L. X. Chung, Zs. Dombradi, S. Franchoo, F. Giacoppo, A. Gottardo, K. Hadynska-Klek, Z. Korkulu, S. Koyama, Y. Kubota, J. Lee, M. Lettmann, R. Lozeva, K. Matsui, T. Miyazaki, S. Nishimura, L. Olivier, S. Ota, Z. Patel, N. Pietralla, E. Sahin, C. Shand, P.-A. Söderström, I. Stefan, D. Steppenbeck, T. Sumikama, D. Suzuki, Zs. Vajta, J. Wu, and Z. Xu. Extension of the $N = 40$ island of inversion towards $N = 50$: Spectroscopy of $^{66}$Cr, $^{70,72}$Fe. *Phys. Rev. Lett.*, 115:192501, Nov 2015.

[30] Z. Y. Xu, S. Nishimura, G. Lorusso, F. Browne, P. Doornenbal, G. Gey, H.-S. Jung, Z. Li, M. Niikura, P.-A. Söderström, T. Sumikama, J. Taprogge, Zs. Vajta, H. Watanabe, J. Wu, A. Yagi, K. Yoshinaga, H. Baba, S. Franchoo, T. Isobe, P. R. John, I. Kojouharov, S. Kubono, N. Kurz, I. Matea, K. Matsui, D. Mengoni, P. Morfouace, D. R. Napoli, F. Naqvi, H. Nishibata, A. Odahara, E. Şahin, H. Sakurai, H. Schaffner, I. G. Stefan, D. Suzuki, R. Taniuchi, and V. Werner. $\beta$-decay half-lives of $^{76,77}$Co,

$^{79,80}$Ni, and $^{81}$Cu: Experimental indication of a doubly magic $^{78}$Ni. *Phys. Rev. Lett.*, 113:032505, Jul 2014.

[31] P. Hosmer, H. Schatz, A. Aprahamian, O. Arndt, R. R. C. Clement, A. Estrade, K. Farouqi, K.-L. Kratz, S. N. Liddick, A. F. Lisetskiy, P. F. Mantica, P. Möller, W. F. Mueller, F. Montes, A. C. Morton, M. Ouellette, E. Pellegrini, J. Pereira, B. Pfeiffer, P. Reeder, P. Santi, M. Steiner, A. Stolz, B. E. Tomlin, W. B. Walters, and A. Wöhr. Half-lives and branchings for $\beta$-delayed neutron emission for neutron-rich Co-Cu isotopes in the $r$-process. *Phys. Rev. C*, 82:025806, Aug 2010.

[32] C. Mazzocchi, R. Grzywacz, J.C. Batchelder, C.R. Bingham, D. Fong, J.H. Hamilton, J.K. Hwang, M. Karny, W. Krolas, S.N. Liddick, A.F. Lisetskiy, A.C. Morton, P.F. Mantica, W.F. Mueller, K.P. Rykaczewski, M. Steiner, A. Stolz, and J.A. Winger. Low energy structure of even–even Ni isotopes close to $^{78}$Ni. *Physics Letters B*, 622(1):45–54, 2005.

[33] M. Madurga, R. Surman, I. N. Borzov, R. Grzywacz, K. P. Rykaczewski, C. J. Gross, D. Miller, D. W. Stracener, J. C. Batchelder, N. T. Brewer, L. Cartegni, J. H. Hamilton, J. K. Hwang, S. H. Liu, S. V. Ilyushkin, C. Jost, M. Karny, A. Korgul, W. Królas, A. Kuźniak, C. Mazzocchi, A. J. Mendez, K. Miernik, S. W. Padgett, S. V. Paulauskas, A. V. Ramayya, J. A. Winger, M. Woli ńska Cichocka, and E. F. Zganjar. New half-lives of $r$-process Zn and Ga isotopes measured with electromagnetic separation. *Phys. Rev. Lett.*, 109:112501, Sep 2012.

[34] National Nuclear Data Center. National Nuclear Data Center, 2013.

[35] O. Sorlin, S. Leenhardt, C. Donzaud, J. Duprat, F. Azaiez, F. Nowacki, H. Grawe, Zs. Dombrádi, F. Amorini, A. Astier, D. Baiborodin, M. Belleguic, C. Borcea, C. Bourgeois, D. M. Cullen, Z. Dlouhy, E. Dragulescu, M. Górska, S. Grévy, D. Guillemaud-Mueller, G. Hagemann, B. Herskind, J. Kiener, R. Lemmon, M. Lewitowicz, S. M. Lukyanov, P. Mayet, F. de Oliveira Santos, D. Pantalica, Yu.-E. Penionzhkevich, F. Pougheon, A. Poves, N. Redon, M. G. Saint-Laurent, J. A. Scarpaci, G. Sletten, M. Stanoiu, O. Tarasov, and Ch. Theisen. ${}^{68}_{28}$Ni$_{40}$: Magicity versus superfluidity. *Phys. Rev. Lett.*, 88:092501, Feb 2002.

[36] O. Perru, O. Sorlin, S. Franchoo, F. Azaiez, E. Bouchez, C. Bourgeois, A. Chatillon, J. M. Daugas, Z. Dlouhy, Zs. Dombrádi, C. Donzaud, L. Gaudefroy, H. Grawe, S. Grévy, D. Guillemaud-Mueller, F. Hammache, F. Ibrahim, Y. Le Coz, S. M. Lukyanov, I. Matea, J. Mrazek, F. Nowacki, Yu.-E. Penionzhkevich, F. de Oliveira Santos, F. Pougheon, M. G. Saint-Laurent, G. Sletten, M. Stanoiu, C. Stodel, Ch. Theisen, and

D. Verney. Enhanced core polarization in $^{70}$Ni and $^{74}$Zn. *Phys. Rev. Lett.*, 96:232501, Jun 2006.

[37] N. Aoi, S. Kanno, S. Takeuchi, H. Suzuki, D. Bazin, M.D. Bowen, C.M. Campbell, J.M. Cook, D.-C. Dinca, A. Gade, T. Glasmacher, H. Iwasaki, T. Kubo, K. Kurita, T. Motobayashi, W.F. Mueller, T. Nakamura, H. Sakurai, M. Takashina, J.R. Terry, K. Yoneda, and H. Zwahlen. Enhanced collectivity in 74Ni. *Physics Letters B*, 692(5):302–306, 2010.

[38] T. Marchi, G. de Angelis, J. J. Valiente-Dobón, V. M. Bader, T. Baugher, D. Bazin, J. Berryman, A. Bonaccorso, R. Clark, L. Coraggio, H. L. Crawford, M. Doncel, E. Farnea, A. Gade, A. Gadea, A. Gargano, T. Glasmacher, A. Gottardo, F. Gramegna, N. Itaco, P. R. John, R. Kumar, S. M. Lenzi, S. Lunardi, S. McDaniel, C. Michelagnoli, D. Mengoni, V. Modamio, D. R. Napoli, B. Quintana, A. Ratkiewicz, F. Recchia, E. Sahin, R. Stroberg, D. Weisshaar, K. Wimmer, and R. Winkler. Quadrupole transition strength in the $^{74}$Ni nucleus and core polarization effects in the neutron-rich Ni isotopes. *Phys. Rev. Lett.*, 113:182501, Oct 2014.

[39] K. Kolos, D. Miller, R. Grzywacz, H. Iwasaki, M. Al-Shudifat, D. Bazin, C. R. Bingham, T. Braunroth, G. Cerizza, A. Gade, A. Lemasson, S. N. Liddick, M. Madurga, C. Morse, M. Portillo, M. M. Rajabali, F. Recchia, L. L. Riedinger, P. Voss, W. B. Walters, D. Weisshaar, K. Whitmore, K. Wimmer, and J. A. Tostevin. Direct lifetime measurements of the excited states in $^{72}$Ni. *Phys. Rev. Lett.*, 116:122502, Mar 2016.

[40] O. Wieland, A. Bracco, F. Camera, R. Avigo, H. Baba, N. Nakatsuka, T. Aumann, S. R. Banerjee, G. Benzoni, K. Boretzky, C. Caesar, S. Ceruti, S. Chen, F. C. L. Crespi, V. Derya, P. Doornenbal, N. Fukuda, A. Giaz, K. Ieki, N. Kobayashi, Y. Kondo, S. Koyama, T. Kubo, M. Matsushita, B. Million, T. Motobayashi, T. Nakamura, M. Nishimura, H. Otsu, T. Ozaki, A. T. Saito, H. Sakurai, H. Scheit, F. Schindler, P. Schrock, Y. Shiga, M. Shikata, S. Shimoura, D. Steppenbeck, T. Sumikama, S. Takeuchi, R. Taniuchi, Y. Togano, J. Tscheuschner, J. Tsubota, H. Wang, K. Wimmer, and K. Yoneda. Low-lying dipole response in the unstable $^{70}$Ni nucleus. *Phys. Rev. C*, 98:064313, Dec 2018.

[41] R. Taniuchi et al. $^{78}$Ni revealed as a doubly magic stronghold against nuclear deformation. *Nature*, 569:53–58, May 2019.

[42] S. Takeuchi, T. Motobayashi, Y. Togano, M. Matsushita, N. Aoi, K. Demichi, H. Hasegawa, and H. Murakami. DALI2: A NaI(Tl) detector array for measurements of $\gamma$ rays from fast nuclei. *Nuclear Instruments and Methods in Physics Research Sec-*

*tion A: Accelerators, Spectrometers, Detectors and Associated Equipment*, 763:596–603, 2014.

[43] S. Franchoo, M. Huyse, K. Kruglov, Y. Kudryavtsev, W. F. Mueller, R. Raabe, I. Reusen, P. Van Duppen, J. Van Roosbroeck, L. Vermeeren, A. Wöhr, K.-L. Kratz, B. Pfeiffer, and W. B. Walters. Beta decay of $^{68-74}$Ni and level structure of neutron-rich Cu isotopes. *Phys. Rev. Lett.*, 81:3100–3103, Oct 1998.

[44] S. Franchoo, M. Huyse, K. Kruglov, Y. Kudryavtsev, W. F. Mueller, R. Raabe, I. Reusen, P. Van Duppen, J. Van Roosbroeck, L. Vermeeren, A. Wöhr, H. Grawe, K.-L. Kratz, B. Pfeiffer, and W. B. Walters. Monopole migration in $^{69,71,73}$Cu observed from $\beta$ decay of laser-ionized $^{68-74}$Ni. *Phys. Rev. C*, 64:054308, Oct 2001.

[45] K. T. Flanagan, P. Vingerhoets, M. Avgoulea, J. Billowes, M. L. Bissell, K. Blaum, B. Cheal, M. De Rydt, V. N. Fedosseev, D. H. Forest, Ch. Geppert, U. Köster, M. Kowalska, J. Krämer, K. L. Kratz, A. Krieger, E. Mané, B. A. Marsh, T. Materna, L. Mathieu, P. L. Molkanov, R. Neugart, G. Neyens, W. Nörtershäuser, M. D. Seliverstov, O. Serot, M. Schug, M. A. Sjoedin, J. R. Stone, N. J. Stone, H. H. Stroke, G. Tungate, D. T. Yordanov, and Yu. M. Volkov. Nuclear spins and magnetic moments of $^{71,73,75}$Cu: Inversion of $\pi 2p_{3/2}$ and $\pi 1f_{5/2}$ levels in $^{75}$Cu. *Phys. Rev. Lett.*, 103:142501, Oct 2009.

[46] C. Petrone, J. M. Daugas, G. S. Simpson, M. Stanoiu, C. Plaisir, T. Faul, C. Borcea, R. Borcea, L. Cáceres, S. Calinescu, R. Chevrier, L. Gaudefroy, G. Georgiev, G. Gey, O. Kamalou, F. Negoita, F. Rotaru, O. Sorlin, and J. C. Thomas. Nearly degenerate isomeric states of $^{75}$Cu. *Phys. Rev. C*, 94:024319, Aug 2016.

[47] U. Köster, N. J. Stone, K. T. Flanagan, J. Rikovska Stone, V. N. Fedosseev, K. L. Kratz, B. A. Marsh, T. Materna, L. Mathieu, P. L. Molkanov, M. D. Seliverstov, O. Serot, A. M. Sjödin, and Yu. M. Volkov. In-source laser spectroscopy of $^{75,77,78}$Cu: Direct evidence for a change in the quasiparticle energy sequence in $^{75,77}$Cu and an absence of longer-lived isomers in $^{78}$Cu. *Phys. Rev. C*, 84:034320, Sep 2011.

[48] E. Sahin, F. L. Bello Garrote, Y. Tsunoda, T. Otsuka, G. de Angelis, A. Görgen, M. Niikura, S. Nishimura, Z. Y. Xu, H. Baba, F. Browne, M.-C. Delattre, P. Doornenbal, S. Franchoo, G. Gey, K. Hadyńska-Klęk, T. Isobe, P. R. John, H. S. Jung, I. Kojouharov, T. Kubo, N. Kurz, Z. Li, G. Lorusso, I. Matea, K. Matsui, D. Mengoni, P. Morfouace, D. R. Napoli, F. Naqvi, H. Nishibata, A. Odahara, H. Sakurai, H. Schaffner, P.-A. Söderström, D. Sohler, I. G. Stefan, T. Sumikama, D. Suzuki, R. Taniuchi, J. Taprogge, Z. Vajta, H. Watanabe, V. Werner, J. Wu, A. Yagi, M. Yal-

cinkaya, and K. Yoshinaga. Shell evolution towards $^{78}$Ni: Low-lying states in $^{77}$Cu. *Phys. Rev. Lett.*, 118:242502, Jun 2017.

[49] L. Olivier et al. Persistence of the Z=28 Shell Gap Around $^{78}Ni$: First spectroscopy of $^{79}Cu$. *Physical Review Letters*, 119:192501, 2017.

[50] National Nuclear Data Center. National Nuclear Data Center, 2024. Accessed: 2024-06-05.

[51] B. Zeidman and J. A. Nolen. Mass and low-lying energy levels of $^{69}$Cu. *Phys. Rev. C*, 18:2122–2126, Nov 1978.

[52] K. Wimmer, P. Doornenbal, N. Aoi, H. Baba, F. Browne, C. Campbell, H. Crawford, H. De Witte, C. Fransen, H. Hess, S. Iwazaki, J. Kim, A. Kohda, T. Koiwai, B. Mauss, B. Moon, T. Parry, P. Reiter, D. Suzuki, R. Taniuchi, S. Thiel, and Y. Yamamoto. HiCARI: High-resolution Cluster Array at RIBF. *RIKEN Accelerator Progress Report*, 54, 2021.

[53] R. Taniuchi, S. Franchoo, D. Suzuki, N. Aoi, H. Baba, F. Browne, C. M. Campbell, S. Chen, R. Crane, H. L. Crawford, H. De Witte, P. Doornenbal, C. Fransen, N. Fukuda, H. Hess, E. Ideguchi, S. Iwazaki, J. Kim, A. Kohda, T. Koike, T. Koiwai, B. Mauss, R. Mizuno, B Moon, M. Niikura, D. Nishimura, T. Parry, M. Petri, P. Reiter, H. Sakurai, Y. Shimizu, H. Suzuki, H. Takahashi, H. Takeda, S. Thiel, K. Wimmer, Y. Yamamoto, and M. Yoshimoto. RIBF181: $\gamma$-ray spectroscopy in the vicinity of $^{78}$Ni. *RIKEN Accelerator Progress Report*, 55, 2022.

[54] H. Okuno, N. Fukunishi, and O. and Kamigaito. Progress of RIBF accelerators. *Progress of Theoretical and Experimental Physics*, 1, 2012.

[55] T. Kubo, D. Kameda, H. Suzuki, N. Fukuda, H. Takeda, Y. Yanagisawa, M. Ohtake, K. Kusaka, K. Yoshida, N. Inabe, T. Ohnishi, A. Yoshida, K. Tanaka, and Y. Mizoi. BigRIPS separator and ZeroDegree spectrometer at RIKEN RI Beam Factory. *Progress of Theoretical and Experimental Physics*, 1(03C003), 2012.

[56] J. P. Dufour, R. Del Moral, H. Emmermann, F. Hubert, D. Jean, C. Poinot, M. S. Pravikoff, A. Fleury, H. Delagrange, and K.-H. Schmidt. Projectile fragments isotopic separation: Application to the lise spectrometer at GANIL. *Nuclear Instruments and Methods in Physics Research Section A: Accelerators, Spectrometers, Detectors and Associated Equipment*, 248.2-3(pp. 267-281), 1986.

[57] K. H. Schmidt, H. Geissel, G. Muenzenberg, J. P. Dufour, and E. Hanelt. The momentum-loss achromat - a new method for the isotopical separation of relativistic

heavy ions. *Nuclear Instruments and Methods in Physics Research Section A: Accelerators, Spectrometers, Detectors and Associated Equipment*, 260.2-3(pp. 287-303), 1987.

[58] D. J. Morrissey and B. M. Sherrill. In-flight separation of projectile fragments. *The Euroschool Lectures on Physics with Exotic Beams*, 1, Springer-Verlag(pp. 113-134), 2004.

[59] N. Fukuda, T. Kubo, T. Ohnishi, N. Inabe, H. Takeda, D. Kameda, and H. Suzuki. Identification and Separation of Radioactive Isotope Beams by the BigRIPS Separator at the RIKEN RI Beam Factory. *Nuclear Instruments and Methods in Physics Research Section B: Beam Interactions with Materials and Atoms*, 317(pp. 323-332), 2013.

[60] H. Kumagai, A. Ozawa, N. Fukuda, K. Smmerer, and I. Tanihata. Delay-line PPAC for high-energy light ions. *Nuclear Instruments and Methods in Physics Research A*, 470(pp. 562-570), 2001.

[61] H. Kumagai, T. Ohnishi, N. Fukuda, H. Takeda, D. Kameda, N. Inabe, K. Yoshida, and T. Kubo. Development of Parallel Plate Avalanche Counter (PPAC) for BigRIPS fragment separator. *Nuclear Instruments and Methods in Physics Research B*, 317(pp. 717-727), 2013.

[62] K. Kimura, T. Izumikawa, R. Koyama, T. Ohnishi, T. Ohtsubo, A. Ozawa, W. Shinozaki, T. Suzuki, M. Takahashi, I. Tanihata, T. Yamaguchi, and Y. Yamaguchi. High-rate particle identification of high-energy heavy ions using a tilted electrode gas ionization chamber. *Nuclear Instruments and Methods in Physics Research A*, 538(pp. 608-614), 2005.

[63] R. Grzywacz, R. Anne, G. Auger, D. Bazin, C. Borcea, V. Borrel, J. M. Corre, T. Drfler, A. Fomichov, M. Gaelens, D. Guillemaud-Mueller, R. Hue, M. Huyse, Z. Janas, H. Keller, M. Lewitowicz, S. Lukyanov, A. C. Mueller, Yu. Penionzhkevich, M. Pftzner, F. Pougheon, K. Rykaczewski, M. G. Saint-Laurent, K. Schmidt, W.-D Schmidt-Ott, O. Sorlin, J. Szerypo, O. Tarasov, J. Wauters, and J. Żylicz. Identification of $\mu$s-isomers produced in the fragmentation of a $^{112}Sn$ beam. *Physics Letters B*, 355, 3-4(pp. 439-446), 1995.

[64] H. Kumagai and K. Yoshida. PPAC for Beam Profile Monitor at the RIPS. *RIKEN Accel. Prog. Rep*, 28(pp. 127), 1995.

[65] H. Kumagai, T. Ohnishi, N. Fukuda, H. Takeda, D. Kameda, N. Inabe, K. Yoshida, and T. Kubo. Development of Parallel Plate Avalanche Counter (PPAC) for BigRIPS

fragment separator. *Nuclear Instruments and Methods in Physics Research Section B: Beam Interactions with Materials and Atoms*, 317, B(pp. 717-727), 2013.

[66] J. Eberth et al. MINIBALL A Ge detector array for radioactive ion beam facilities. *Progress in Particle and Nuclear Physics.*, 46(1):389–398, 2001.

[67] S. Pascalis et al. The performance of the Gamma-Ray Energy Tracking In-beam Nuclear Array GRETINA. *Nuclear Instruments and Methods in Physics Research Section A: Accelerators, Spectrometers, Detectors and Associated Equipment*, 709:44–55, 2013.

[68] L. Plagnol. *Intruder states and shape coexistence beyond N=50 close to 78Ni studied by neutron knockout at RIBF-RIKEN.* PhD thesis, Université de Caen Normandie, 2023.

[69] V.S Praher et al. Sensitivity of GRETINA position resolution to hole mobility. *Nuclear Instruments and Methods in Physics Research Section A: Accelerators, Spectrometers, Detectors and Associated Equipment*, 846:50–55, 2017.

[70] J.T. Anderson et al. Data acquisition and trigger system of the Gamma Ray Energy Tracking In-Beam Nuclear Array (GRETINA). *2007 IEEE Nuclear Science Symposium Conference Record.*, 3:1751–1756, 2007.

[71] A. korichi and T. Lauritsen. Tracking $\gamma$-rays in highly segmented HPGe detectors: A review of AGATA and GRETINA. *The European Physics Journal A*, 55, 2019.

[72] H. Baba, T. Ichihara, T. Ohnishi, S. Takeuchi, K. Yoshida, Y. Watanabe, S. Ota, and S. Shimoura. New data acquisition system for the RIKEN Radioactive Isotope Beam Factory. *Nuclear Instruments and Methods in Physics Research A*, 616(65-68), 2010.

[73] O.B. Tarasov and D. Bazin. LISE++: Radioactive beam production with in-flight separators. *Nuclear Instruments and Methods in Physics Research Section B: Beam Interactions with Materials and Atoms.*, 266(4657-4664), 2008.

[74] G. F. Knoll. *Radiation Detection and Measurement.* John Wiley & Sons, Inc, 4th edition, 2010.

[75] S. Collaboation. Source activities. *url: https://www.nishina.riken.jp/collaboration/SUNFLOWER/misc/util/sources.php.*

[76] K. Wimmer. Simulations for HiCARI the high resolution cluster array at the RIBF. 2019.

[77] K. Wimmer. Simulations for the High Resolution array. *High Resolution Gamma-Ray Spectroscopy at the RIBF*, 2019.

[78] J.M. Daugas et al. The $8^+$ isomer in $^{78}Zn$ and the doubly magic character of $^{78}Ni$. *Physics Letters B*, 476:213–218, 2000.

[79] J. Van de Walle et al. Low-energy Coulomb excitation of neutron-rich zinc isotopes. *Physical Review C*, 79:014309, 2009.

[80] Ameenah R. Farhan and B. Singh. *Nucl. Data Sheets 110, 1917*, 2009.

[81] Y. Avni. Energy spectra of X-ray clusters of galaxies . *Astrophysical Journal*, 210:642–646, 1976.

[82] R. G. Sachs and M. Ross. Evidence for non-additivity of nucleon moments. *Phys. Rev.*, 84:379–380, Oct 1951.

[83] Larry Spruch and Aubey Rotenberg. Interaction contribution to nuclear isomerism. *Phys. Rev.*, 103:365–373, Jul 1956.

[84] I. Stefanescu, G. Georgiev, D. L. Balabanski, N. Blasi, A. Blazhev, N. Bree, J. Cederkäll, T. E. Cocolios, T. Davinson, J. Diriken, J. Eberth, A. Ekström, D. Fedorov, V. N. Fedosseev, L. M. Fraile, S. Franchoo, K. Gladnishki, M. Huyse, O. Ivanov, V. Ivanov, J. Iwanicki, J. Jolie, T. Konstantinopoulos, Th. Kröll, R. Krücken, U. Köster, A. Lagoyannis, G. Lo Bianco, P. Maierbeck, B. A. Marsh, P. Napiorkowski, N. Patronis, D. Pauwels, G. Rainovski, P. Reiter, K. Riisager, M. Seliverstov, G. Sletten, J. Van de Walle, P. Van Duppen, D. Voulot, N. Warr, F. Wenander, and K. Wrzosek. Interplay between single-particle and collective effects in the odd-$A$ Cu isotopes beyond $N = 40$. *Phys. Rev. Lett.*, 100:112502, Mar 2008.

[85] K. P. Singh, D. C. Tayal, and H. S. Hans. Low-lying levels in Cu and Zn isotopes. *Phys. Rev. C*, 58:1980–1985, Oct 1998.

[86] Y. Ichikawa, H. Nishibata, Y. Tsunoda, A. Takamine, K. Imamura, T. Fujita, T. Sato, S. Momiyama, Y. Shimizu, D. S. Ahn, K. Asahi, H. Baba, D. L. Balabanski, F. Boulay, J. M. Daugas, T. Egami, N. Fukuda, C. Funayama, T. Furukawa, G. Georgiev, A. Gladkov, N. Inabe, Y. Ishibashi, T. Kawaguchi, T. Kawamura, Y. Kobayahi, S. Kojima, A. Kusoglu, I. Mukul, M. Niikura, T. Nishizaka, A. Odahare, Y. Ohtomo, T. Otsuka, D. Ralet, G. S. Simpson, T. Sumikama, H. Suzuki, H. Takeda, L. C. Tao, Y. Togano, D. Tominaga, H. Ueno, H. Yamazaki, and X. F. Yang. Interplay between nuclear shell evolution and shape deformation revealed by the magnetic moment of Cu-75. *Nature Physics*, 15(4):321–325, April 2019.

[87] K. Sieja and F. Nowacki. Shell quenching in $^{78}$Ni: A hint from the structure of neutron-rich copper isotopes. *Phys. Rev. C*, 81:061303, Jun 2010.

[88] S.E. Arnell, A. Nilsson, and O. Stankiewicz. States of high spin in $^{87}$Sr, $^{88}$Sr and $^{89}$Sr. *Nuclear Physics A*, 241(1):109–134, 1975.

[89] L. P. Ekstrom, G. D. Jones, F. Kearns, T. P. Morrison, A. Nilsson, V. Paar, P. J. Twin, R. Wadsworth, E. Wallander, and N. J. Ward. Gamma-ray spectroscopy on $^{87}$Sr and the energy-B(E2) rule. *Journal of Physics G: Nuclear Physics*, 7(1):85, jan 1981.

[90] J. Bisping, J. Ernst, F. Rauch, and B. Seim. Transition rates of low-lying states in $^{89}$Zr by study of the $^{86}$Sr($\alpha$, $n\gamma$) reaction. *Nuclear Physics A*, 230(2):221–234, 1974.

[91] J. P. Omtvedt, B. Fogelberg, and P. Hoff. The decay of $^{85}As$. *Zeitschrift fur Physik A Hadrons and Nuclei*, 339:349–353, 1991.

[92] J.V. Kratz, H. Franz, N. Kaffrel, and G. Herrmann. Gamma-ray emission from $^{80-86}$As isotopes. *Nuclear Physics A*, 250(1):13–37, 1975.

[93] Giacomo de Angelis. Nuclear structure far from stability at LNL: From high intensity stable to radioactive nuclear beams. *Nuclear Physics A*, 787(1):74–83, 2007. Proceedings of the Ninth International Conference on Nucleus-Nucleus Collisions.

[94] M. G. Porquet et al. High-spin excitations of $^{81,82,83,85}$Se : Competing single-particle and collective structures around N = 50. *The European Physical Journal A*, 39:295–306, 2009.

[95] J. S. Thomas, G. Arbanas, D. W. Bardayan, J. C. Blackmon, J. A. Cizewski, D. J. Dean, R. P. Fitzgerald, U. Greife, C. J. Gross, M. S. Johnson, K. L. Jones, R. L. Kozub, J. F. Liang, R. J. Livesay, Z. Ma, B. H. Moazen, C. D. Nesaraja, D. Shapira, M. S. Smith, and D. W. Visser. Single-neutron excitations in neutron-rich $^{83}$Ge and $^{85}$Se. *Phys. Rev. C*, 76:044302, Oct 2007.

[96] J. Kurpeta, W. Urban, T. Materna, H. Faust, U. Köster, J. Rissanen, T. Rząca-Urban, C. Mazzocchi, A. G. Smith, J. F. Smith, J. P. Greene, and I. Ahmad. Low-spin structure of $^{85}$Se and the $\beta n$ branching of $^{85}$As. *Phys. Rev. C*, 85:027302, Feb 2012.

[97] F. Didierjean, D. Verney, G. Duchêne, J. Litzinger, K. Sieja, A. Dewald, A. Goasduff, R. Lozeva, C. Fransen, G. de Angelis, S. Aydin, D. Bazzacco, A. Bracco, S. Bottoni, L. Corradi, F. Crespi, E. Ellinger, E. Farnea, E. Fioretto, S. Franchoo, A. Gottardo, L. Grocutt, M. Hackstein, F. Ibrahim, K. Kolos, S. Leoni, S. Lenzi, S. Lunardi, R. Menegazzo, D. Mengoni, C. Michelagnoli, T. Mijatovic, V. Modamio, O. Möller, G. Montagnoli, D. Montanari, A. I. Morales, D. Napoli, M. Niikura, F. Recchia, E. Sahin, F. Scarlassara, L. Sengele, S. Szilner, J. F. Smith, A. M. Stefanini, C. Ur, J. J. Valiente-Dobón, and V. Vandone. Neutron effective single-particle energies above

$^{78}$Ni: A hint from lifetime measurements in the $N = 51$ isotones $^{85}$Se and $^{87}$Kr. *Phys. Rev. C*, 96:044320, Oct 2017.

[98] E. Wallander, A. Nilsson, L.P. Ekström, G.D. Jones, F. Kearns, T.P. Morrison, H.G. Price, P.J. Twin, R. Wadsworth, and N.J. Ward. States in $^{89}$Sr excited by the $^{86}$Kr$(\alpha, n)^{89}$Sr reaction. *Nuclear Physics A*, 361(2):387–398, 1981.

[99] M.J.A. De Voigt and R.N. Boyd. Gamma-ray decay scheme of $^{89}$Sr from the $^{88}$Sr(d, p$\gamma$)$^{89}$Sr reaction. *Nuclear Physics A*, 228(2):301–313, 1974.

[100] E. E. Peters, A. Chakraborty, B. P. Crider, B. H. Davis, M. K. Gnanamani, M. T. McEllistrem, F. M. Prados-Estévez, J. R. Vanhoy, and S. W. Yates. Level lifetimes in the stable Zr nuclei: Effects of chemical properties in Doppler-shift measurements. *Phys. Rev. C*, 88:024317, Aug 2013.

[101] J. Dudouet, A. Lemasson, G. Maquart, F. Nowacki, D. Verney, M. Rejmund, G. Duchêne, O. Stezowski, E. Clément, C. Michelagnoli, A. Korichi, C. Andreoiu, A. Astier, G. de Angelis, G. de France, C. Delafosse, I. Deloncle, F. Didierjean, Z. Dombradi, C. Ducoin, A. Gadea, A. Gottardo, D. Guinet, B. Jacquot, P. Jones, T. Konstantinopoulos, I. Kuti, F. Le Blanc, S. M. Lenzi, G. Li, R. Lozeva, B. Million, D. R. Napoli, A. Navin, R. M. Pérez-Vidal, C. M. Petrache, D. Ralet, M. Ramdhane, N. Redon, C. Schmitt, and D. Sohler. Excitations of the magic $N = 50$ neutron-core revealed in $^{81}$Ga. *Phys. Rev. C*, 100:011301, Jul 2019.

[102] V. Paziy, L. M. Fraile, H. Mach, B. Olaizola, G. S. Simpson, A. Aprahamian, C. Bernards, J. A. Briz, B. Bucher, C. J. Chiara, Z. Dlouhý, I. Gheorghe, D. Ghiţă, P. Hoff, J. Jolie, U. Köster, W. Kurcewicz, R. Lică, N. Mărginean, R. Mărginean, J.-M. Régis, M. Rudigier, T. Sava, M. Stănoiu, L. Stroe, and W. B. Walters. Fast-timing study of $^{81}$Ga from the $\beta$ decay of $^{81}$Zn. *Phys. Rev. C*, 102:014329, Jul 2020.

[103] L.M. Fraile et al. l-forbidden M1 transitions in semi-magic nuclei. *Nuclear Structure and Dynamics NSD*, 2024.

[104] P.D. Bond and G.J. Kumbartzki. Coulomb excitation of $^{85}Rb$ and $^{87}Rb$. *Nuclear Physics A*, 205(2):239–248, 1973.

[105] L. W. Fagg, E. H. Geer, and E. A. Wolicki. Coulomb excitation of V, Ni, Ga, and Rb. *Phys. Rev.*, 104:1073–1076, Nov 1956.

[106] D. G. Alkhazov, V. D. Vasil'ev, I. Kh. Gusinskii, I. Kh. Lemberg, and V. A. Nabichvrishvili. Angular distribution of gamma radiation emitted in Coulomb excitation of

odd-A nuclei. *Bulletin of the Academy of Sciences of the USSR / Physical series*, 28:1575–1587, 1964.

[107] H. Blok, E.A.J.M Offermann, C.W. De Jager, and H. De Vries. Path reconstruction and resolution improvement in magnetic spectrometers. *Nuclear Instruments and Methods in Physics Research A*, 262(291-297), 1987.